Title
E Pluribus Unum: Cosmological Analysis of Heterogenous Supernova Ia Datasets

Author
Rubin, David Arnold

Publication Date
2013

Peer reviewed|Thesis/dissertation

E Pluribus Unum: Cosmological Analysis of Heterogenous Supernova Ia Datasets

by

David Arnold Rubin

A dissertation submitted in partial satisfaction of the

requirements for the degree of

Doctor of Philosophy

in

Physics

in the

Graduate Division

of the

University of California, Berkeley

Committee in charge:

Professor Saul Perlmutter, Chair

Professor Daniel Kasen

Professor James Graham

Spring 2013

E Pluribus Unum: Cosmological Analysis of Heterogenous Supernova Ia Datasets

Abstract

E Pluribus Unum: Cosmological Analysis of Heterogenous Supernova Ia Datasets

by

David Arnold Rubin

Doctor of Philosophy in Physics

University of California, Berkeley

Professor Saul Perlmutter, Chair

This dissertation chronicles the development of the "Union" SN Ia analyses. These analyses address the challenges of supernova cosmology with uniform treatment of light-curve fitting, selection cuts, and outlier rejection. They were the first analyses to propagate systematic uncertainties into a covariance matrix, allowing constraints including systematics to be computed for any cosmological model. To minimize unintentional biases towards the concordance cosmology, each analysis was developed with the cosmology hidden ("blinded"). With each Union compilation version, we combine with BAO and CMB constraints to compute the then-best constraints on dark energy.

Chapter 2 provides the basic analysis outline that remains in place for subsequent compilations. Using the resulting compilation of 307 SNe (after cuts), we combine with BAO and CMB data and find that the equation of state parameter w is constrained to be $-0.969^{+0.059}_{-0.063}$ (statistical uncertainties only) $^{+0.086}_{-0.091}$ (with systematics) for a flat universe with constant w. For non-constant w, no real constraints ($\sigma_w \sim 1$) are possible above redshift 0.5.

Chapter 3 follows our application of the Union compilation to a range of dynamical dark energy models. We find that many classes of physical models are indistinguishable from ΛCDM with the current level of data.

In Chapter 4, we present an update of the Union compilation framework, with improved light-curve fitting and an improved treatment of systematic uncertainties. This new compilation, now consisting of 557 supernovae, gives constraints of $w = -0.997^{+0.050}_{-0.054}$ (statistical) $^{+0.077}_{-0.082}$ (with systematics) when combined with BAO and CMB data.

Chapter 5 outlines supernova discoveries from the HST Cluster Supernova Survey, with 14 cosmologically useful high-redshift SNe passing Union selection cuts. We present the photometry of the undersampled IR images, accomplished by directly modeling the pixels as observed. The photometry quality approaches photon-limited statistics. We also update the Union compilation to remove the effect of host-galaxy environment on corrected supernova distances. Using our updated compilation of 580 SNe, with BAO, CMB, and H_0 measurements, we find a constraint on the equation of state parameter of $w = -1.008^{+0.050}_{-0.054}$ (statistical) or $-1.013^{+0.068}_{-0.073}$ (with systematics).

Chapter 6 presents the analysis of a SN discovered in an SCP search of GOODS that did not have a firm redshift at the time of discovery. An archival WFC3 IR spectrum enabled us to get the redshift of the likely host galaxy. With this redshift in hand, we used a novel PCA-like classification to confirm the supernova as a Ia with 92% confidence. At $z = 1.713$, this was until recently the highest-redshift SN Ia with spectroscopic confirmation, and it remains the highest one with a precision color measurement. Although limited by our sample size of one, we see no evidence of population evolution.

Finally, Chapter 7 concludes with proposed Bayesian improvements that will yield even better cosmological constraints.

Dedicated to my parents, Jan and Michael,
my grandfather, Aaron,
and my wife, Ashley.

Acknowledgments

This was the result of a team effort and I am indebted to many people. First, I would like to thank **Kyle Dawson** and **Saul Perlmutter** for recruiting me to work in the Supernova Cosmology Project (SCP), **Natalia Connolly** for helping me get started with processing images and subtractions, **Gerson Goldhaber** for teaching me to find supernovae, and **Kyle Barbary** for his work on the subtraction pipeline (and HST proposals!).

I owe a lot to **Marek Kowalski** for inviting me to participate in the cosmological analysis and developing the Union concept with me. I would also like to thank **Eric Linder** for answering many cosmology-related questions, and really applying his cosmological understanding to our Beyond Lambda paper. **Chris Lidman** contributed greatly to my understanding of observations and calibration.

I am also thankful to **Nao Suzuki** for his work processing the ACS images, and his insistence that PCA should be always be used. **Eric Hsiao** did the dirty work of cleaning up NICMOS images and **Vitality Fadeyev** taught me about photometry so that I could make good use of the data. Thanks also to **Eli Rykoff** for his work on the HST processing pipeline, and **Jakob Nordin** for his work also with HST (and HST proposals!). I would also like to thank **Susana Deustua** and **Andy Fruchter** for all their HST-related advice.

I was always happy to run ideas by **Josh Meyers**, **Hannah Fakhouri** (whom I also have to thank for her thorough manuscript feedback), **Clare Saunders**, and **Rahman Amanullah**. Thanks also should go to **Alex Gude** for many computing and weightlifting discussions. **Tony Spadafora** deserves many thanks for so much SCP knowledge and advice. **Greg Aldering** and **Saul Perlmutter** deserve special thanks for valuable in-depth feedback every step of the way (and especially thorough reviews of manuscripts!). I would also like to thank **Alex Kim** and **Rollin Thomas** for their feedback on everything from WFIRST to data analysis. **Mark Strovink**'s feedback on an analysis was always valuable; no one is better at keeping people on their toes.

So many of us in the Physics Division are indebted to **Bryan Abshier** and **Jeff Anderson** for keeping our computing running smoothly.

These acknowledgements are nowhere near complete. I have gained so much from many teachers, colleagues, and relatives who have shaped and encouraged my intellectual development.

I would also like to thank my dissertation committee, **Dan Kasen**, **Saul Perlmutter**, and **James Graham**.

Finally, I obviously owe a great debt of gratitude to **Ashley Rubin** for enriching me in so many ways.

Financial support for this work was provided by NASA through program GO-10496 from the Space Telescope Science Institute, which is operated by AURA, Inc., under NASA contract NAS 5-26555. This work was also supported in part by the Director, Office of Science, Office of High Energy and Nuclear Physics, of the U.S. Department of Energy under contract No. AC02-05CH11231, as well as a JSPS core-to-core program International Research Network for Dark Energy and by JSPS research grant 20040003.

Contents

List of Figures

List of Tables

CHAPTER 1

Introduction: Type Ia Supernova Cosmology

1.1 Cosmology with Type Ia Supernovae

Going back to Baade and Zwicky, there have been proposals to measure the expansion of the universe with supernovae as standard candles. Unfortunately, the magnitude dispersion of all classes of SNe was too large to achieve this goal. After Type Ia were recognized as their own class (Panagia 1985; Uomoto & Kirshner 1985; Wheeler & Levreault 1985) and studied in more detail, light-curve corrections (discussed below) made them practical distance indicators.

The rapid progression of CCD detectors, computing, and wide-field cameras (Couch et al. 1991), as well as the "SNe on-demand" strategy (Perlmutter et al. 1994), allowed efficient pre-scheduling of followup spectroscopy and imaging. After ten years of work, these SN measurements enabled the discovery of the accelerating expansion of the universe (Riess et al. 1998; Perlmutter et al. 1999). In the fifteen years since that discovery, greater numbers of SNe, spanning up to double the redshift of the original samples, are key to providing the best constraints yet on the behavior of dark energy. As the SN Ia Hubble diagram gained statistical power with larger and larger sets of SNe, the systematic uncertainties became dominant. This dissertation is devoted to the detailed treatment of the use of SNe Ia for cosmological constraints, and the understanding and impact of the systematic uncertainties present in the data.

1.1.1 Light-Curve Fitting

Currently, SN Ia cosmological constraints are obtained from photometric observations, with spectroscopy only used for identifying SNe Ia and obtaining redshifts. Although much information about each supernova is undoubtably lost in integrating the SED over filters, current spectroscopic observations are not good enough at cosmological redshifts to significantly improve on photometric-only distances (Walker et al. 2011).

SNe Ia show a relation between slower decline rates and brighter luminosities (Phillips 1993). The decline rate and the inverse rise time also have a good correlation (Perlmutter et al. 1997; Goldhaber et al. 2001; Strovink 2007), enabling the useful concept of lightcurve "stretch," a linear temporal scale factor. This lightcurve diversity is related to the properties of the progenitor (Hamuy et al. 1996a; Sullivan et al. 2003), which likely evolves with redshift. Correcting for this relation is therefore essential, requiring lightcurves spanning the peak of the lightcurve to at least ~ 1 magnitude fainter.

There is also a relation between broadband bluer optical colors and brighter luminosities (Tripp 1998). Some of this must be due to extinction, but this is also confounded by variation in spectral features. Only with spectrophotometry can the two be distinguished (Chotard et al. 2011). In addition to removal of some of the evolution in dust with redshift (as younger galaxies have more dust on average), correcting the color-magnitude relation also removes most of the Malmquist bias. This correction requires multi-band lightcurves with S/N of at least ~ 20.

The distance estimates discussed here rely on fitting a parametrized SED to the observed photometry. In the light curve fitters discussed here[1], four parameters must be fit: the phase of the supernova, a normalization value, the supernova color, and the light-curve decline rate or shape. The SALT model (Guy et al. 2005) uses a single model of an SED, which it warps with lightcurve stretch and color. SALT2 (Guy et al. 2007) improves on this with a linearized model for the change in SED with lightcurve stretch, but still warps this with color.

1.1.2 Systematic Uncertainties

The dominant systematic uncertainty in supernova cosmology is photometric calibration (see Section 5.3.5 and Conley et al. (2011)). Although this is an area where there has been rapid improvement, the large numbers of SNe coming from forthcoming surveys will likely imply that calibration uncertainties will remain important for the foreseeable future. Note however that subdivisions within a sample may be much less sensitive to calibration uncertainties than sample-to-sample comparisons, allowing searches for astrophysical systematics that are not calibration-limited.

The next-most important systematic uncertainty is likely the proper treatment of supernova diversity. As no light-curve fitter can perfectly match all data, an estimate of the unexplained variance must be simultaneously determined with the training of the fitter. I briefly discuss this important point in Chapter 7. Without high-quality spectroscopy, our controls over population drift are limited and must be searched for using correlations with host galaxy properties (e.g., Sullivan et al. 2003, 2006; Kelly et al. 2010).

[1] There is evidence that fitting more than these parameters can significantly improve distance estimation (Kim et al. 2013).

1.1.3 The Heterogenous Existing Datasets

There are multiple sources of data heterogeneity. High-redshift datasets tend to lack red rest-frame observations, as these would require expensive near-IR measurements, forcing most high-redshift data to rely on a bluer rest-frame wavelength range than low-redshift SNe. Most high-redshift SNe are discovered and measured in "rolling" searches, in which lightcurves are built up by periodically imaging the same fields, giving phase coverage generally starting well before maximum light. In contrast, most nearby SNe are discovered with a separate search, then followed up to build their lightcurves. These SNe tend to have data starting closer to maximum, so sensitivity to the pre-max shape of the template can enter the cosmological fits.

Much of the systematic uncertainties plaguing supernova cosmology are especially acute at the low-redshift end. Most nearby SNe come from targeted galaxy searches, in which known galaxies are repeatedly observed to find candidates. These searches necessarily have a higher (by a factor of several) average host mass (and higher host metallicity, with a lower specific star-formation rate) than untargeted surveys, adding astrophysical systematics. Nearby lightcurves are typically calibrated to Landolt system (Landolt 1992), which is an amalgam of stellar observations that have been matched together. There is therefore more internal tension than in more modern standard star networks which are assembled from one instrument. The Landolt system effective filter throughputs can only be approximated, and it is therefore difficult to precisely calibrate to spectrophotometric standards. I note that a new low-redshift spectrophotometric dataset will soon be available from the Nearby SuperNova factory (SNf). This dataset is calibrated to spectrophotometric standards, and will remove about half of the current calibration uncertainties, but I do not discuss this in my dissertation.

1.2 Dissertation Outline

The remainder of this dissertation presents the chronological development of the "Union" supernova Ia compilations and their extension with data from the *Hubble Space Telescope*.

Chapter 2 covers the challenges of working with the (then) existing supernova datasets, discussing selection cuts, outlier rejection, tension between samples, heterogenous quality, and systematic uncertainties. This effort was developed with the cosmological constraints hidden until the analysis was finalized, a practice that still sets Supernova Cosmology Project (SCP) and SuperNova factory (SNf) work apart in the supernova community. It was also the first analysis to estimate a covariance matrix describing the impact of systematic uncertainties on distance moduli. Prior systematics analysis computed the impact of each systematic on Ω_m or w and summed these effects in quadrature, which is not a generalizable approach. This work was previously published as Sections 3 to 7 of Kowalski et al. (2008). The omitted sections of that paper presented a new low-redshift dataset to which this author did not contribute.

Chapter 3 applies this "Union" compilation to a diverse array of dark energy models. I take advantage of the covariance-matrix-based systematics approach to compute cosmological constraints including systematic uncertainties for models not envisioned when conducting the systematics analysis. This chapter was previously published as Rubin et al. (2009).

After the analysis presented in Chapter 2, the Union compilation still had significant room for improvement. We treated each supernova as equally affected by each systematic. The Union2 compilation, described in Chapter 4, changed this. I began computing the sensitivity of each supernova to each calibration systematic. In addition to accurate propagation of photometric calibration uncertainties, these sensitivities also allowed me to exactly propagate the uncertainties in Milky-Way and intergalactic extinction. This material was previously published as Sections 6, 7, 8, and the final appendix of Amanullah et al. (2010). The omitted sections of that paper presented a new high-redshift dataset to which this author did not contribute.

Chapter 5 extends the Union2 analysis with the data from the *Hubble Space Telescope* Cluster Supernova Survey. This survey was conducted by a small team of which this author was a key member. In Section 5.2, I describe the construction of the generative models (forward models) that I used for the IR photometry. Section 5.3.1 describes my removal of the effect of supernova environment on corrected distance modulus, as discovered by Kelly et al. (2010); Sullivan et al. (2010). This chapter was previously published as Sections 1-3 from Suzuki et al. (2012). The omitted sections contain some background material and the description of the optical photometry, to which this author did not contribute.

I used recent serendipitous observations to obtain a redshift (and therefore a secure type) for a supernova from an SCP search of GOODS, described in Chapter 6. This supernova was, until 2013, the highest-redshift spectroscopically confirmed type Ia and remains the highest redshift supernova with a precision distance. This chapter was previously published as Rubin et al. (2013).

Chapter 7 concludes this work and discusses future Bayesian improvements to this compilation.

CHAPTER 2

Union

2.1 Introduction

This chapter describes the construction of the first "Union" supernova Ia compilation. The then existing supernova datasets were heterogeneous in light-curve quality and wavelength coverage, making a consistent selection of SNe across redshift challenging. We search for tension between datasets, which could be indicative of calibration systematics, selection effects, or supernova evolution. No significant tensions are seen. Prior systematics analyses have been of the "shift-and-add" variety: the impact of each systematic on Ω_m or w is computed and summed in quadrature. This limited approach cannot be generalized after the fact to cosmological models and data not considered in the original analysis. The Union analysis was the first to estimate a covariance matrix describing the impact of systematic uncertainties on the distance moduli, [1] allowing the community to use this compilation for new cosmological constraints. Additionally, this compilation was developed with the cosmological constraints hidden until the analysis was finalized, a practice that still sets Supernova Cosmology Project (SCP) and SuperNova factory (SNf) work apart in the supernova community. I use this compilation to compute the then-best constraints on the dark energy equation of state. [2]

2.2 Lightcurves

2.2.1 Literature supernovae

Here we discuss the set of previously published nearby and distant supernovae included in the analysis. Not all SN lightcurves are of sufficiently good quality to allow their cosmological use. For all supernovae in the sample, we require that data from at least two bands

[1] The discussion in this chapter is in terms of nuisance parameters that are fit out with the cosmology, see Section A.1 for the relationship between these nuisance parameters and the equivalent covariance matrix.

[2] This work was previously published as Sections 3 to 7 of Kowalski et al. (2008). The omitted sections of that paper presented a new low-redshift dataset to which this author did not contribute.

with rest-frame central wavelength between 3470 Å (U-band) and 6600 Å (R-band) exist and that there are in total at least five data points available.

Further, we require that there is at least one observation existing between 15 days before and 6 days after the date of maximal B-band brightness, as obtained from an initial fit to the lightcurves (see section 2.2.2). The 6 day cut is scaled by stretch for consistency. In addition, we observed that for a smaller number of poorer lightcurves, the uncertainties resulting from the fits are unphysically small compared to what is expected from the photometric data. In these cases, we randomly perturb each data point by a tenth (or if necessary by a fifth) of its photometric error and refit the lightcurves. The remaining 16 SNe, where convergence can not be obtained even after perturbation of the data, are excluded from further analysis (note that these SNe are generally poorly measured and would have low weight in any cosmological analysis).

For the nearby SN sample, we use only supernovae with CMB-centric redshifts $z > 0.015$, in order to reduce the impact of uncertainty due to host galaxy peculiar velocities. We checked that our results do not depend significantly on the value of the redshift cut-off (tested for a range $z = 0.01 - 0.03$).

The number of SNe passing these cuts are summarized in Table 2.1. Each individual supernova is listed in Table 11, and the last column indicates any cuts that the supernova failed.

The list contains 17 supernovae from Hamuy et al. (1996b), 11 from Riess et al. (1999), 16 from Jha et al. (2006), and 6 from Krisciunas et al. (2004a,b, 2001). Our lightcurve data for SN 1999aa are merged with that of Jha et al. (2006). To this list of nearby supernovae from the literature we add the 8 new nearby supernovae presented in Kowalski et al. (2008). For SN 1999aw, we use only the lightcurve data presented in that paper. Hence the sample contains 58 nearby supernovae.

The sample of high redshift supernovae is comparably heterogeneous. We use all of the 11 SNe from Knop et al. (2003) that have lightcurves obtained with HST. Of the 42 supernovae from Perlmutter et al. (1999), 30 satisfy the selection cuts described above. Of the 16 SNe used by the High-Z Team (HZT) (Riess et al. 1998; Garnavich et al. 1998; Schmidt et al. 1998), two are already included in the Perlmutter et al. (1999) sample and of the remaining 14, 12 pass our cuts.

Included also are 22 SNe from Barris et al. (2004), and the 8 SNe from Tonry et al. (2003) that are typed to be secure or likely SNe Ia. We do not use SN 1999fv and SN 1999fh, as the number of available data points does not exceed the number of lightcurve fit parameters.

We add the 73 SNe Ia from the first year of SNLS (Astier et al. 2006), of which one does not pass the first phase cut (03D3cc). Note that, in Astier et al. (2006), 2 of the 73 supernovae were excluded from their cosmological parameter fits because they were significant outliers (see discussion in section 2.3.3). Riess et al. (2004, 2007) have published 37 supernovae which were discovered and followed using HST. Of these, 29 passed our lightcurve quality cuts. This sample contains the highest redshift supernovae in our compilation. Finally, we use the 84 SNe from the ESSENCE survey (Miknaitis et al. 2007;

Wood-Vasey et al. 2007), of which 75 pass our cuts.

Requirement	$N_{\rm SN}$
all	414
$z > 0.015$	382
Fit successful	366
Color available	351
First phase < 6 d	320
≥ 5 data points	315
Outlier rejection	307

Table 2.1. Number of SNe after consecutive application of cuts. See 2.3.3 for a discussion of the outlier rejection cut.

2.2.2 Lightcurve fitting

The spectral-template-based fit method of Guy et al. (2005) (also known as SALT) is used to fit consistently both new and literature lightcurve data. This method is based on a spectral template (Nugent et al. 2002) which has been adapted in an iterative procedure to reproduce a training set of nearby SNe $UBVR$ lightcurve data. The training set consists of mostly $z < 0.015$ SNe and hence does not overlap with the sample we use for determination of cosmological parameters. To obtain an expected magnitude for a supernova at a certain phase, the model spectrum is first redshifted to the corresponding redshift followed by an integration of the product of spectrum and band pass transmission. The spectral-template based fit method has the advantage that it consistently allows the simultaneous fit of multi-band light curves with arbitrary (but known) band pass transmission functions. In view of the large number of filters and instruments used for the new nearby SN samples as well as the very diverse lightcurve data found in the literature, this is particularly important here. In addition, frequent practical problems associated with K-corrections—such as the propagation of photometric errors—are handled naturally.

The spectral template based fit method of Guy et al. (2005) fits for the time of maximum, the flux normalization as well as rest-frame color at maximum defined as $c{=}B - V|_{t=B_{\rm max}} + 0.057$ and time-scale stretch s. It is worth noting that by construction, the stretch in SALT has a related meaning to the conventional time-axis stretch (Perlmutter et al. 1997; Goldhaber et al. 2001). However, as a parameter of the lightcurve model it also absorbs other, less pronounced, stretch dependent lightcurve dependencies. The same is true for the color c.

Recently, direct comparisons between alternative fitters, such as SALT, its update (Guy et al. 2007) as well as MLCS2k2 (Jha et al. 2007) show good consistency between the fit results, e.g. the amount of reddening (Conley et al. 2007). Our own tests have shown that

for well observed supernovae, the method produces very consistent results (peak magnitude, stretch) when compared to the more traditional method of using light-curve templates (Perlmutter et al. 1997). However, we noticed that fits of poorly observed lightcurves in some cases do not converge properly. Part of the explanation is that in the case of the spectral template based fit method, the data before $t < -15$ days is not used as an additional constraint. More typically, the SALT fitter can fall into an apparent false minimum and we then found it necessary to restart it repeatedly to obtain convergence. Note that the small differences between the lightcurve fit parameters of Table 11 and the values shown in Table 10 of Wood-Vasey et al. (2007) are primarily cases where the Wood-Vasey et al. (2007) SALT fit did not converge (some of which are noted in Wood-Vasey et al. (2007)) and a few cases where we found it necessary to remove an extreme outlier photometry point from the lightcurve.

The lightcurves from Barris et al. (2004) and the I-band lightcurves of 4 supernovae of Perlmutter et al. (1999) (SNe 1997O, 1997Q, 1997R, and 1997am, see also Knop et al 2003) need a different analysis procedure, since in these cases the light of the host galaxy was not fully subtracted during the image reduction. We hence allow for a constant contribution of light from the host galaxy in the lightcurve fits. These supernovae were fit with additional parameters: the zero-level of the I-band lightcurve in case of the four SNe from the Perlmutter et al. (1999) set and the zero-level of all the bands in case of the Barris et al. (2004) data. The additional uncertainties due to these unknown zero-levels have been propagated into the resulting lightcurve fit parameters.

The fitted lightcurve parameters of all SNe can be found in Table 11 which is also available in electronic form[3].

2.3 Hubble diagram construction and cosmological parameter fitting

The full set of lightcurves as described in section 2.2.1 have been fitted, yielding B-band maximum magnitude $m_B^{\max}$, stretch s, and color c=$B - V|_{t=B_{\max}} + 0.057$. In this section, these are input to the determination of the distance modulus. The analysis method is chosen to minimize bias in the estimated parameters (see section 2.3.2). An outlier rejection based on truncation is performed which is further described in section 2.3.3, before constraints on the cosmological parameters are computed.

2.3.1 Blind analysis

Following Conley et al. (2006a), we adopt a blind analysis strategy. The basic aim of pursuing a blind analysis is to remove potential bias introduced by the analyst. In particular, there is a documented tendency (see for example Yao et al. (2006)) for an analysis

[3] http://supernova.lbl.gov/Union

to be checked for errors in the procedure (even as trivial as bugs in the code) up until the expected results are found but not much beyond. The idea of a blind analysis is to hide the experimental outcome until the analysis strategy is finalized and debugged. However, one does not want to blind oneself entirely to the data, as the analysis strategy will be partially determined by the properties of the data. The following blindness strategy is used, which is similar to the one invented in Conley et al. (2006a). The data is fit assuming a ΛCDM cosmology, with the resulting fit for $\Omega_{\rm M}$ stored without being reported. The flux of each supernova data point is then rescaled according to the ratio of luminosity distances obtained from the fitted parameters and arbitrarily chosen dummy parameters (in this case $\Omega_{\rm M} = 0.25, \Omega_\Lambda = 0.75$). This procedure preserves the stretch and color distribution, and as long as the fitted parameters are not too different from the target parameters approximately preserves the residuals from the Hubble diagram. In developing the analysis, one is only exposed to data blinded by the procedure described above. Only after the analysis is finalized and the procedure frozen, is the blinding turned off.

Note that this prescription allows — in a consistent way — the inclusion of future data samples. A new data sample would be first investigated in a blind manner following the tests outlined in section 2.3.4, and if no anomalies are observed, one would combine it with the other data sets.

2.3.2 Unbiased parameter estimation

Type Ia supernova obey a redder-dimmer relation and a wider-brighter relation (Phillips 1993). The redder-dimmer relation in principle can be explained by dust extinction; however, the total to selective extinction ratios generally obtained empirically are smaller than expected from Milky-Way-like dust (Tripp 1998; Tripp & Branch 1999; Parodi et al. 2000; Guy et al. 2005; Wang et al. 2006). At the same time, the exact slope of the stretch-magnitude relation is not (yet) predicted by theory. The absence of a strong theoretical prediction motivates an empirical treatment of stretch and color corrections. Here we adopt the corrections of Tripp (1998) (see also Tripp & Branch (1999); Wang et al. (2006); Guy et al. (2005) and Astier et al. (2006)):

$$\mu_B = m_B^{\rm max} - M + \alpha(s-1) - \beta c, \tag{2.1}$$

Since the β-color correction term must account for both dust and any intrinsic color-magnitude relation, it is clearly an empirical approximation. The validity of β-color correction relies on only one assumption, that is, nearby supernovae and distant supernovae have an identical magnitude-color relation. If either the intrinsic SNe properties or the dust extinction properties of the supernovae are evolving with redshift, these assumptions may be violated. Observational selection effects may also introduce biases which invalidate equation 2.1. These potential sources of systematic error will be evaluated in section 2.4.1.

The χ^2 corresponding to Eq. 2.1 is given as:

$$\chi^2 = \sum_{\mathrm{SNe}} \frac{(\mu_B - \mu(\Omega_{\mathrm{M}}, \Omega_\Lambda, w))^2}{\sigma_{m_B}^2 + \sigma_{\mathrm{tot}}^2 + \sigma_{\mathrm{sys}}^2 + (\beta\sigma_c)^2 + (\alpha\sigma_s)^2 + 2\alpha C(m,s) - 2\beta C(m,c) - 2\alpha\beta C(s,c)}. \tag{2.2}$$

σ_{m_B}, σ_c and σ_s represent the statistical uncertainty on the peak magnitude, color and stretch, as obtained from the light-curve fit, and $C(m,s)$, $C(m,c)$ and $C(c,s)$ represent their respective covariance terms. σ_{tot} represents an astrophysical dispersion obtained by adding in quadrature the dispersion due to lensing, $\sigma_{\mathrm{lens}} = 0.093z$ (see Section 2.4.6), the uncertainty in the Milky-Way dust extinction correction (see Section 2.4.8) and a term reflecting the uncertainty due to host galaxy peculiar velocities of 300 km/s. The dispersion term σ_{sys} contains an observed sample-dependent dispersion due to possible unaccounted-for systematic and statistical errors. In section 2.3.3 we discuss the contribution σ_{sys} further.

Note that Eq. 2.2 can be derived using minimization of a generalized χ^2. Defining a residual vector for a supernova $\mathbf{R} = (\mu_B - \mu_{\mathrm{model}}, s - s', c - c')$ and supposing that the light-curve fit returns covariance matrix $\mathbf{C}$, we can write

$$\chi^2 = \sum_{\mathrm{SNe}} \mathbf{R}^T \mathbf{C}^{-1} \mathbf{R}. \tag{2.3}$$

Here, s' and c' take the role of the true stretch and color, which have to be estimated from the measured ones. Minimizing this equation over all possible values of s' and c' gives the χ^2 in Eq. 2.2. The χ^2 is minimized, not marginalized, over α and β; marginalization would yield a biased result due to the asymmetry of the χ^2 about the minimum.[4]

Frequently, Eq. 2.2 is minimized by updating the denominator iteratively, i.e. only between minimizations (see for example Astier et al. (2006)). As shown in Fig. 2.1 and discussed next, this method produces biased fit results, an artifact previously noted by Wang et al. (2006).

We use a Monte Carlo simulation to estimate any biases from the fitting procedure. Random supernova samples resembling the observed one are generated and then fitted. The true stretch and color are sampled from a normal distribution of width 0.1 and for the peak magnitude an intrinsic dispersion of 0.15 magnitudes is assumed. A further dispersion corresponding to the measurement errors is added. By construction, the SN samples have the same redshift and stretch, color and peak magnitude uncertainties as the real sample. The test values for α and β were chosen as 1.5 and 2.5. This bias on α and β, as would be obtained from the iterative method's fits to the simulated data sets, is visible in Figure 2.1 as the unshaded histogram. The large potential bias on β ($\Delta\beta \sim -0.5$), if the χ^2 had been chosen according to Equation 2.2 with the iteratively updated denominator, is a result of the fact that the measurement error on c for high redshift SNe is similar to and often even exceeds the width of the color distribution itself.

We have investigated other sources of bias in the fitted parameters. A measurement bias will be introduced because overall, brighter SNe will have smaller photometric errors, and

[4]Note that using the angle of the line (i.e., $\beta = \tan\theta$) gives a much more symmetric minimum.

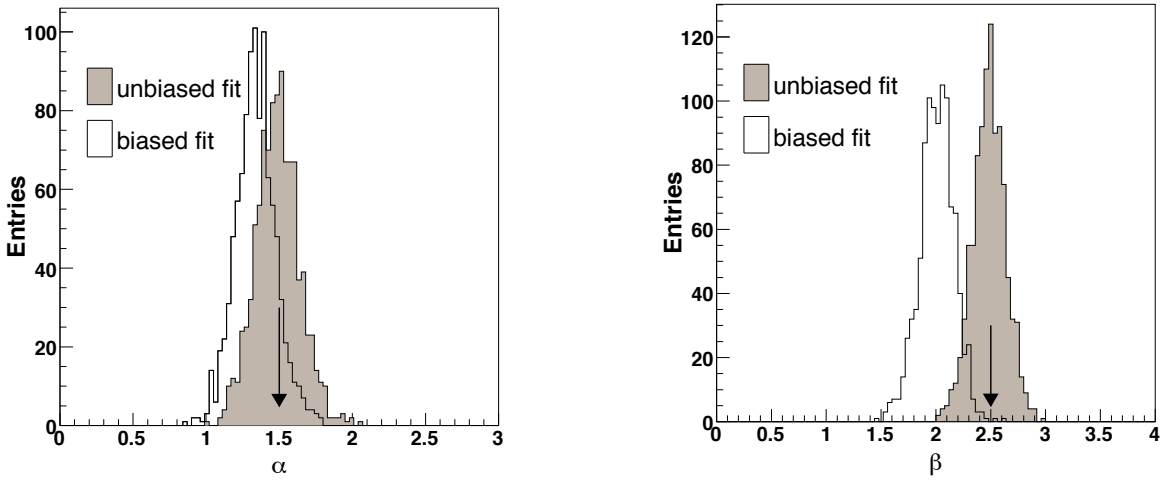

Figure 2.1. Monte Carlo simulation of the resulting α (left) and β (right) distributions as fitted with the unbiased and biased method. The true values $\alpha = 1.5$ and $\beta = 2.5$ are represented by the arrows.

hence larger weights, than dimmer ones. If the photometric error bars are small enough that the intrinsic dispersion dominates the uncertainty, this bias will be small. Hence low-

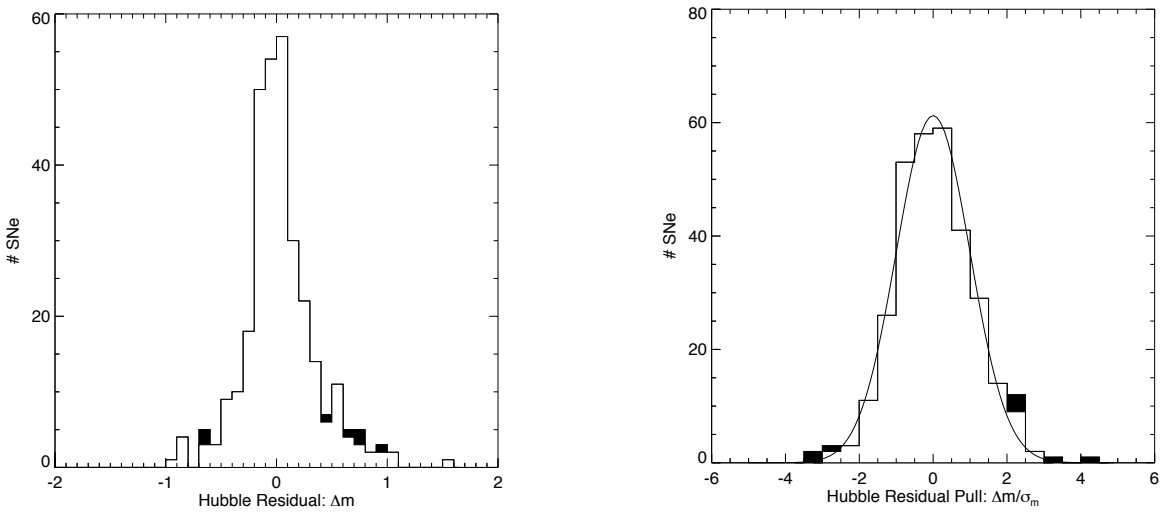

Figure 2.2. Residual of restframe, stretch and color corrected, B-band magnitude (left) and pull distribution (right) from the best fitting cosmology. The filled histogram shows the rejected outliers. The pull distribution is overlayed with a normal distribution of unit width.

redshift, well observed SNe are biased less than high-redshift, poorly observed SNe, resulting in biased cosmological parameters. This bias was studied using the Monte Carlo simulation described above. For the sample under investigation it was found to introduce a bias $\delta M = 0.01$. In principle this bias can be corrected; however, since it is roughly a factor of three smaller than the statistical or systematic uncertainties, we choose not to carry out this step.

2.3.3 Robust statistics

Figure 2.2 shows the distribution of rest-frame B-band corrected magnitude residuals (left) from the best fit as obtained with the full data set. The right plot shows the pull distribution, where the pull is defined as the corrected B magnitude residual divided by its uncertainty. The distributions have outliers which, if interpreted as statistical fluctuations, are highly improbable. Hence these outliers point to non-Gaussian behavior of the underlying data, due to either systematic errors in the observations, contamination or intrinsic variations in Type Ia SNe. The fact that an outlier is present even in the high quality SNLS supernova set (see Table 2.2) suggests that contamination or unmodeled intrinsic variations might be present. However, other samples that typically were observed with a more heterogeneous set of telescopes and instruments show larger fractions of outliers, indicating additional potential observation-related problems.

In order to limit the influence of outliers, we use a robust analysis technique. First, the SN samples are fit for M, the absolute magnitude of the SNe, using median statistics (see Gott et al. (2001) for a discussion of median statistics in the context of SN cosmology). The quantity minimized is $\chi = \sum_{\rm SNe} \frac{|\mu_B - \mu_{\rm model}|}{\sigma}$, where the uncertainty σ in the denominator includes the covariance terms in the denominator of the right hand side of Equation 2.2. We then proceed to fit each sample by itself using the α, β, and $\Omega_{\rm M}$ from the combined fit, as χ is not a well-behaved quantity for small numbers of SNe.

For each sample, we remove SNe with a pull exceeding a certain value $\sigma_{\rm cut}$ relative to the median fit of the sample. Currently available algorithms, which correct the peak magnitude using, e.g., stretch or Δm_{15}, are capable of standardizing SNe Ia to a level of $\sim 0.10 - 0.15$ magnitudes. To reflect this we add in quadrature a systematic dispersion to the known uncertainties. The list of known uncertainties include observational errors, distance modulus uncertainties due to peculiar velocities (with Δv =300 km/s) and gravitational lensing (relevant only for the highest redshift SNe; see section 2.4.6 for a discussion). The additional systematic dispersion has two components: a common irreducible one, possibly associated with intrinsic variations in the SN explosion mechanism, as well as an observer-dependent component. To obtain self-consistency the systematic dispersion is recalculated during the analysis. One starts by assuming a systematic dispersion of $\sigma_{\rm sys} = 0.15$ magnitudes, then computes the best fitting cosmology for the particular sample using median statistics, removes the outlier SNe with residuals larger than a cut value $\sigma_{\rm cut}$, iterates $\sigma_{\rm sys}$ such that the total χ^2 per degree of freedom is unity, and in a final step redetermines the best fitting cosmology using regular χ^2 statistics to obtain an updated $\sigma_{\rm sys}$. From

that point in the analysis, after outliers are rejected and $\sigma_{\rm sys}$ determined, only regular χ^2 statistics are applied.

When using a robust analysis, it is necessary to check that $a)$ in the absence of contamination the results are not altered from the Gaussian case and $b)$ in presence of a contaminating contribution, the impact of it is indeed reduced. In order to investigate this, we begin with a model for the contamination. We assume the data sample to be composed of two types of objects, one representing the desired SNe Ia and a second contribution characterizing the contamination. We then use a maximum-likelihood analysis of the observed pull distribution shown in Figure 2.2 (right) to determine the normalization, width and mean of the contaminating distribution. The uncontaminated pull distribution is assumed to be a Gaussian distribution of unit width and zero mean. The observed pull distribution is best fitted by an additional contaminating contribution that is 50% wider ($\sigma_m = 0.23$ mag) and which has a mean shifted by $\Delta m = 0.3\sigma_m$, normalized to 18 % of the area. A mock simulation that is based on this superposition of two normal distributions illustrates the benefits of using the robust analysis. Figure 2.3 (right) shows the bias of the mean relative to the center of the main component as a function of the outlier rejection cut value. Outlier rejection can reduce the bias by a factor of three with a remaining bias of less than 0.01 magnitude. Even for a wide range of contaminant parameters ($\sigma_m = 0.15 - 2; \Delta m = 0 - 2$ magnitudes) the bias obtained for the robust analysis remains below 0.015 magnitudes. Only in cases where the contamination is larger than 30% does the outlier rejection algorithm become unstable.

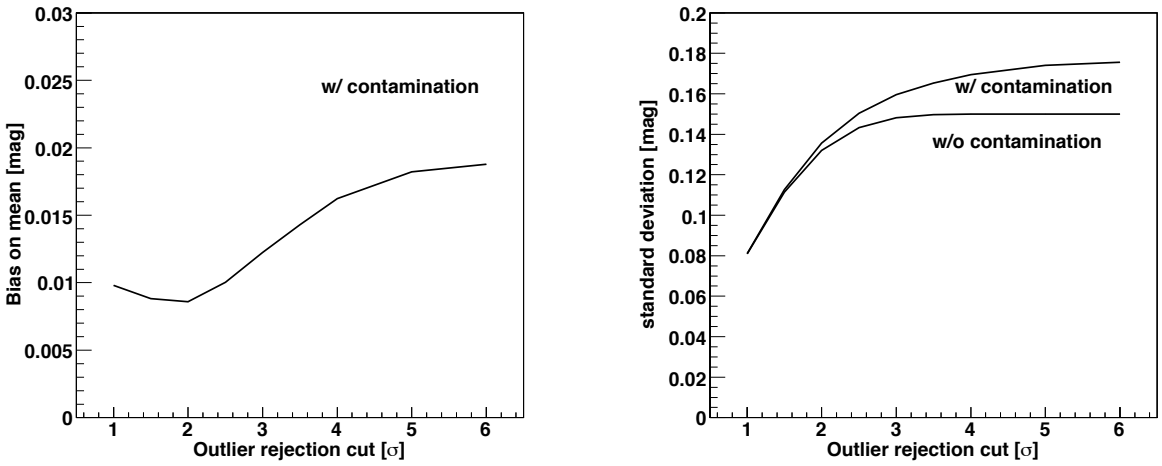

Figure 2.3. Mock simulation of bias (left panel) and standard deviation (right) of the mean magnitude as a function of the outlier rejection cut. The simulated SN set consists of one population of 270 SNe with intrinsic dispersion of 0.15 magnitudes and zero mean and a second population of 50 SNe with intrinsic dispersion of 0.26 mag and mean 0.13 mag. The effect of outlier rejection on a single population without contamination is shown as a reference curve.

Besides reducing the potential bias due to contamination, robust statistics can also lead

to tighter parameter constraints through reduction of the intrinsic dispersion. The right panel of Figure 2.3 shows for the simulated data the average standard deviation as a function of the outlier rejection cut for the 16 % contamination case described above. As a reference, the case of a single uncontaminated population of SNe is shown as well. Note that a cut at 3σ reduces the dispersion noticeably in the case of a contaminated sample, while the uncontaminated single population is affected negligibly (the standard deviation is reduced by 1.3 %, e.g. from 0.15 to 0.148 magnitudes).

For the real data, we consider two values $\sigma_{\rm cut} = 2, 3$ as well as the case in which all SNe are kept. We chose as our main cut value $\sigma_{\rm cut} = 3$ since, after application of the outlier rejection, standard χ^2 statistics is still a good approximation while at the same time a potential bias introduced by contamination is significantly reduced. Note also that the impact of individual SNe that have residuals close to $\sigma_{\rm cut}$ is small for large statistics: an additional SN will shift the mean distance modulus of $N_{\rm SNe}$ by at most $\sigma_{\rm cut}/\sqrt{N_{\rm SNe}}$ standard deviations. Hence for $N_{\rm SNe} \gtrsim 10$ and $\sigma_{\rm cut} = 3$ the algorithm can be considered stable relative to fluctuations of individual SNe.

2.3.4 Sample characteristics, dispersion and pull

Figure 2.4 illustrates the heterogeneous character of the samples. It shows the Hubble and residual diagrams for the various samples, as well as the histogram of the SN residuals and pulls from the best fit. The difference in photometric quality is illustrated in the rightmost column of Fig. 2.4, by showing the error on the color measurement. As can be seen, some samples show a significant redshift dependent gradient in the errors, while others have small, nearly constant errors (most notably the sample of Knop et al. (2003)). The sample of Astier et al. (2006) shows a small color uncertainty up to $z \leq 0.8$, and degrades significantly once the color measurement relies on the poorer z-band data (c.f. SALT2 (Guy et al. 2007), which is capable of incorporating lightcurve data bluer than rest-frame U).

Our analysis is optimized for large, multi-color samples such as that of Astier et al. (2006), since these now dominate the total sample. There is often a better analysis approach for any given specific sample that would emphasise the strengths of that sample's measurements and yield a tighter dispersion and more statistical weight. However, for this combined analysis of many samples it was more important to use a single uniform analysis for every sample, at the cost of degrading the results for some of the smaller samples. This particularly affects some of the very earliest samples, such as Riess et al. (1998), Perlmutter et al. (1999), and Barris et al. (2004), where the color measurements had originally been used with different priors concerning the dust distribution. Treating these samples with the current analysis thus gives significantly larger dispersions (and hence less weight) to these samples than their original analyses. As a check, we have verified that by repeating the analysis according to Perlmutter et al. (1999) we reproduce the original dispersions using SALT.

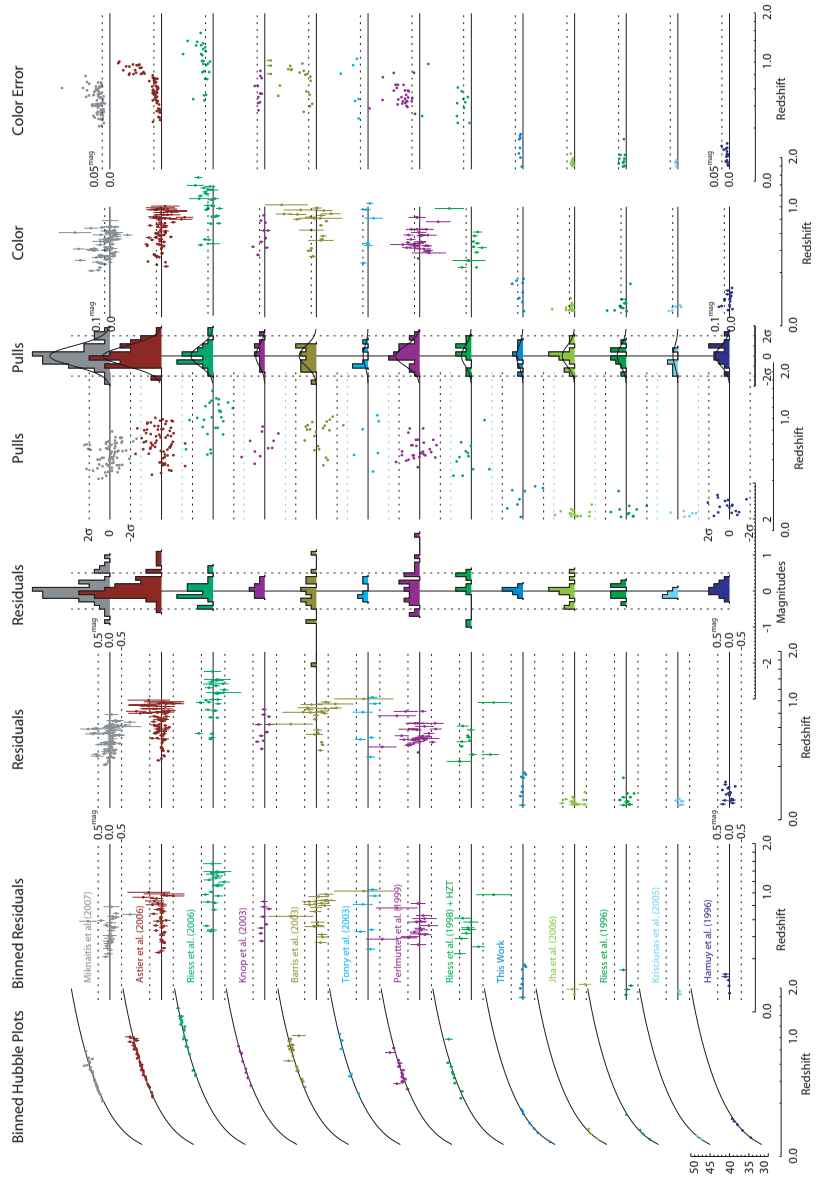

Figure 2.4. From left to right: a) Hubble diagrams for the various samples; b) binned magnitude residuals from the best fit (bin-width: $\Delta z = 0.01$); c) unbinned magnitude residuals from the best fit; d) histogram of the residuals from the best fit; e) pull of individual SNe as a function of redshift; f) histogram of pulls; g) SN color as a function of redshift; h) uncertainty of the color measurement as an illustration of the photometric quality of the data.

Table 2.2. Shown is the number of SNe passing the different outlier rejection cuts, as well as the sample dependent systematic dispersion ($\sigma_{\rm sys}$) and the RMS around the best fit model. The compilation obtained with the $\sigma_{\rm cut} = 3$ cut will be referred to as the Union robust set.

	No Outlier Cut			$\sigma_{\rm cut} = 3$			$\sigma_{\rm cut} = 2$		
Set	SNe	$\sigma_{\rm sys}(68\%)$	RMS (68%)	SNe	$\sigma_{\rm sys}(68\%)$	RMS (68%)	SNe	$\sigma_{\rm sys}(68\%)$	RMS (68%)
Hamuy et al. (1996)	17	$0.14^{+0.04}_{-0.03}$	$0.16^{+0.03}_{-0.03}$	17	$0.14^{+0.04}_{-0.03}$	$0.16^{+0.03}_{-0.03}$	16	$0.12^{+0.05}_{-0.03}$	$0.15^{+0.02}_{-0.03}$
Krisciunas et al. (2005)	6	$0.06^{+0.11}_{-0.05}$	$0.10^{+0.03}_{-0.04}$	6	$0.05^{+0.11}_{-0.05}$	$0.10^{+0.03}_{-0.04}$	6	$0.08^{+0.12}_{-0.07}$	$0.12^{+0.03}_{-0.04}$
Riess et al. (1996)	11	$0.16^{+0.07}_{-0.04}$	$0.18^{+0.03}_{-0.04}$	11	$0.16^{+0.07}_{-0.03}$	$0.17^{+0.03}_{-0.04}$	11	$0.18^{+0.08}_{-0.04}$	$0.20^{+0.04}_{-0.05}$
Jha et al. (2006)	16	$0.30^{+0.09}_{-0.05}$	$0.31^{+0.05}_{-0.06}$	15	$0.26^{+0.08}_{-0.05}$	$0.27^{+0.05}_{-0.06}$	1 1	$0.10^{+0.08}_{-0.06}$	$0.15^{+0.03}_{-0.04}$
This Work	8	$0.01^{+0.06}_{-0.01}$	$0.09^{+0.02}_{-0.03}$	8	$0.00^{+0.05}_{-0.00}$	$0.07^{+0.02}_{-0.02}$	8	$0.07^{+0.06}_{-0.03}$	$0.12^{+0.03}_{-0.04}$
Riess et al. (1998) + HZT	12	$0.29^{+0.20}_{-0.11}$	$0.50^{+0.09}_{-0.12}$	12	$0.28^{+0.19}_{-0.10}$	$0.48^{+0.09}_{-0.11}$	10	$0.16^{+0.19}_{-0.10}$	$0.49^{+0.10}_{-0.13}$
Perlmutter et al. (1999)	30	$0.43^{+0.13}_{-0.09}$	$0.65^{+0.08}_{-0.09}$	29	$0.33^{+0.10}_{-0.07}$	$0.50^{+0.06}_{-0.07}$	24	$0.19^{+0.11}_{-0.09}$	$0.43^{+0.06}_{-0.07}$
Tonry et al. (2003)	6	$0.00^{+0.33}_{-0.00}$	$0.24^{+0.06}_{-0.09}$	6	$0.06^{+0.28}_{-0.06}$	$0.24^{+0.06}_{-0.09}$	6	$0.00^{+0.32}_{-0.00}$	$0.26^{+0.07}_{-0.09}$
Barris et al. (2003)	22	$0.31^{+0.12}_{-0.07}$	$0.64^{+0.09}_{-0.11}$	21	$0.23^{+0.12}_{-0.08}$	$0.62^{+0.09}_{-0.10}$	19	$0.11^{+0.16}_{-0.11}$	$0.71^{+0.11}_{-0.13}$
Knop et al. (2003)	11	$0.10^{+0.08}_{-0.04}$	$0.17^{+0.03}_{-0.04}$	11	$0.10^{+0.07}_{-0.04}$	$0.17^{+0.03}_{-0.04}$	11	$0.11^{+0.08}_{-0.05}$	$0.18^{+0.04}_{-0.04}$
Riess et al. (2006)	29	$0.22^{+0.05}_{-0.04}$	$0.31^{+0.04}_{-0.04}$	27	$0.16^{+0.05}_{-0.04}$	$0.26^{+0.03}_{-0.04}$	24	$0.08^{+0.05}_{-0.06}$	$0.22^{+0.03}_{-0.03}$
Astier et al. (2006)	72	$0.14^{+0.03}_{-0.02}$	$0.31^{+0.03}_{-0.03}$	71	$0.12^{+0.03}_{-0.02}$	$0.29^{+0.02}_{-0.03}$	70	$0.12^{+0.03}_{-0.02}$	$0.30^{+0.02}_{-0.03}$
Miknaitis et al. (2007)	75	$0.21^{+0.04}_{-0.03}$	$0.32^{+0.02}_{-0.03}$	73	$0.18^{+0.04}_{-0.03}$	$0.30^{+0.02}_{-0.03}$	66	$0.00^{+0.05}_{-0.00}$	$0.23^{+0.02}_{-0.02}$
Union	315			307			282		

Figure 2.5 shows diagnostic variables used to test for consistency between the various samples. The leftmost plot shows the systematic dispersion and RMS around the best fit model. One expects that there is an intrinsic dispersion associated with all SNe, which provides a lower limit to the sample dependent systematic dispersion. To estimate the intrinsic dispersion one can look at various quantities, as for example the smallest $\sigma_{\rm sys}$ or, perhaps more appropriate, by the median of $\sigma_{\rm sys}$. The median of $\sigma_{\rm sys}$, which is about 0.15 mag (shown as the leftmost dashed vertical line), is a robust measure of the intrinsic dispersion, as long as the majority of samples are not dominated by observer dependent, unaccounted-for uncertainties.

As a test for tension between the data sets, we compare for each sample the average residual from the best fit cosmology. This is shown in the middle panel of Fig. 2.5. As can be seen, most samples fall within 1σ and none deviate by more then 2σ. The larger samples show no indication of inconsistency. This changes if one considers, instead of the mean, the slope, $d\mu_{\rm residual}/dz$, of the residuals as a function of the redshift. The right panel of Fig. 2.5 shows a large fraction of significant outliers in the slope. The largest slope outlier is found for the Miknaitis et al. (2007) sample (see also the middle panel of Fig. 2.4). The sign of the slope is consistent with the presence of a Malmquist bias (see Wood-Vasey et al. (2007) for a discussion). The uncertainties associated with such a Malmquist bias are discussed in Section 2.4.5. While in general there is no clear trend in the sign of the slope deviations, it is clear that any results that depend on the detailed slope, such as a changing equation of state, should be treated with caution.

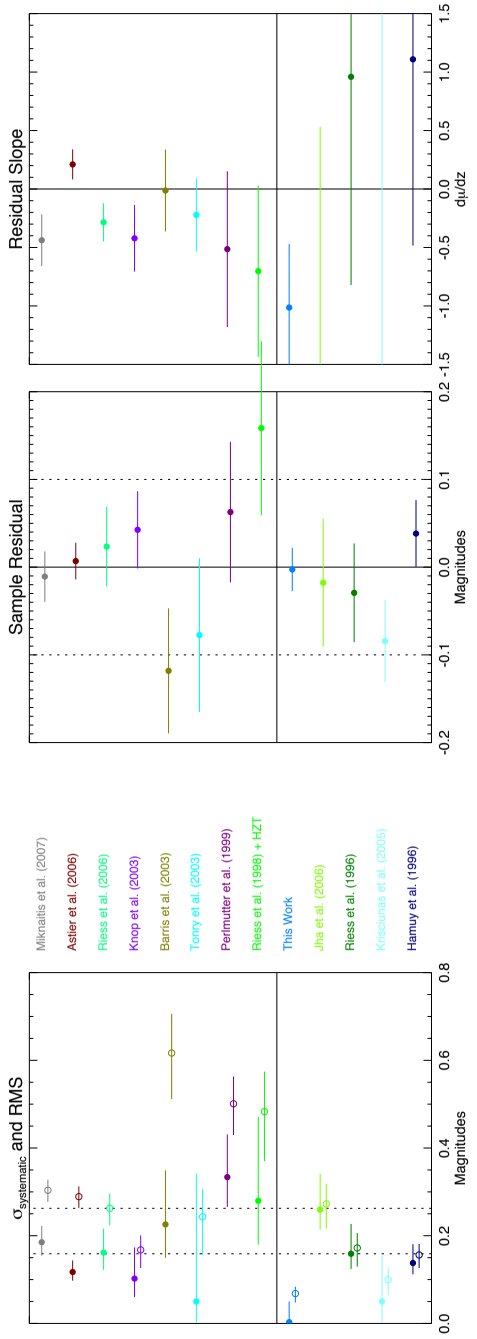

Figure 2.5. From left to right: Systematic dispersion (filled circles) and RMS around the best fit model (empty circles); The mean, sample averaged, deviation from the best fit model; The slope of the Hubble-residual (in magnitudes) versus redshift, $d\mu_{\rm residual}/dz$. The parameters characterizing the different samples are used to uncover potential systematic problems.

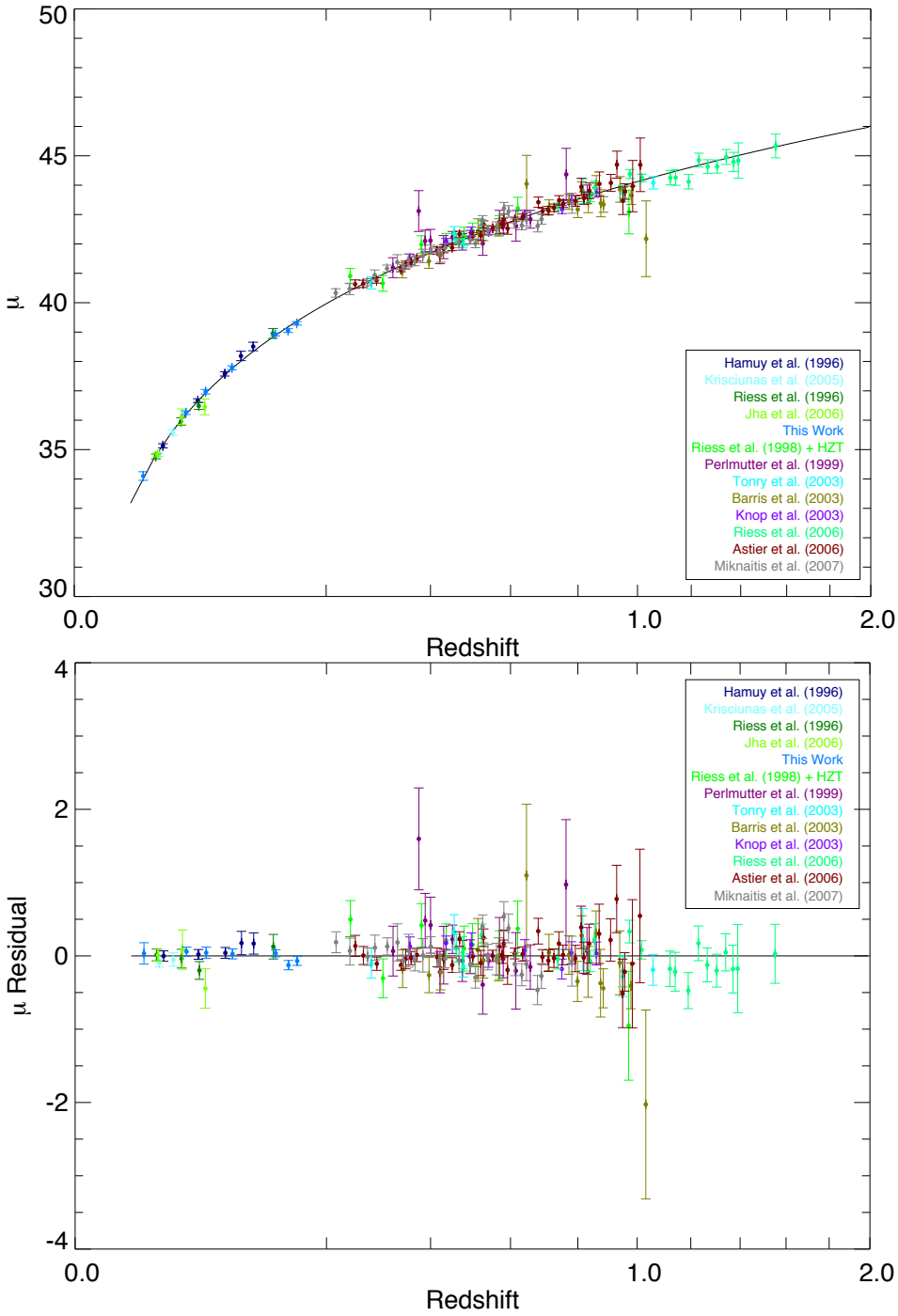

Figure 2.6. Top: Binned Hubble diagram (bin-size $\Delta z = 0.01$). Bottom: Binned residuals from the best fitting cosmology.

2.4 Systematic errors

Detailed studies of the systematic effects have been published as part of the analysis of individual data sets. The list includes photometric zero points, Vega spectrum, lightcurve fitting, contamination, evolution, Malmquist bias, K-corrections and gravitational lensing, which have also been discussed in earlier work (Perlmutter et al. 1997, 1999; Knop et al. 2003; Astier et al. 2006; Ruiz-Lapuente 2007; Wood-Vasey et al. 2007).

Some sources of systematic errors are common to all surveys and will be specifically addressed for the full sample. Other sources of systematic errors are controlled by the individual observers. The degree with which this has been done for the various data samples entering the analysis is very different. The SNLS—which is using a single telescope and instrument for the search and followup, and which has detailed multi-band photometry for nearly all its SNe—has a strong handle on a subset of the observation-dependent systematics uncertainties. With the exception of the ESSENCE SN data sample, other high redshift samples are smaller and will contribute less to the final results.

We handle the two types of systematic errors separately: systematic errors that can be associated with a sample (e.g. due to observational effects), and those that are common to all the samples (e.g. due to astrophysical or fundamental calibration effects). To first order, the measurement of cosmological parameters depends on the relative brightness of nearby SNe ($z \sim 0.05$) compared to their high redshift counterparts ($z \sim 0.5$). If low and high redshift SNe are different, this can be absorbed in different absolute magnitudes M. We hence cast the common systematic uncertainties into an uncertainty in the difference $\Delta M = M_{\rm low-z} - M_{\rm high-z}$. 'We have chosen $z_{\rm div} = 0.2$ as the dividing redshift as it conveniently splits the samples according nearby and distant SN searches. Note, however, that our resulting systematic errors change by less then 25% of its value for $z_{\rm div}$ in the range $0.1 - 0.5$. In addition we allow for a set of extra parameters, ΔM_i, one for each sample i.

Systematic uncertainties are then propagated via these nuisance parameters:

$$\begin{array}{ll} \mu_B = m_B^{\rm max} - M + \alpha(s-1) - \beta c + \Delta M_i & \text{for } z_{\rm div} < 0.2 \\ \mu_B = m_B^{\rm max} - M + \alpha(s-1) - \beta c + \Delta M_i + \Delta M & \text{for } z_{\rm div} > 0.2, \end{array} \tag{2.4}$$

with the term $\Delta M^2/\sigma^2_{\Delta M} + \sum_{i=1}^{N_{\rm samples}} \Delta M_i^2/\sigma^2_{\Delta M_i}$ being added to the χ^2 as defined through Eq. 2.2. We have checked that this treatment of systematic errors is consistent (in our case to better than 5 % of its value) with the more common procedure, applicable to one-dimensional constraints, in which part of the input data is offset by $\pm\sigma_{\Delta M}$ to obtain the systematic variations in the resulting parameter (e.g. w or $\Omega_{\rm M}$).

In the following we discuss the different contributions to $\sigma_{\Delta M}$, and summarize them in section 2.4.9. The resulting systematic errors on the cosmological parameters are discussed in section 2.5.

2.4.1 Stretch & evolution

With the large statistics at hand one can test the errors associated with the empirical stretch and color corrections. These corrections would become sources of systematic error if a) different SN populations were to require different corrections and b) if the SN populations were to show differences between nearby and distant objects (either due to selection effects or due to evolution of the SN environment).

A potential redshift dependence of the correction parameters can be tested by separately fitting low redshift and high redshift objects. For this test, a ΛCDM cosmology was assumed with $\Omega_{\rm M} = 0.28$ and $\Omega_{\rm M} = 0.72$ (the values we obtain from the fit of the full sample); however, the results are rather insensitive to the assumed cosmological parameters. The obtained fit parameters α and β are presented in table 2.3.

The values of β at high and low redshift agree very well, providing strong constraints on evolution of the color-correction. Such evolution effects could arise, for example, due to a different mix of dust reddening and intrinsic color at different redshifts. The fact that β agrees so well supports the choice of the empirical color correction[5].

subset	$N_{\rm SN}$	α	β	$\Omega_{\rm M}^a$	w^b
all	307	1.24(0.10)	2.28(0.11)	0.29(0.03)	-0.97(0.06)
$z > 0.2$	250	1.46(0.16)	2.26(0.14)	-	-
$z \leq 0.2$	57	1.07(0.12)	2.23(0.21)	-	-
$s < 0.96$	155	1.56(0.27)	2.18(0.18)	0.27(0.05)	-0.98(0.09)
$s \geq 0.96$	152	1.51(0.37)	2.34(0.17)	0.30(0.04)	-0.93(0.07)

Table 2.3. Fit parameters as obtained for different SN subsamples. (^{a})A flat Universe was assumed in the constraints on $\Omega_{\rm M}$. (^{b})Constraints on w were obtained from combining SNe with CMB and BAO measurements. A flat Universe was also assumed. (see section 2.5 for more details).

The α at low-redshift and high-redshift are only marginally consistent with each other. We will take the difference at face value and estimate the impact it would have on the final result. The average stretch is $\langle s \rangle \approx 0.96$ and hence the difference in the average stretch correction is $\langle 1 - s \rangle \, \Delta\alpha \approx 0.015$. If α indeed is redshift dependent and this was not accounted for, one would obtain a bias of $\Delta M = 0.015$ mags.

Effects of potentially different SN populations should be considered as well. It has recently been argued by Scannapieco & Bildsten (2005) and Mannucci et al. (2006) that one needs to allow for two types of SN-progenitor timescales to explain the observed rates in different galaxy types. One class of objects traces the star formation rate directly, while the second class has a delay time trailing the star formation rate by a few billion years. If indeed two populations are present, they might evolve differently with redshift. It is

[5] Note that if β were not obtained by fitting but instead was fixed, e.g. $\beta = R_{\rm B} = 4.1$, a bias can be expected (and might have already been observed, see Conley et al. (2007)) if the average reddening changes as a function of redshift.

therefore important to check that the empirical corrections suit both populations. To test the effect of different SN populations one can subdivide the sample according to SN subtypes or host environments (Sullivan et al. 2003; Howell et al. 2007). Sullivan et al. (2006) have found using well observed SNe and hosts from SNLS that the stretch of a light curve is correlated with its host environment as well as with the two classes of SN-progenitor systems postulated by Scannapieco & Bildsten (2005); Mannucci et al. (2006). Therefore, we divide the SN sample into two approximate equally large samples with $s < 0.96$ and $s \geq 0.96$. The two independent samples are then fitted, with the results shown in Table 2.3. The resulting parameters $\Omega_{\rm M}$ (for a flat Universe) and w (for a flat Universe together with BAO+CMB) for the two samples are less than 1σ apart and hence there is no evidence for an underlying systematic effect. Nevertheless, this will be a very important number to watch, once future high quality SN data sets will be added. (Note that, while the resulting values of αs for the two samples are consistent with each other, they appear inconsistent with the value obtained for the complete sample. This apparent inconsistency arises in part due to a bias introduced by dividing the stretch distribution in the middle. Larger stretch SNe, misclassified due to measurement errors as belonging to the low stretch SNe sample, as well as lower stretch SNe, misclassified as belonging to the large stretch SNe sample, will for both samples result in a α biased to larger values.)

We have also investigated whether the sample can be sub-divided according to the color of the SNe. We found that the results of such a test can be very misleading. While in principle one would expect to find that the best fitted cosmological parameters do not depend on color selection criteria (e.g. $c < c_{\rm cut}$ and $c > c_{\rm cut}$), we find by means of Monte Carlo simulation described in Section 2.3.2 that a significant bias is introduced into the measurements. This bias is also observed in the data. For example, by choosing $c_{\rm cut} = 0.02$ we find that for our sample of SNe $\Omega_{\rm M}$ changes by ± 0.1. The bias arises from truncating an asymmetric distribution. In the case of color, the asymmetry in the distribution is introduced by the fact that extinction by dust leads only to reddening. Hence the number of objects which would belong to $c_{\rm true} < c_{\rm cut}$ but, due to a large measurement error, are fitted with $c_{\rm observed} > c_{\rm cut}$, are not compensated by objects misclassified in the opposite way. The number of misclassified objects is a function of the measurement errors, and hence is larger towards higher redshift. The simulated data sets result in a significant bias both in $\Omega_{\rm M}$ as well as β. The size of the bias, however, depends on assumptions made for the underlying color distribution. Hence, for the current data sample, splitting the data set in two color bins introduces a bias so large and difficult to control, that the results of the test become meaningless. Note that if one had very small error bars on the color measurement over the full redshift range (as obtained from a dedicated space based survey (Aldering 2005)), the bias can be kept small. This would allow for additional tests of systematic uncertainties due to reddening corrections.

2.4.2 Sample contamination

As discussed in Section 2.3.3, the method of robust statistics was applied to limit the effect of outliers, which could be present if the data is contaminated by non Type Ia SNe, or by other events which do not have the standard candle properties of regular SN Ia. It was shown in Section 2.3.3 that the bias due to contamination can be limited for this analysis to $\Delta M = 0.015$ mag, which we hence use as the uncertainty due to contamination.

In previous compilations, such as that of Riess et al. (2004, 2007), no formal outlier criteria were applied. Instead, with some exceptions, the original classifications made by the authors of the data sample were used. Spurious candidates are sometimes removed from the data samples by hand (see for example Astier et al. (2006)), making it extremely difficult to estimate the effect of the remaining contamination. Our method of outlier rejection provides a simple and objective alternative.

2.4.3 Lightcurve model & K-corrections

The lightcurve model (Guy et al. 2005) is a parametric description with two free parameters. As such it has limitations in capturing the full diversity of Type Ia SNe. By visual inspection we find, for example, that the fitted maximum magnitude can differ from the data by a few hundredths of a magnitude. A particular problem could arise if the observation strategies for nearby and distant SNe differ. In fact, the high-redshift data sets have on average earlier observations of the lightcurve, which is a result of the rolling-search techniques frequently used to find and follow-up SNe. Hence, when comparing low-z to high-z SNe, the fitted lightcurve parameters are obtained from slightly different parts of the lightcurve. The mismatch between template and the data lightcurve might thus be more pronounced in one sample than the other. To quantify the effect, we have performed an extensive Monte Carlo simulation. A set of BVR lightcurve templates are obtained from a quartic spline fit to data including the well observed SNe 1990N, 1994D, 1998aq, 2001el, 2002bo, 2003du, 2004eo, and 2005cf (Strovink 2007). The templates are then used to sample random realizations of the lightcurves with cadence, signal-to-noise and date of the first detection of the nearby and distant SN sample. These simulated lightcurves are then fitted. The difference in the stretch and color corrected peak magnitude between the nearby and distant sample can be used to estimate the systematic uncertainty. For the nine templates we obtain the average difference between nearby and distant SNe of -0.02 magnitudes with an RMS scatter of 0.015. We adopt an associated systematic uncertainty of $\Delta M = 0.02$ magnitudes due to this.

There is another source of uncertainty arising from the diversity of SNe Ia lightcurves. If a certain class of SNe is misrepresented (for example if they are brighter than average for their typically fitted stretch value) and if the fraction of such SNe changes as a function of redshift, it will lead to a systematic bias in the cosmological parameters. Section 2.4.1 has addressed this issue by subdividing the sample according to stretch and redshift. If a significant lightcurve misrepresentation were present, one would expect to see differences

in the fitted lightcurve-correction parameters. No statistically significant differences have been observed and we assign no additional contribution to the uncertainties from such an effect.

The lightcurve model is based on a spectral template series. It thereby eliminates the need for a separate K-correction (see Section 2.2.2). The model has been trained with nearby SNe data and hence will be affected by systematic errors associated with that training data. These are largest for the U-band, which suffers from low training statistics and difficult flux calibration. However, the validity of the model in the U-band has been verified with the SNLS data set to better than 0.02 magnitudes (Astier et al. 2006). Here we adopt their assessment of the resulting systematic error of $\Delta M = 0.02$.

2.4.4 Photometric zero points

With present methods, ground based photometric zero point calibration is generally limited to an accuracy of $\gtrsim 1\%$ (Stubbs & Tonry 2006). The largest contribution to the photometric error of the peak magnitude arises from the color correction $\Delta M \sim \beta \Delta c$. The color measurement is based on the measurement of the relative flux in two (or more bands), and as a result some of the uncertainties cancel. Nevertheless, since the color of SNe at different redshifs are obtained from different spectral regions, the uncertainty in the reference Vega spectrum limits the achievable accuracy to $\Delta c \approx 0.01 - 0.015$ mag (Stritzinger et al. 2005; Bohlin & Gilliland 2004).

Here we assume an uncertainty of $\Delta M = 0.03$ for the photometric peak magnitude due to zero point calibration. Part of this uncertainty is common to all samples (as the same set of calibration stars is being used), while the other part is sample dependent (e.g. tied to the calibration procedure) and we divide the error equally among the two categories.

2.4.5 Malmquist bias

Malmquist bias arises in flux limited surveys, when SNe are detected because they are overly bright. What matters for cosmology is whether the bias is different for the low-z and high-z samples. Perlmutter et al. (1999), Knop et al. (2003) and Astier et al. (2006) have evaluated the effects of Malmquist bias for the SCP and SNLS SN samples as well as the nearby SN sample and found that they nearly cancel. Since an individual estimate of Malmquist bias for all the different samples is beyond the scope of this work, we attribute a conservative systematic uncertainty of $\Delta M = 0.02$ (Astier et al. 2006) for all samples, which is consistent with previous estimates.

In addition, we investigated whether the significant redshift dependence of the Hubble residuals observed for the Miknaitis et al. (2007) sample (see section 2.3.4), if interpreted as due to Malmquist bias, exceeds our claimed uncertainty. A simulation was performed in which we introduced a magnitude cut-off such that the resulting slope, $d\mu/dz$, matches the observed slope of -0.6. The associated Malmquist bias with that sample is then ~ 0.05 mags. If this is compared to the average Malmquist bias obtained for magnitude limited

searches, the extra bias is only 0.03 mags larger– not much larger than the systematic uncertainty we have adopted. While we do not treat the ESSENCE data sample differently from the others, we note that Wood-Vasey et al. (2007) made their extinction prior redshift-dependent to account for the fact that at higher redshifts an increasingly larger fraction of the reddened SNe was not detected. The linear color correction employed in our analysis is independent of a prior and therefore unaffected by a redshift dependent reddening distribution.

2.4.6 Gravitational lensing

Gravitational lensing decreases the mode of the brightness distribution and causes increased dispersion in the Hubble diagram at high redshift. The effect has been discussed in detail in the literature (Sasaki 1987; Linder 1988a; Bergström et al. 2000; Holz & Linder 2005). We treat lensing as a statistical phenomenon only, although with the detailed optical and NIR data available for the GOODS field, the mass-distribution in the line-of-sight and hence the lensing (de)magnification may be estimated for individual SNe (Jönsson et al. 2006). Important for this work is that they find no evidence for selection effects (i.e. Malmquist bias) due to lensing of the high redshift SNe.

Considering both strong and weak lensing, Holz & Linder (2005) found that lensing will add a dispersion of $0.093 \times z$ mag, which if the statistics of SNe is large enough, can be approximated as an additional Gaussian error. Here, we added the additional dispersion from gravitational lensing in quadrature to the "constant" systematic dispersion and observational error. This effectively deweights the high redshift SNe. However, only for the highest redshift SNe is the additional uncertainty comparable to that of the intrinsic dispersion.

Flux magnification and demagnification effects due to over- or under-densities of matter near the line of sight cancel. But one obtains a bias if magnitudes instead of fluxes are used. However, the bias is $0.004 \times z$ mag and therefore still much smaller than the statistical error on the luminosity distance obtained from the ensemble of high redshift SNe. While not yet relevant for this analysis, future high-statistics samples will have to take this effect into account.

Another potential bias is introduced by the 3σ outlier rejection, since the lensing PDF is asymmetric. Using the PDFs of Holz & Linder (2005) we have checked that the bias is never larger than $0.006 \times z$ mag. We take the worst case value of 0.009 magnitude (i.e. for a SNe at $z \approx 1.5$) as a conservative systematic uncertainty for gravitational lensing, since this is still an almost negligible value.

2.4.7 Gray intergalactic dust

The possibility that SNe are dimmed due to hypothetical gray intergalactic dust, as suggested by Aguirre (1999), was constrained by Östman & Mörtsell (2005); Mörtsell & Goobar (2003) by studying the colors of high-redshift quasars. Applying their constraints

on intergalactic dust, we find that the cosmological parameters are shifted by about one statistical standard deviation, i.e. for a flat Universe $\Delta\Omega_{\rm M} = -0.03$. This should not be considered a systematic uncertainty, but rather an upper limit on the effect of hypothetical large grains of cosmic dust in the line of sight.

2.4.8 Galactic Extinction

All lightcurve data were corrected for Galactic extinction using the extinction law of Cardelli et al. (1989) using an R_V of 3.1. The $E(B-V)$ values were derived from the sky map of Schlegel et al. (1998) and have a typical statistical error of 10%. For nearby SNe we hence obtain an additional uncertainty of

$$\Delta\mu_B \approx (R_B - \beta) \cdot \sigma\left(E(B-V)\right) \approx 0.2 \cdot E(B-V), \tag{2.5}$$

where β is the color correction coefficient from Eq. 2.1. We add this statistical error in quadrature to each nearby SNe. High redshift SNe are measured in redder bands and, since $R_R \approx \beta$, are less affected by Galactic extinction.

There is also a common systematic error of 10% in the overall reddening normalization. The average Galactic $E(B-V)$ for the low redshift sample is 0.063 and we add $0.063{\cdot}0.2 = 0.013$ mag systematic uncertainty to ΔM.

2.4.9 Summary of systematic errors

In our treatment of the above systematic errors we distinguish between systematic errors common between datasets, which are largely of astrophysical nature, and the more observer dependent ones associated with individual samples. Table 2.4 summarizes what are considered the relevant contributions to the systematic uncertainties in this analysis. They are propagated into the final result through Eq. 2.4.

Source	common (mag)	sample-dependent (mag)
$\alpha\&\beta$ correction	0.015	-
Contamination	-	0.015
Lightcurve model	0.028	-
Zero point	0.021	0.021
Malmquist bias	-	0.020
Gravitational lensing	-	0.009*
Galactic extinction normalization	0.013	-
Total in mag	$\Delta M = 0.040$	$\Delta M_i = 0.033$

Table 2.4. Most relevant common and sample dependent systematic errors of this analysis (in magnitudes).

2.5 Cosmological fit results

Our analysis of cosmological model fits includes both statistical and systematic errors. The individual contributions to the systematic error identified in Table 2.4 are of very different nature and hence are assumed uncorrelated. We hence obtain the combined systematic error by adding in quadrature the individual contributions. The resulting error was propagated according to the prescription described in Section 2.4. Our constraints on the matter density $\Omega_{\rm M}$, assuming a flat Universe, are summarized in Table 2.5. Both statistical (68 % CL) and systematic errors are quoted.

Figure 2.7 plots our results for the joint fit to the matter density and cosmological constant energy density, $\Omega_{\rm M}$ and Ω_Λ, and the effect of varying the outlier cut, while Fig. 2.8 illustrates the effects of systematics. For comparison with previous work, Figure 2.9 shows our joint constraints on $\Omega_{\rm M}$ and Ω_Λ (statistical error only) and the Riess et al. (2007) constraints obtained from the Gold compilation of data primarily from the HZT, SCP and SNLS (Riess et al. 2007) and a recent compilation of Davis et al. (2007), which is based on lightcurve fits from Riess et al. (2007) and Wood-Vasey et al. (2007). The results obtained in this work are consistent with those of previous studies; however, compared to the recent SN fit results of Astier et al. (2006); Riess et al. (2007); Wood-Vasey et al. (2007); Davis et al. (2007), we obtain a 15-30 % reduction in the statistical error.

About half the improvement can be attributed to the new SCP Nearby 1999 SNe. Their impact is evident in the rightmost column of Fig. 2.9 (as well as in Fig. 2.10). The impact of these SNe is somewhat larger because the sample has a best-fit systematic uncertainty of zero. If instead one would introduce the requirement that $\sigma_{\rm sys} \geq 0.1$, there would be an increase of about 10% in the uncertainties of the cosmological parameters.

Figure 2.9 shows the constraints on the equation of state parameter w (assumed constant) and $\Omega_{\rm M}$. A flat Universe was assumed. Again, the constraints are consistent with, but stronger than, those from Riess et al. (2007) and Davis et al. (2007). The current SN data do not provide strong constraints on the equation of state parameter w by itself, since it is to a large extent degenerate with $\Omega_{\rm M}$. However, the degeneracy can be broken by combining with other measurements involving $\Omega_{\rm M}$. Figure 2.10 shows the constraints obtained from the detection of baryon acoustic oscillations (BAO) (Eisenstein et al. 2005) and from the five year data release of the Wilkinson Microwave Anisotropy Probe (CMB) (Dunkley et al. 2008). The constraints from the CMB data follow from the reduced distance to the surface of last scattering at $z = 1089$ (or shift parameter). It is important to realize that for parameter values far from the concordance model, the shift in the sound horizon must also be taken into account. The reduced distance R is often written as

$$R_{\rm conc} = (\Omega_{\rm M} H_0^2)^{1/2} \int_0^{1089} dz/H(z), \tag{2.6}$$

where the Hubble parameter is $H(z) = H_0 \left[\Omega_{\rm M}(1+z)^3 + (1-\Omega_{\rm M})(1+z)^{3(1+w)}\right]^{1/2}$. The WMAP-5 year CMB data alone yields $R_0 = 1.715 \pm 0.021$ for a fit assuming a constant w (Dunkley et al. 2008; Lambda-website 2008). Defining the corresponding χ^2 as

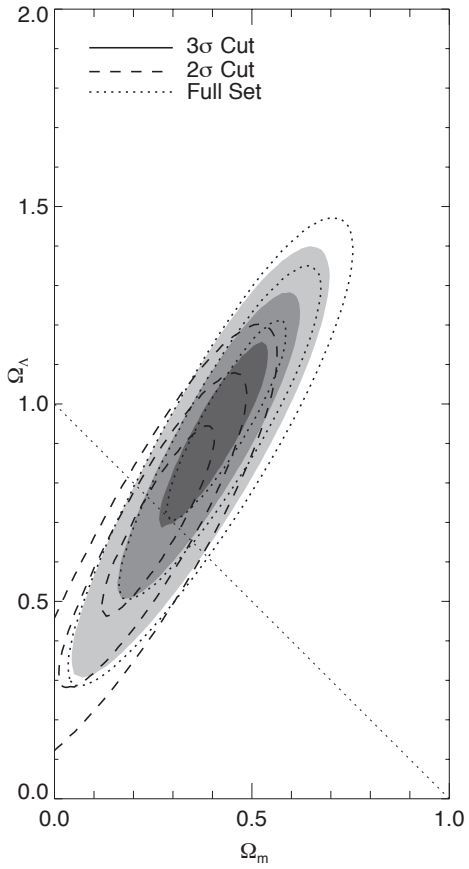

Figure 2.7. 68.3 %, 95.4 % and 99.7% confidence level contours on Ω_Λ and Ω_M plane from the Union SNe set. The result from the robustified set, obtained with a $\sigma_\mathrm{cut} = 3$ outlier cut, is shown as filled contours. The empty contours are obtained with the full data set (dotted line) and $\sigma_\mathrm{cut} = 2$ outlier rejected data set (dashed line). As can be seen, outlier rejection shifts the contours along the degenerate axis by as much as 0.5σ towards a flat Universe. In the remaining figures, we refer to the $\sigma_\mathrm{cut} = 3$ outlier rejected set as the Union set.

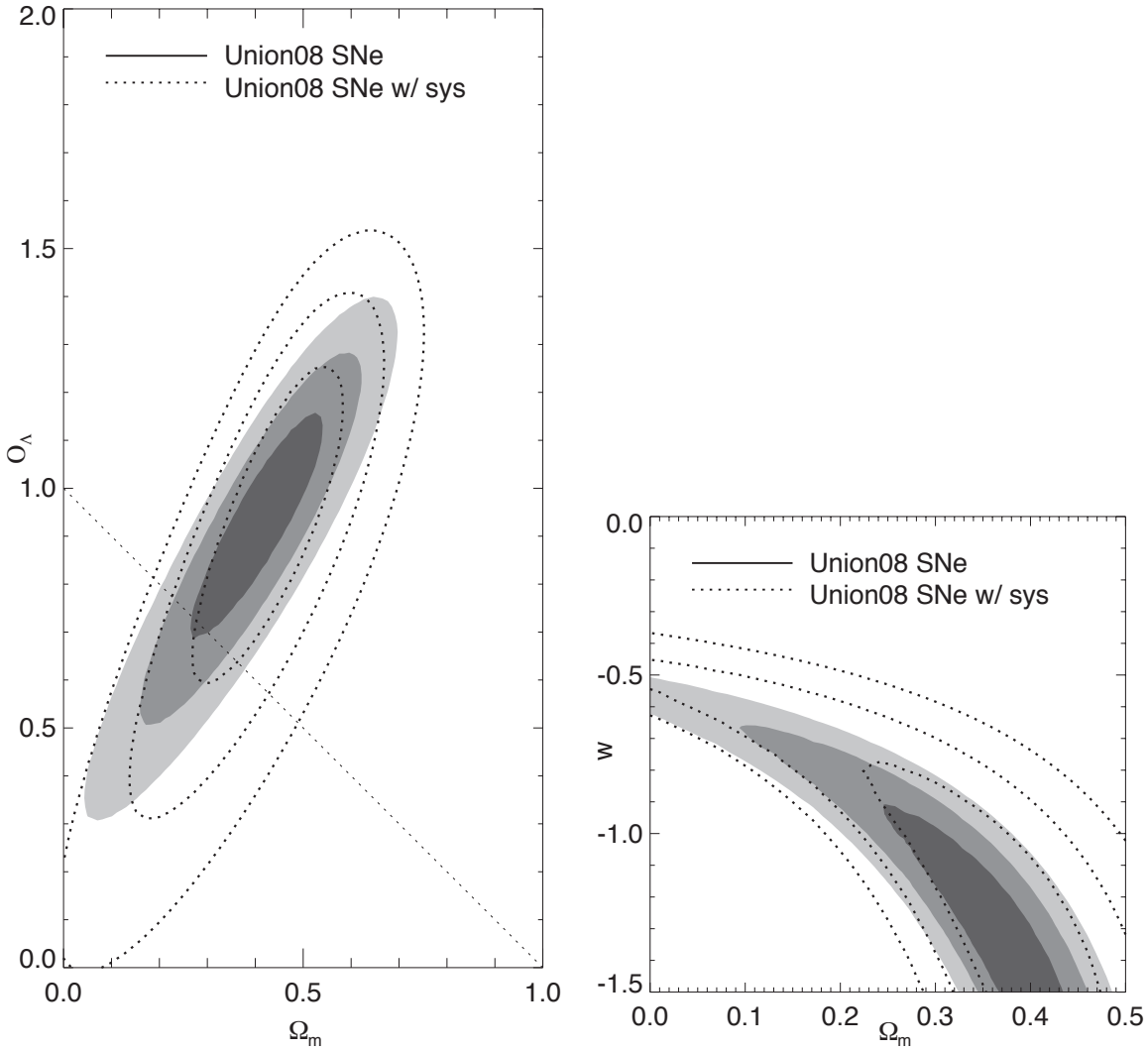

Figure 2.8. Left plot: 68.3 %, 95.4 % and 99.7% confidence level contours on Ω_Λ and Ω_M obtained with the Union set, without (filled contours) and with inclusion of systematic errors (empty contours). The right plot shows the corresponding confidence level contours on the equation of state parameter w and Ω_M, assuming a constant w.

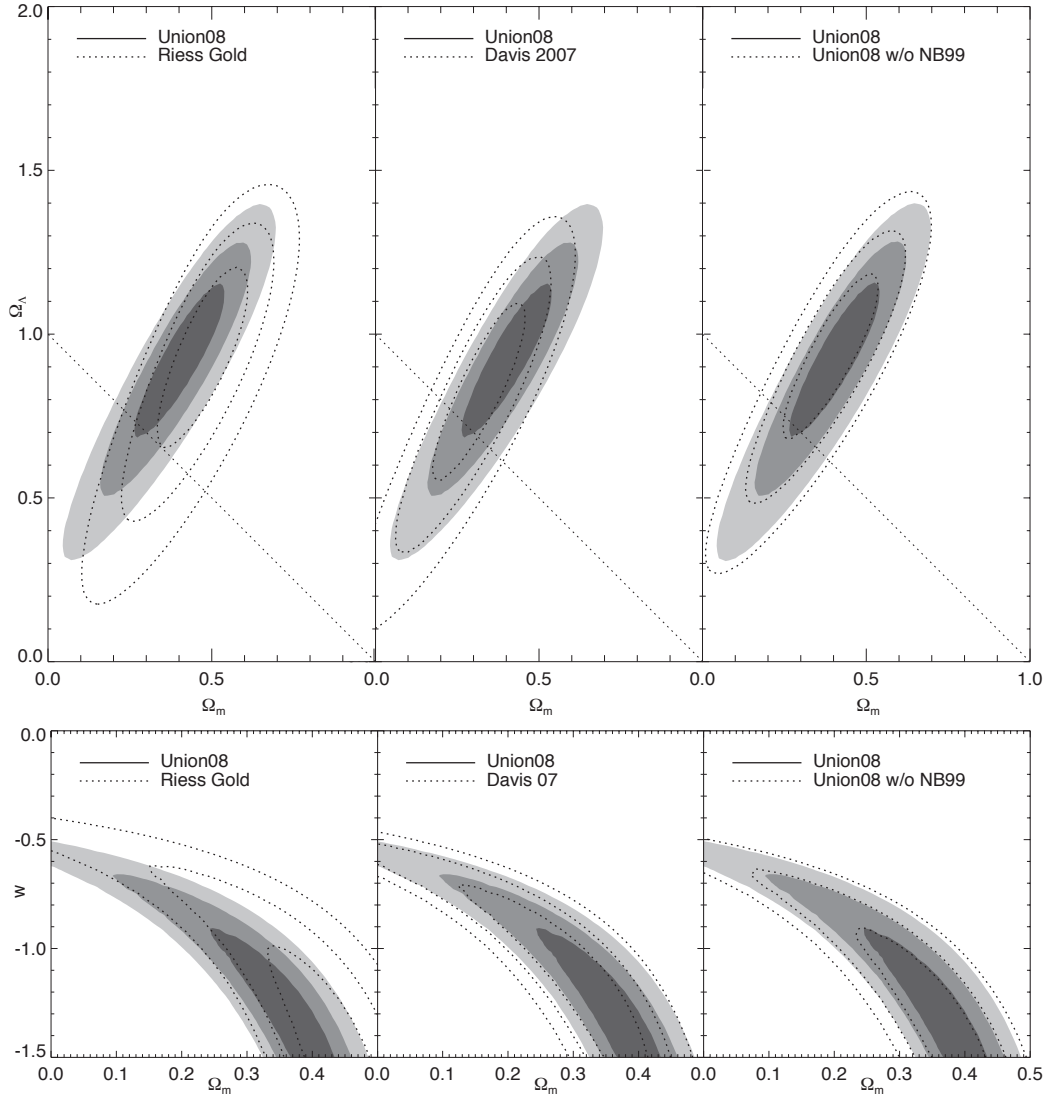

Figure 2.9. 68.3 %, 95.4 % and 99.7% confidence level contours on Ω_Λ and Ω_M (top row) and Ω_M and w (bottom row). The results from the Union set are shown as filled contours. The empty contours in the left column represent the Gold sample (Riess et al. 2004, 2007) and the middle column the constraints from Davis et al. (2007). While our results are statistically consistent with the previous work, the improvements in the constraints on the cosmological parameters are evident. The right column shows the impact of the SCP Nearby 1999 data.

$\chi^2 = [(R_{\rm conc} - R_0)/\sigma_{R_0}]^2$ one can then deduce constraints on $\Omega_{\rm M}$ and w. However, this assumes a standard matter (and radiation) dominated epoch for calculating the sound horizon. The more proper expression for the shift parameter accounts for deviation in the sound horizon:

$$R = (\Omega_m H_0^2)^{1/2} \int_0^{1089} dz/H(z) \times \left[\int_{1089}^{\infty} dz/\sqrt{\Omega_m (1+z)^3} \Big/ \int_{1089}^{\infty} dz/(H(z)/H_0) \right]. \tag{2.7}$$

Since dark energy is generally negligible at high redshift, the factor in square brackets is usually unity (for example, it deviates from unity by less than 1% even for $w_0 = -1$, $w_a = 0.9$, i.e. $w(z = 1089) = -0.1$). However, for extreme models that upset the matter dominated behavior at high redshifts, the correction will be important in calculating whether the geometric shift parameter accords with CMB observations (apart from any issue of fitting other observations). Violation of early matter domination causes the "wall" in likelihood apparent in Fig. 2.12. Also see, for example, Linder & Miquel (2004); Wright (2007).

BAO measurements from the SDSS data (Eisenstein et al. 2005) provide a distance constraint at a redshift $z = 0.35$. Percival et al. (2007) have derived BAO distances for $z = 0.2$, in addition to the $z = 035$ SDSS-data point, using the combined data from SDSS and 2dFGRS. However, some points of tension were noted between the data sets (Percival et al 2007, see also Sánchez & Cole (2008)), especially evident for ΛCDM models. We confirm this observation and found that the $z = 0.2$ data point, if combined with SN and CMB data according to the prescription in Appendix A of Percival (2007) leads to an 2.5 sigma inconsistency. Neither the $z = 0.35$ BAO data point from Percival et al. (2007) nor the slightly weaker constraint from Eisenstein et al. (2005) shows such kind of tension. Given the differences between the two data sets, we use the $z = 0.35$ SDSS data point of Eisenstein et al. (2005), but with the caveat that BAO constraints need further clarification. Eisenstein et al. (2005) provides a constraint on on the distance parameter A:

$$\begin{aligned} A(z) &= (\Omega_{\rm M} H_0^2)^{1/2} H(z)^{-1/3} z^{-2/3} \left[\int_0^z dz'/H(z')\right]^{2/3} \times \\ &\quad \left[\int_{1089}^{\infty} dz/\sqrt{\Omega_m (1+z)^3} \Big/ \int_{1089}^{\infty} dz/(H(z)/H_0) \right], \end{aligned} \tag{2.8}$$

to be $A(z = 0.35) = 0.469 \pm 0.17$. Note that BAO also depend on accurate accounting of the sound horizon and receive the same correction factor shown in brackets in Eq. 2.7. This results in a similar wall to the acceptable confidence contour reflecting violation of early matter domination. To see that such violation has severe implications, note that most models above the wall have a total linear growth factor a factor ten below the concordance cosmology.

The joint constraints from SN data, BAO, and CMB are shown in Fig. 2.10 and the corresponding numbers are given in Table 2.5. As can be seen, the constraints obtained from combining either BAO or CMB with SNe data give consistent results and comparable error bars, while the combination of all three measurements improves only the statistical

Fit	$\Omega_{\rm M}$	Ω_k	w
SNe	$0.287^{+0.029+0.039}_{-0.027-0.036}$	0 (fixed)	-1 (fixed)
SNe + BAO	$0.285^{+0.020+0.011}_{-0.020-0.009}$	0 (fixed)	$-1.011^{+0.076+0.083}_{-0.082-0.087}$
SNe + CMB	$0.265^{+0.022+0.018}_{-0.021-0.016}$	0 (fixed)	$-0.955^{+0.060+0.059}_{-0.066-0.060}$
SNe + BAO + CMB	$0.274^{+0.016+0.013}_{-0.016-0.012}$	0 (fixed)	$-0.969^{+0.059+0.063}_{-0.063-0.066}$
SNe + BAO + CMB	$0.285^{+0.020+0.011}_{-0.019-0.011}$	$-0.009^{+0.009+0.002}_{-0.010-0.003}$	-1 (fixed)
SNe + BAO + CMB	$0.285^{+0.020+0.010}_{-0.020-0.010}$	$-0.010^{+0.010+0.006}_{-0.011-0.004}$	$-1.001^{+0.069+0.080}_{-0.073-0.082}$

Table 2.5. Fit results on cosmological parameters $\Omega_{\rm M}$, Ω_k and w. The parameter values are followed by their statistical and systematic uncertainties. The first fit to the SNe data alone results in a χ^2 of 310.8 for 303 degrees of freedom with a $\Delta\chi^2$ of less then one for the other fits.

error. The impact of including systematic errors (only from SNe, from Eq. 2.4) is shown in the middle panel of Fig. 2.10.

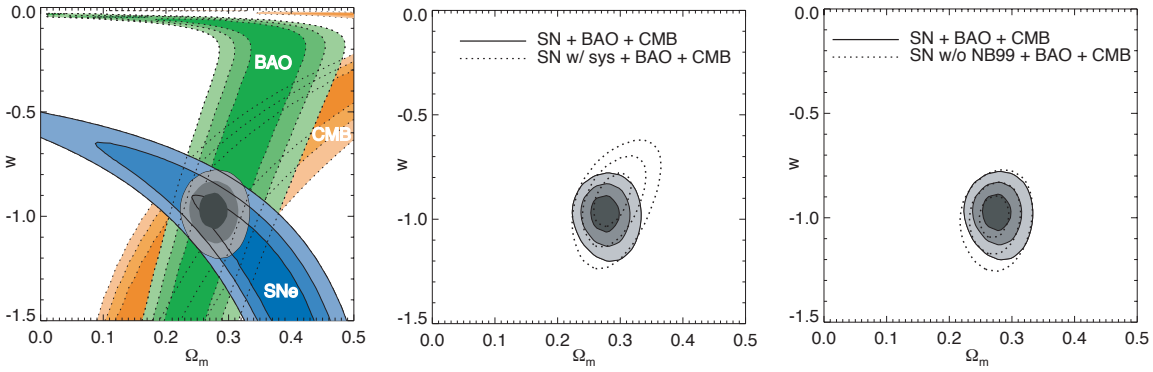

Figure 2.10. 68.3 %, 95.4 % and 99.7% confidence level contours on w and $\Omega_{\rm M}$, for a flat Universe. The left plot shows the individual constraints from CMB, BAO and the Union SN set, as well as the combined constraints (filled contours, statistical errors only). The middle plot shows the effect of including systematic errors. The right plot illustrates the impact of the SCP Nearby 1999 data.

The results quoted so far were derived assuming a flat Universe. Allowing for spatial curvature Ω_k, our constraints from combining SNe, CMB and BAO are consistent with a flat ΛCDM Universe (as seen in Table 2.5). Fig. 2.11 shows the corresponding constraints in the $\Omega_{\rm M} - \Omega_\Lambda$ plane.

Finally, one can attempt to investigate constraints on a redshift dependent equation of state (EOS) parameter $w(z)$. Initially we consider this in terms of

$$w(z) = w_0 + w_a \frac{z}{1+z}, \tag{2.9}$$

shown by Linder (2003a) to provide excellent approximation to a wide variety of scalar field and other dark energy models. Later, we examine other aspects of time variation of the

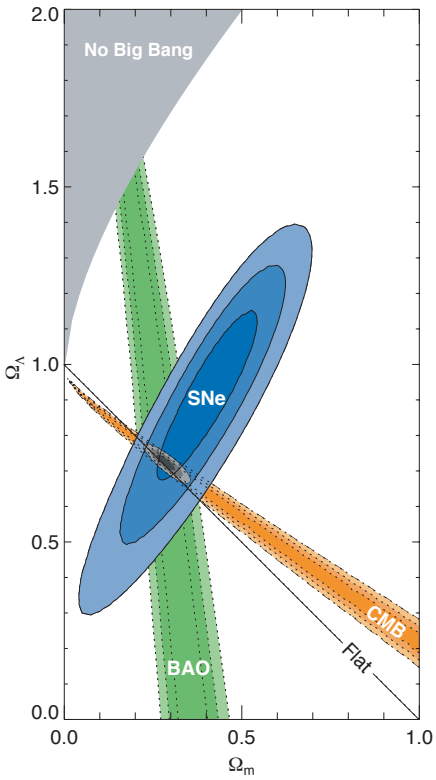

Figure 2.11. 68.3 %, 95.4 % and 99.7% confidence level contours on Ω_Λ and Ω_M obtained from CMB, BAO and the Union SN set, as well as their combination (assuming $w = -1$).

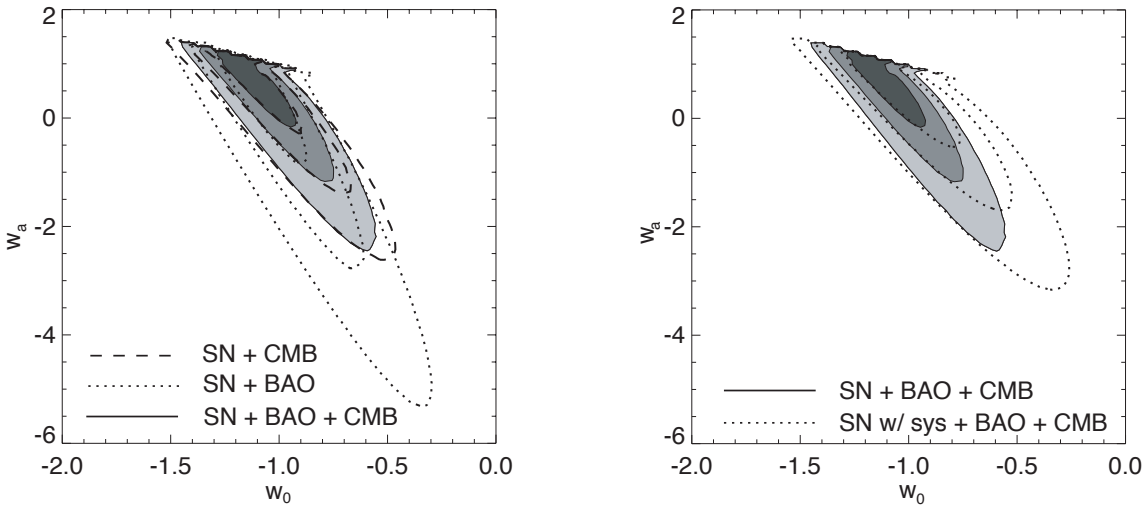

Figure 2.12. 68.3 %, 95.4 % and 99.7% confidence level contours on w_a and w_0 for a flat Universe. Left: The Union SN set was combined with CMB or BAO constraints. Right: Combination of SNe, CMB and BAO data, with and and without systematic uncertainties included. The diagonal line represents $w_0 + w_a = 0$; note how the likelihoods based on observational data remain below it, favoring matter domination at $z \gg 1$.

dark energy EOS. Assuming a flat Universe and combining the Union set with constraints from CMB, we obtain constraints on w_0, the present value of the EOS, and w_a, giving a measure of its time variation, as shown in Fig. 2.12. (A cosmological constant has $w_0 = -1$, $w_a = 0$.) Due to degeneracies within the EOS and between the EOS and the matter density $\Omega_{\rm M}$, the SN dataset alone does not give appreciable leverage on the dark energy properties. By adding other measurements, the degeneracies can be broken and currently modest cosmology constraints obtained.

Fig. 2.12 (left) shows the combination of the SN data with either the CMB constraints or the BAO constraints. The results are similar; note that including either one results in a sharp cut-off at $w_0 + w_a = 0$, from the physics as mentioned in regards to Eq. 2.7. Since $w(z \gg 1) = w_0 + w_a$ in this parameterization, any model with more positive high-redshift w will not yield a matter-dominated early Universe, altering the sound horizon in conflict with observations.

Note that BAO do not provide a purely "low" redshift constraint, because implicit within the BAO data analysis, and hence the constraint, is that the high redshift Universe was matter dominated (so the sound horizon at decoupling is properly calculated). Thus, one cannot avoid the issue of modeling how the dark energy EOS behaves at high redshifts by using this constraint rather than the CMB. (We differ here from Riess et al. 2007, who treat BAO as a low-redshift constraint.) SN data are especially useful in constraining $w(z)$ because there is no dependence at all on the high redshift behavior, unlike CMB and BAO data.

As one might expect, because of the different orientations of the confidence contours

and the different physics that enters, combining both the CMB and BAO constraints with the SN data clears up the degeneracies somewhat, as seen in Fig. 2.12, with and without systematics. Inclusion of curvature does not substantially increase the contours.

We emphasize that the wall in w_0-w_a space is not imposed a priori and does not represent a breakdown of the parameterization, but a real physical effect from violating early matter domination. Nevertheless, we can ask what limits could be put on the early dark energy behavior – either its presence or its equation of state – if we do not use the w_0-w_a parameterization. A simple, but general model for $w(z)$ creates a series of redshift bins and assumes w is constant over each bin. The constraints from this are shown in Fig. 2.13. Note that the data points are correlated.

Riess et al. (2007) made a somewhat similar investigation with the emphasis on the impact of the highest redshift SNe. A difference to the work of Riess et al. (2007) is that we do not decorrelate the constraints in the different redshift bins. While this implies that the bin-wise constraints shown in Fig. 17 are correlated, it ensures that the w-constraints shown for a given bin are confined to the exact redshift range of the bin. If instead one applies a decorrelation procedure, some of the tight constraints from lower redshifts feed through to higher redshifts (i.e. $z > 1$). See de Putter & Linder (2007) for general discussion of this issue. Unlike Riess et al. (2007), we additionally place a w bin at higher redshift than the SN data ($z > 2$), to account for the expansion history of the early Universe, and do not fix w in this bin. The Riess "strong" prior has a fourth bin for $z > 1.8$, but fixes $w = -1$. The "strongest" prior does not have a fourth bin. Forcing either of these behaviors on the $z > 2$ Universe results in unfairly tight constraints and the danger of bias (Linder 2007; de Putter & Linder 2007); in failing to separate the SN bins from those of the CMB and BAO essentially the entire constraint in the redshift $z \gtrsim 1$ bin is from the CMB (see also Wright 2007).

Consider the top row of Fig. 2.13. These results are for bins with $z < 0.5, 0.5 < z < 1.0, 1.0 < z < 2.0$ and $z > 2.0$. The only constraint that can be concluded from the highest redshift bin is that $w_{[2,\infty]} \lesssim 0$, but this constraint comes entirely from CMB and BAO, which requires that the early Universe is matter-dominated (see the above the discussion of the wall in the $w_a - w_0$ plane). We then look at the $z = 1 - 2$ bin for constraints on w which would be due to the $z > 1$ SNe and we find essentially no constraint.

The lowest redshift bin is constrained to $w_{[0,0.5]} \approx -1 \pm 0.1$. The next bin is compatible with -1, but the central value is high. This deviation from -1 seems to be due to the unexpected brightness (by about 0.1 magnitudes) of the Hubble data at $z > 1$ (see Fig. 2.6). (Recall that w at some z influences distances at larger redshifts.) We clearly see that to be sensitive to appreciable deviations from $w = -1$ such as 0.1 mags at $z \sim 1$, which is key to constraining theories of dark energy, one requires better statistics for the very high-redshift supernovae (and comparably good systematics).

Given that the strongest constraints on w are contained in the first bin, one might attempt to search for a redshift dependence of w at lower redshifts by changing the borders of the bins. The smallest errors are obtained roughly with the binning $z < 0.1, 0.1 < z < 0.4, 0.4 < z < 2.0$, and $2.0 < z$. These constraints are shown in the bottom row of Fig.

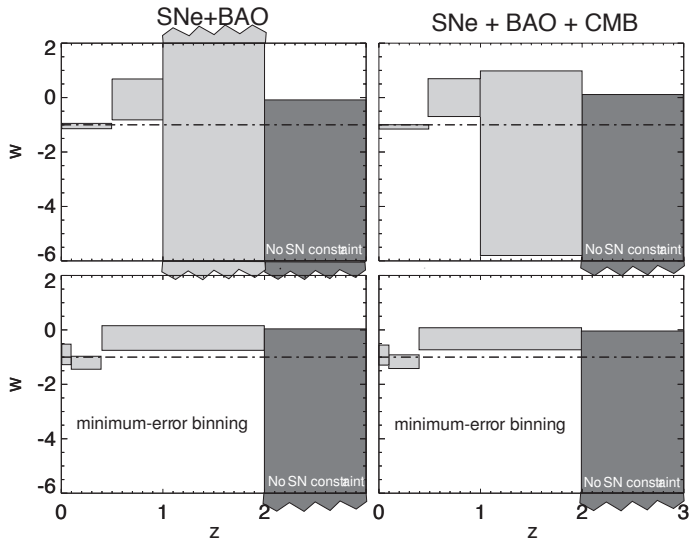

Figure 2.13. 68 % constraints on $w(z)$, where $w(z)$ is assumed to be constant over each redshift bin. The left column combines the Union SN set with BAO constraints only, while the right column includes also constraints from the CMB. The top row illustrates the fact that only extremely weak constraints on the equation of state exist at $z > 1$. The bottom row shows a different binning that minimizes the mean bin error. Note that for $z > 2$ (dark gray-"No SN constraint") only upper limits exist, basically enforcing matter domination, coming from either CMB data or, in the case without CMB data, from requiring substantial structure formation (a linear growth factor within a factor of 10 of that observed).

2.13. The results are similar to the results from the other binning, with the lowest two bins centered around $w = -1$ and the next bin centered around a more positive value. No significant redshift dependence is observed. Note the tight limit on the $0.4 < z < 2$ bin is *not* saying $w(z > 1) \approx -1$, even approximately, since the leverage on $w(z)$ is coming from the $0.4 < z < 1$ part of the bin (this illustrates the importance of considering multiple binnings).

To sum up, even in combination with current BAO and CMB data, current SN data sets cannot tell us whether an energy density component other than matter existed at $z > 1$, and cannot tell us whether such a component if it existed had an equation of state with negative pressure. In the future, however, SN data that achieves Hubble diagram accuracy of 0.02 mag out to $z = 1.7$ will be able to address these questions and provide independent checks of the $z > 1$ Universe.

Note that while constraints on a possible redshift dependency of w have been shown in Figures 2.12 and 2.13, we do not present values for the projected, one-dimensional constraints for several reasons. First, the bounds are still very weak and as a result the error bars show highly non-gaussian errors (as visible in Fig. 2.12). In addition, our treatment of systematic errors has not been optimized for a redshift dependent w and a potential sys-

tematic redshift dependence of the distance modulus is only partially taken into account. As a consequence, the resulting (already large) systematic errors on $w(z)$ would be underestimated.

In this analysis so far we have not excluded any SNe based on extreme values of stretch or color, therefore including also the peculiar class of under-luminous 1991bg-like SNe that are typically associated with small stretch values. After unblinding, in an effort to study the robustness of our results, we have introduced a stretch cut, $s > 0.6$, to eliminate SN1991bg-like SNe from the sample. The most significant consequence of this cut came with the removal of SN 1995ap, a supernova in the Riess et al. (1998) sample. By itself the removal of this one supernova can change the cosmological fit parameters in the $\Omega_{\rm M} - \Omega_\Lambda$ and $\Omega_{\rm M} - w$ planes by nearly 1σ along the more degenerate contour axis (and away from a flat Universe). However, without SN 1995ap, the test for tension between data sets that we applied in Section 4.4 would show the Riess et al. (1998) dataset to be a 3.5σ outlier and one would be forced, unless the tension can be resolved otherwise, to remove the data set from the compilation. The net result of the $s > 0.6$ cut would then be a 0.25σ change in w, Ω_M and Ω_Λ in the direction of the more degenerate contour axis. The results presented in this work are based on the sample without the stretch cut; however, since the parameters along the direction of the degeneracy are well constrained once CMB or BAO data are added, the combined constraints essentially do not depend on whether or not the stretch cut is applied.

2.6 Conclusion

The cosmological parameter constraints from the Union SN Ia compilation shown in Figures 2.8, 2.10, 2.12 and 2.13 reflect the current best knowledge of the world's Type Ia supernova datasets. Specifically, in addition to the older data, they include the new datasets of nearby Hubble-flow SNe Ia we presented in Kowalski et al. (2008), the recent large, homogeneous, high-signal-to-noise SNLS and ESSENCE datasets published by Astier et al. (2006) and Miknaitis et al. (2007) as well as the high redshift supernovae in Riess et al. (2004, 2007). Equally important is that a number of outstanding analysis issues have been addressed that improve the reliability and reduce the biases of the current Union SN Ia compilation, and should stand us in good stead for future compilations. We are making the ingredients and results of the Union compilation available at the associated web site[6] and we intend to provide occasional updates to this as new information becomes available.

Several conclusions can be drawn from the new larger SCP Union SN Ia compilation that could not be approached with smaller datasets. In particular the large statistics can be used to address systematic uncertainties in novel ways.

We test for evolution by subdividing the sample into low-stretch and high-stretch SNe. According to recent evidence (Sullivan et al. 2006) these two samples might be dominated by different progenitor systems (Scannapieco & Bildsten 2005; Mannucci et al. 2006),

[6] http://supernova.lbl.gov/Union

which are likely to show different evolution. Hence performing consistent but independent cosmology fits for the two sub-samples provides a powerful test for potential evolutionary effects. The resulting cosmological fit parameters are found to be consistent. This comparison is particularly meaningful, as the statistical uncertainties from the subsamples are comparable to the total ($stat + sys$) uncertainties obtained from the full sample.

With the larger Union dataset, it is possible to begin to examine the rate of true outliers from the Hubble-plot fit. It appears that the current selection criteria for SNe Ia can find very homogeneous sets of supernovae, but not perfectly homogeneous sets. With these criteria, there are apparently true outliers, at the percent level for the SNLS sample and up to 10% for other samples. The analysis performed here was made robust to outliers, reducing the associated error on cosmological parameters to a level comparable to other sources of systematic error.

Compilations offer the chance to test for observer dependent systematic effects, i.e. tension between the datasets. The blind analysis performed here is an important element in rigorous estimation of systematics. While in general we find a high degree of consistency between samples, we see modest tension when comparing the slope of the Hubble-residuals as a function of redshift, $d\mu/dz$. For the present compilation, our cosmology results are expected to hold within the quoted systematic uncertainties. However, once the homogeneous datasets get larger—and the systematic errors dominate over the statistical ones for the different sets—such tests will become even more important, as they allow one to perform cross-checks with different datasets calibrated in different ways. Future data samples can be added to the Union set, by first blinding the data and then performing a diagnostic analysis similar to the one performed here. Only after any inconsistencies can be resolved, would the new data be unblinded.

We proposed a scheme to incorporate both sample dependent and common systematic errors. We showed in Section 2.4 that systematic errors can be approached by treating the systematics as a normal distribution of a parameterized systematic term. We find that the combination of SNe constraints with CMB constraints, due to their larger complementarity with SNe data, results in smaller systematic errors than the combination with BAO constraints. Adding BAO, CMB and SNe constraints leads to yet smaller statistical error bars, while the error bars including systematics do not improve.

The robustness of the detection of the accelerating expansion of the Universe is continually increasing as improved systematics analysis is reinforced by larger SN data sets. The current knowledge of the nature of dark energy is still modest, however, with the uncertainty on the assumed-constant equation of state only under 10% *if* multiple probes are combined. The current "world" estimate presented here employing the full set of current SN data, plus other measurements, gives a best constraint of $w = -0.969^{+0.059}_{-0.063}(\mathrm{stat})$ $^{+0.063}_{-0.066}(\mathrm{sys})$ on a constant EOS parameter w at 68.3% confidence level. However, allowing for time variation in the dark energy equation of state further opens the possibilities for the physics driving the acceleration, consistent with all current observations. In particular, present SN data sets do not have the sensitivity to answer the questions of whether dark energy persists to $z > 1$, or whether it had negative pressure then.

On the positive side, with the more sophisticated analyses and tests carried out here, we still have encountered no limits to the potential use of future, high accuracy SN data as cosmological probes. New data sets for nearby, moderate, and high redshift well-characterized SNe Ia are forthcoming and we expect realistic, robust constraints to catch up with our optimistic hopes on understanding the accelerating Universe. [7]

[7] The work described in this chapter is supported, in part by the Director, Office of Science, Office of High Energy and Nuclear Physics, U.S. Department of Energy, through contract DE-AC02-05CH11231. This research used resources of the National Energy Research Scientific Computing Center, which is supported by the Office of Science of the U.S. Department of Energy under Contract No. DE-AC02-05CH11231. M.K. acknowledges support from the Deutsche Forschungsgemeinschaft (DFG). P.E.N. acknowledges support from the US Department of Energy Scientific Discovery through Advanced Computing program under contract DE-FG02-06ER06-04. A.M.M. acknowledges financial support from Fundação para a Ciência e Tecnologia (FCT), Portugal, through project PESO/P/PRO/15139/99.

CHAPTER 3

Beyond Λ

This chapter combines the Union compilation, Baryon Acoustic Oscillation (BAO), and Cosmic Microwave Background (CMB) data to compute constraints on a diverse array of dark energy models. I take advantage of the covariance-matrix-based systematics approach of the Union compilation to compute these cosmological constraints including systematic uncertainties. The constraints we place on these models have significant room for deviations from cosmological-constant-like behavior that will require far more data to resolve. [1]

3.1 Introduction

A decade after the discovery of the acceleration of the cosmic expansion (Perlmutter et al. 1999; Riess et al. 1998) we still understand little about the nature of the dark energy physics responsible. Improved data continues to show consistency with Einstein's cosmological constant Λ, and in terms of a constant equation of state, or pressure to density, ratio w, the best fit to the data is $w = -0.969^{+0.059}_{-0.063}(\mathrm{stat})^{+0.063}_{-0.066}(\mathrm{sys})$, where Λ has $w = -1$ (Chapter 2). However, the magnitude of Λ required and the coincidence for it becoming dominant so close to the present remain unexplained, and an abundance of motivated or unmotivated alternative models fills the literature. Using the latest, most robust data available we examine the extent to which data really have settled on the cosmological constant.

The vast array of models proposed for dark energy makes comparison of every model in the literature to the data a Sisyphean task. Here we select some dozen models with properties such as well defined physical variables, simplicity, or features of particular physical interest. These embody a diversity of physics, including scalar fields, phase transitions, modified gravity, symmetries, and geometric relations. While far from exhaustive, they provide roadmarks for how well we can say that current data have zoomed in on Λ as the solution.

For such comparisons it is critical to employ robust data clearly interpretable within

[1] This chapter was previously published as Rubin et al. (2009).

these "beyond Λ" cosmologies. Geometric probes from the Type Ia supernovae (SN) distance-redshift relation, cosmic microwave background (CMB) acoustic peak scale shift parameter, and baryon acoustic oscillations (BAO) angular scale serve this essential role. Equally important is confidence in the error estimates, incorporating systematics as well as statistical uncertainties. This has been studied in detail in the recent unified analysis of the world's published heterogeneous SN data sets – the Union compilation (described in Chapter 2).

This SN compilation includes both the large data samples from the SNLS and ESSENCE survey, the compiled high redshift SNe observed with the Hubble Space Telescope, a new sample of nearby SNe, as well as several other, small data sets. All SNe have been analyzed in a uniform manner and have passed a number of quality criteria (such as having data available in two bands to measure a color, and sufficient lightcurve points to make a meaningful fit). The samples have been carefully tested for inconsistencies under a blinded protocol before combining them into a single final data set comprising 307 SNe, the basis for this analysis. In this work the SNe data will be combined with the constraints obtained from the baryon acoustic oscillation scale (Eisenstein et al. 2005) and from the five year data release of WMAP and ground based CMB measurements (Komatsu et al. 2009).

In Section 3.2 we describe the general method for cosmological parameter estimation and present a summary table of the various models considered and the χ^2 statistics of the fit. Sections 3.3–3.12 then briefly describe the dark energy models, their parameters, and show the likelihood contours. The concluding discussion occurs in Section 3.13.

3.2 Constraining Models

Achieving informative constraints on the nature of dark energy requires restricting the degrees of freedom of the theory and the resulting degeneracies in the cosmological model being tested. One degree of freedom entering the model is the present matter density Ω_m. For the case of the spatially flat cosmological constant Λ model (or some of the other models considered below), this is the sole cosmological parameter determining the distances entering the supernova (SN) magnitude-redshift, baryon acoustic oscillation scale (BAO), and cosmic microwave background (CMB) shift parameter relations.

Generally, further degrees of freedom to describe the nature of the dark energy, i.e. its equation of state (EOS), or pressure to density, ratio, are needed. In a few cases the EOS is parameter free, as in the Λ case where $w = -1$, or is determined by the matter density, as in some subcases below (such as the flat DGP braneworld gravity model of §3.4). One way to categorize models is by the number of independent EOS parameters, or general parameters beyond the matter density (so flat Λ models have zero such parameters, Λ models with curvature have one). In general, combining SN with CMB or BAO data can deliver reasonable constraints on one parameter descriptions of dark energy.

In addition to exploring the nature of dark energy through its EOS, one might also include another parameter for the dark energy density, i.e. allow the possibility of nonzero

spatial curvature. In this case individual probes then generally do a poor job constraining the model with current data, although the combined data can sometimes still have leverage. Since crosschecks and testing consistency between probes is important (as particularly illustrated below in the DGP case), we consider spatial curvature only in the otherwise zero parameter cases of Λ and DGP, and for the constant EOS dark energy model.

In the following sections we investigate various one parameter EOS models, discussing their physical motivation or lack thereof, and features of interest, and the observational constraints that can be placed upon them. In the last sections we also investigate some two parameter models of interest, with constrained physical behaviors and particular motivations. As a preview and summary of results, Table 3.1 lists the models, number of parameters, and goodness of fit for the present data.

The SN, CMB, and BAO data are combined by multiplying the likelihoods. Especially when testing models deviating from the cosmological constant one must be careful to account for any shift of the CMB sound horizon arising from violation of high redshift matter domination on the CMB and BAO scales; details are given in Chapter 2. Note that some doubt exists on the use of the BAO constraints for cosmologies other than $\Lambda\mathrm{CDM}$, or possibly constant w, (Dick et al. 2006; Rydbeck et al. 2007) since $\Lambda\mathrm{CDM}$ is assumed in several places in the Eisenstein et al. (2005) analysis, e.g. computation of the correlation function from redshift space, nonlinear density corrections, structure formation and the matter power spectrum, and color and luminosity function evolution. Properly, a systematic uncertainty should be assigned to BAO to account for these effects; however, this requires a complex analysis from the original data and we show only the statistical error. At the current level of precision, simplified estimates show this does not strongly affect the results, but such systematics will need to be treated for future BAO data. All figures use the likelihood maximized over all relevant parameters besides those plotted, and contours are at the 68.3%, 95.4%, and 99.7% confidence level.

It is particularly important to note the treatment of systematic errors, included only for SN. We employ the prescription in Chapter 2 for propagation of systematic errors. This introduces a new distance modulus $\mu^{\rm sys} = \mu + \Delta M_i + \Delta M$, which is simply the usual distance modulus $\mu = 5\log(H_0 d_L(z))$, where $d_L(z)$ is the luminosity distance and H_0 the Hubble constant, shifted by a sample dependent magnitude offset ΔM_i and a single sample independent magnitude offset ΔM added only for the higher redshift SNe ($z > 0.2$). The magnitude offsets ΔM_i reflect possible heterogeneity among the SNe samples while the ΔM step from SNe at $z < 0.2$ to $z > 0.2$ allows a possible common systematic error in the comparison of low vs. high redshift SNe. Treating ΔM_i and ΔM as additional fit parameters, one defines $\chi^2_{\rm sys} = \chi^2 + \sum_i (\Delta M_i/\sigma_{M_i})^2 + (\Delta M/\sigma_M)^2$ to absorb the uncertainty in the nuisance parameters, σ_{M_i} and σ_M, and obtain constraints on the desired physical fit parameters that include systematic errors. This procedure of incorporating systematic errors provides robust quantification of whether or not a model is in conflict with the data and is essential for accurate physical interpretation. See Chapter 2 for further, detailed discussion of robust treatment of systematics within the current world heterogeneous SN data.

Model	Motivation	Parameters	χ^2 (stat)	χ^2 (sys)
ΛCDM (flat)	gravity, zeropoint	Ω_m	313.1	309.9
			$\Delta\chi^2$ (stat)	$\Delta\chi^2$ (sys)
ΛCDM	gravity, zeropoint	Ω_m, Ω_Λ	-1.1	-1.3
Constant w (flat)	simple extension	Ω_m, w	-0.3	-1.2
Constant w	simple extension	Ω_m, Ω_k, w	-1.1	-1.6
Braneworld	consistent gravity	Ω_m, Ω_k	15.0	2.7
Doomsday	simple extension	$\Omega_m, t_{\rm doom}$	-0.1	-0.7
Mirage	CMB distance	Ω_m, w_0	-0.2	-0.1
Vacuum Metamorphosis	induced gravity	$\Omega_m, \Omega_\star$	0.0	0.0
Geometric DE $\mathrm{R}_{\rm low}$	kinematics	r_0, r_1 (Ω_m, w_0)	0.1	-1.1
Geometric DE $\mathrm{R}_{\rm high}$	matter era deviation	$\Omega_m, w_\infty, \beta$	-1.9	-2.2
PNGB	naturalness	Ω_m, w_0, f	-0.1	-0.7
Algebraic Thawing	generic evolution	Ω_m, w_0, p	-1.6	-2.3
Early DE	fine tuning problem	Ω_m, w_0, Ω_e	-0.3	-1.2
Growing ν-mass	coincidence problem	$\Omega_m, \Omega_e, m_\nu^0$	-0.6	-1.6

Table 3.1. "Beyond Λ" dark energy models considered in this chapter, together with ΛCDM models. Models are listed in the order of discussion, and the cosmological fitting parameters shown. The χ^2 of the matter plus cosmological constant case is given, and all other models list the $\Delta\chi^2$ from that model. The values refer to the best fit to the joint data of SN+CMB+BAO; in the last column the SN systematics as analyzed in Chapter 2 are included.

3.3 Constant Equation of State

Models with constant equation of state w within 20%, say, of the cosmological constant value $w = -1$, but not equal to -1, do not have much physical motivation. To achieve a constant equation of state requires fine tuning of the kinetic and potential energies of a scalar field throughout its evolution. It is not clear that a constant $w \neq -1$ is a good approximation to any reasonable dynamical scalar field, where w varies, and certainly does not capture the key physics. However, since current data cannot discern EOS variation on timescales less than or of order the Hubble time, traditionally one phrases constraints in terms of a constant w. We reproduce this model from Chapter 2 to serve as a point of comparison. Also see Chapter 2 for models using the standard time varying EOS $w(a) = w_0 + w_a(1-a)$, where $a = 1/(1+z)$ is the scale factor, and models with $w(z)$ given in redshift bins.

In the constant w case the Hubble expansion parameter $H = \dot{a}/a$ is given by

$$H^2/H_0^2 = \Omega_m(1+z)^3 + \Omega_w(1+z)^{3(1+w)} + \Omega_k(1+z)^2, \tag{3.1}$$

where Ω_m is the present matter density, Ω_w the present dark energy density, and $\Omega_k = 1 - \Omega_m - \Omega_w$ the effective energy density for spatial curvature.

Figure 3.1 shows the confidence contours in the w-Ω_m plane both without and with (minimized in the likelihood fit) spatial curvature. Note that allowing for spatial curvature does not strongly degrade the constraints. This is due to the strong complementarity of SN,

CMB, and BAO data, combined with the restriction to a constant w model. As shown in Chapter 2, the constraint on curvature in this model is $\Omega_k = -0.010 \pm 0.012$. See Chapter 2 for more plots showing the individual probe constraints.

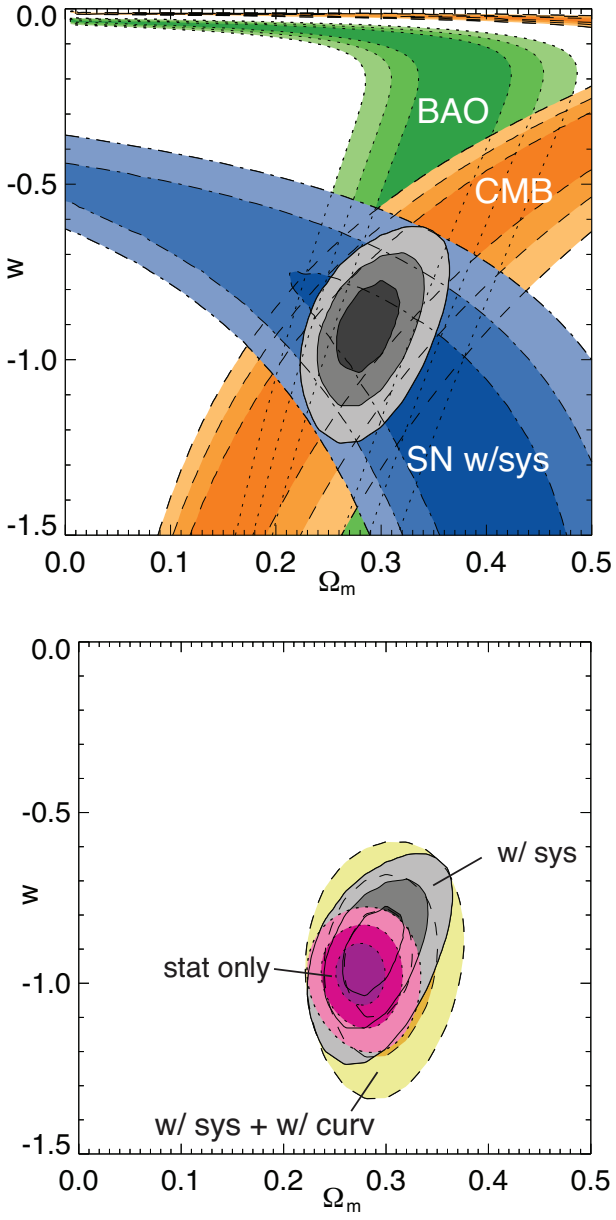

Figure 3.1. 68.3%, 95.4%, and 99.7% confidence level contours on a constant EOS w and the matter density Ω_m for the individual and combined data sets. The left panel shows individual and combined probes in the flat universe case; the right panel repeats the combined systematics contour, and also compares to the statistical only contour, and to the systematics contour when simultaneously fitting for spatial curvature.

3.4 Braneworld Gravity

Rather than from a new physical energy density, cosmic acceleration could be due to a modification of the Friedmann expansion equations arising from an extension of gravitational theory. In braneworld cosmology (Dvali et al. 2000; Deffayet et al. 2002), the acceleration is caused by a weakening of gravity over distances near the Hubble scale due to leaking into an extra dimensional bulk from our four dimensional brane. Thus a physical dark energy is replaced by an infrared modification of gravity. For DGP braneworld gravity, the Hubble expansion is given by

$$H^2/H_0^2 = \left(\sqrt{\Omega_m(1+z)^3+\Omega_{\rm bw}}+\sqrt{\Omega_{\rm bw}}\right)^2+\Omega_k(1+z)^2 \quad (3.2)$$

$$\to \Omega_m(1+z)^3+2\Omega_{\rm bw}+2\sqrt{\Omega_{\rm bw}}\sqrt{\Omega_m(1+z)^3+\Omega_{\rm bw}}, \qquad ({\rm flat})\,. \quad (3.3)$$

Here the present effective braneworld energy density is

$$\Omega_{\rm bw} = \frac{(1-\Omega_m-\Omega_k)^2}{4(1-\Omega_k)} \quad (3.4)$$

$$\to \frac{(1-\Omega_m)^2}{4}, \qquad ({\rm flat})\,, \quad (3.5)$$

and is related to the five dimensional crossover scale $r_c = M_{\rm Pl}^2/(2M_5^3)$ by $\Omega_{\rm bw} = 1/(4H_0^2r_c^2)$. Note that the only cosmological parameters for this model are Ω_m and Ω_k (or $\Omega_{\rm bw}$), so it has the same number of parameters as ΛCDM.

The effective dark energy equation of state is given by the simple expression

$$w(z) = -\frac{1-\Omega_k(z)}{1+\Omega_m(z)-\Omega_k(z)}, \quad (3.6)$$

where $\Omega_m(z) = \Omega_m(1+z)^3/(H^2/H_0^2)$ and $\Omega_k(z) = \Omega_k(1+z)^2/(H^2/H_0^2)$. Thus the dark energy equation of state at present, w_0, is determined by Ω_m and Ω_k; while time varying, it is not an independent parameter. So rather than plotting w_0 vs. Ω_m or showing constraints on the somewhat nonintuitive parameters r_c or $\Omega_{\rm bw}$ (but see the clear discussion and plots in Davis et al. (2007); Rydbeck et al. (2007), though without systematics), Figure 3.2 illustrates the confidence contours in the Ω_k-Ω_m plane. This makes it particularly easy to see how deviations from flatness pull the value of the matter density. In this and following figures, dotted contours show the BAO constraints, dashed for CMB constraints, dot-dashed for SN with systematics, and solid contours give the joint constraints.

For a flat universe, in order for w to approach -1 the matter density is forced to small values. Alternately, pushing the curvature density Ω_k negative, i.e. introducing a positive spatial curvature k, allows $w \approx -1$ with higher matter density. For a given w_0, the amount of curvature needed can be derived from Eq. (3.6) to be approximately $\Delta\Omega_k \approx -\Delta\Omega_m/\Omega_m$, so to move a flat, $\Omega_m = 0.2$ universe to $\Omega_m = 0.3$ requires $\Omega_k = -0.5$, in agreement with the SN contour (being most sensitive to w_0) of Figure 3.2.

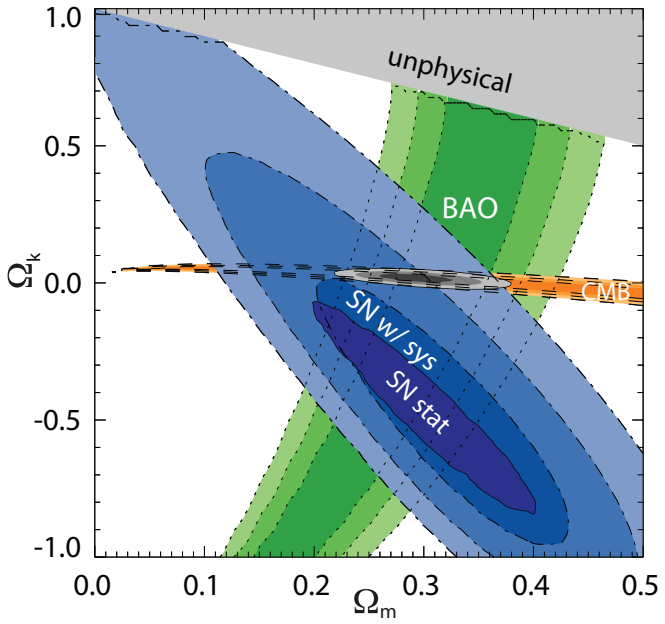

Figure 3.2. The extradimensional DGP braneworld gravity model does not achieve an acceptable fit to the combined data, even allowing for a spatial curvature parameter. The joint best fit is in fact a nearly flat model, but with poor goodness of fit: $\Delta\chi^2 = 2.7$ relative to the ΛCDM case; also shown is the statistical error only SN contour, which gives a joint $\Delta\chi^2 = 15$ relative to ΛCDM.

Note that the curvature density cannot exceed $1 - \Omega_m$, corresponding to an infinite crossover scale r_c, so the likelihood contours are cut off at this line and the region beyond is unphysical. However, this does not affect the joint contours. The BAO data contours do extend to the limit $\Omega_k = 1 - \Omega_m$; here $\Omega_{\rm bw} = 0$, equivalent to the simple OCDM (open, cold dark matter) nonaccelerating universe.

Most importantly, the three probes do not reach concordance on a given cosmological model. The areas of intersection of any pair are distinct from other pairs, indicating that the full data disfavors the braneworld model, even with curvature. This is further quantified by the poor goodness of fit to the data, with $\Delta\chi^2 = 2.7$ relative to the flat ΛCDM model possessing one fewer parameter, or $\Delta\chi^2 = 4.0$ relative to ΛCDM allowing curvature. This indicates the crucial importance of crosschecking probes. Moreover, if we had used only the statistical estimates of uncertainties (see the "SN stat" 68% cl contour of Fig. 3.2), we would have found that $\Delta\chi^2 = 15$ rather than 2.7, and possibly drawn exaggerated physical conclusions – considering the DGP model 2000 times less likely than it really is, as an illustration. Inclusion of systematics is essential for robust interpretation of results.

3.5 Doomsday Model

Perhaps the simplest generalization of the cosmological constant is the linear potential model, pioneered by Hawking & Israel (1987) and discussed recently by Weinberg (2008), motivated from high energy physics. Interestingly, while this gives a current accelerating epoch, in the future the potential becomes negative and not only deceleration of the expansion but collapse of the universe ensues. Hence the name of doomsday model.

The potential has two parameters: the amplitude and slope. The amplitude V_0 essentially gives the dark energy density, which is fixed by Ω_m in a flat universe. (For the remainder of this chapter we assume a flat universe, for the reasons discussed in §3.2.) The slope $V' = dV/d\phi$ can be translated into the present equation of state value w_0. Thus this is a one parameter model in our categorization. See Kallosh et al. (2003) for discussion of the cosmological properties of the linear potential, Hawking & Israel (1987) for a view of it as a perturbation about zero cosmological constant, and Dimopoulos & Thomas (2003) for links to the large kinetic term approach in particle physics. More recently, this has been considered as a textbook case by Weinberg (2008), so we will examine this model in some detail. Such dark energy is an example of a thawing scalar field (Caldwell & Linder 2005), starting with $w(z \gg 1) = -1$ and slowly rolling to attain less negative values of w; that is, it departs from Λ. If it has not evolved too far from -1 then its behavior is well described by $w_a \approx -1.5(1 + w_0)$ where $w(a) = w_0 + w_a(1 - a)$. However we solve the scalar field equation of motion exactly (numerically) for all results quoted here.

As the scalar field rolls to small values of the potential the expansion stops accelerating, and when it reaches $V = 0$ then $w = 1$. However it crosses through zero to negative values of the potential, further increasing w, and eventually the dark energy density itself becomes negative, causing w to go to positive and then negative infinity. Thereafter the negative dark energy density, acting now with an attractive gravitational force, causes not only deceleration but forces the universe to start contracting. The rapid collapse of the universe ends in a Big Crunch, or cosmic doomsday in a finite time.

In the notation used in Weinberg (2008), $V(\phi) = V_0 + (\phi - \phi_0)\, V_0'$, with V_0 the potential energy during the initial frozen state (during high Hubble drag at high redshift) and V_0' is the constant potential slope. Figure 3.3 shows the constraints in this high energy physics plane V_0-V_0'. Note the tight constraints on the initial potential energy V_0, given in units of the present critical density. The cosmological constant corresponds to the limit of $V_0' = 0$, but the slope must always be less than or of order 10^{-120} in Planck units, i.e. unity when shown in terms of the present energy density, to match the data.

We can also translate these high energy physics parameters into the recent universe quantities of the matter density Ω_m and the present equation of state w_0. Moreover, this is directly related to the doomsday time $t_{\rm doom}$, or future time until collapse. A useful approximation (though we employ the exact solution) between $t_{\rm doom}$, w_0, and the approximate time variation $w_a = -1.5(1 + w_0)$ is

$$t_{\rm doom} \approx 0.5 H_0^{-1} (1 + w_0)^{-0.8} \approx 0.6 H_0^{-1} (-w_a)^{-0.8}. \tag{3.7}$$

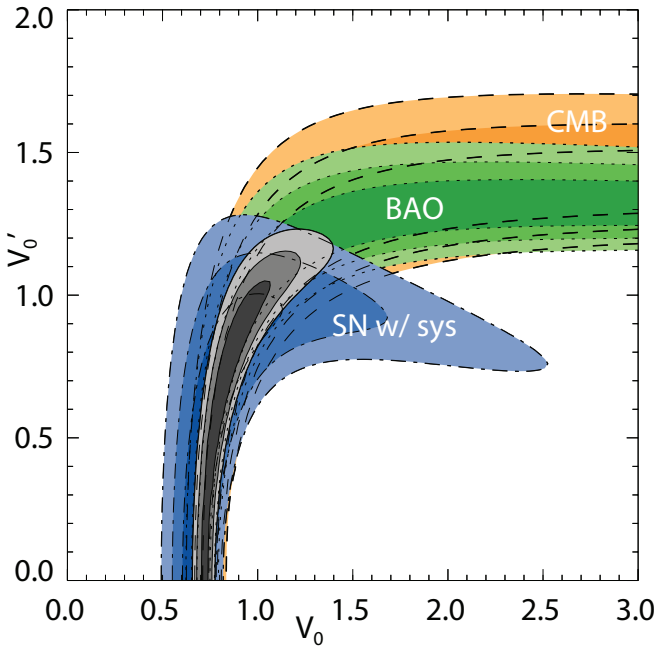

Figure 3.3. Constraints on the linear potential model in terms of the high energy physics quantities of the primordial amplitude and slope of the potential. Note there is less complementarity between some of the probes than for the constant w model. Fig. 3.4 translates these constraints into ones on the cosmological parameters.

Figure 3.4 shows the likelihood contours in the $t_{\rm doom}$-Ω_m and w_0-Ω_m planes. The 95% confidence limit on $t_{\rm doom}$ from present observations is $1.24\,H_0^{-1}$, i.e. we are 95% likely to have at least 17 billion more years before doomsday!

3.6 Mirage Model

Given their limited sensitivity to the dynamics of dark energy, current data can appear to see a cosmological constant even in the presence of time variation. This is called the "mirage of Λ", and we consider mirage models, with a form motivated by the observations as discussed below, specifically to test whether the concordance cosmology truly narrows in on the cosmological constant as the dark energy.

Since cosmological distances involve an integral over the energy density of components, which in turn are integrals over the equation of state as a function of redshift, there exists a chain of dependences between these quantities. Fixing a distance, such as $d_{\rm lss}$ to the CMB last scattering surface, can generally lead to an "attractor" behavior in the equation of state to a common averaged value or the value at a particular redshift. Specifically, Linder (2007) pointed out that if CMB data for $d_{\rm lss}$ is well fit by the ΛCDM model then this

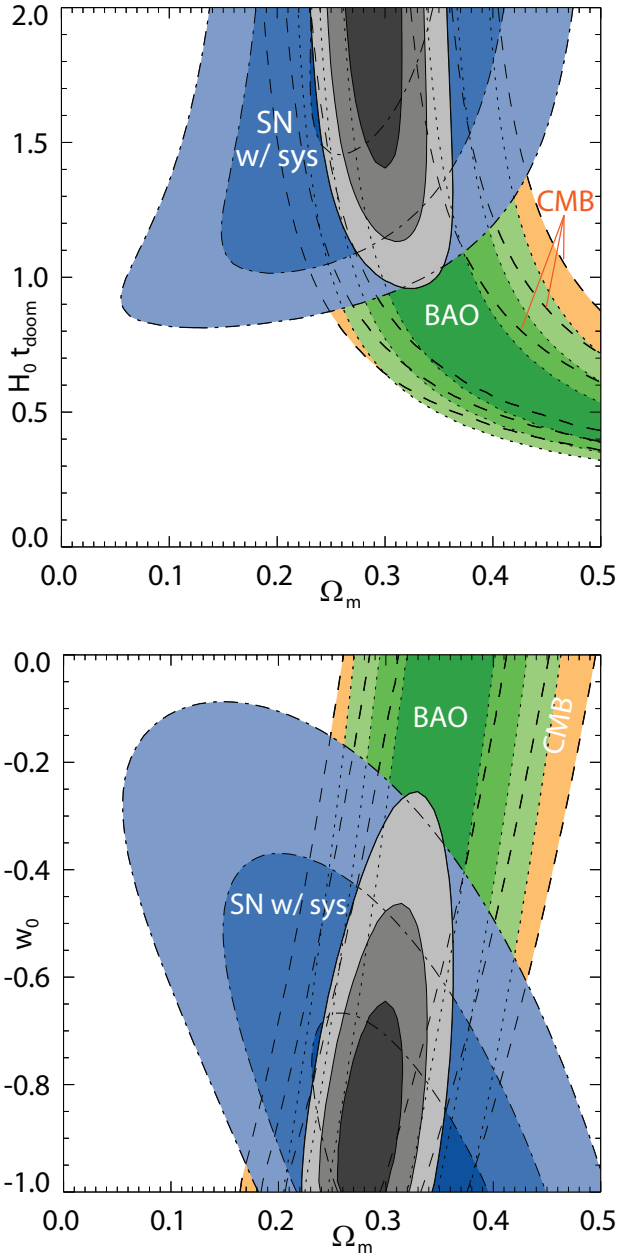

Figure 3.4. The future expansion history in the linear potential model has a collapse, or cosmic doomsday, at a finite time in the future. The left panel shows the confidence contours for the time remaining until collapse; the likelihood contours extend to infinity, with $t_{\rm doom} = \infty$ corresponding to the Λ model. The contours can also be viewed in the equivalent w_0-Ω_m plane (right panel). Current data constraints indicate cosmic doomsday will occur no sooner than $\sim$1.24 Hubble times from now at 95% confidence.

forces $w(z \approx 0.4) \approx -1$ for quite general monotonic EOS. So even dark energy models with substantial time variation could thus appear to behave like the cosmological constant at $z \approx 0.4$, near the pivot redshift of current data.

Since current experiments insensitive to time variation inherently interpret the data in terms of a constant w given by the EOS value at the pivot redshift, this in turn thus leads to the "mirage of Λ": thinking that $w = -1$ everywhere, despite models very different from Λ being good fits. See §5.2 of Linder (2008a) for further discussion. (Also note that attempting to constrain the EOS by combining the CMB $d_{\rm lss}$ with a precision determination of the Hubble constant H_0 only tightens the uncertainty on the pivot equation of state value (already taken to be nearly -1) and so similarly does not reveal the true nature of dark energy.)

We test this with a family of "mirage" models motivated by the reduced distance to CMB last scattering $d_{\rm lss}$. These correspond to the one parameter subset of the two parameter EOS model $w(a) = w_0 + w_a(1-a)$ with $w_a \approx -3.63(1+w_0)$ as shown in Linder (2007). They are not exactly equivalent to imposing a CMB prior since $d_{\rm lss}$ will still change with Ω_m; that is, they essentially test the uniqueness of the current concordance model for cosmology: ΛCDM with $\Omega_m = 0.28$.

For any model well approximated by a relation $w_a = -A(1+w_0)$, as this model (and the previous one) is, the Hubble parameter is given by

$$H^2/H_0^2 = \Omega_m (1+z)^3 + (1-\Omega_m)(1+z)^{3(1+w_0+w_a)} e^{-3w_a z/(1+z)} \quad (3.8)$$

$$= \Omega_m (1+z)^3 + (1-\Omega_m)(1+z)^{3(1+w_0)(1-A)} e^{3A(1+w_0)z/(1+z)} . \quad (3.9)$$

Figure 3.5 shows constraints in the w_0-Ω_m plane. It is important to note that w is not constant in this model. A significant range of w_0 (and hence a larger range of w_a too, roughly $+0.55$ to -1.1 at 68% cl) is allowed by the data, even though these models all look in an averaged sense like a cosmological constant. Thus experiments sensitive to the time variation w_a (e.g. $\sigma(w_a) < 0.36$ to know that $w(z)$ is really, not just apparently, within 10% of -1) are required to determine whether the mirage is reality or not.

3.7 Vacuum Metamorphosis

An interesting model where the cosmic acceleration is due to a change in the behavior of physical laws, rather than a new physical energy density, is the vacuum metamorphosis model (Parker & Raval 2000; Caldwell et al. 2006). As in Sakharov's induced gravity (Sakharov 1968), quantum fluctuations of a massive scalar field give rise to a phase transition in gravity when the Ricci scalar curvature R becomes of order the mass squared of the field, and freezes R there. This model is interesting in terms of its physical origin and nearly first principles derivation, and further because it is an example of a well behaved phantom field, with $w < -1$.

The criticality condition

$$R = 6(\dot{H} + 2H^2) = m^2 \quad (3.10)$$

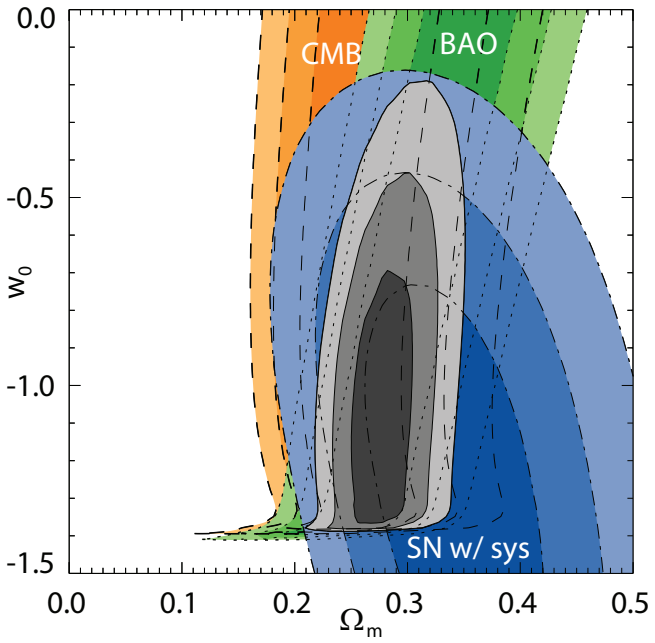

Figure 3.5. The mirage subclass of time varying dark energy looks like Λ in an averaged sense. Note that CMB contours are almost vertical, indicating both that the mirage holds, preserving the ΛCDM distance to last scattering, and yet imposes little constraint on w_0, and hence w_a. Thus the appearance of Λ does not actually exclude time variation. The mirage is broken when the equation of state at high redshift exceeds the matter domination value of zero; this causes the wall in the likelihood at $w_0 = A/(1-A) \approx -1.4$ (see Eq. 3.9).

after the phase transition at redshift z_t leads to a Hubble parameter

$$H^2/H_0^2 = (1-\frac{m^2}{12})(1+z)^4 + \frac{m^2}{12}\,, \qquad z < z_t\,, \tag{3.11}$$

$$H^2/H_0^2 = \Omega_m(1+z)^3 + \frac{m^2}{3}\frac{1-\Omega_\star}{4-3\Omega_\star}\,, \qquad z > z_t\,. \tag{3.12}$$

There is one parameter, $\Omega_\star = \Omega_m(z_t)$, in addition to the present matter density Ω_m, where $1-\Omega_\star$ is proportional to the cosmological constant. The variables z_t and m are given in terms of Ω_m, $\Omega_\star$ by $z_t = (m^2\Omega_\star/[3\Omega_m(4-3\Omega_\star)])^{1/3} - 1$ and $m^2 = 3\Omega_m[(4-3\Omega_\star)/\Omega_\star]^{1/4}[(4/m^2)-(1/3)]^{-3/4}$. The original version of the model had fixed $\Omega_\star = 1$, i.e. no cosmological constant, but if the scalar field has nonzero expectation value (which is not required for the induced gravity phase transition) then there will be a cosmological constant, and $\Omega_\star$ deviates from unity.

Figure 3.6 shows the confidence contours in the $\Omega_\star$-Ω_m plane. To consider constraints on the original vacuum metamorphosis model, without an extra cosmological constant, slice across the likelihood contours at the $\Omega_\star = 1$ line. We see that the three probes are

inconsistent with each other in this case, with disjoint contours (indeed the $\Delta\chi^2 = 28.5$ relative to flat ΛCDM). Allowing for a cosmological constant, i.e. $\Omega_\star \neq 1$, brings the probes into concordance, and the best joint fit approaches the lower bound of the region $\Omega_\star \geq \Omega_m$. The condition $\Omega_\star = \Omega_m$ corresponds to the standard cosmological constant case, with $\Omega_\Lambda = 1-\Omega_m$, since the phase transition then only occurs at $z_t = 0$. Thus the data do not favor any vacuum phase transition. Although this model comprises very different physics, and allows phantom behavior, the data still are consistent with the cosmological constant.

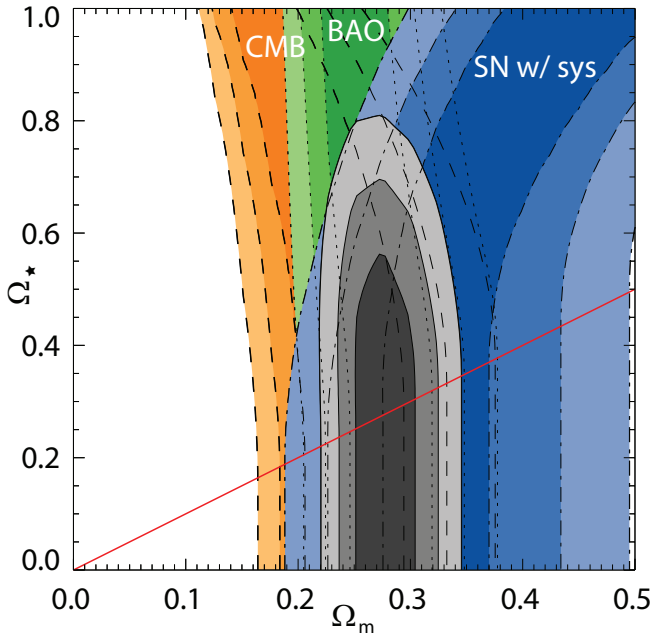

Figure 3.6. The vacuum metamorphosis model involves a phase transition in gravitational laws due to quantum effects. Where the quantum field inducing the gravitational deviation has no additional zeropoint energy, i.e. cosmological constant, then $\Omega_\star = 1$, and the data gives discordant results. As the model approaches the $\Omega_\star = \Omega_m$ line of pure cosmological constant plus matter without a phase transition in the past, the data provide an increasingly good fit. (Below the line, the transition takes place further into the future, with no effect on the data likelihood.)

3.8 Geometric Dark Energy

According to the Equivalence Principle, acceleration is manifest in the curvature of spacetime, so it is interesting to consider geometric dark energy, the idea that the acceleration arises from some property of the spacetime geometry. One example of this involves the holographic principle of quantum field theory as applied to cosmology. This limits

the number of modes available to the vacuum energy and so could have an impact on the cosmological constant problem (Bousso 2002). The basic idea is that there is a spacelike, two dimensional surface on which all the field information is holographically encoded, and the covariant entropy bound relates the area of this surface to the maximum mode energy allowed (UV cutoff). The vacuum energy density resulting from summing over modes ends up being proportional to the area, or inverse square of the characteristic length scale. However, what is perhaps the natural surface to choose (see Bousso (2002)), the causal event horizon, does not lead to an energy density with accelerating properties.

Many of the attempts in the literature to overcome this have grown increasingly distant from the original concept of holography, though they often retain the name. It is important to realize that, dimensionally, any energy density, including the vacuum energy density, has $\rho \sim L^{-2}$, so merely choosing some length L does not imply any connection to quantum holography. We therefore do not consider these models but turn instead to the spacetime curvature.

3.8.1 Ricci dark energy $\mathrm{R_{low}}$

A different approach involves the spacetime curvature directly, as measured through the Ricci scalar. This is similar in motivation to the vacuum metamorphosis model of §3.7. Here we consider it purely geometrically, with the key physical quantity being the reduced scalar spacetime curvature, in terms of the Ricci scalar and Hubble parameter, as in the model of Linder (2004),

$$\mathcal{R} \equiv \frac{R}{12H^2} = r_0 + r_1(1-a). \tag{3.13}$$

Through the equivalence principle, this quantity directly involves the acceleration. Moreover, we can treat it purely kinematically, as in the last equality above, assuming no field equations or dynamics. Of course, any functional form contains an implicit dynamics (see, e.g., Linder (2008a)), but we have chosen effectively a Taylor expansion in the scale factor a, valid for any dynamics for small deviations $1-a$ from the present, i.e. the low redshift or low scalar curvature regime.

At high redshift, as $1-a$ is no longer small, we match it onto an asymptotic matter dominated behavior for $a < a_t = 1-(1-4r_0)/(4r_1)$. Solving for the Hubble parameter,

$$H^2/H_0^2 = a^{4(r_0+r_1-1)}\, e^{4r_1(1-a)}, \quad a > a_t \tag{3.14}$$

$$H^2/H_0^2 = \Omega_m\, a^{-3}, \quad a < a_t\,. \tag{3.15}$$

The matching condition determines

$$\Omega_m = \left(\frac{4r_0+4r_1-1}{4r_1}\right)^{4r_0+4r_1-1} e^{1-4r_0}, \tag{3.16}$$

so there is only one parameter independent of the matter density.

Note also that we can define an effective dark energy as that part of the Hubble parameter deviating from the usual matter behavior, with equation of state generally given by

$$w(a) = \frac{1-4\mathcal{R}}{3}\left[1-\Omega_m\, e^{-\int_a^1 (da/a)(1-4\mathcal{R})}\right]^{-1}. \tag{3.17}$$

For the particular form of Eq. (3.13) we have

$$w_0 \to \frac{1-4r_0}{3(1-\Omega_m)}. \tag{3.18}$$

This model has one EOS parameter in addition to the matter density. We can therefore explore constraints either in the general kinematic plane r_0-r_1, or view them in the Ω_m-w_0 plane. Figure 3.7 shows both.

Good complementarity, as well as concordance, exists among the probes in the r_0-r_1 plane. One obtains an excellent fit with $(r_0, r_1) = (0.81, -0.72)$. The value of $\mathcal{R}$ today, r_0, approaches unity, the deSitter value. Recall that $\mathcal{R} = 1/4$ corresponds to matter domination, and $\mathcal{R} = 1/2$ to the division between decelerating and accelerating expansion, so this kinematic approach clearly indicates the current acceleration of the universe.

An interesting point to note is that ΛCDM is not a subset of this ansatz, i.e. the physics is distinct. No values of r_0 and r_1 give a ΛCDM cosmology. However, the Hubble diagram for the best fit agrees with that for ΛCDM to within 0.006 mag out to $z = 2$ and 0.3% in the reduced distance to CMB last scattering. This is especially interesting as this geometric dark energy model is almost purely kinematic. The agreement appears in the Ω_m-w_0 plane as contours tightly concentrated around $w_0 = -1$, despite there being no actual scalar field or cosmological constant. Again we note the excellent complementarity between the individual probes, even in this very different model.

3.8.2 Ricci dark energy $\mathrm{R_{high}}$

Rather than expanding the spacetime curvature around the present value we can also consider the deviation from a high redshift matter dominated era. That is, we start with a standard early universe and ask how the data favors acceleration coming about. In this second geometric dark energy model (call it $\mathrm{R_{high}}$ for high redshift or large values of scalar curvature), the value of $\mathcal{R}$ evolves from $1/4$ at high redshift. From the definition of $\mathcal{R}$, it must behave asymptotically as

$$\mathcal{R} = \frac{1}{4}\left[1 - 3w_\infty \frac{\delta H^2}{H^2}\right] \approx \frac{1}{4}\left[1 + 4\alpha\, a^{-3w_\infty}\right], \tag{3.19}$$

where $\delta H^2 = (H^2/H_0^2) - \Omega_m\,(1+z)^3$ is the deviation from matter dominated behavior, and w_∞ is the associated, effective equation of state at high redshift, approximated as asymptotically constant.

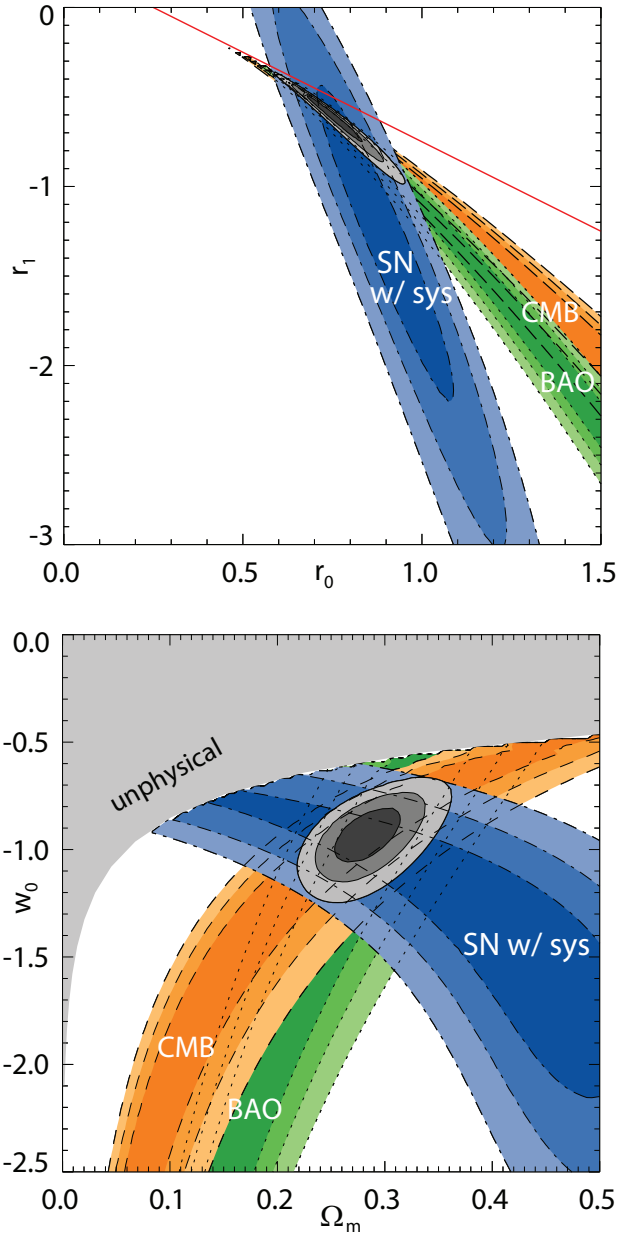

Figure 3.7. Geometric dark energy in the $\mathrm{R_{low}}$ model describes the acceleration directly through the reduced Ricci scalar, or spacetime curvature. This can be viewed in a kinematic sense, in the r_0-r_1 plane, or in a dark energy sense in the Ω_m-w_0 plane. The data favor $w_0 = -1$ but this is not Λ, instead representing distinct physics. For $r_0 + r_1 > 1/4$, above the diagonal line, early matter domination is violated, and the CMB and BAO likelihoods avoid this region, as seen in the left panel; the matter density also cannot then be uniquely defined so the equivalent region is excluded from the right panel.

Next we extend this behavior to a form that takes the reduced scalar curvature to a constant in the far future (as it must if the EOS of the dominant component goes to an asymptotic value):

$$\mathcal{R} = \frac{1}{4} + \frac{\alpha\, a^{-3w_\infty}}{1+\beta\, a^{-3w_\infty}}. \tag{3.20}$$

So today $\mathcal{R} = 1/4 + \alpha/(1+\beta)$ and in the future $\mathcal{R} = 1/4 + \alpha/\beta$. By requiring the correct form for the high redshift Hubble expansion, one can relate the parameters α and β by

$$\alpha = (3\beta w_\infty/4)[\ln \Omega_m/\ln(1+\beta)]\,, \tag{3.21}$$

and finally

$$H^2/H_0^2 = \Omega_m\, a^{-3}\,(1+\beta a^{-3w_\infty})^{-\ln\Omega_m/\ln(1+\beta)}. \tag{3.22}$$

The $\mathrm{R_{high}}$ geometric dark energy model has two parameters β and w_∞, in addition to the matter density Ω_m. This is the first such model we consider, and all remaining models also have two EOS parameters. Although current data cannot in general satisfactorily constrain two parameters, and so for all remaining models we do not show individual probe constraints, if the EOS phase space behavior of the model is sufficiently restrictive then reasonable joint constraints may result.

Figure 3.8 shows the joint likelihoods in the Ω_m-w_∞ and Ω_m-β planes, with the third parameter minimized over (see the caption for discussion of the individual probe likelihoods). We see that the data are consistent with the cosmological constant behavior $w_\infty = -1$ in the past (this is only a necessary, not sufficient condition for $\Lambda\mathrm{CDM}$), and indeed constrain the asymptotic high redshift behavior reasonably well, in particular to negative values of w_∞. This indicates that the Ricci scalar curvature definitely prefers a nearly-standard early matter dominated era, i.e. the deviations faded away into the past. This has important implications as well for scalar-tensor theories that would modify the early expansion history; in particular, the data indicate that deviations in $\mathcal{R}$ must go approximately as a^3 (see Linder & Cahn (2007)) not as a as sometimes assumed.

The parameter β helps determine the rapidity of the Ricci scalar transition away from matter domination. This varies between $\beta = 0$, giving a slow transition but one reaching a deceleration parameter $q = -\infty$ in the asymptotic future, and $\beta \gg 1$, giving a rapid deviation but with smaller magnitude. A cosmological constant behavior has $\beta \approx 3$, as discussed below.

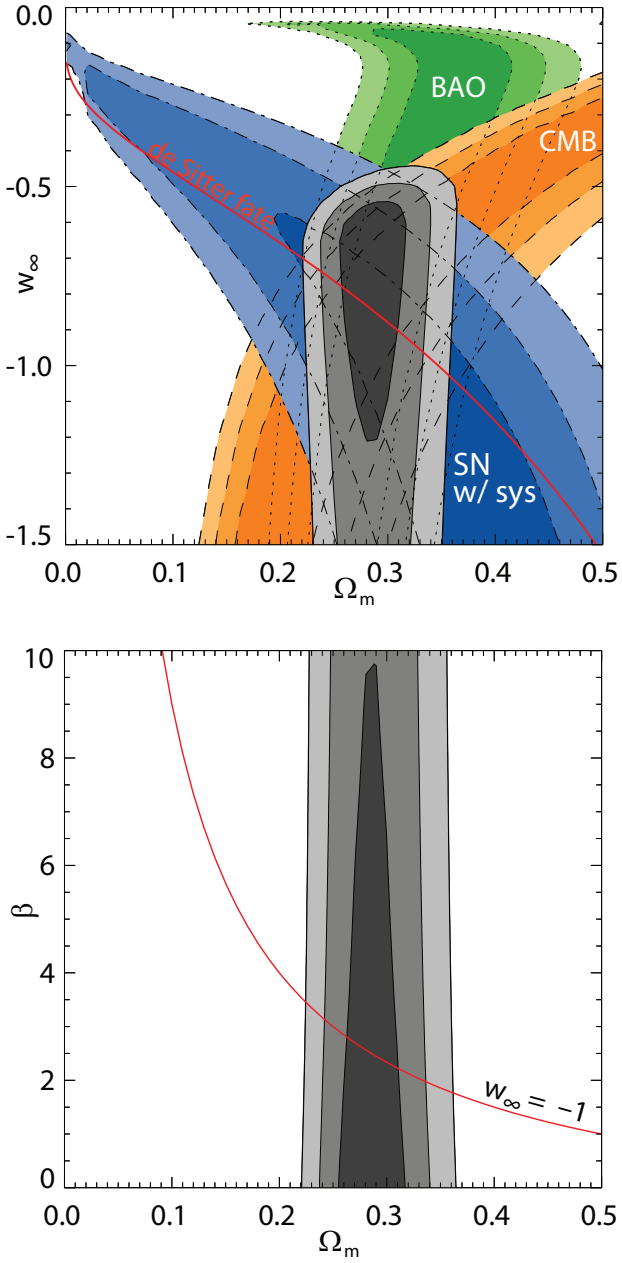

Figure 3.8. Geometric dark energy in the $\mathrm{R_{high}}$ model describes the acceleration directly through the reduced Ricci scalar curvature and deviations from early matter domination. The left panel shows the Ω_m-w_∞ plane, indicating the nature of the deviation ($w_\infty = 0$ corresponds to no transition away from matter domination), and the right panel shows the Ω_m-β plane, indicating the rapidity and fate of the deviation. The curve in the left panel corresponds to the parameter combination for which the fate of the universe is de Sitter; we also show the individual probe constraints, fixing β to the de Sitter value (not minimizing over β as for the joint contour), to show that SN closely map the fate of the universe. In the right panel the curve is the cut through parameter space, fixing $w_\infty = -1$, corresponding to ΛCDM.

Within the three dimensional parameter space, two subspaces are of special interest. One is where $w_\infty = -1$, a necessary condition for consistency with Λ, as mentioned. The other corresponds to a deSitter asymptotic future, defined by the line

$$\beta_{\rm deS} = \Omega_m^{w_\infty} - 1. \tag{3.23}$$

Note that unlike the previous geometric model $\rm R_{low}$, the $\rm R_{high}$ model does include Λ as the limit when both these conditions are satisfied, $w_\infty = -1$ and $\beta = \Omega_m^{-1} - 1$. This relation for the Λ limit is shown as a curve in the Ω_m-β plane. There is an overlap with the joint data likelihood, though one must be careful since the contours have been minimized over w_∞.

Interestingly, we can actually use the data to test consistency with a de Sitter asymptotic future. This is shown by the curve in the Ω_m-w_∞ plane. We see that SN are the probe most sensitive to testing the fate of the universe, with the SN contour oriented similarly to the curve given by Eq. (3.23) that passes through the best fit. Thus the data are consistent with $w_\infty = -1$ and with a de Sitter fate separately, though some tension exists between satisfying them simultaneously. Thus, this geometric dark energy may be distinct from the cosmological constant.

3.9 PNGB Model

Returning to high energy physics models for dark energy, one of the key puzzles is how to prevent quantum corrections from adding a Planck energy scale cosmological constant or affecting the shape of the potential. This is referred to as the issue of technical naturalness. Pseudo-Nambu Goldstone boson (PNGB) models are technically natural, due to a shift symmetry, and so can be considered strongly physically motivated (perhaps even more so than Λ). See Frieman et al. (1995) for an early cosmological analysis of PNGB as dark energy and more recent work by Dutta & Sorbo (2007); Abrahamse et al. (2008).

The potential for the PNGB model is

$$V(\phi) = V_\star\,[1 + \cos(\phi/f)], \tag{3.24}$$

with $V_\star$ setting the magnitude, f the symmetry energy scale or steepness of the potential, and ϕ_i is the initial value of the field when it thaws from the high redshift, high Hubble drag, frozen state. These three parameters determine, and can be thought of as roughly analogous to, the dark energy density, the time variation of the equation of state, and the value of the equation of state. The dynamics of this class of models is sometimes approximated by the simple form

$$w(a) = -1 + (1 + w_0)a^F, \tag{3.25}$$

with F roughly inversely related to the symmetry energy scale f, but we employ the exact numerical solutions of the field evolution equation.

PNGB models are an example of thawing dark energy, where the field departs recently from its high redshift cosmological constant behavior, evolving toward a less negative equation of state. Since the EOS only deviates recently from $w = -1$, the precision in measuring w_0 is more important than the precision in measuring an averaged or pivot EOS value. SN data provide the tightest constraint on w_0. In the future the field oscillates around its minimum with zero potential and ceases to accelerate the expansion, acting instead like nonrelativistic matter.

Figure 3.9 illustrates the constraints in both the particle physics and cosmological parameters. The symmetry energy scale could provide a key clue for revealing the fundamental physics behind dark energy, and it is interesting to note that these astrophysical observations essentially probe the Planck scale. For values of f below unity (the reduced Planck scale), the potential is steeper, causing greater evolution away from the cosmological constant state. However, the field may be frozen until recently and then quickly proceed down the steep slope, allowing values of w_0 far from -1 but looking in an average or constant w sense like $\langle w \rangle \approx -1$. Small values of ϕ_i/f have the field set initially ever more finely near the top of the potential; starting from such a flat region the field rolls very little and w stays near -1 even today. In the limit $\phi_i/f = 0$ the field stays at the maximum, looking exactly like a cosmological constant. The two effects of the steepness and initial position mean that the cosmological parameter likelihood can accommodate both $w_0 \approx -1$ and w_0 approaching 0 as consistent with current data. However, to agree with data *and* $1 + w_0 \sim 1$ requires $f \ll 1$ and fine tuning – e.g. for $f = 0.1$ one must balance the field to within one part in a thousand of the top. Thus in the left panel there exists an invisibly narrow tail extending along the y-axis to $f = 0$. In the right panel, we show how taking more natural values $f \gtrsim 0.5$ removes the more extreme values of w_0 caused by the unnatural fine tuning.

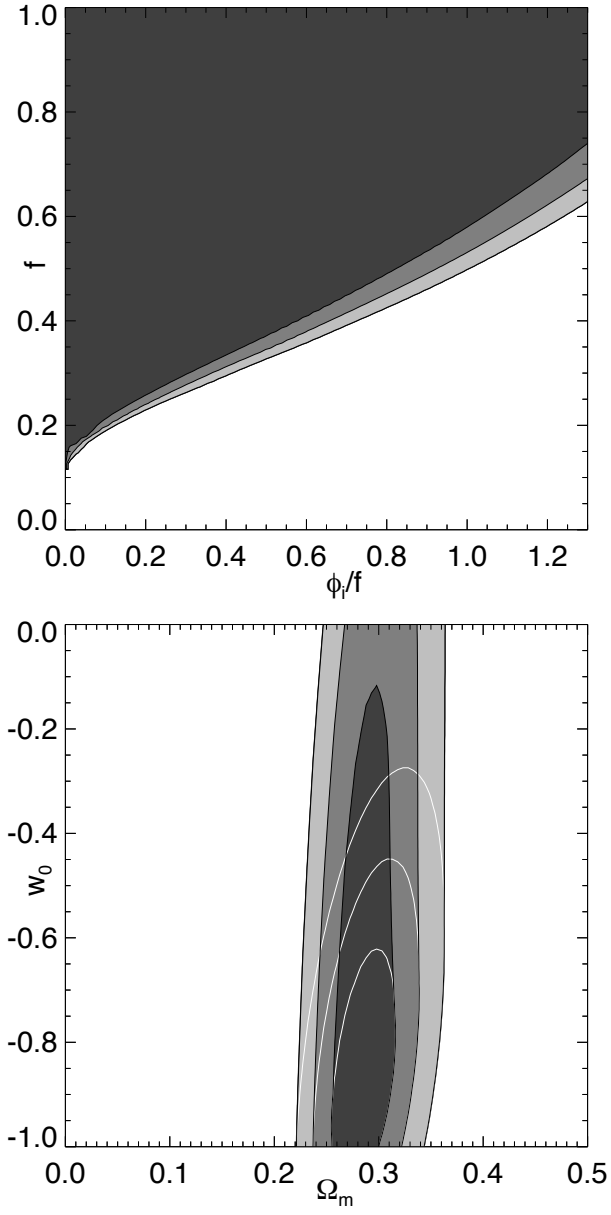

Figure 3.9. Left panel: PNGB model dynamics involves a competition between the steepness of the potential, given by the symmetry energy scale f, and the initial field position ϕ_i/f. If the potential is very steep, $f \ll 1$, the field will roll so rapidly to the potential minimum that the dark energy density never becomes significant, unless ϕ_i/f is fine tuned very near zero. For natural energy scale values near the Planck scale, $f \approx 1$, a wide variety of ϕ_i/f are viable. **Right panel:** The field spends a long period frozen, acting as a cosmological constant before thawing and evolving to a present EOS w_0. For steep potentials with $f \ll 1$, the thawing can be rapid and result in evolution to w_0 far from -1, yet still be consistent with data. The solid confidence level contours in the w_0-Ω_m plane show PNGB results for energy scales $f \geq 0.1$, while the white outline contours consider only PNGB models with more natural energy scales $f \geq 0.5$; the latter favors models closer to the cosmological constant behavior.

3.10 Algebraic Thawing Model

While PNGB models involve a pseudoscalar thawing field, we can also consider scalar fields with thawing behavior. Any such fields that are neither fine tuned nor have overly steep potentials must initially depart from the cosmological constant behavior along a specific track in the EOS phase space, characterized by a form of slow roll behavior in the matter dominated era. (See Caldwell & Linder (2005); Linder (2006); Scherrer & Sen (2008); Cahn et al. (2008).) Here we adopt the algebraic thawing model of Linder (2008b), specifically designed to incorporate this physical behavior:

$$1+w = (1+w_0)\,a^p\left(\frac{1+b}{1+ba^{-3}}\right)^{1-p/3} \tag{3.26}$$

$$H^2/H_0^2 = \Omega_m\,a^{-3}+(1-\Omega_m)\,\exp\left[\frac{3(1+w_0)}{\alpha p}\left\{1-(1-\alpha+\alpha a^3)^{p/3}\right\}\right], \tag{3.27}$$

where $\alpha = 1/(1+b)$ and $b = 0.3$ is a fixed constant not a parameter. The two parameters are w_0 and p and this form follows the scalar field dynamics not only to leading but also next-to-leading order (see Cahn et al. (2008)).

The physical behavior of a minimally coupled scalar field evolving from a matter dominated era would tend to have $p \in [0,3]$. Since we want to test whether the data points to such a thawing model, we consider values of p outside this range. Results are shown in Figure 3.10.

For $p < 0$, the field has already evolved to its least negative value of w and returned toward the cosmological constant. The more negative p is, the less negative (closer to 0) the extreme value of w is, so these models can be more tightly constrained as p gets more strongly negative. As p gets more positive, the field takes longer to thaw, increasing its similarity to the cosmological constant until recently, when it rapidly evolves to w_0. Such models will be very difficult to distinguish from Λ. If we restrict consideration to the physically expected range $p \in [0,3]$, this implies $w_0 < -0.57$ at 95% confidence in these thawing models, so considerable dynamics remains allowed under current data. This estimation is consistent with the two specific thawing models already treated, the doomsday and PNGB cases.

The goodness of fit to the data is the best of all models considered here ($\Delta\chi^2 = -2.3$), even taking into account the addition of two fit parameters. This may indicate that we should be sure to include a cosmological probe sensitive to w_0 (not necessarily the pivot EOS w_p) and to recent time variation w_a, such as SN, in our quest to understand the nature of dark energy.

3.11 Early Dark Energy

The other major class of dark energy behavior is that of freezing models, which start out dynamical and approach the cosmological constant in their evolution. The tracking

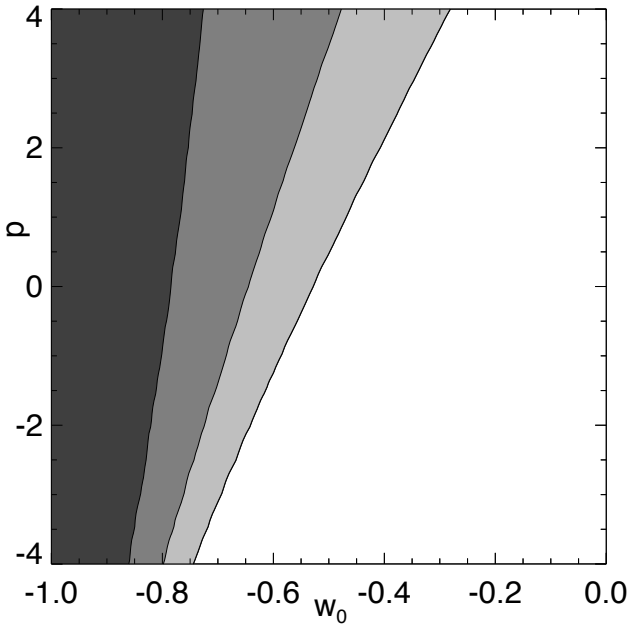

Figure 3.10. Algebraic thawing model incorporates the expected physical behavior of a thawing scalar field rolling slowly from a matter dominated era. Such a model is a fairly generic parametrization for this class of physics when $p \in [0, 3]$, and has a strong goodness of fit.

subclass is interesting from the point of view again of fundamental physics motivation: they can ameliorate the fine tuning problem for the amplitude of the dark energy density by having an attractor behavior in their dynamics, drawing from a large basin of attraction in initial conditions (Zlatev et al. 1999). Such models generically can have nontrivial amounts of dark energy at high redshift; particularly interesting are scaling models, or tracers, where the dark energy has a fixed fraction of the energy density of the dominant component. These can be motivated by dilatation symmetry in particle physics and string theory (Wetterich 1988).

As a specific model of such early dark energy we adopt that of Doran & Robbers (2006), with

$$\Omega_{\rm DE}(a) = \frac{1-\Omega_m-\Omega_e\,(1-a^{-3w_0})}{1-\Omega_m+\Omega_m a^{3w_0}} + \Omega_e\,(1-a^{-3w_0}) \tag{3.28}$$

for the dark energy density as a function of scale factor $a = 1/(1+z)$. Here $\Omega_{\rm DE} = 1-\Omega_m$ is the present dark energy density, Ω_e is the asymptotic early dark energy density, and w_0 is the present dark energy EOS. In addition to the matter density the two parameters are Ω_e and w_0.

The Hubble parameter is given by $H^2/H_0^2 = \Omega_m\, a^{-3}/[1-\Omega_{\rm DE}(a)]$. The standard formula for the EOS, $w = -1/(3[1-\Omega_{\rm DE}(a)])\, d\ln\Omega_{\rm DE}(a)/d\ln a$, does not particularly simplify in this model. Note that the dark energy density does not act to accelerate expan-

sion at early times, and in fact $w \to 0$. However, although the energy density scales like matter at high redshift, it does not appreciably clump and so slows growth of matter density perturbations. We will see this effect is crucial in constraining early dark energy.

Figure 3.11 shows the constraints in the Ω_m-Ω_e and Ω_e-w_0 planes. Considerable early dark energy density appears to be allowed, but this is only because we used purely geometric information, i.e. distances and the acoustic peak scale. The high redshift Hubble parameter for a scaling solution is multiplied by a factor $1/\sqrt{1-\Omega_e}$ relative to the case without early dark energy (see Doran et al. (2007b)). This means that the sound horizon is shifted according to $s \sim \sqrt{1-\Omega_e}$, but a geometric degeneracy exists whereby the acoustic peak angular scale can be preserved by changing the value of the matter density Ω_m (see Linder & Robbers (2008) for a detailed treatment). This degeneracy is clear in the left panel.

However, as mentioned, the growth of perturbations is strongly affected by the unclustered early dark energy. This suppresses growth at early times, leading to a lower mass amplitude σ_8 today. To explore the influence of growth constraints, we investigate adding a growth prior of 10% to the data, i.e. we require the total linear growth (or σ_8) to lie within 10% of the concordance model. The innermost, white contour of the left panel of Fig. 3.11 shows the constraint with the growth prior. In the right panel we zoom in, and show Ω_e vs. w_0, seeing that the degeneracy is effectively broken. The amount of early dark energy is limited to $\Omega_e < 0.038$ at 95% cl. Similar conclusions were found in a detailed treatment by Doran et al. (2007a).

We find a convenient theoretical fitting formula is that for an early dark energy model the total linear growth to the present, g_0, is suppressed by

$$\frac{\Delta g_0}{g_0} \approx \left(\frac{\Omega_e}{0.01}\right) \times 5.1\%, \tag{3.29}$$

relative to a model with $\Omega_e = 0$ but all other parameters fixed. Thus appreciable amounts of early dark energy have significant effects on matter perturbations, and we might expect nonlinear growth to be even more sensitive (e.g. see Bartelmann et al. (2006)).

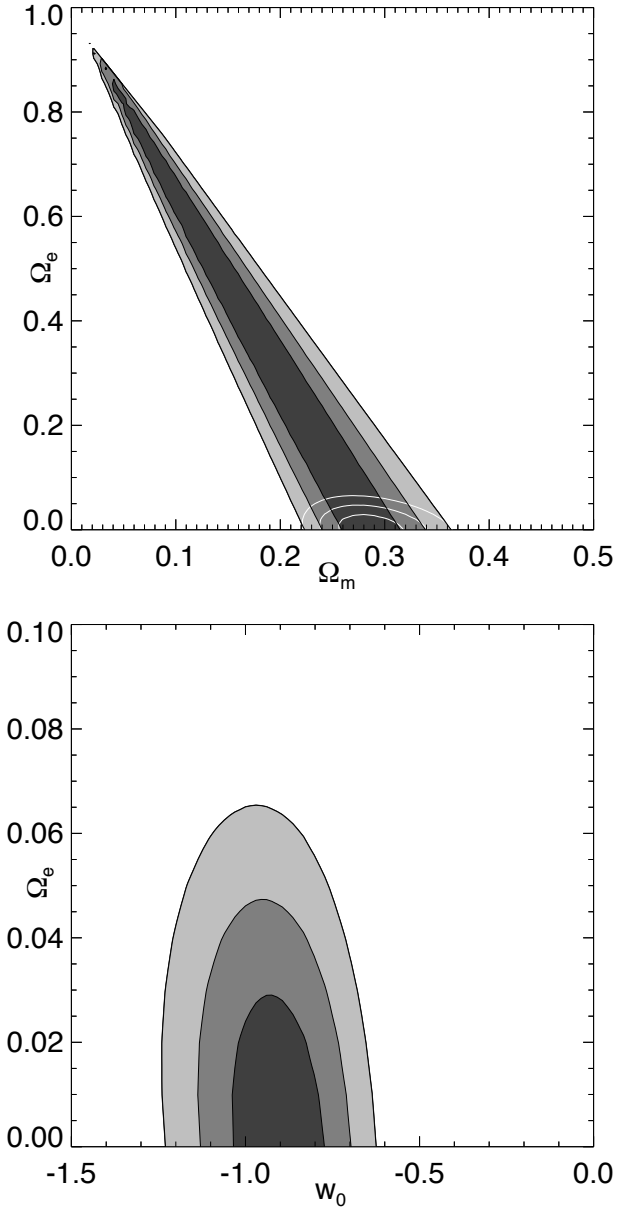

Figure 3.11. Early dark energy represents an example of a freezing model with interesting particle physics motivations. The left panel shows the constraints on Ω_e and Ω_m from purely geometric data, as used throughout this article. The degeneracy evident in the contours leaves the acoustic scales unchanged, but hides the shift in the sound horizon caused by early dark energy, leading to possible misinterpretation of the correct cosmological model. The degeneracy can be broken by adding growth information, here an assumed 10% prior on total linear growth (or σ_8), as shown by the white outline contours. This tightly restricts the early dark energy density to contribute no more than a few percent. The right panel shows the Ω_e-w_0 constraints including the growth prior.

3.12 Growing Neutrino Model

While freezing or scaling models such as the early dark energy model just considered are interesting from the physics perspective, they generically have difficulty in evolving naturally to sufficiently negative EOS by the present. The growing neutrino model of Amendola et al. (2008); Wetterich (2007) solves this by coupling the scalar field to massive neutrinos, forcing the scalar field to a near cosmological constant behavior when the neutrinos go nonrelativistic. This is an intriguing model that solves the coincidence problem through cosmological selection (the time when neutrinos become nonrelativistic) rather than tuning the Lagrangian.

The combined dark sector (cosmon scalar field plus mass-running neutrinos) energy density is

$$\Omega_{\rm ds}(a) = \frac{\Omega_{\rm ds}a^3 + 2\Omega_\nu(a^{3/2}-a^3)}{1-\Omega_{\rm ds}(1-a^3)+2\Omega_\nu(a^{3/2}-a^3)}, \qquad a > a_t \tag{3.30}$$

$$\Omega_{\rm ds}(a) = \Omega_e, \qquad a < a_t\,, \tag{3.31}$$

where $\Omega_{\rm ds} = 1-\Omega_m$ is the present dark sector energy density. The Hubble parameter can be found by $H^2/H_0^2 = \Omega_m a^{-3}/[1-\Omega_{\rm ds}(a)]$ as usual. The two free dark parameters are the neutrino mass or density $\Omega_\nu = m_\nu(z=0)/(30.8h^2\,{\rm eV})$ and the early dark energy density Ω_e. The transition scale factor a_t is determined by intersection of the two behaviors given for $\Omega_{\rm ds}(a)$.

The equation of state is

$$w = -1 + \frac{\Omega_\nu a^{-3/2}}{\Omega_{\rm ds}+2\Omega_\nu(a^{-3/2}-1)}, \qquad a > a_t \tag{3.32}$$

with $w=0$ before the transition, i.e. a return to the standard early dark energy model. One can therefore translate Ω_ν or $m_\nu(z=0)$ into $w_0 = -1+\Omega_\nu/\Omega_{\rm ds} = -1+\Omega_\nu/(1-\Omega_m)$.

Figure 3.12 shows the constraints in the $m_\nu(z=0)$-Ω_e plane. As in the previous early dark energy model, the geometric degeneracy is clear. Again, when we add growth information in the form of a 10% prior on the total linear growth (or the mass variance σ_8), the constraints tighten considerably, as shown in the right panel. Note that the neutrinos themselves cluster and large scale observations may be able to provide future constraints on model parameters (Mota et al. 2008). The 95% confidence level limit on the neutrino mass from the current cosmological data (plus growth) is $2.1\,(h/0.7)^2$ eV (1.2 if only statistical uncertainties are taken into account). These limits are comparable to astrophysical constraints from similar types of data applied to standard, constant mass neutrinos (Goobar et al. 2006; Tegmark et al. 2006). Note that because the neutrino mass grows due to the coupling, the value today can actually be larger than that at, say, $z\approx 3$ where Lyman alpha forest constraints apply (Seljak et al. 2006).

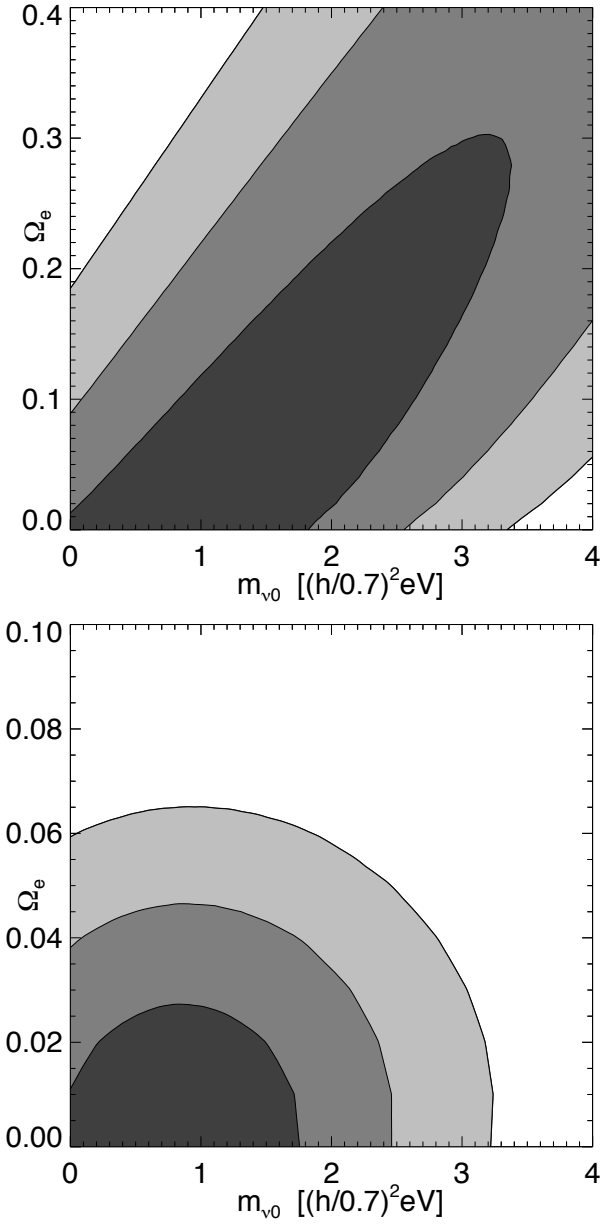

Figure 3.12. Growing neutrino model, coupling a dark energy scalar field to massive neutrinos, can solve the coincidence problem. The left panel shows the constraints from purely geometric data, while the right panel (note the different vertical scale) adds a 10% prior on total linear growth (also see Fig. 3.11). The neutrino mass today becomes tightly constrained to an interesting range, and comparison with laboratory limits could lead to evidence of varying neutrino mass.

3.13 Conclusion

We have considered a wide variety of dark energy physics quite different from the cosmological constant. These include a diversity of physical origins for the acceleration of the expansion: from dynamical scalar fields to dark energy that will eventually cause deceleration and collapse, to gravitational modifications arising from extra dimensions or from quantum phase transitions, to geometric or kinematic parametrization of the acceleration, to dark energy that may have influenced the early universe and that may have its magnitude set by the neutrino mass. The comparison to ΛCDM and constant w cases covers 5 one-parameter and 5 two-parameter dark energy equation of state models. (Linder & Huterer (2005) detail how even next generation data will not generically be able to tightly constrain more than two such parameters.)

Two key results to emphasize are that current data 1) are consistent with Λ, and 2) are also consistent with a diversity of other models and theories, even when we restrict consideration to those with at least modest physical motivation or justification. As explicitly shown by the mirage model, any inclination toward declaring Λ the answer based on consideration of a constant w has an overly restricted view. The need for next generation observations with far greater accuracy, and the development of precision growth probes, such as weak gravitational lensing, is clear. All major classes of physics to explain the nature of dark energy are still in play.

However there are already quite hopeful signs of imminent progress in understanding the nature of dark energy. For example, for the braneworld model tight control of systematics would decrease the goodness of fit to $\Delta\chi^2 = +15$, even allowing for spatial curvature, diminishing its likelihood by a factor 2000 naïvely, effectively ruling out the model. For the doomsday model, improving errors by 30% extends our "safety margin" against cosmic collapse by 10 billion years – a nonnegligible amount! Every improvement in uncertainties pushes the limits on the neutrino mass within the growing neutrino model closer toward other astrophysical constraints – plus this model essentially guarantees a deviation from $w = -1$ of $0.1\,(m_{\nu 0}/\mathrm{eV})$, excitingly tractable. Terrestrial neutrino oscillation bounds already provide within this model that $1 + w > 0.005$.

As points of interest, we note that the model with noticeably positive $\Delta\chi^2$ relative to Λ, and hence disfavored, is completely distinct from the cosmological constant, i.e. the braneworld model has no limit within its parameter spaces equivalent to Λ. This does not say that no such model could fit the data – the $R_{\rm low}$ model is also distinct from Λ but fits as well as many models. Certainly many successful models under current data do look in some averaged sense like a vacuum energy but this does not necessarily point to static dark energy. Two serious motivations to continue looking for deviations are that physicists have failed for 90 years to explain the magnitude required for a cosmological constant, and that the previous known occurrence of cosmic acceleration – inflation – evidently involved a dynamical field not a cosmological constant.

To guide further exploration of the possible physics, we highlight those models which do better than Λ: the geometric dark energy and algebraic thawing approaches. One of the

sole models where adding a degree of freedom is justified (albeit modestly) by the resulting reduction in χ^2 is the $\mathrm{R_{high}}$ model directly studying deviations of the spacetime curvature from the matter dominated behavior. This has one more parameter than the constant w EOS approach, but improves in χ^2 by 1. In addition, it has a built-in test for the asymptotic de Sitter fate of the future expansion. We recommend that this model be considered a model of interest for future fits. The other model improving by at least one unit of χ^2 is the algebraic thawing model, performing better than the other thawing models, with a general parametrization explicitly incorporating the physical conditions imposed by matter domination on the scalar field dynamics.

The diversity of models also illustrates some properties of the cosmological probes beyond the familiar territory of vanilla $\Lambda\mathrm{CDM}$. For example, for the algebraic thawing and other such evolutionary models, the premium is on precision of w_0 and w_a much more than the averaged or pivot EOS value w_p. Not all models possess the wonderful three-fold complementarity of the probes seen in the constant w case; for many of the examples BAO and CMB carry much the same information as each other. However, we clearly see that for every model SN play a valuable role, complementary to CMB/BAO, and often carries the most important physical information: such as on the doomsday time or the de Sitter fate of the universe or the Planck scale nature of the PNGB symmetry breaking.

The diversity of physical motivations and interpretations of acceptable models highlights the issue of assumptions, or priors, on how the dark energy should behave. For example, in the R_{low} model should priors be flat in r_0, r_1 or in Ω_m, w_0; in the PNGB model should they be flat in $f, \phi_i/f$ or in Ω_m, w_0, etc.? Lacking clear physical understanding of the appropriate priors restricts the physical meaning of any Bayesian evidence one might calculate to employ model selection; the χ^2 goodness of fit used here does not run into these complications that can obscure physical interpretation.

We can use our diversity of models for an important consistency test of our understanding of the *data*. If there would be systematic trends in the data which do not directly project into the $\Lambda\mathrm{CDM}$ parameter space (i.e. look like a shift in those parameters), then one might expect that one of the dozen models considered might exhibit a significantly better fit. The fact that we do not observe this can be viewed as evidence that the data considered here is not flawed by significant hidden systematic uncertainties. The data utilize the Union compilation of uniformly analyzed and crosscalibrated Type Ia supernovae data, constituting the world's published set, with systematics treated and characterized through blinded controls. The data are publicly available at http://supernova.lbl.gov/Union, and will be supplemented as further SN data sets become published; the site contains high resolution figures for this work as well.

However, to distinguish deeply among the possible physics behind dark energy requires major advances in several cosmological probes, enabling strong sensitivity to the time variation of the equation of state. This is especially true for those models that are now or were in the past close to the cosmological constant behavior. We are getting our first glimpses looking beyond Λ, but await keen improvements in vision before we can say we understand

the new physics governing our universe. [2]

[2]We thank Andy Albrecht, Robert Caldwell, Roland de Putter, Steven Weinberg, and Christof Wetterich for helpful discussions. The work described in this chapter has been supported in part by the Director, Office of Science, Office of High Energy Physics, of the U.S. Department of Energy under Contract No. DE-AC02-05CH11231. M.K. acknowledges support from the Deutsche Forschungsgemeinschaft (DFG).

CHAPTER 4

Union2

4.1 Introduction

In the original Union analysis described in Chapter 2, each supernova is assumed equally affected by each systematic. This is especially problematic towards the high-redshift end of the Hubble diagram, where the data quality is quite heterogeneous. Although we computed constraints on two-parameter descriptions of dark energy including systematics (w_0-w_a in Chapter 2 and numerous models in Chapter 3), we hesitated to compute constraints on binned-w models. These types of many-parameter models require a fidelity to the systematics analysis that was somewhat lacking in the original treatment.

This chapter presents a number of improvements to the Union analysis. I now compute the sensitivity of each supernova to each calibration systematic. Supernovae measured with only two photometric bands, for example, are generally far less robust to calibration uncertainties than supernovae measured with three or four bands. In addition to accurate propagation of photometric calibration uncertainties, these sensitivities also allow for the propagation of uncertainties in Milky-Way and intergalactic extinction. In addition, we replace the SALT light-curve fitter (which is based around warping a single supernova spectral time series) with the SALT2 fitter (which has a time-series that varies with light-curve shape). Our tests, and those of Guy et al. (2007); Conley et al. (2008), show that SALT2 outperforms SALT. This new compilation, consisting of 557 supernovae, is called the Union2 compilation and we use it to derive many-parameter dark-energy constraints including systematic uncertainties for the first time.[1]

4.2 Light curve fitting

SN Ia that have bluer colors or broader light curves tend to be intrinsically brighter (Phillips 1993; Tripp 1998). Several methods of combining this information into an accu-

[1] This material was previously published as Sections 6, 7, 8, and the final appendix of Amanullah et al. (2010).

rate measure of the relative distance have been used (Riess et al. 1996; Goldhaber et al. 2001; Wang et al. 2003; Guy et al. 2005, 2007; Jha et al. 2007; Conley et al. 2008).

In Chapter 2, we consistently fitted all light curves using the SALT (Guy et al. 2005) fitter, which is built on the SN Ia SED from Nugent et al. (2002). In this chapter, we use SALT2 (Guy et al. 2007), which is based on more data.

Conley et al. (2008) compared the performances of different light curve fitters while also introducing their own empirical fitter, SiFTO, and concluded that SALT2 along with SiFTO perform better than both SALT (which is conceptually different from its successor SALT2) and MLCS2k2 (Jha et al. 2007) when judged by the scatter around the best-fit luminosity distance relationship. Furthermore, SALT2 and SiFTO produce consistent cosmological results when both are trained on the same data. Recently KS09 made a thorough comparison between SALT2 and their modified version of MLCS2k2 (Jha et al. 2007) for a compilation of public data sets, including the one from the SDSS SN survey. The two light curve fitters result in an estimate of w (for a flat wCDM cosmology) that differs by 0.2. The difference exceeds their statistical and systematic (from other sources) error budgets. They determine that this deviation originates almost exclusively from the difference between the two fitters in the rest-frame U-band region, and the color prior used in MLCS2k2. They also noted that MLCS2k2 is less accurate at predicting the rest-frame U-band using data from filters at longer wavelengths.

This difference in U-band performance is not surprising: observations carried out in the observer-frame U-band are in general associated with a high level of uncertainty due to atmospheric variations. While the training of MLCS2k2 is exclusively based on observations of nearby SNe, the SiFTO and SALT2 training address this difficulty by also including high redshift data where the rest-frame U-band is observed at redder wavelengths. This approach also allows these fitters to extend blueward of the rest-frame U-band.

In addition, for this work, we have conducted our own test validating the performance of SALT2 by carrying out the Monte-Carlo simulation described in 4.3.3, where we compare the fitted SALT2 parameters to the corresponding real values for mock samples with poor cadence and low signal-to-noise drawn from individual well-measured nearby SNe.

Given these tests that have been carried out on SALT2, and its high redshift source for rest-frame U-band, we have chosen to use SALT2 for this work.

4.2.1 SALT2

The SALT2 SED model has been derived through a pseudo-Principal component analysis based on both photometric and spectroscopic data. Most of these data come from nearby SN Ia data, but SNLS supernovae are also included. To summarize, the SALT2 SED, $F(\mathrm{SN}, p, \lambda)$, is a function of both wavelength, λ, and time since B-band maximum, p. It consists of three components; a model of the time dependent average SN Ia SED, $M_0(p, \lambda)$, a model of the variation from the average, $M_1(p, \lambda)$, and a wavelength dependent function that warps the model, $CL(\lambda)$. The three components have been determined

from the training process (Guy et al. 2007) and are combined as

$$F(\mathrm{SN}, p, \lambda) = x_0 \times [M_0(p, \lambda) + x_1 \times M_1(p, \lambda)] \times \exp[c \times CL(\lambda)] \ ,$$

where x_0, x_1 and c are free parameters that are fit for each individual SN.

Here, x_0, describes the overall SED normalization, x_1, the deviation from the average decline rate ($x_1 = 0$) of a SN Ia, and c, the deviation from the mean SN Ia $B - V$ color at the time of B-band maximum. These parameters are determined for each observed SN by fitting the model to the available data. The fit is carried out in the observer frame by redshifting the model, correcting for Milky Way extinction (using the CCM-law from Cardelli et al. (1989) with $R_V = 3.1$), and multiplying by the effective filter transmission functions provided by the different observatories. All synthetic photometry is carried out in the Vega system using the spectrum from Bohlin (2007a). Following Astier et al. (2006) we adopt the magnitudes $(U, B, V, R_C, I_C) = (0.020, 0.030, 0.030, 0.030, 0.024)$ mag (Fukugita et al. 1996) for Vega. For the near-infrared we adopt the values $J = 0$ and $H = 0$.

The three parameters $m_B^{\max} = -2.5 \log_{10} \left[\int_B F(\mathrm{SN}, 0, \lambda)\, \lambda\, d\lambda\right]$, x_1 and c, can for each SN be combined to form the distance modulus (Guy et al. 2007),

$$\mu_B = m_B^{\mathrm{corr}} - M_B = m_B^{\max} + \alpha \cdot x_1 - \beta \cdot c - M_B \,, \tag{4.1}$$

where M_B is the absolute B-band magnitude. The parameters α, β and M_B are nuisance parameters which are fitted simultaneously with the cosmological parameters.

4.3 The Union2 Compilation

Chapter 2 presented an analysis framework for combining different SN Ia data sets in a consistent manner. Since then two other groups (H09 and KS09) have made similar compilations, using different fitters. In this work we carry out an improved analysis, using and refining the Chapter 2 approach. We extend the sample with the six SNe presented here, the SNe from Amanullah et al. (2008), the low-z and intermediate-z data from Hicken et al. (2009) and Holtzman et al. (2008) respectively[2].

First, all light curves are fitted using a single light curve fitter (the SALT2 method) in order to eliminate differences that arise from using different fitters. For all SNe going into the analysis we require:

1. data from at least two bands with rest-frame central wavelengths between 2900Å and 7000Å, the default wavelength range of SALT2

2. that there is at least one point between -15 days and 6 rest frame days relative to the B-band maximum.

[2]The SALT2 fit results for these samples are presented along with the entire Union2 compilation fits at `http://supernova.lbl.gov/Union/`.

3. that there are in total at least five valid data points available.

4. that the fitted x_1 values, including the fitted uncertainties, lie between $-5 < x_1 < 5$. This is a more conservative cut than that used in Chapter 2 and results in several poorly measured SNe being excluded. Part of the discrepancy observed by KS09 when using different light curve models could be traced to poorly measured SNe.

5. that the CMB-centric redshift is greater than $z > 0.015$.

We also exclude one SN from the Union compilation that is 1991bg-like, which neither the SALT nor the SALT2 models are trained to handle. Note that another 1991bg-like SN from the Union compilation was removed by the outlier rejection.

All SNe Ia considered in this compilation are listed in Table 13 of Amanullah et al. (2010). For each SN, the redshift and fitted light curve parameters are presented as well as the failed cuts, if any.

It should be pointed out that the choice of light curve model also has an impact on the sample size. Using SALT2 will allow more SNe to pass the cuts above, since the SALT2 model covers a broader wavelength range than SALT. This is particularly important for high-z data that heavily rely on rest-frame UV data. For example, two net SNe would have been cut from the Riess et al. (2007) sample with the SALT model.

4.3.1 Revised HST zero-points and filter curves

Since Riess et al. (2007), the reported zero-points of both NICMOS and ACS were revised. For the F110W and F160W filters of NICMOS, the revision is substantial. Using the latest calibration (Thatte et al. 2009, and references within), the revised zero-points are, for both filters, approximately $5\,\%$ fainter than those reported in Riess et al. (2007) and subsequently used in Chapter 2.

For SNe Ia at $z > 1.1$, observations with NICMOS cover the rest frame optical, so the fitted peak B-band magnitudes and colors and the corrected B-band magnitudes of these SNe Ia depend directly on the accuracy of the NICMOS photometry. With the new zero-points, SNe Ia at $z > 1.1$ are measured to be fainter and bluer. Our current analysis also corrects an error in the NICMOS filter curves that were used in Chapter 2, which also acts in the same direction.

In the introduction, we had noted that almost all SNe at $z > 1.1$ were redder than the average SN color over the redshift interval 0.3 to 1.1. This is surprising as redder SNe are also fainter and should therefore be the harder to detect in magnitude limited surveys. Chapter 2 noted that these SNe, after light curve shape and color corrections, are also on average ~ 0.1 mag brighter than the line tracing the best fit ΛCDM cosmology. They also noted that this was the reason for the relatively high value for the binned value of w in the $[0.5, 1]$ redshift bin.

After taking the NICMOS zero-point and filter updates just discussed into account, we repeated the Chapter 2 analysis. This made the NICMOS observed SNe up to ~ 0.1 mag

fainter, and there no longer is a significant offset from the best-fit cosmology. Nor are these SNe unusually red when compared to SNe over the redshift interval 0.3 to 1.1. For SALT2 the SNe at $z > 1.1$ have an average color of $c = 0.06 \pm 0.03$, compared to $c = 0.02 \pm 0.01$ for $0.3 < z < 1.1$, and no significant offset in the Hubble diagram.

There could however still be unresolved NICMOS issues. For example the NICMOS SN photometry depends on extrapolating the non-linearity correction to low flux levels. We have a program (HST GO-11799) to obtain a calibration of NICMOS at low flux levels. The photometry of the SNe observed with NICMOS will be revised once this program is completed.

4.3.2 Fitting Cosmology

Following Conley et al. (2006a) and Chapter 2, we adopt a blind analysis approach for cosmology fitting where the true fitted values are not revealed until the complete analysis framework has been settled. The blind technique is implemented by adjusting the magnitudes of the SNe until they match a fiducial cosmology ($\Omega_M = 0.25$, $w = -1$). This procedure leaves the residuals only slightly changed, so that the performance of the analysis framework can be studied. The best fitted cosmology with statistical errors is obtained through an iterative χ^2-minimization of

$$\chi^2_{\rm stat} = \sum_{\rm SNe} \frac{\left[\mu_B(\alpha, \beta, M) - \mu(z; \Omega_M, \Omega_w, w)\right]^2}{\sigma^2_{\rm ext} + \sigma^2_{\rm sys} + \sigma^2_{\rm lc}}\,, \tag{4.2}$$

where,

$$\sigma^2_{\rm lc} = V_{m_B} + \alpha^2 V_{x_1} + \beta^2 V_c + 2\alpha V_{m_B,x_1} - 2\beta V_{m_B,c} - 2\alpha\beta V_{x_1,c} \tag{4.3}$$

is the propagated error from the covariance matrix, V, of the light curve fits, with α and β being the x_1 and color correction coefficients of equation 4.1. Uncertainties due to host galaxy peculiar velocities of 300 km/s and uncertainties from Galactic extinction corrections and gravitational lensing as described in 4.3.3 are included in $\sigma_{\rm ext}$. A floating dispersion term, $\sigma_{\rm sys}$, which contains potential sample-dependent systematic errors that have not been accounted for and the observed intrinsic SN Ia dispersion, is also added. The value of $\sigma_{\rm sys}$ is obtained by setting the reduced χ^2 to unity for each sample. Computing a separate $\sigma_{\rm sys}$ for each sample prevents samples with poorer-quality data from increasing the errors of the whole sample. This approach does however still assume that all SNe within a sample are measured with roughly the same accuracy. If this is not the case there is a risk in degrading the constraints from the sample by down weighting the best measured SNe. It should also be pointed out that the fitted values of $\sigma_{\rm sys}$ will be less certain for small samples and can therefore deviate significantly from the average established by the larger samples (in particular, the six high-z SNe presented in this work are consistent with $\sigma_{\rm sys} = 0$), as are three other samples.

A number of systematic errors are also being considered for the full cosmology analysis. These are taken into account by constructing a covariance matrix for the entire sample

which will be described below in 4.3.3. The terms in the denominator of equation 4.2 are then added along the diagonal of this covariance matrix.

As in Chapter 2, we carry out an iterative χ^2 minimization with 3σ outlier rejection. Each sample is fit for its own absolute magnitude by minimizing the sum of the absolute residuals from its Hubble line (rather than the sum of the squared residuals). The line is then used for outlier rejection. This approach was investigated in detail in Chapter 2, and it was shown with simulations that the technique is robust and that the results are unaltered from the Gaussian case in the absence of contamination and that in the presence of a contaminating contribution, its impact is reduced. Table 4.1 summarizes the effect of the outlier cut on each sample. We also note that the residuals have a similar distribution to a Gaussian in that $\sim 5\%$ of the sample is outside of 2σ.

Table 4.1. Statistics of each sample with no outlier rejection or 3σ outlier rejection (used in this chapter). Here, $\sigma_{\rm sys}$ has the same meaning as in equation 4.2. Both $\sigma_{\rm sys}$ and the RMS are also plotted for each sample in Figure 4.3. Although each sample is independently fit for its $\sigma_{\rm sys}$ and RMS, a global α and β are always used. This explains the minor shifts in parameters for samples where no supernovae are cut. A 2σ cut removes 34 more supernovae, so going from 3 to 2σ is consistent with Gaussian residuals.

	No Outlier Cut			$\sigma_{\rm cut} = 3$		
Set	SNe	$\sigma_{\rm sys}(68\%)$	RMS (68%)	SNe	$\sigma_{\rm sys}(68\%)$	RMS (68%)
Hamuy et al. (1996)	18	$0.15^{+0.05}_{-0.03}$	$0.17^{+0.03}_{-0.03}$	18	$0.15^{+0.05}_{-0.03}$	$0.17^{+0.03}_{-0.03}$
Krisciunas et al. (2005)	6	$0.01^{+0.14}_{-0.01}$	$0.11^{+0.02}_{-0.03}$	6	$0.04^{+0.13}_{-0.04}$	$0.11^{+0.03}_{-0.03}$
Riess et al. (1999)	11	$0.16^{+0.07}_{-0.03}$	$0.17^{+0.03}_{-0.04}$	11	$0.15^{+0.07}_{-0.03}$	$0.17^{+0.03}_{-0.04}$
Jha et al. (2006)	15	$0.20^{+0.07}_{-0.04}$	$0.22^{+0.04}_{-0.04}$	15	$0.21^{+0.07}_{-0.04}$	$0.22^{+0.04}_{-0.04}$
Kowalski et al. (2008)	8	$0.04^{+0.08}_{-0.04}$	$0.14^{+0.03}_{-0.04}$	8	$0.07^{+0.09}_{-0.06}$	$0.15^{+0.03}_{-0.04}$
Hicken et al. (2009)	104	$0.18^{+0.02}_{-0.02}$	$0.21^{+0.01}_{-0.01}$	102	$0.15^{+0.02}_{-0.01}$	$0.19^{+0.01}_{-0.01}$
Holtzman et al. (2009)	133	$0.19^{+0.02}_{-0.01}$	$0.23^{+0.01}_{-0.01}$	129	$0.10^{+0.01}_{-0.01}$	$0.15^{+0.01}_{-0.01}$
Riess et al. (1998) + HZT	11	$0.31^{+0.19}_{-0.09}$	$0.53^{+0.10}_{-0.12}$	11	$0.31^{+0.19}_{-0.09}$	$0.52^{+0.10}_{-0.12}$
Perlmutter et al. (1999)	33	$0.41^{+0.12}_{-0.09}$	$0.64^{+0.07}_{-0.08}$	33	$0.41^{+0.12}_{-0.09}$	$0.64^{+0.07}_{-0.08}$
Barris et al. (2004)	19	$0.19^{+0.13}_{-0.10}$	$0.39^{+0.06}_{-0.07}$	19	$0.18^{+0.13}_{-0.10}$	$0.38^{+0.06}_{-0.07}$
Amanullah et al. (2008)	5	$0.18^{+0.21}_{-0.06}$	$0.20^{+0.05}_{-0.07}$	5	$0.19^{+0.21}_{-0.06}$	$0.21^{+0.05}_{-0.07}$
Knop et al. (2003)	11	$0.04^{+0.10}_{-0.04}$	$0.15^{+0.03}_{-0.03}$	11	$0.05^{+0.10}_{-0.05}$	$0.15^{+0.03}_{-0.03}$
Astier et al. (2006)	73	$0.18^{+0.03}_{-0.03}$	$0.25^{+0.02}_{-0.02}$	72	$0.13^{+0.03}_{-0.02}$	$0.21^{+0.02}_{-0.02}$
Miknaitis et al. (2007)	77	$0.25^{+0.04}_{-0.03}$	$0.34^{+0.03}_{-0.03}$	74	$0.19^{+0.04}_{-0.03}$	$0.29^{+0.02}_{-0.02}$
Tonry et al. (2003)	6	$0.17^{+0.21}_{-0.10}$	$0.24^{+0.06}_{-0.07}$	6	$0.15^{+0.21}_{-0.12}$	$0.23^{+0.05}_{-0.07}$
Riess et al. (2007)	33	$0.27^{+0.07}_{-0.04}$	$0.49^{+0.06}_{-0.06}$	31	$0.16^{+0.06}_{-0.05}$	$0.45^{+0.05}_{-0.06}$
This Work	6	$0.00^{+0.00}_{0.00}$	$0.12^{+0.03}_{-0.04}$	6	$0.00^{+0.00}_{0.00}$	$0.12^{+0.03}_{-0.04}$
Total	569			557		

Figure 4.2 shows the individual residuals and pulls from the best fit cosmology together with the fitted SALT2 colors for the different samples. The photometric quality is illustrated by the last column in the figure showing the color uncertainty. It is notable how the photometric quality on the high redshift end has improved from the analysis presented in Chapter 2. This is due to the extended rest-frame range of the SALT2 model compared to SALT.

Figure 4.3 shows the diagnostics used for studying the consistency between the different samples. The left panel shows the fitted $\sigma_{\rm sys}$ values for each sample together with the RMS

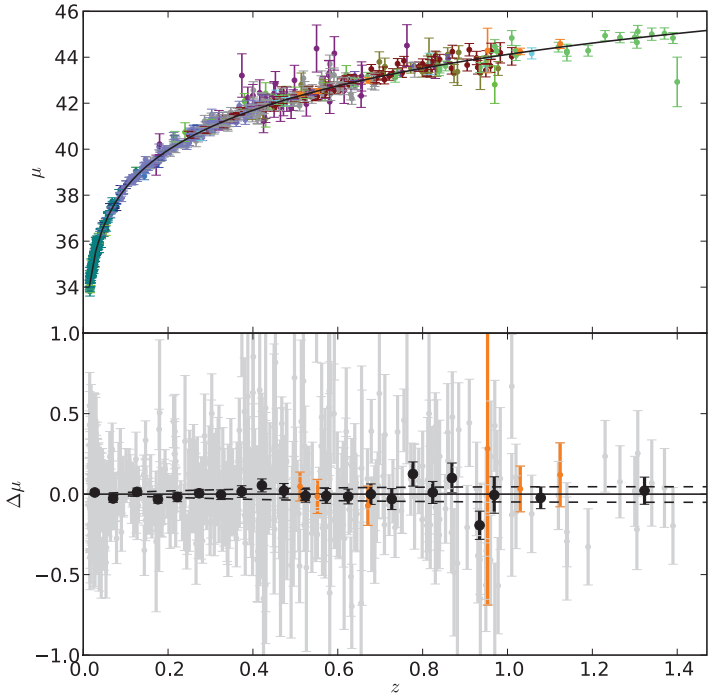

Figure 4.1. *Upper panel:* Hubble diagram for the Union2 compilation. The solid line represents the best fitted cosmology for a flat Universe including the CMB and BAO constraints discussed in the text. The different colors have the same interpretation as in Figures 4.2 and 4.3. *Lower panel:* Hubble diagram residuals where the best fitted cosmology has been subtracted from the light curve shape and color corrected peak magnitudes. The gray points show the residuals for individual SNe, while the black points show the binned values in redshifts bins of 0.05 for $z < 1.0$ and 0.2 for $z > 1.0$. The orange points show the previously unpublished SNe introduced in this work. The dashed lines show the expected Hubble diagram residuals for cosmological models with $w \pm 0.1$ from the best fitted value.

around the best fitted cosmology. The intrinsic dispersion associated with all SNe can be determined as the median of $\sigma_{\rm sys}$ as long as the majority of the samples are not dominated by observer-dependent uncertainties that have not been accounted for. The median $\sigma_{\rm sys}$ for this analysis is 0.15 mag, indicated by the leftmost dashed vertical line in the figure. The two mid-panels show the tensions for the individual samples, by comparing the average residuals from the best-fit cosmology. The two panels show the tensions without and with systematic errors (described in 4.3.3) being considered. Most samples fall within 1σ and no sample exceeds 2σ. The right panel shows the tension of the slopes of the residuals as a function of redshift. This test may not be very meaningful for sparsely sampled data sets, but could reveal possible Malmquist bias for large data sets.

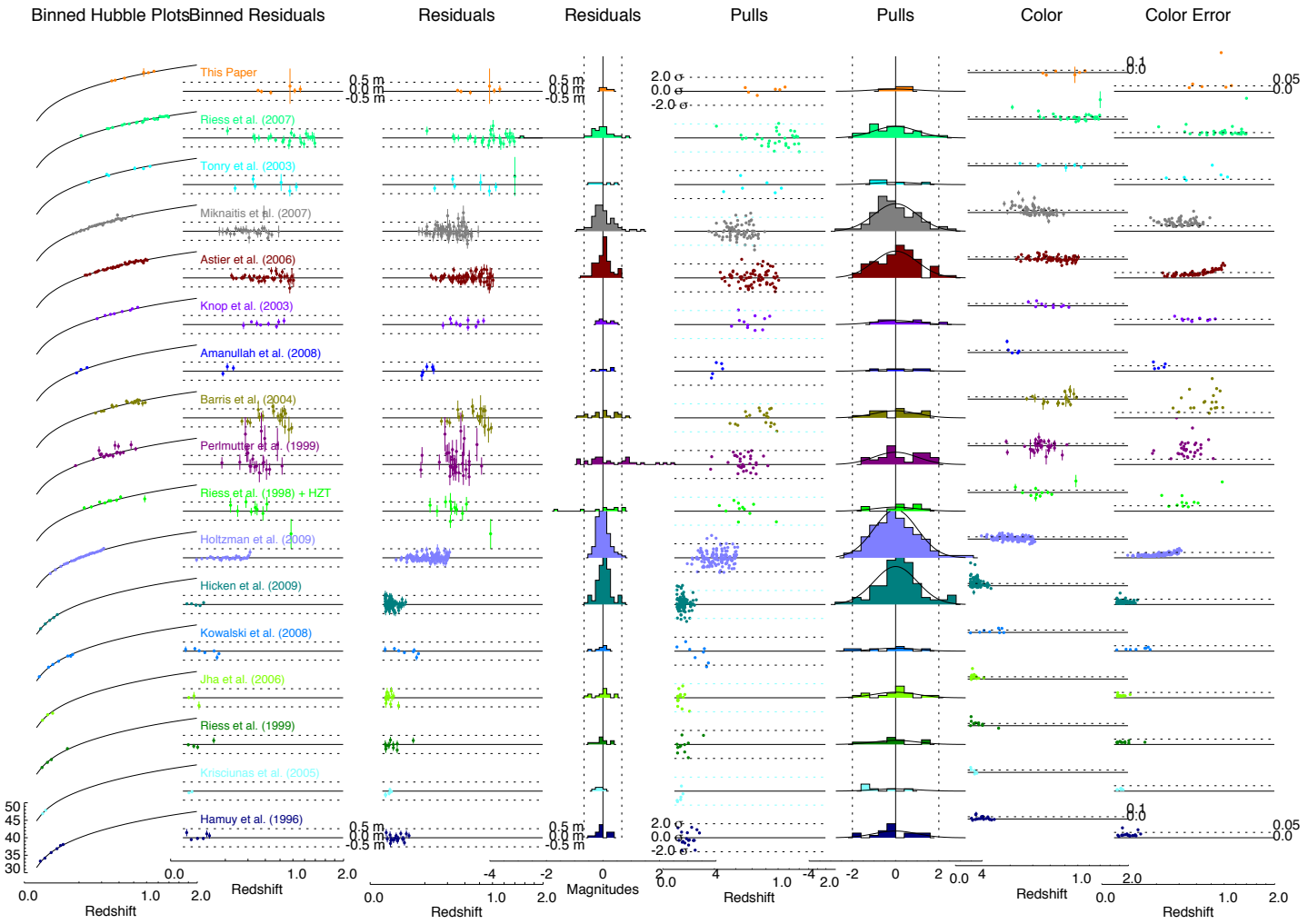

Figure 4.2. Individual diagrams and distributions for the different data sets. From left to right: a) Hubble diagrams for the various samples; b) binned magnitude residuals from the best fit cosmology (bin-width: $\Delta z = 0.01$); c) unbinned magnitude residuals from the best fit; d) histogram of the residuals from the best fit; e) pull of individual SNe as a function of redshift; f) histogram of pulls; g) SN color as a function of redshift; h) uncertainty of the color measurement as an illustration of the photometric quality of the data.

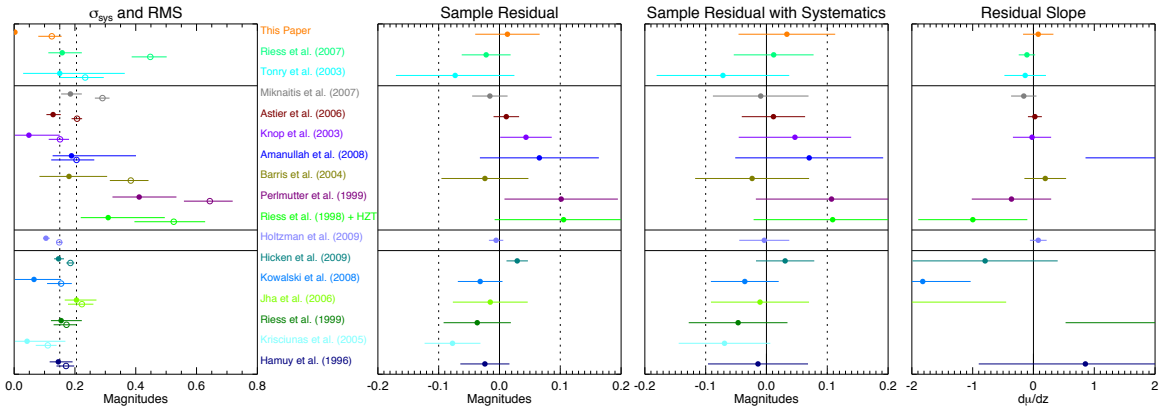

Figure 4.3. Diagnostics plot for the individual data sets. From left to right: Systematic dispersion (filled circles) and RMS around the best fit model (open circles); The mean, sample averaged, deviation from the best fit model; The slope of the Hubble-residual (in magnitudes) versus redshift, $d\mu_{\rm residual}/dz$. Note that the errors on the systematic dispersion are the statistical errorbars and do not include possible systematic effects such as misestimating photometry errors.

The SNe introduced in this work show no significant tension in any of the panels. The Hubble residuals for these are also presented in Figure 4.1. Here, the individual SNe are consistent with the best fit cosmology.

All tables and figures, including the complete covariance matrix for the sample, are available in electronic format on the Union webpage[3]. We also provide a CosmoMC module for including this supernova compilation with other datasets.

4.3.3 Systematic errors

The analysis in Chapter 2 split systematic errors into two categories: the first type affects each SN sample independently, the second type affects SNe at similar redshifts. Malmquist bias and uncertainty in the colors of Vega are examples of the first and second type, respectively. Typical numbers were derived for both of these types of systematics, and they were included as covariances[4] between SNe. Each sample received a common covariance, and all of the high-redshift ($z > 0.2$) SNe shared an additional common covariance.

Other analyses (Astier et al. (2006), Wood-Vasey et al. (2007), KS09) have estimated the effect on w for each systematic error and summed these in quadrature. However, Kim & Miquel (2006) show that parameterizing systematic errors (such as uncertain zeropoints) with nuisance parameters is a more appropriate approach and gives better cosmological constraints. For this analysis, all contributing factors, described below, were translated

[3] `http://supernova.lbl.gov/Union/`

[4] Note that adding a covariance is equivalent to minimizing over a nuisance parameter that has a Gaussian prior around zero; the discussion in Chapter 2 is in terms of these nuisance parameters. This is further discussed in Appendix A.1.

to nuisance parameters, which were then incorporated into a covariance matrix for the distances of the individual SNe. Appendix A.1 contains the details of converting nuisance parameters to a covariance matrix.

Zero-point Uncertainties

In order to correctly propagate calibration uncertainties, we computed numerically the effect of each photometric passband on the distance modulus. For each SN, the photometry from each band was shifted in turn by 0.01 magnitudes and then refit for μ. We then computed the change in distance modulus, giving $\frac{d\mu(\alpha,\beta)}{d(\mathrm{ZP})}$ for each band. A list of zero-point uncertainties is given in Table 5.3. For two SNe, i and j, with calibrated photometry obtained in the same photometric system, the zero-point uncertainty, σ_{ZP} of that system was propagated into the covariance matrix element U_{ij} as $\frac{d\mu_i}{d(\mathrm{ZP})}\frac{d\mu_j}{d(\mathrm{ZP})}\sigma^2_{\mathrm{ZP}}$ according to Appendix A.1.2.

This procedure is a more efficient way of including zero-point uncertainties than including a common magnitude covariance (multiplicative in flux space) when performing all of the light curve fits. In testing, both of these methods gave results that agreed at the couple of a percent level. Our method has the advantage that the zero-point errors can be adjusted without rerunning the light curve fits.

Zero-point uncertainties are one of the largest systematic errors (see Table 5.4). However, we should note that this number is based on a heterogeneous assessment of errors from different datasets (Table 5.3); the accuracy will vary.

Table 4.2. Assumed zero-point uncertainties for SNe in the Union2 compilation.

Source	Band	ZP Uncertainty	Reference
HST	WFPC2	0.02	Heyer et al. (2004)
	ACS	0.03	Bohlin (2007b)
	NICMOS	0.03	Thatte et al. (2009)
SNLS	g, r, i	0.01	Astier et al. (2006)
	z	0.03	
ESSENCE	R, I	0.014	Wood-Vasey et al. (2007)
SDSS	u	0.014	Kessler et al. (2009)
	g, r, i	0.009	
	z	0.010	
Amanullah et al. (2010)	R, I	0.03	
	J	0.02	
Other	U-band	0.04	Hicken et al. (2009)
	Other Band	0.02	Hicken et al. (2009)

Vega

Astier et al. (2006) estimated the broadband Vega magnitude system uncertainty to be within $1\,\%$ by comparing spectroscopy from D. S. Hayes, L. E. Pasinetti, & A. G. D. Philip (1985) and Bohlin & Gilliland (2004). In their analysis, only the uncertainties of Vega colors had implications for cosmological measurements, which they chose to include by adopting a flux uncertainty linear in wavelength that would offset the Vega $B-R$ color by 0.01. The uncertainty of Vega is the single largest source of systematic error when estimating w, as shown in Table 5.4, suggesting that a better-understood reference would allow for a significant reduction in systematic errors.

KS09, and recently SNLS (Regnault et al. 2009), chose BD$+17^{\circ}4708$ as their primary reference star. This star has the advantage of having a well-known SED, measured Landolt magnitudes (in contrast to Vega) and colors that are close to the average colors of the Landolt standards (in contrast to Vega which is much bluer). KS09 studied the implications of switching between BD$+17^{\circ}4708$ and Vega and found zeropoints consistent to $\sim 1\%$.

Given this small difference between using BD$+17^{\circ}4708$ and Vega, we have chosen, for this work, to continue using Vega as our primary reference star. To account for the uncertainty of the magnitude of Vega on the Landolt system, we have assumed a correlated uncertainty of 0.01 mag for all photometry with a rest-frame wavelength in each of six wavelength intervals defined by the following wavelength boundaries: 2900Å, 4000Å, 5000Å, 6000Å, 7000Å, 10000Å, 16000Å.

Rest-frame U-Band

SNe Ia are known to show increasing spectroscopic and photometric diversity for wavelengths shorter than the rest-frame B-band. Part of this could perhaps be explained by differences in progenitor metallicity (Hoeflich et al. 1998; Lentz et al. 2000), but the spectral variations in the rest-frame UV (Ellis et al. 2008) are larger than predicted by existing models.

As discussed in Section 4.2, KS09 studied how well the SALT2 model describes the rest-frame U-band by first running SALT2 with the rest frame U-band excluded. Using these fits, they then generated a model for the rest frame U-band and binned the magnitude residuals from the actual rest-frame U-band data as a function of phase. For the SDSS and SNLS datasets, the residuals around the time of maximum are $\sim 3\%$. For SNLS, this is not surprising, as the SNLS data was used to train the SALT2 model. In this analysis, we use the SDSS sample as a validation set, and include a correlated 0.03 magnitude uncertainty for all photometric bands bluer than rest-frame 3500Å.

We note that the HST and low-redshift datasets are less useful for assessing the size of rest-frame U-band uncertainty. For the HST data, the light curves are poorly constrained without the rest-frame U-band. In the case of the nearby sample, the rest-frame U-band overlaps with the observed U-band for which accurate photometry is generally difficult to obtain (any potential problems with the nearby U-band will not impact the light curve fits much, as the low-z fits are typically very well constrained with the remaining bands).

Malmquist bias

In Chapter 2, we added a 0.02 magnitude covariance for each sample representing Malmquist bias uncertainty. More recently, KS09 completed a thorough simulation of selection effects for each of the samples in their analyses. They find a 0.024 change in w when making a correction for selection effects. As the 0.02 magnitude covariance yields a quite similar 0.026 error on w, and conducting a full simulation is beyond the scope of this work, we reuse the covariance from Chapter 2.

Gravitational lensing

The effects from gravitational lensing on the Hubble diagram have been discussed in detail in the literature (Sasaki 1987; Linder 1988b; Bergström et al. 2000; Amanullah et al. 2003; Holz & Linder 2005). Gravitational lensing only affects the high redshift end of the data that is currently available, and potential bias on the cosmological parameters from the analysis carried out here due to the asymmetry of the lensing probability density function is expected to be negligible. We adopt the approach in Chapter 2 of only treating gravitational lensing as a statistical uncertainty by adding a value of $0.093z$ (Holz & Linder 2005) in quadrature to $\sigma_{\rm ext}$ in equation 4.2. This is a conservative approach with respect to the values presented by Jönsson et al. (2006), where they attempt to measure the lensing of individual SNe by determining the mass distribution along the line of sight. A very important conclusion of their work is that there is no evidence for selection effects due to lensing of the high-redshift SNe.

Light curve model

We have studied any potential bias that could arise from poor light curve sampling, by carrying out a similar analysis to that in Chapter 2, updated for SALT2. We use nine *BVR* AQUAA templates (Strovink 2007) constructed from observations of very well-observed nearby supernovae. Each set of *BVR* templates is combined with a SALT2 U-band template generated for that supernova, as there were insufficient observations in the U-band to construct an AQUAA template.

Mock data sets are then sampled from these templates with the same rest frame dates and signal-to-noise ratios of the real SNe in our sample. The mock sets are then fitted with SALT2 and the offset between AQUAA corrected magnitude and the corresponding SALT2 fitted value is investigated as a function of the fitted phase of each supernova's first data point (the phase is with respect to B-band maximum). In Chapter 2, we looked at other possible biases, but first phase was the only significant one found. The test is carried out for each of the nine template SNe.

For SNe with a first phase at B-band maximum, the average bias is close to zero, with an RMS of about 0.03. For SNe with a first phase at six days past B-band maximum, the average bias is still close to zero, but the RMS has increased to about 0.08. Of course, our nine SN templates might not be a representative sample, but these results are encouraging,

since they both suggest that there is no significant bias and indirectly validate the SALT2 performance with respect to the AQUAA templates.

We use a first phase cut of six days, but we conservatively give each SN that has first phase greater than zero a 0.03 magnitude covariance. Note that SALT2 does not stretch its definition of phase with light curve width.

Contamination

As already mentioned, we perform an iterative χ^2 minimization with a 3σ outlier rejection before fitting cosmology. In Chapter 2 we showed that this technique greatly reduces the impact of potential contamination, while maintaining roughly Gaussian statistics. Contamination could either come from non-SN Ia or SNe that are typed as normal SN Ia but show peculiarities (see e.g. Foley et al. (2010)).

We carried out a Monte-Carlo study showing that the effect of contamination on any individual sample is limited to less than 0.015 magnitudes. This is under the assumption that the dispersion of the contaminating distribution is of the same order, or greater than, the dispersion of SNe Ia and that the contamination is less than $30\,\%$. We include a 0.015 magnitude uncertainty, correlated for each sample, to account for possible contamination.

Minimum redshift

In order to test for possible effects from using a given minimum redshift cut, we started by constructing a new sample with no minimum redshift. Using this sample, we performed fits which allowed the absolute magnitude to vary independently below and above a dividing redshift in the range 0.01 to 0.03. This procedure should test for a Hubble bubble or significantly correlated peculiar velocities. The extra degree of freedom allowed by this step in M_B improved the χ^2 by $\lesssim 1$ regardless of the dividing redshift and the inclusion of systematic errors. This confirms the results of Conley et al. (2007) for SALT2. We conclude that there is no statistically significant difference between minimum redshifts and use the value of 0.015, as was used in the analysis in Chapter 2.

Galactic extinction

All light curve photometry is corrected for Galactic extinction using the extinction law from Cardelli et al. (1989), assuming $R_V = 3.1$, together with the dust maps from Schlegel et al. (1998).

In the same procedure as with calibration uncertainties, we increased the Galactic $E(B-V)$ by 0.01 for each supernova and repeated the fit, giving $\frac{d\mu(\alpha,\beta)}{d(E(B-V))}$. A 16% statistical and 10% systematic error was assumed for the Galactic extinction of each supernova (Schlegel et al. 1998).

Intergalactic extinction

Dimming of SNe Ia by hypothetical intergalactic gray dust has been suggested by Aguirre (1999) as an alternative to dark energy to explain the SN results (Goobar et al. 2002). This potential dimming was however constrained by studying the colors of high-z quasars (Mörtsell & Goobar 2003; Östman & Mörtsell 2005) and by observations SNe Ia in the rest frame I-band (Nobili et al. 2005, 2009).

Another possible extinction systematic comes from the dust in galaxy halos that are along the line of sight. Ménard et al. (2009) used distant quasars to detect and measure extinction in galactic halos at $z \sim 0.3$. They find an average R_V for their galaxies of 3.9 ± 2.6. Using their observed $A_V(r)$, we find an average rest frame V-band extinction of 0.004 magnitudes per intersected halo, assuming $R_V = 3.1$. At redshift 0.5, an average of three halos have been intercepted. At redshift 1.0, the average is seven.

There are three mitigating factors. One is that expansion redshifts photons between the supernova and the intervening galaxy. The CCM law decreases with wavelength (in the relevant wavelength range), so less light is absorbed. Ménard et al. (2008) finds that $\rho_{\rm dust} \propto (1+z)^{-1.1}$, which we use to scale the extinction. Finally, most of the extinction is corrected by color correction. The exact amount corrected depends on the redshift and the filters used in the observations, but is around two thirds.

We find an error on w of 0.008 due to this extinction, significantly lower than the value of 0.024 derived by Ménard et al. (2010). However, they used $R_V = 3.9$, rather than 3.1; the fraction of extinction that is corrected by the color correction will decrease with R_V. We also numerically sum the CCM laws, rather than using an analytic approximation. Since we know the exact redshift and filters used in each observation, we can exactly calculate the amount of extinction already handled by the color correction (using our $\frac{d\mu}{dz\rm p}$ values), without approximation.

Shape and Color Correction

The most uncertain contribution to the dimming of SNe Ia is host galaxy extinction. Several studies of SN Ia colors (Guy et al. 2005, 2007; Wang et al. 2008; Nobili & Goobar 2008, and references therein) indicate that the observed SN Ia reddening does not match the Galactic CCM extinction law with $R_V = 3.1$. A stronger wavelength dependence has been found in the optical in most cases, and it remains unclear if CCM models with any value of R_V can be used to describe the data accurately. It is possible that the observed steep reddening originates from a mixture of local effects and host galaxy extinction. Local effects could be intrinsic SN variations, but also multiple scattering on dust in the circumstellar environment has been suggested (Wang 2005; Goobar 2008). This model is potentially supported by detection (Patat et al. 2007; Simon et al. 2009; Blondin et al. 2009) of circumstellar material but also by color excess measurements for two of the best observed reddened SN Ia (Folatelli et al. 2010) being consistent with the expected extinction from circumstellar material.

The SALT2 method approaches the lack of a consistent understanding of SN Ia reddening by adopting a purely empirical approach. For SALT2, the SN Ia luminosity is standardized by assuming that the standardization is linear in both x_1 and c as described in equation 4.1, where β is the empirically determined correction coeffecient that accounts for all linear relations between color and observed peak magnitude. For example if the only source for such SN Ia reddening originated from CCM extinction then β is identically equal to $R_V + 1$. We test this approach and propagate relevant systematic uncertainties by dividing the full sample into smaller sets and carrying out independent fits for the x_1 and c correction coefficients, α and β, as shown in Table 4.5.

When subdividing into redshift bins, we find that the values of α and β for the full sample are consistent with values for the three first redshift bins. It is encouraging to see consistency between the global values fit for the full dataset and the values in the best-understood redshift range. Beyond this important test, we also note that the value of β in the redshift range 0.5 to 1 is significantly lower than the other values, while the value for $z > 1$ is higher than the global value, but is poorly measured. The trend is similar to what was seen in KS09, but we use different binning. This behavior is inconsistent with a monotonic drift in redshift, so we consider other explanations for these results. That conclusion is also supported by the observation that samples at similar redshifts (e.g. Miknaitis et al. (2007) and Astier et al. (2006)) can have very different values of β when fitted independently. The value of α is consistent across redshift ranges, except at $z > 1$, where many light curves are so poorly sampled that it may not be possible to assign reasonable x_1 errors.

When subdividing into the four largest data sources (the lower half of Table 4.5), we find values of α and β generally consistent with the global values, with the exception of a lower value of β for the SNLS SNe (Astier et al. 2006). In general, ignoring or underestimating the errors in c or x_1 will decrease the associated correction coefficients, β and α, as investigated in Chapter 2 and KS09 and this may be relevant here. Specifically, two potential sources of problems are an incomplete understanding of calibration and underestimated SN model variations, either of which could affect these fits. If the SNLS SNe are physically different, and they are allowed their own β, then w shifts by 0.02. Alternatively, as one β is used for the global sample, the possibility that that β is biased from the true global value must be considered. Selecting the global value of β from any of the other large samples shifts w by less than 0.02. We have accounted for this systematic by assigning each sample a 0.02 magnitude covariance (giving a 0.03 error on w), which avoids the problem of handling an error on elements of the covariance matrix. To study these details further, we look forward to more data for $z > 0.5$, with improved calibration and light curve models.

We also perform one additional sanity check by subdividing the data by x_1 and c. There is evidence for two populations of normal SN Ia, divided by light curve width (see Chapter 2, and references therein). Star-forming galaxies tend to host the population with broader light curves, while SN hosted by passive galaxies tend to have narrower light curves. As described below, we derive consistent cosmology for these subdivisions as well.

We subdivide[5] the full sample into two roughly equal subsamples, split first by color and then by x_1. In total, this makes four subsamples. We find that the cosmology is close for all subsamples (as can be seen in Table 4.5) so the difference from these subdivisions does not contribute significantly to the systematic error on w.

It is interesting to note that α is substantially different for the two samples split by light curve width. Likewise, β is substantially different for the two samples split by color. This might suggest that the relationships between color and brightness and light curve width and brightness are more complex than a simple linear relationship, or it could be that the errors on x_1 and c are not perfectly understood. We also find that β is higher for the redder SNe Ia which is similar to the results from Conley et al. (2008) based on comparisons of $U-B$ colors to $B-V$, after correcting for the effect of stretch on the U-band. At the same time it should be pointed out that evidence of low R_V values have also been found for a few well-studied, and significantly reddened, nearby SNe Ia Folatelli et al. (2010).

Summary of systematic errors

The effect of these systematic errors on w is given in Table 5.4. The improvement in cosmology constraints over the simple quadrature sum is also shown. Zeropoint and Vega calibration dominate the systematics budget, but understanding the color variations of SNe is also important. The benefit from making a Malmquist bias correction can be seen; by doing so, KS09 reduce this systematic error by a factor of two.

4.4 Results and Discussion

In the cosmology analysis presented here, the statistical errors on Ω_M have decreased by a significant 24% over the Union analysis, while the estimated systematic errors have only improved by 13%. When combining the SN results with BAO and CMB constraints, statistical errors on w have improved by 16% over Union, though the quoted systematic errors have increased 7%. Figure 4.6 shows a comparison between the constraints from Union and this new compilation in the $(\Omega_M - w)$ plane. Even with some improvement on the understanding of systematic errors, it is clear that the dataset is dominated by systematic error (at least at low to mid-z).

[5]Subdividing by x_1 or c must be done carefully. When there are errors in both the dependent and independent variables (in this case, magnitude and x_1 or c), the true values of the independent variables must be explicitly solved for as part of the fit. Otherwise, the subdividing will be biased. For example, suppose that a supernova has a color that is poorly measured, and an uncorrected magnitude that is well-measured. If this supernova is faint and blue, then a fit for the true color will give a redder color. A color cut will place this supernova in the blue category, when the supernova is actually more likely to be red. As mentioned in Chapter 2, whenever one fits for α and β, the true values of x_1 and c are only implicitly solved for; equation 4.3 is derived by analytically minimizing over the true x_1 and c. Equation 2.3 shows the result with the true values made explicit, we also include a discussion in Appendix A.1.

Table 4.3. Effect on w errorbar (including BAO and CMB constraints) for each of the systematic errors included. The proper way to sum systematic errors is to include each error in a covariance matrix.

Source	Error on w
Zero point	0.037
Vega	0.042
Galactic Extinction Normalization	0.012
Rest-Frame U-Band	0.010
Contamination	0.021
Malmquist Bias	0.026
Intergalactic Extinction	0.012
Light curve Shape	0.009
Color Correction	0.026
Quadrature Sum (not used)	*0.073*
Summed in Covariance Matrix	0.063

The best fit cosmological parameters for the compilation are presented in Table 4.4 with constraints from CMB and BAO. The confidence regions in the $(\Omega_M, \Omega_\Lambda)$ and (Ω_M, w) planes for the last fit in the table are shown in Figures 5.5 and 5.6 respectively.

Table 4.4. Fit results on cosmological parameters Ω_M, w and Ω_k. The parameter values are followed by their statistical (first column) and statistical and systematic (second column) uncertainties.

Fit	Ω_M	Ω_M w/ Sys	Ω_k	Ω_k w/ Sys	w	w w/ Sys
SNe	$0.270^{+0.021}_{-0.021}$	$0.274^{+0.040}_{-0.037}$	0 (fixed)	0 (fixed)	-1 (fixed)	-1 (fixed)
SNe+BAO+H_0	$0.309^{+0.032}_{-0.032}$	$0.316^{+0.036}_{-0.035}$	0 (fixed)	0 (fixed)	$-1.114^{+0.098}_{-0.112}$	$-1.154^{+0.131}_{-0.150}$
SNe+CMB	$0.268^{+0.019}_{-0.017}$	$0.269^{+0.023}_{-0.022}$	0 (fixed)	0 (fixed)	$-0.997^{+0.050}_{-0.055}$	$-0.999^{+0.074}_{-0.079}$
SNe+BAO+CMB	$0.277^{+0.014}_{-0.014}$	$0.279^{+0.017}_{-0.016}$	0 (fixed)	0 (fixed)	$-1.009^{+0.050}_{-0.054}$	$-0.997^{+0.077}_{-0.082}$
SNe+BAO+CMB	$0.279^{+0.014}_{-0.014}$	$0.282^{+0.018}_{-0.016}$	$-0.003^{+0.006}_{-0.006}$	$-0.004^{+0.006}_{-0.007}$	-1 (fixed)	-1 (fixed)
SNe+BAO+CMB	$0.282^{+0.016}_{-0.015}$	$0.282^{+0.018}_{-0.016}$	$-0.004^{+0.007}_{-0.007}$	$-0.005^{+0.008}_{-0.007}$	$-1.029^{+0.056}_{-0.059}$	$-1.038^{+0.093}_{-0.097}$
SNe+BAO+CMB+H_0	$0.275^{+0.015}_{-0.014}$	$0.274^{+0.016}_{-0.015}$	$-0.001^{+0.006}_{-0.006}$	$-0.002^{+0.007}_{-0.007}$	$-1.024^{+0.055}_{-0.058}$	$-1.052^{+0.092}_{-0.096}$

For the CMB data we implement the constraints from the 7 year data release of the Wilkinson Microwave Anisotropy Probe (WMAP) as outlined in Komatsu et al. (2011). We take their results on $z_\star$ (the redshift of last scattering), $l_A(z_\star)$, and $R(z_\star)$, updating the central values for the cosmological model being considered. Here, $l_A(z_\star)$ is given by

$$l_A(z_\star) \equiv (1+z_\star)\frac{\pi D_A(z_\star)}{r_s(z_\star)}\,,$$

where D_A is the angular distance to $z_\star$, while

$$R(z_\star) \equiv \frac{\sqrt{\Omega_M H_0^2}}{c}(1+z_\star)D_A(z_\star)\,.$$

Percival et al. (2010) measures the position of the BAO peak from the SDSS DR7 and 2dFGRS data, constraining $d_z \equiv r_s(z_d)/D_V(0.275)$ to 0.1390 ± 0.0037, where $r_z(z_d)$ is the comoving sound horizon and $D_V(z) \equiv [(1+z)^2 D_A^2 cz/H(z)]^{1/3}$.

For the SNe + BAO fit in Table 4.4, we add an H_0 measurement of 74.2 ± 3.6 km/s/Mpc from Riess et al. (2009), creating a constraint without the CMB that is therefore largely independent of the high-redshift behavior of dark energy (as long as the dark energy density contribution is negligible in the early universe). Note that the H_0 constraint relies on most of the nearby supernovae used in this compilation. However, the effect on w through H_0 from these supernovae is several times smaller than the effect through the Hubble diagram. Alternatively, adding a CMB constraint on $\Omega_m h^2$ of 0.1338 ± 0.0058 from the WMAP7 webpage[6] allows us to create a constraint that is independent of H_0. This final result for SNe +BAO+CMB does not improve significantly if the current H_0 constraint is added.

4.4.1 Time variation of the dark energy equation of state

The constraints shown in Figure 5.6 were obtained assuming that the dark energy equation of state (EOS) is redshift independent. SNe Ia are useful for constraining a redshift dependent $w(z)$ since, unlike e.g. CMB, their measured distances at a given redshift are independent of the behavior of dark energy at higher redshifts. A common method to parameterize $w(z)$ is

$$w(z) = w_0 + w_a\frac{z}{1+z}$$

where a cosmological constant is described by $(w_0, w_a) = (-1, 0)$. It can be shown (Linder 2003b) that this parameterization provides an excellent approximation to a wide variety of dark energy models. The constraints from the current SN data together with the CMB and BAO data are presented in Figure 4.7. In terms of the figure of merit[7], introduced by the dark energy task force (Albrecht et al. 2006), these constraints correspond to 1.2 and 1.8 with and without systematics respectively. The flattening of the contours in this diagram at

[6] http://lambda.gsfc.nasa.gov/product/map/current/params/wcdm_sz_lens_wmap7.cfm

[7] Defined as the inverse area of the joint 2σ region in the Gaussian limit ($\Delta\chi^2 = 6.17$).

$w_0 + w_a = 0$ comes from the implicit constraint of matter domination in the early Universe imposed by the CMB and BAO data. Only modest constraints can currently be placed on w_a.

It can be illuminating to study $w(z)$ in redshift bins, where w is assumed constant in each bin. This method has the advantage that $w(z)$ can be studied without assuming a specific form for the relation (Huterer & Starkman 2003). We carry out the analysis following Chapter 2 and fit a constant w in each bin, while the remaining cosmological parameters are fit globally for the entire redshift range. Figure 4.8 shows three such models for the combined constraints from SNe, BAO, CMB, and H_0 measurements where we assume a flat Universe. In these scenarios, the H_0 measurement does not contribute much, but due to its small improvement on the CMB constraints it gives a small ($\sim 10\%$) improvement on the errorbar of the highest redshift bin.

The left panel shows constraints on w for three bins. The first bin ($0 < z < 0.5$) shows a well-constrained w. The middle bin ($0.5 < z < 1$) shows a poorly-constrained w, though one that is distinct from $-\infty$ (which would drive ρ to 0 above $z = 0.5$, resulting in a matter-only universe) at high confidence, indicating the detection of some kind of dark energy in this redshift range. For $z > 1$, there is little constraint on w, and only a weak constraint on the existence of dark energy.

The middle panel shows the effect of dividing the highest redshift bin. The constraints on w for $z > 1$ get much weaker, showing that most of the (weak) constraint on the highest bin in the left panel comes from a combination of the CMB with the well-constrained low-redshift supernova data. Current supernovae at $z > 1$ offer no real constraint on $w(z > 1)$. Providing a significant constraint at these redshifts requires significantly better supernova measurements. As in the left panel, w in the highest redshift bin is constrained to be less than zero by the requirement from BAO and CMB constraints that the early universe have a matter-dominated epoch.

The right panel shows the effect of dividing the lowest redshift bin. While no significant change in w with redshift is detected, there is still considerable room for evolution in w, even at low redshift.

Figure 4.9 shows dark energy *density* constraints, assuming the same redshift binning as in Figure 4.8. Note that this is not equivalent to the left and center panels of Figure 4.8; only in the limit of an infinite number of bins do binned ρ and binned w give the same model. Dark energy can be detected at high significance in the middle bin (redshift 0.5 to 1), but there is only weak evidence for dark energy above redshift 1 (left panel). When the bin above redshift 1 is split at a redshift greater than the supernova sample (right panel), it can be seen that the current small sample of supernovae cannot constrain the existence of dark energy above redshift 1.

4.4.2 SNe with ground-based near-IR data

Obtaining near-IR data of $z \gtrsim 1$ SNe Ia, whether from space or from the ground, is critical for constraining the SALT2 color parameter, c. Without the near-IR data, the

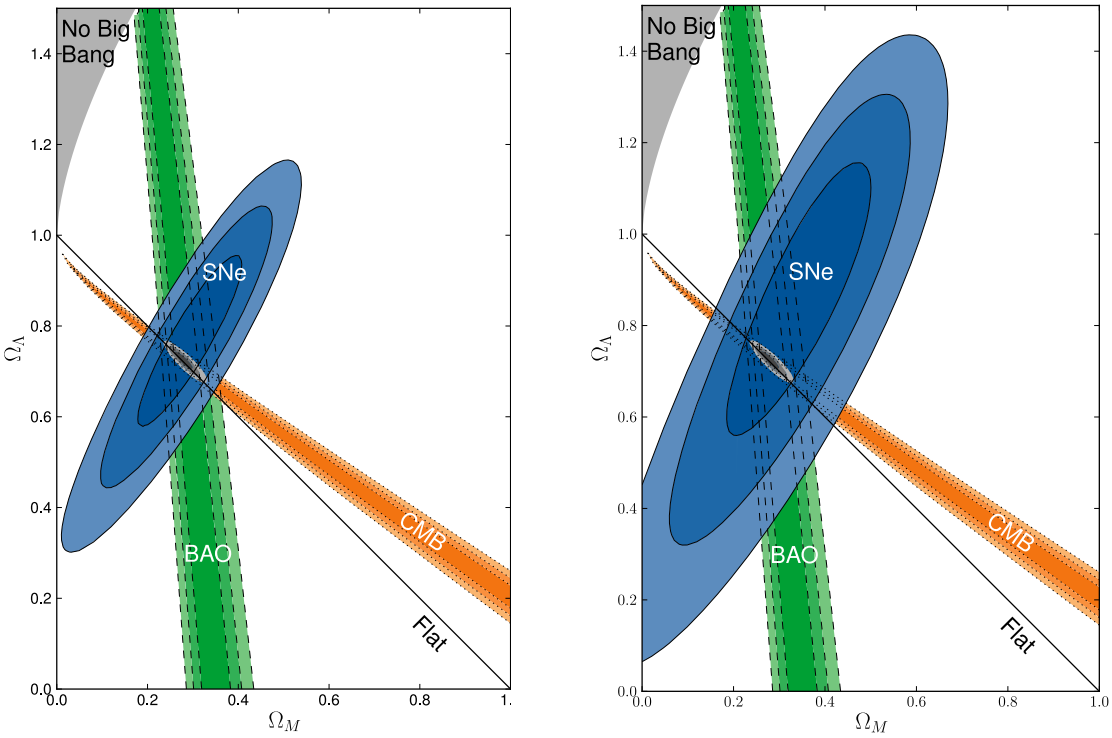

Figure 4.4. 68.3%, 95.4%, and 99.7% confidence regions in the $(\Omega_M, \Omega_\Lambda)$ plane from SNe combined with the constraints from BAO and CMB both without (left panel) and with (right panel) systematic errors. Cosmological constant dark energy ($w = -1$) has been assumed.

uncertainty in this parameter for 2001hb and 2001gn, both beyond $z = 1$, increases by a factor of two. Precise measurements of c are important, since uncertainties in c are inflated by $\beta \approx 2.5$ and tend to dominate the error budget when the corrected peak B-brightness of SNe Ia are calculated.

Both 2001hb and 2001gn were observed with ground-based near-IR instruments. The operational challenges associated in obtaining these data are significant. Long exposure times (ten hours or more taken within a few days) in excellent observing conditions are necessary. Even with queue mode scheduling, these observations are just feasible. Despite the challenges, the uncertainty in the SALT2 color of these two SNe Ia is comparable to the uncertainty in the color of the *best* space-based measured SNe Ia at $z \gtrsim 1$.

The ground based near-IR data also allow us to search for systematic offsets with near-IR data taken from space. For $z > 1.1$ SNe Ia observed with NICMOS, the average SALT2 c value is $c = 0.06 \pm 0.03$ mag. By comparison, the weighted average color of the three SNe Ia at $z \sim 1.1$ with ground-based near-IR data (2001hb and 2001gn from this work, together with 1999fk from Tonry et al. (2003)) that pass the light curve cuts is, 0.01 ± 0.07. Neither the ground-based or space-based measurements show any Hubble diagram offset, ($\Delta\mu = 0.03 \pm 0.10$ and -0.01 ± 0.06, respectively), from the best fit cosmology. These results include a 0.1 magnitude dispersion in color, and the fitted systematic dispersions in

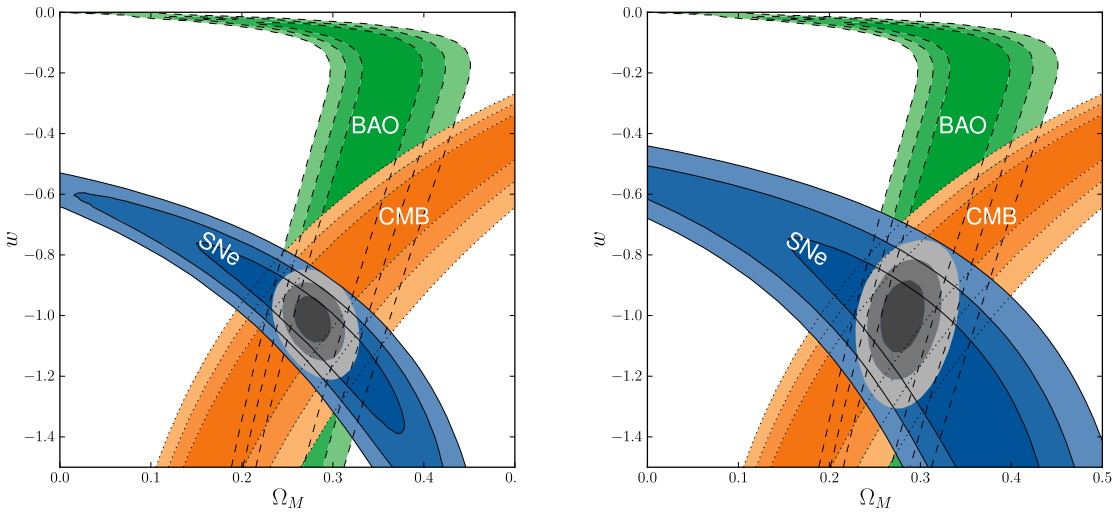

Figure 4.5. 68.3%, 95.4%, and 99.7% confidence regions of the (Ω_M, w) plane from SNe combined with the constraints from BAO and CMB both without (left panel) and with (right panel) systematic errors. Zero curvature and constant w have been assumed.

magnitude. Additional SNe Ia at $z \sim 1.1$ with ground based near-IR photometry are given in Chpater 5, where we also incorporate the results from the NICMOS calibration program referenced in section 4.3.1.

4.4.3 Comparison of KeplerCam and SDSS Photometry

H09 and KS09 share three normal supernovae in common: 2005hc, 2005hj, and 2005ir. In comparing the data for these SNe, we noticed that the H09 KeplerCam r-band photometry is generally 0.05 ± 0.02 magnitudes fainter than the KS09 SDSS r-band photometry based on SALT2 fits including both data sets. The quoted uncertainty is completely dominated by the zero-point uncertainties, as both sets of data have high S/N. The offset is consistent for each supernova. This offset is the correct size and direction to explain the tension in Hubble residuals seen between these datasets in second panel of Figure 4.3.

SN 2005hc and SN 2005ir were also observed by CSP using the Swope telescope. In these cases, the Swope photometry agrees with the SDSS r-band photometry.

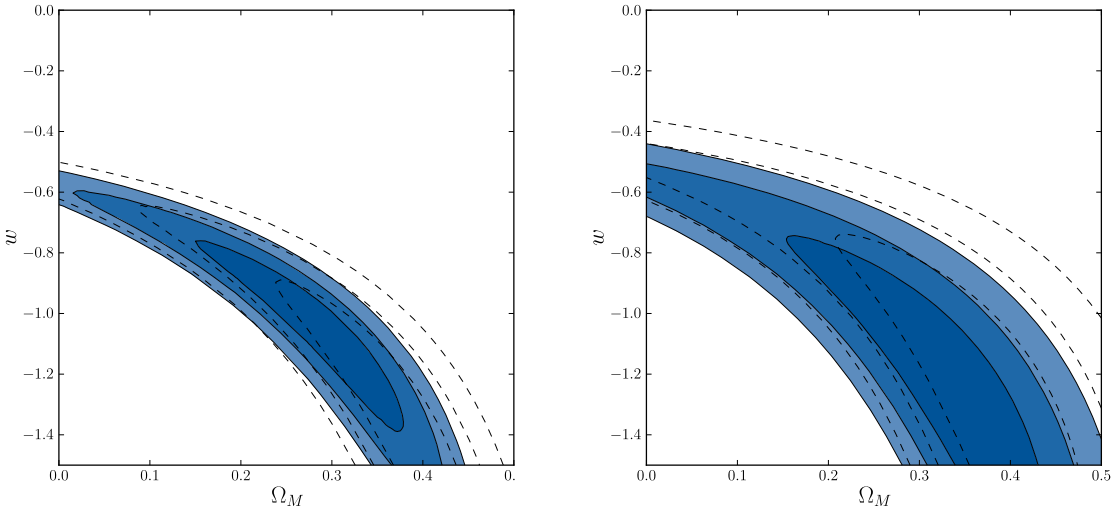

Figure 4.6. $68.3\%, 95.4\%$, and 99.7% confidence regions of the (Ω_M, w) plane from SNe alone from Chapter 2 (dashed contours) and this compilation (shaded contours). Systematic errors are included in the right panel. Zero curvature has been assumed.

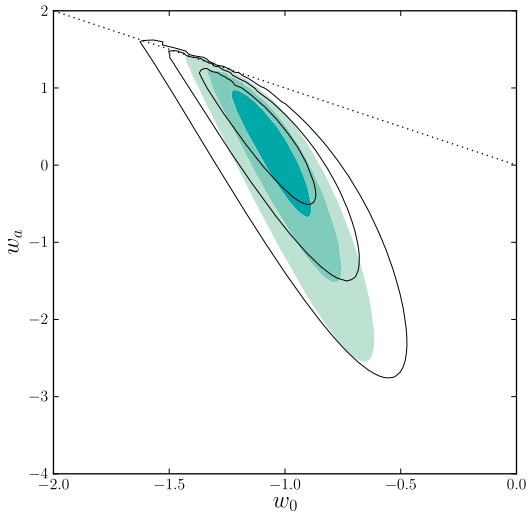

Figure 4.7. $68.3\%, 95.4\%$, and 99.7% confidence regions of the (w_0, w_a) plane from SNe combined with the constraints from BAO and CMB both with (solid contours) and without (shaded contours) systematic errors. Zero curvature has been assumed. Points above the dotted line ($w_0 + w_a = 0$) violate early matter domination and are implicitly disfavored in this analysis by the CMB and BAO data.

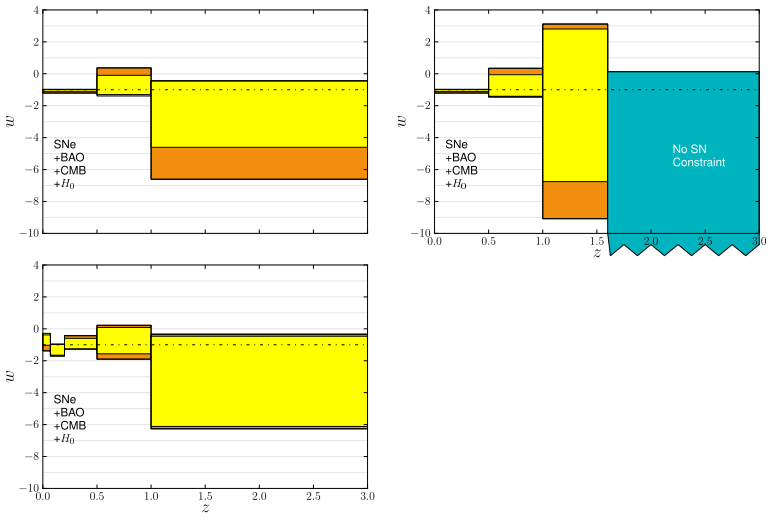

Figure 4.8. Constraints on $w(z)$, where $w(z)$ is assumed to be constant in each redshift bin, are plotted at the 68% probability level. The results were obtained assuming a flat Universe for the joint data set of supernovae, BAO, CMB, and H_0, with (dark/orange) and without (light/yellow) SN systematics. The *left* panel shows three redshift bins, with the highest redshift bin keeping w constant for all $z > 1$. Dark energy is seen to exist at $z > 1$ (at least at $68\,\%$ cl) since w does not reach an infinitely negative value, indicating its density does not go to zero. The *middle* panel splits this last bin into two, showing that the seemingly tight constraints on dark energy at $z > 1$ with current data depend on the combination of CMB with low-redshift data. No current probe alone can constrain the existence of dark energy at $z > 1$. The *right* panel shows the effects of w binning at low redshift. The best fit values of w go from less than -1 at $z = 0.14$ to greater than -1 at $z = 0.04$. While such a steep, late time transition in w (corresponding to $dw/d\ln a \approx 7$) is unusual in physical models, it can easily appear due to offsets between heterogeneous data sets. We emphasize that the results are still consistent with the cosmological constant (dot-dashed line) at the $68\,\%$ confidence level.

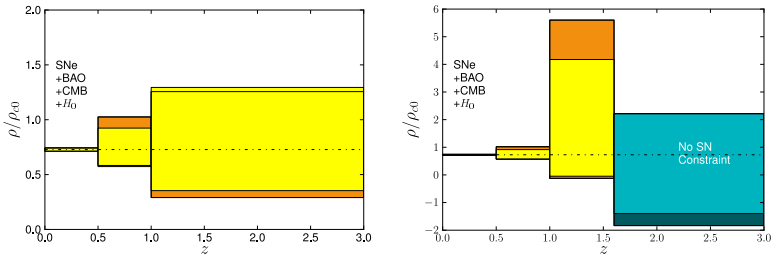

Figure 4.9. Here the dark energy density in units of the critical density today, ρ/ρ_{c0}, is assumed constant in each bin. The same binning as the left/center panels in Figure 4.8 is chosen. As can be seen in the left panel, dark energy is detected between redshift 0.5 and 1 at high significance, but only hints of dark energy are seen above redshift 1. When the CMB and SNe are separated, neither one alone can provide any evidence for dark energy at z¿1.

Table 4.5. Subdivisions of the Union2 compilation. Values of absolute B-band magnitude, M_B (assuming $H_0 = 70$ km/s/Mpc), as well as stretch and color correction coefficients, α and β, for several redshift ranges. Ω_M and w are shown for properly conducted x_1 and c cuts, chosen to give similar uncertainty of the fitted w. The outlier rejection is redone for each bin, so the totals may not add up to the whole sample. The constraints are computed including BAO and CMB data.

Cut	Number	M_B	α	β	Ω_M	w
$0.015 \leq z \leq 0.10$	166	$-19.323^{+0.016}_{-0.016}$	$0.112^{+0.011}_{-0.011}$	$2.77^{+0.09}_{-0.09}$	0.270 (fixed)	-1.000 (fixed)
$0.100 \leq z \leq 0.25$	74	$-19.326^{+0.020}_{-0.020}$	$0.154^{+0.019}_{-0.018}$	$2.49^{+0.15}_{-0.14}$	0.270 (fixed)	-1.000 (fixed)
$0.250 \leq z \leq 0.50$	154	$-19.305^{+0.014}_{-0.014}$	$0.110^{+0.013}_{-0.013}$	$2.50^{+0.12}_{-0.11}$	0.270 (fixed)	-1.000 (fixed)
$0.500 \leq z \leq 1.00$	133	$-19.309^{+0.016}_{-0.017}$	$0.129^{+0.018}_{-0.018}$	$1.45^{+0.19}_{-0.19}$	0.270 (fixed)	-1.000 (fixed)
$z \geq 1.000$	16	$-19.450^{+0.083}_{-0.106}$	$-0.124^{+0.085}_{-0.118}$	$3.84^{+1.20}_{-0.85}$	0.270 (fixed)	-1.000 (fixed)
$c \geq 0.05$	245	$-19.373^{+0.026}_{-0.026}$	$0.112^{+0.011}_{-0.011}$	$2.96^{+0.10}_{-0.10}$	$0.283^{+0.017}_{-0.016}$	$-0.969^{+0.070}_{-0.074}$
$c \leq 0.05$	308	$-19.305^{+0.019}_{-0.020}$	$0.122^{+0.010}_{-0.010}$	$1.13^{+0.30}_{-0.28}$	$0.284^{+0.015}_{-0.015}$	$-0.959^{+0.058}_{-0.062}$
$x_1 \geq -0.25$	302	$-19.358^{+0.023}_{-0.023}$	$0.026^{+0.021}_{-0.021}$	$2.60^{+0.10}_{-0.09}$	$0.278^{+0.015}_{-0.014}$	$-0.996^{+0.061}_{-0.065}$
$x_1 \leq -0.25$	254	$-19.335^{+0.031}_{-0.032}$	$0.147^{+0.020}_{-0.019}$	$2.42^{+0.10}_{-0.10}$	$0.276^{+0.016}_{-0.015}$	$-1.016^{+0.069}_{-0.073}$
Holtzman et al. (2009)	129	$-19.315^{+0.013}_{-0.013}$	$0.147^{+0.014}_{-0.013}$	$2.38^{+0.15}_{-0.14}$	0.270 (fixed)	-1.000 (fixed)
Hicken et al. (2009)	102	$-19.299^{+0.021}_{-0.022}$	$0.113^{+0.013}_{-0.013}$	$2.73^{+0.10}_{-0.10}$	0.270 (fixed)	-1.000 (fixed)
Miknaitis et al. (2007)	74	$-19.325^{+0.032}_{-0.033}$	$0.112^{+0.037}_{-0.035}$	$2.50^{+0.17}_{-0.16}$	0.270 (fixed)	-1.000 (fixed)
Astier et al. (2006)	71	$-19.287^{+0.016}_{-0.017}$	$0.140^{+0.017}_{-0.017}$	$1.72^{+0.18}_{-0.17}$	0.270 (fixed)	-1.000 (fixed)
$z \geq 0.015$	557	$-19.310^{+0.014}_{-0.014}$	$0.121^{+0.007}_{-0.007}$	$2.51^{+0.07}_{-0.07}$	$0.277^{+0.014}_{-0.014}$	$-1.009^{+0.050}_{-0.054}$

4.5 Summary and Conclusions

Following Chapter 2, we add six high-redshift SNe from Amanullah et al. (2010) and other SN Ia data sets to the Union compilation. We have also improved the Union analysis in a number of respects, creating the new Union2 compilation. The most important improvements are: (1) Systematic errors are directly computed using the effect they have on the distance modulus (2) All SN light curves are fitted with the SALT2 light curve fitter.

We determine the best fit cosmology for the Union2 compilation, and the concordance ΛCDM model remains an excellent fit. The new analysis results in a significant improvement over the Union compilation in constraining w over the redshift interval $0 < z < 1$. Above $z \gtrsim 1$, evidence for dark energy is weak. This will remain the case until there is much more high redshift data, with better signal-to-noise and wavelength coverage. [8]

[8]The work presented in this chapter is supported in part by a JSPS core-to-core program "International Research Network for Dark Energy" and by JSPS research grants (20040002).

This work was also supported by the Director, Office of Science, Office of High Energy Physics, of the U.S. Department of Energy under Contract No. DE- AC02-05CH11231.

T.M. is financially supported by the Japan Society for the Promotion of Science (JSPS) through the JSPS Research Fellowship.

C.L. acknowledges the support provided by the Oskar Klein Centre at Stockholm University.

Support for programs HST-GO-08585.14-A and HST-GO-09075.01-A was provided by NASA through a grant from the Space Telescope Science Institute, which is operated by the Association of Universities for Research in Astronomy, Inc., under NASA contract NAS 5-26555.

The authors would like to thank the anonymous referee for its helpful comments and suggestions.

CHAPTER 5

Union2.1

In order to efficiently build the high-redshift end of the Hubble diagram, the SCP proposed a survey of the 25 most massive $0.9 < z < 1.5$ galaxy clusters with the *Hubble Space Telescope*. We were awarded 219 orbits in cycle 14 to carry out this program (referred to as the *Hubble Space Telescope* Cluster Supernova Survey), discovering 16 $z > 0.9$ secure or probable SNe Ia. In this chapter, I describe the construction of the generative models (forward models) that I used for the IR photometry. These models allowed an optimal use of a scarce resource that proved crucial to getting precise color measurements (and thus precise distances). In addition, we make use of the SCP calibration of the IR count-rate nonlinearity, which differs from the STScI calibration by ~ 0.06 magnitudes, an amount equal to more than one statistical error bar for the high-redshift SNe.

I made other improvements as well. Kelly et al. (2010); Sullivan et al. (2010) presented strong evidence that host galaxy environment affects the magnitude of SNe Ia, even after the standard color and light-curve shape corrections are applied. Section 5.3.1 describes my addition of this effect to the cosmology fitting, shifting constant w by about half its error bar. These corrections are especially important for the cluster-hosted SNe, as they come from a biased sample of galaxies (more massive, more metal-rich, lower specific star-formation-rate). With these improvements in hand, I computed the then best constraints on time-varying dark energy. [1]

5.1 SN Discoveries and Data

5.1.1 SN Sample

As described in Dawson et al. (2009), the survey produced a total of 39 likely SNe during the active phase of the search. In Barbary et al. (2012a), types are determined for 29 of these candidates. (The remaining 10 do not have enough light curve information to determine type, since they lie outside of our fiducial search time window or our signal-to-noise cuts.) Twenty SNe are classified as SNe Ia, with confidence levels of secure, probable

[1] This chapter was previously published as sections 3, 4, 5, and 6 from Suzuki et al. (2012).

or plausible. A secure SN Ia is one that either has a spectrum that directly confirms it to be a SN Ia *or* one that satisfies two conditions: (1) it occurred in a host whose spectroscopic, photometric and morphological properties are consistent with those of an early-type galaxy with no detectable signs of recent star formation, and (2) it has a lightcurve shape consistent with that of a SN Ia and inconsistent with all other known SN types. A probable SN Ia is one that does not have a secure spectrum but satisfies one of the two non-spectroscopic conditions that are required for a secure classification. A plausible SN Ia is one that has an indicative lightcurve but we do not have enough data to rule out other types. Details of the classification scheme can be found in Barbary et al. (2012a), and details of the galaxy typing can be found in Meyers et al. (2011).

Table 5.1. Supernovae from HST Cluster Supernova Survey. a Spectroscopically confirmed as a SNe Ia b Redshift from SNe Ia or host galaxy (Morokuma et al. 2010, Barbary et al. 2010, Meyers et al. 2011) c Redshift from cluster (Meyers et al. 2011, references therein) d Galactic Extinction from Schlegel et al. (1998)

SN name	Nickname	z	$z_{\rm cluster}$	RA (J2000)	DEC (J2000)	E(B-V)	Confidence
SNe Hosted by Cluster Early-Type Galaxies							
SCP05D0[a]	Frida	1.014	1.017	02:21:42.066	−03:21:53.12	0.025	secure
SCP06H5	Emma	1.231	1.241	14:34:30.140	+34:26:57.30	0.019	secure
SCP06K0	Tomo	1.415	1.414	14:38:08.366	+34:14:18.08	0.015	secure
SCP06K18	Alexander	1.411	1.414	14:38:10.665	+34:12:47.19	0.014	probable
SCP06R12	Jennie	1.212	1.215	02:23:00.083	−04:36:03.05	0.026	secure
SCP06U4[a]	Julia	1.050	1.037	23:45:29.430	−36:32:45.75	0.014	secure
SNe Hosted in the Cluster							
SCP06C1[a]	Midge	0.98	0.974	12:29:33.013	+01:51:36.67	0.019	secure
SCP06F12	Caleb	1.110	1.110	14:32:28.749	+33:32:10.05	0.010	probable
SNe Hosted by Early-Type Non-Cluster Members							
SCP05D6	Maggie	1.315	1.017	02:21:46.484	−03:22:56.18	0.025	secure
SCP06G4[a]	Shaya	1.350	1.259	14:29:18.744	+34:38:37.39	0.015	secure
SCP06A4	Aki	1.192	1.457	22:16:01.078	−17:37:22.10	0.026	probable
SCP06C0	Noa	1.092	0.974	12:29:25.655	+01:50:56.59	0.020	secure
SNe Hosted by Late Type Galaxies							
SCP06G3	Brian	0.962	1.259	14:29:28.430	+34:37:23.15	0.015	plausible
SCP06H3[a]	Elizabeth	0.850	1.241	14:34:28.879	+34:27:26.62	0.019	secure
SCP06N33	Naima	1.188	1.026	02:20:57.699	−03:33:23.98	0.023	probable
SCP05P1	Gabe	0.926	1.1	03:37:50.352	−28:43:02.67	0.011	plausible
SCP05P9[a]	Lauren	0.821	1.1	03:37:44.513	−28:43:54.58	0.011	secure
SCP06X26	Joe	1.440	1.101	09:10:37.888	+54:22:29.06	0.019	plausible
SCP06Z5[a]	Adrian	0.623	1.390	22:35:24.967	−25:57:09.61	0.021	secure
SNe with No Definitive Redshift Measurement							
SCP06E12	Ashley	...	1.026 (cluster redshift)	14:15:08.141	+36:12:42.93	0.009	plausible

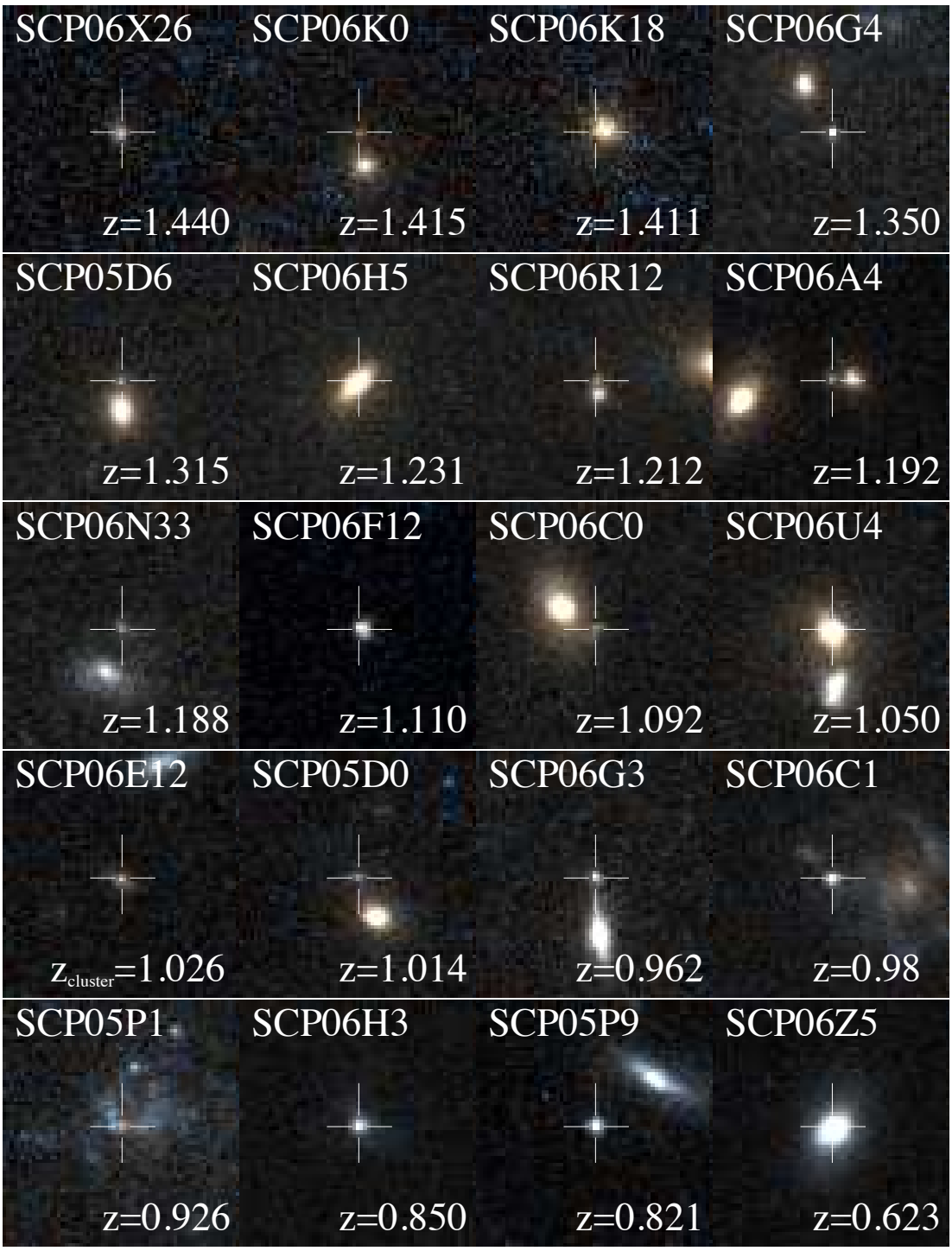

Figure 5.1. Composite color (i_{775} and z_{850}) images of 20 SNe Ia from the HST Cluster Supernova Survey. Each SN Ia is shown in a box of $3.2'' \times 3.3''$ (North up and East left). Note the redshift of SCP06E12 is uncertain, and we use the cluster redshift as a guide.

Sixteen SNe are classified as either secure or probable. We use these SNe in the cosmological analysis. We include the photometry and lightcurves of an additional four plausible SNe Ia to illustrate the quality of the data and the potential for a similar sample with complete classification (and because additional host galaxy data may later bring one of these into the larger sample). Secure, probable and plausible SN Ia are listed in Table 5.1, together with their position, redshift and typing. Postage stamp images of the SNe and host galaxies are shown in Figure 5.1.

We labeled each of our 25 clusters with a letter from 'A' to 'Z' (excluding 'O' to avoid confusion with zero) and assigned supernova names as 'SCP'+[discovery year]+ [discovered cluster]+[SN ID]. The cluster IDs, coordinates, and redshifts are found in tables in Dawson et al. (2009); Barbary et al. (2012a); Meyers et al. (2011). The cluster membership is discussed in Meyers et al. (2011) in detail and summarized in Table 5.1 along with host type information.

5.2 Photometry

For the Near Infrared Camera and Multi-Object Spectrometer (NICMOS) data, we processed the data to compensate for amplifier offsets, bright Earth persistence, contamination from the passage of the telescope through the South Atlantic Anomaly (SAA), residual amplifier glow and fringing, and applied a wavelength-dependent non-linearity correction. A more detailed description of the individual steps now follows.

5.2.1 NICMOS Processing and Photometry

All NICMOS science frames were processed with the latest `CALNICA` pipeline (version 4.4.1 Dahlen et al. 2008). This pipeline includes accurate weighting of each readout and optimal removal of cosmic-rays, as recommended in Fadeyev et al. (2006). `CALNICA` does not account for the affect of cosmic ray hits on neighboring pixels (Fadeyev et al. 2006), but these were found to have no appreciable impact for the data reported here. Subsequently the science frames were corrected for three well-known anomalies: the offset between amplifiers, which affects all NICMOS exposures and is removed using the STSDAS `PyRAF` task `PEDSKY`; persistence after passage of the telescope through the South Atlantic Anomaly (SAA); and persistence after exposing the detectors to the limb of the Earth. Nine exposures are affected by the SAA, which leaves persistent signals from SAA cosmic rays. We applied the STSDAS `PyRAF` task `SAACLEAN` (Barker et al. 2007) to remove SAA persistence effects from the images. When a NICMOS observation is immediately preceded by an ACS data dump, the process could delay the NICMOS placement of the filter blank, subjecting the detectors to the bright limb of the Earth, which imprints a persistent pattern on subsequent exposures (Riess & Bergeron 2008). Four exposures were affected in this way and were corrected using the STSDAS software `NIC_REM_PERSIST`.

At this point, the mode of the flux distribution in each image is measured and recorded. These values are used as the sky levels for the count-rate non-linearity correction.

Even after correcting NICMOS data for these well-studied anomalies, significant large-scale background non-uniformities remain. We developed methods to extract and remove the background structures; these are detailed in Hsiao et al. (2011). Briefly, the models for the background structures are studied and characterized using approximately 600 NICMOS exposures observed through the F110W filter and processed with the procedures described above. Principal component analysis applied on these images revealed that the intensity of the residual corner amplifier glow depends on the exposure sequence. The amount of residual glow decays exponentially and resets every orbit. With exposure times on the order of 1000 seconds, the exposures can be separated into two glow groups, each with approximately constant intensity. This makes it possible to extract the residual glow algebraically. The structured background is modeled as a combination of a constant component and a component that scales with the sky level and exposure time. The models are derived from the algebraic manipulation of stacked images for each glow group. The resulting constant component of the model is dominated by residual amplifier glow at the corners and residual persistence structure at the center. The model component which scales with sky level and exposure time displays a curious fringe pattern whose origin is unknown. The model components are fit to individual exposures via scale parameters to create the customized background models to be subtracted from the individual exposures. In a final step, the bias offsets apparent in the middle column and middle row are removed. Additional details can be found in Hsiao et al. (2011).

NICMOS Count-rate non-linearity

The NICMOS data are critically important for measuring the color of $z > 1$ SNe Ia. Any uncertainty in the NICMOS calibration severely limits the usefulness of SNe Ia observed with NICMOS. In particular, the NIC2 detector exhibits a count-rate dependent non-linearity (Bohlin et al. 2005), the severity of which is a function of wavelength.

This non-linearity previously has only been studied at count rates three orders of magnitude higher (de Jong et al. 2006) than the count rate of a typical SN Ia at $z = 1$, meaning that correcting the flux of SN Ia at $z = 1$ requires significant extrapolation and has a level of uncertainty that is difficult to quantify. For example, comparisons between ground-based near-IR data and a different NICMOS camera (NIC3) showed that little or no correction is required for that camera (Mobasher & Riess 2005). It is difficult to reconcile this finding with the findings of Bohlin et al. (2006) and de Jong et al. (2006). A simple test at the flux levels relevant for the supernovae in this work shows a difference of 12% between NIC2 and NIC3 when the non-linearity corrections are made, revealing significant problems with these extrapolations.

For the NIC2/F110W filter, the degree of count-rate non-linearity is $\sim$ 0.06 mag per factor of 10 change in count rate (Bohlin et al. 2006; de Jong et al. 2006). The count rates from stars that are used to determine the NICMOS zero points are five orders of magnitude

higher than the count rate of a typical SN Ia at $z = 1$. This corresponds to a $\sim$ 0.3 mag correction for the NIC2/F110W filter!

Since this is so important to the cosmological results, we have developed a method to address this count-rate non-linearity calibration directly (Ripoche et al. 2013). We analyze ACS, NICMOS, and ground-based near-IR observations of early-type galaxies from clusters RCS J0221.6−0347 ($z = 1.02$), RDCS J1252.9−2927 ($z = 1.24$), and XMMU J2235.3−2557 ($z = 1.39$). The space and ground-based data are used to constrain the spectral energy distributions (SED) of these galaxies, which are then numerically integrated through the F110W filter transmission curve and compared to the counts measured with NICMOS. The principle advantage of the technique is that the count rate from early type galaxies at this redshift is similar to that measured for SNe Ia, i.e. about 0.03 counts/second/pixel (the contribution from amplifier glow is comparable). We applied this technique using three galaxy clusters that have deep ground based near-IR imaging data from the VLT and deep images with the ACS and NICMOS camera. All three clusters are at different redshifts and produced consistent results. At the low count rates that are applicable to high-redshift SNe Ia, we find that the prescription of Bohlin (2007b) and de Jong et al. (2006) over-predicts the zeropoint correction for the NIC2 camera with the F110W filter by 0.065 mag. We therefore use our zeropoint of 23.029 (Vega magnitude) or 23.757 (AB magnitudes). Additional details can be found in Ripoche et al. (2013).

At high count rates, the count-rate non-linearity size has a strong dependence with wavelength across filters (de Jong et al. 2006), being considerably stronger in bluer filters. The SED of an early-type galaxy at $z \sim 1.2$, is a good match to a SN Ia about 20 rest-frame days after maximum, but is redder than a supernova SED at maximum (though this is compensated somewhat by the fact that the background level is about 1/3 of the source flux and is blue in the F110W bandpass). The size of the count-rate non-linearity correction will thus also depend weakly on the phase and redshift, varying from 0.02 magnitudes at maximum to no additional correction 20 rest-frame days after maximum. Since the wavelength-dependence of the non-linearity may not be even this strong at low count rates, we apply half the correction applicable at each phase, and add (in quadrature) an additional 0.01 magnitudes to the F110W zeropoint error to account for this uncertainty. When added to the 0.006 mag statistical error, and 0.021 mag systematic error (Ripoche et al. 2013), this gives a total uncertainty on the zeropoint of 0.024 magnitudes. For the GOODS supernovae with NICMOS observations, we start with the original flux given by Riess et al. (2007) (after converting the magnitude measurements to fluxes using the given zeropoint of 22.92), but increase the flux by 0.01 magnitudes, representing half the correction for the (possible) wavelength-dependence of the count-rate non-linearity.

Galaxy Models

After the postprocessing described above (Hsiao et al. 2011), we measure fluxes from the eight SNe Ia with NICMOS observations by performing PSF photometry on the images. In all cases, the SNe Ia are not separated enough from their hosts to allow us to fit for the

supernova flux alone; rather we fit a model of the host galaxy as well. By performing PSF photometry using analytic galaxy models, we avoid resampling the images (the better PSF sampling for the ACS data negates this advantage of PSF photometry), and extract the maximum possible signal-to-noise from our observations. We fit an analytic model of the host galaxy even when we have reference images, as this gives higher signal-to-noise, and nearly uncorrelated photometry between epochs[2].

Model PSFs for the supernovae are obtained with the TinyTim software using supernova SED templates from Hsiao et al. (2007) redshifted to the supernova redshift and warped as a function of wavelength to match the photometry. After the lightcurve fitting is complete, new PSFs are generated from the SEDs based on this photometry and the process is repeated. Model PSFs for the galaxies are obtained with TinyTim by appropriately redshifting a galaxy spectrum from Bruzual & Charlot (2003) with an age of 2.5 Gyr and a solar metallicity; the exact shape of the galaxy spectrum does not greatly affect the results. The PSFs used are $3''$ in diameter, comparable to the patch fit in each NICMOS image.

Although there is virtually no information at scales smaller than about half a pixel, all PSFs are seven times oversampled. This oversampling is necessary because the PSF is made slightly wider by the convolution with the subsampled pixels, increasing the flux of the derived photometry. In order for this effect to be negligible, seven times oversampling must be used. Finally, a correction is made to match the photometry from the $3''$ TinyTim PSFs to the $30''$ TinyTim PSFs used in Ripoche et al. (2013). These differently-sized PSFs show different structure far in the wings, but the flux in the core changes by 3.5%, with negligible variation.

We generally model the host galaxies as ellipsoids, with radial profiles given by second degree polynomial splines. These splines have ten nodes, with spacing that asymptotically approaches an exponential away from the core. The higher node density near the core provides more freedom to model the host where the flux changes quickly with position. In the few pixels closest to the core, where the spline changes rapidly, we numerically integrate over each subpixel before convolving with the PSF. On the basis of our tests (see §5.2.1), the hosts of some supernovae were modeled with modifications to this basic scheme, as discussed in the following section.

Photometry Testing

Three ingredients all have to be correct in order to achieve photometry with low bias and variance: the PSF model, the galaxy model, and the supernova centroid. Deriving a PSF from a field star (details in the SN SCP06C0 discussion below) and comparing against TinyTim gives photometry consistent to a few mmags, so we do not believe this is a major contribution to our errors.

[2]Had we subtracted the flux in the reference images at the location of the supernova, the errors from this flux would have to be propagated as a covariance for all the other epochs. The errors on the galaxy model at the position of the supernova are typically much smaller.

Testing the host galaxy model and supernova centroiding is more involved. For each observation, we subtract the best-fit supernova light, and place simulated supernovae (at the same flux level) in the images. The only place one cannot do this test is at the location of the actual supernova, as putting a simulated PSF in this location yields a measurement that will be highly correlated with the measurement of the supernova. We therefore do not place any simulated supernovae closer than two pixels to the best-fit location of the supernova. By examining the bias and variance of the extracted fluxes from a large number of simulations (~ 100), we can choose the galaxy model which gives the most precise and accurate[3] fluxes for each particular supernova. We emphasize that the results of these simulations were the only metric used in choosing the detailed model. In particular, there was no feedback from the shape of the lightcurve or the Hubble diagram since these would have undercut the principles of "blind" analysis we tried to maintain (see §5.3). The same basic galaxy model (discussed above) was used for the NICMOS photometry of each supernova, with the following exceptions.

- SN SCP06C0: As mentioned in §5.1.1, there is a small galaxy about $0.6''$ from the likely host of SN SCP06C0, and just $0.2''$ from SN SCP06C0 itself. We note that the surface brightness of the small galaxy is one fourth of that host at the location of the supernova. The host also has some azimuthal asymmetry visible, indicating a possible merger. The cluster XMM1229+01 was also observed as part of a program to cross-calibrate NICMOS (Ripoche et al. 2013) and deep, well-dithered images were obtained in the WFC3 F110W filter, allowing a more-flexible background model to subtract both galaxies. We modeled the galaxies with a 2D second-order spline, with nodes placed in a grid every $0.076''$ (the natural pixel scale of NICMOS). The WFC3 F110W PSF was modeled as a combination of the elliptical galaxy model and a 2D spline (with a spacing of $0.1''$) using dithered images of a field star. (This is the same empirical PSF model used for testing TinyTim for NICMOS, although there the 2D spline nodes are spaced at the natural pixel scale of NICMOS.) Our testing indicates that this method achieves the same signal-to-noise ratio as the other supernovae that have simpler galaxy subtractions.

- SN SCP06A4: We found a small amount of azimuthal asymmetry in the host. Adding a second-order 2D spline to the galaxy model, with a node spacing of $0.38''$ (five times the natural pixel scale of NICMOS 2) successfully modeled this asymmetry, without adding additional measurement uncertainty to the supernova flux.

- SN SCP05D6: The host galaxy requires two elliptical components to be fitted well. These components are forced to have the same centroid, but are allowed different orientations, ellipticities, and radial profiles. One component forms a bulge, while the other one forms a disk. In one epoch contaminated by the SAA, aperture photometry with a one-pixel radius aperture on the galaxy-model-subtracted images gave better signal-to-noise than PSF photometry, so we used this instead.

[3] We found that precision and accuracy correlated in our simulations.

- SN SCP06U4: This supernova was on the core of a galaxy that appears to be merging with another galaxy. Similarly to SN SCP05D6, a second elliptical component was needed to model the host, (in this case, a third, detached component was used to model the fainter companion). Our simulated supernovae revealed that, rather than using one host galaxy model to extract photometry, even more precise results were obtained averaging photometry results derived using the elliptical model and the 2D spline model (discussed above for SN SCP06C0). Using this procedure results in a change in flux well inside the error bar.

- SN SCP06H5: The one NICMOS observation of this supernova was our most challenging extraction. The observation of the supernova was 11 rest-frame days after maximum, and it is only $\sim 0.1''$ from the core. As with SN SCP05D6, the host galaxy requires two elliptical components to be fitted well.(Comparing to the 2D spline model discussed above, we obtain photometry that is the same to within a small fraction of the error bar.)

  The signal-to-noise ratio of this measurement is low, likely implying some amount of bias due to centroiding error. However, this is the only measurement with a signal-to-noise this low, so no correlation is introduced with any other measurement.

5.3 Augmenting the Union2 Supernova Compilation: Union2.1

SNe Ia are an excellent probe of dark energy, as they measure the magnitude-redshift relation with very good precision over a wide range of redshifts, from $z = 0$ up to $z \sim 1.5$ and possibly beyond. While some individual sets of SNe Ia are now, by themselves, large enough to provide constraints on some cosmological parameters (Guy et al. 2010; Kessler et al. 2009), they do not yet constrain the properties of dark energy as well as analyses that combine individual data-sets to create a compilation of SNe Ia that covers a broader range of redshifts. In Chapter 2, we developed a systematic methodology for combining the many available datasets into one compilation, called the "Union" compilation.

There are many positive features behind the philosophy adopted by the Union analysis. It includes all SN Ia data-sets on an equal footing, with the same lightcurve fitting, cuts, and outlier rejection. Estimates of the systematic error are entered into a covariance matrix, which can be used for fitting any cosmological model. Choices about how to do the analysis and what cuts to apply are done with the cosmological results hidden. This type of "blind" analysis mitigates biases that arise from inadvertently scrutinizing some data more than others. In Chapter 4 (Amanullah et al. 2010), we adopted this strategy to create the Union2 compilation. This work also revised and improved the Union analysis in several significant ways. Firstly, it augmented the Union sample with new SN Ia data-sets from the literature, including 102 low-redshft SNe Ia from the CfA3 survey (Hicken et al. 2009), 129 intermediate-redshift SNe Ia from the SDSS SN survey (Holtzman et al.

2008), five intermediate-redshift SNe Ia discovered from La Palma (Amanullah et al. 2008), and six new high-redshift SNe Ia. This work revised the analysis by replacing the SALT lightcurve fitter with SALT2 (Guy et al. 2005, 2007), and handled many systematic errors on a supernova-by-supernova basis in a covariance matrix.

In the current chapter, we use the analysis procedure that was used for the Union2 compilation with only one significant change: a correction for the host-mass SN Ia-luminosity relation, described below. The HST calibration and the associated errors have also been updated, as described in Section 5.3.4. We refer to this new compilation as "Union2.1."

5.3.1 Host Mass Correction to SN Ia Luminosities

There is evidence that SN Ia luminosity correlates with the mass of the host galaxy, even after the corrections for color and light curve width have been applied (Kelly et al. 2010; Sullivan et al. 2010; Lampeitl et al. 2010). Since low-redshift SNe Ia are predominantly from surveys that target catalogued galaxies, the host galaxies of SNe Ia in these surveys are, on average, more massive than the host galaxies of distant SNe Ia from untargeted surveys. SNe Ia from low-redshift samples therefore have brighter absolute magnitudes. Left uncorrected, the correlation biases cosmological results (Sullivan et al. 2010).

Sullivan et al. (2010) find that the correlation can be corrected by fitting a step in absolute magnitude at $m_\star^{\rm threshold} = 10^{10} m_\odot$. There are two complications with making this correction: most of the SNe in the Union2 compilation do not have host mass data available in the literature, and SN Ia hosts with masses close to the cutoff may scatter across, decreasing the fitted size of the step. To address these problems, we adopt a probabilistic approach to determining the proper host mass correction to apply to each supernova, correcting each supernova by the probability that it belongs in the low-host-mass category. (The low-host-mass category was chosen because most of the low-redshift supernovae are from high-mass galaxies, so correcting the low-host-mass supernovae minimizes the correlation between M_B and the correction coefficient.)

Suppose we have a mass measurement $m_\star^{\rm obs}$ and we would like to estimate the probability that the true mass $m_\star^{\rm true}$ is less than the mass threshold. We begin by noting that

$$P(m_\star^{\rm obs}, m_\star^{\rm true}) = P(m_\star^{\rm obs}|m_\star^{\rm true}) P(m_\star^{\rm true}) \ . \tag{5.1}$$

We can then integrate this probability over all true host masses less than the threshold:

$$P(m_\star^{\rm true} < m_\star^{\rm threshold}|m_\star^{\rm obs}) = \int_{m_\star^{\rm true}=0}^{m_\star^{\rm threshold}} P(m_\star^{\rm obs}|m_\star^{\rm true}) P(m_\star^{\rm true}) \tag{5.2}$$

up to a normalization constant found by requiring the integral to be unity when integrating over all possible true masses. $P(m_\star^{\rm true})$ is estimated from the observed distribution for

each type of survey. The SNLS (Sullivan et al. 2010) and SDSS (Lampeitl et al. 2010) host masses were assumed to be representative of untargeted surveys, while the mass distribution in Kelly et al. (2010) was assumed typical of nearby targeted surveys. As these distributions are approximately log-normal, we use this model for $P(m_\star^{\rm true})$ using the mean and RMS from the log of the host masses from these surveys (with the average measurement errors subtracted in quadrature), giving $\log_{10} P(m_\star^{\rm true}) = \mathcal{N}(\mu = 9.88, \sigma^2 = 0.92^2)$ for untargeted surveys and $\log_{10} P(m_\star^{\rm true}) = \mathcal{N}(10.75, 0.66^2)$ for targeted surveys. When host mass measurements are available, $P(m_\star^{\rm obs}|m_\star^{\rm true})$ is also modeled as a log-normal; when no measurement is available, a flat distribution is used.

For a supernova from an untargeted survey with no host mass measurement (including supernovae presented in this work which are not in a cluster), $P(m_\star^{\rm true} < m_\star^{\rm threshold})$ is the integral of $P(m_\star^{\rm true})$ up to the threshold mass: 0.55. Similarly, nearby supernovae from targeted surveys without host galaxy mass measurements are given a $P(m_\star^{\rm true} < m_\star^{\rm threshold})$ of 0.13. (Very similar numbers of 0.50 and 0.09 are derived from the observed distribution, without using the log-normal approximation.) We must make the correction for supernovae in clusters, as these are from a targeted survey. We take advantage of the simpler SEDs of early-type galaxies to precisely measure these masses[4].

The best-fit mass-correction coefficient, δ, is much smaller in magnitude (-0.03) than that found in other studies (≈ -0.08). This may be due to the small value for δ from the first-year SNLS data, as shown in Table 5.5. We include the difference in δs as a systematic, as discussed in §5.3.5. For this analysis, we assumed the host-mass correction does not evolve with redshift.

5.3.2 Light-Curve Fitting

Amanullah et al. (2010), we use SALT2 (Guy et al. 2007) to fit supernova lightcurves. The SALT2 model fits three parameters to each SNe: an overall normalization, x_0, to the time dependent spectral energy distribution (SED) of a SN Ia, the deviation, x_1, from the average lightcurve shape, and the deviation, c, from the mean SN Ia $B-V$ color. The three parameters, x_1, c, and integrated B-band flux of the model SALT2 SED at maximum light, $m_B^{\rm max}$, are then combined with the host mass to form the distance modulus

$$\mu_B = m_B^{\rm max} + \alpha \cdot x_1 - \beta \cdot c + \delta \cdot P(m_\star^{\rm true} < m_\star^{\rm threshold}) - M_B \,, \tag{5.3}$$

where M_B is the absolute B-band magnitude of a SN Ia with $x_1 = 0, c = 0$ and $P(m_\star^{\rm true} < m_\star^{\rm threshold}) = 0$. The parameters α, β, δ and M_B are nuisance parameters that are fitted simultaneously with the cosmological parameters. The SN Ia photometry data and SALT2 light curve fits are shown in Figure 5.2. The fitted SALT2 parameters are listed in Table 5.2 as well as the host galaxy host stellar mass and lensing magnification factor.

[4]C-001 and F-012 are in clusters, but are not hosted by early-type hosts. We use the untargeted value for their host-mass–luminosity relation correction.

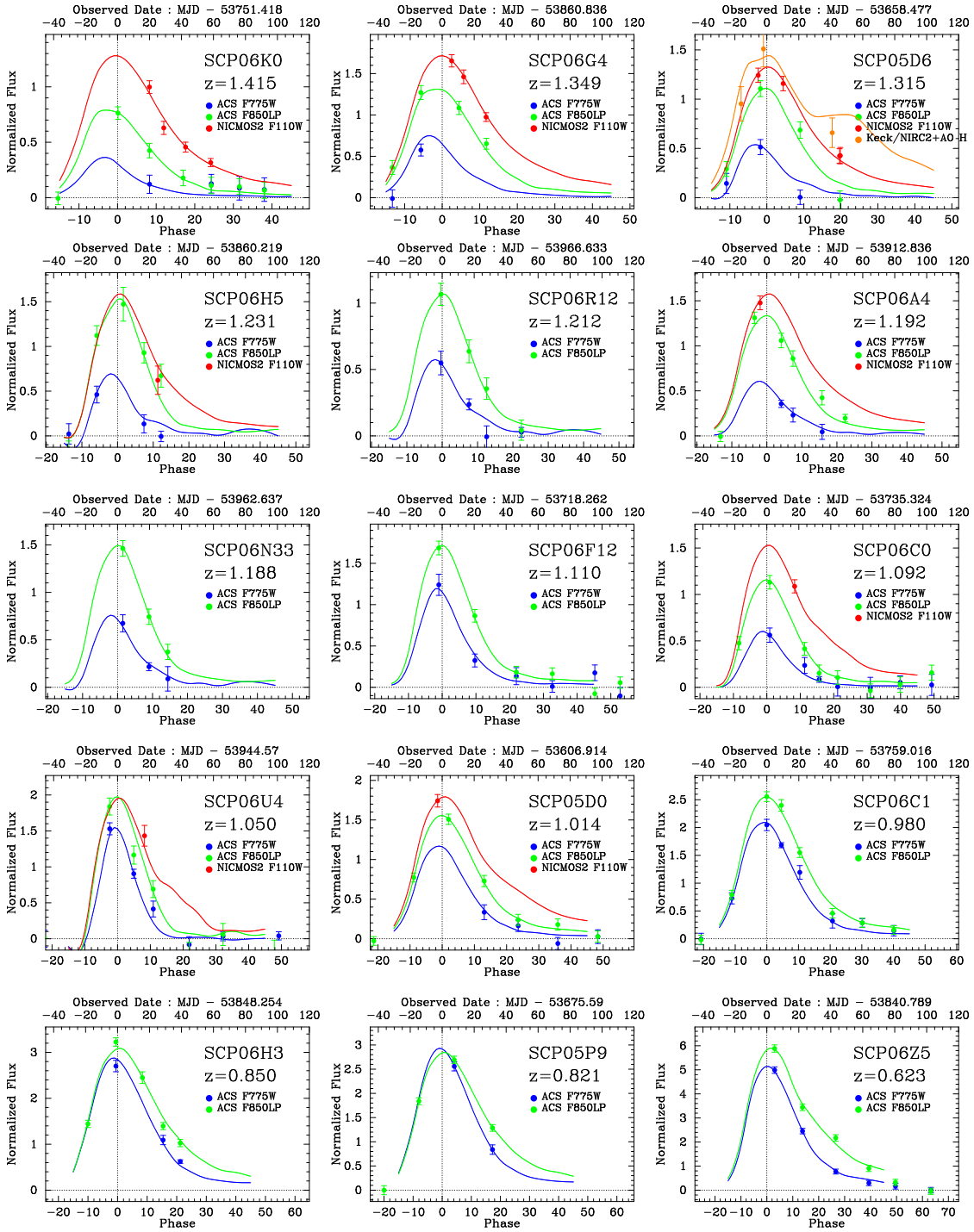

Figure 5.2. 15 SNe Ia light curve fits by SALT2. Flux is normalized to the z_{850}-band zeropoint magnitude. ACS i_{775}, ACS z_{850} and NICMOS F110W data is color coded in blue, green and red respectively. Note that SCP 05D06 (z=1.314) has H-band data from Keck AO system (orange) (Melbourne et al. 2007) and that this data is consistent with the HST/ACS and HST/NICMOS light curve data.

Table 5.2. SALT2 Lightcurve Fit Results . The details of host galaxy identifications, coordinates and its stellar mass measurements can be found in Meyers et al. (2011). Gravitational lensing magnification factor (see §5.1.1 for details). For cosmological analysis we must divide the corrected SNe fluxes by this factor to make use of these supernovae. SCP06U4 is not included in our current cosmological results, but will likely be included in future compilations (see §5.3 for details).

SN name	z	$\mathrm{MJD_{Bmax}}$	m_B	x_1	c	Galaxy Mass ($10^{11}\mathrm{M}_\odot$)	Magnification
SCP06A4	1.192	53912.7 ± 1.5	25.497 ± 0.048	-1.45 ± 0.68	0.065 ± 0.084	0.44	...
SCP06C0	1.092	53735.4 ± 1.0	25.636 ± 0.066	-2.66 ± 0.65	0.257 ± 0.083	1.97	$1.030^{+0.007}_{-0.005}$
SCP06C1	0.980	53759.0 ± 0.7	24.613 ± 0.028	-0.35 ± 0.33	0.014 ± 0.053	...	...
SCP06F12	1.110	53718.4 ± 2.3	25.253 ± 0.068	-2.09 ± 1.29	-0.133 ± 0.142	...	...
SCP06G4	1.350	53860.9 ± 1.4	25.424 ± 0.052	0.15 ± 0.64	-0.029 ± 0.052	1.72	$1.015^{+0.005}_{-0.004}$
SCP06H3	0.850	53848.2 ± 0.6	24.345 ± 0.038	0.58 ± 0.31	0.089 ± 0.067	...	...
SCP06H5	1.231	53860.2 ± 1.5	25.389 ± 0.111	-3.12 ± 1.10	-0.103 ± 0.187	3.66	...
SCP06K0	1.415	53751.3 ± 2.8	25.811 ± 0.087	0.30 ± 0.97	0.147 ± 0.081	2.30	...
SCP06N33	1.188	53962.6 ± 4.3	25.407 ± 0.132	-2.15 ± 1.32	-0.038 ± 0.175	...	$1.066^{+0.017}_{-0.014}$
SCP05D0	1.014	53606.9 ± 0.9	25.201 ± 0.066	-0.61 ± 0.65	0.061 ± 0.085	0.40	...
SCP05D6	1.315	53658.5 ± 1.3	25.660 ± 0.046	-1.26 ± 0.56	-0.058 ± 0.061	2.61	$1.021^{+0.012}_{-0.008}$
SCP05P9	0.821	53675.6 ± 0.6	24.367 ± 0.049	0.25 ± 0.50	0.022 ± 0.075	...	...
SCP06R12	1.212	53966.6 ± 3.5	25.789 ± 0.114	-2.06 ± 1.50	-0.158 ± 0.198	0.23	...
SCP06U4	1.050	53944.4 ± 1.1	25.056 ± 0.063	-4.62 ± 1.09	-0.102 ± 0.096	1.11	...
SCP06Z5	0.623	53840.5 ± 3.0	23.482 ± 0.144	-0.76 ± 0.88	0.070 ± 0.120	...	...

5.3.3 Union2.1

To the Union2 SN Ia compilation (Amanullah et al. 2010), we add 16 SNe Ia from this work that were classified as either secure or probable, including six SNe Ia hosted by high-z cluster elliptical galaxies. The four SNe Ia that were classified as possible are not used. We also add 18 SNe Ia from the low-redshift sample of Contreras et al. (2010), 9 of which were not in Union2 (the others had published data from CfA). As in Union2, for all SNe we require

1. that the CMB-centric redshift is greater than 0.015;
2. that there is at least one point between -15 and 6 rest-frame days from B-band maximum light;
3. that there are at least five valid data points;
4. that the entire 68% confidence interval for x_1 lies between -5 and $+5$;
5. data from at least two bands with rest-frame central wavelength coverage between 2900 Å and 7000 Å; and
6. at least one band redder than rest-frame U-band (4000 Å). This cut is new to this analysis, but only affects SN 2002fx, a GOODS supernova which is very poorly measured.

In addition to these quality cuts, we removed any supernova spectroscopically classified as SN 1991bg-like. These SNe Ia are a distinct subclass which is not modeled well by SALT2. In cases when spectroscopic sub-typing is not possible or not available, we screen for these supernovae photometrically by searching for any supernovae with red ($c > 0.2$) and narrow-width ($x_1 < -3$) lightcurves. In the current dataset, none are cut by this screening. When fit with SALT2, and color-corrected and shape-corrected (as though they were normal SNe Ia), spectroscopically identified members of this class have an average absolute magnitude only 0.2 magnitudes fainter than normal SNe Ia; any contamination from the handful of supernovae near this cut will have only a small impact (and one well-accounted for by our contamination systematic, see Amanullah et al. (2010)).

From the 16 SNe Ia that were classified as either secure or probable (see Table 5.1), SN SCP06U4 and SN SCP06K18 fail to pass these cuts. SN SCP06K18 lacks good enough light-curve coverage and SN SCP06U4 fails the x_1 cut[5]. This leaves 14 SNe Ia that are used to constrain the cosmology.

[5]Using an updated version (2-18-17) of SALT2 (or using SALT1), SN SCP06U4 would pass this cut, so this supernova may be included in future analyses.

5.3.4 Fitting the Cosmology

Following Amanullah et al. (2010), the best-fit cosmology is determined by minimizing

$$\chi^2_{\rm stat} = \sum_{\rm SNe} \frac{\left[\mu_B(\alpha,\beta,\delta,M_{\rm B}) - \mu(z;\Omega_m,\Omega_w,w)\right]^2}{\sigma^2_{\rm lc} + \sigma^2_{\rm ext} + \sigma^2_{\rm sample}}. \quad (5.4)$$

A detailed discussion of the terms in this equation can be found in Amanullah et al. (2010). We only comment on the final term in the denominator, $\sigma^2_{\rm sample}$, which is computed by setting the reduced χ^2 of each sample to unity. This term was referred to as "$\sigma^2_{\rm systematic}$" in Chapters 2 and 4. We note that $\sigma^2_{\rm sample}$ includes intrinsic dispersion as well as sample-dependent effects. This term effectively further deweights samples with poorer-quality data that has sources of error which have not been accounted for. As noted in Amanullah et al. (2010), this may occasionally deweight an otherwise well-measured supernova.

Following Conley et al. (2006b), Chapter 2 and Chapter 4, we hide our cosmology results until the full analysis approach is settled. As in previous Union analysis, we carry out an iterative χ^2 minimization with outlier rejection. Each sample is fit for a flat ΛCDM cosmology independently of the other samples (but with α, β, and δ set to their global values). An M_B is chosen for each sample by minimizing the absolute variance-weighted sum of deviations, minimizing the effects of outliers. We then reject any supernova more than 3σ from this fit. All of the SNe Ia in our new sample pass the outlier rejection. As each sample is fit independently with its own Hubble line, systematic errors and the choice of cosmological model are not relevant in this selection.

Diagnostics

A diagnostic plot, which is used to study possible inconsistencies between SN Ia samples, is shown in Figure 5.3. The median of $\sigma_{\rm sample}$ can be used as a measure of the intrinsic dispersion associated with all SNe Ia. The intrinsic dispersion is a reflection of how well our empirical models correct for the observed dispersion in supernova luminosities. The median $\sigma_{\rm sample}$ for this work is 0.15 mag and is indicated with the leftmost dashed vertical line in the left panel.

The variance weighted RMS about the best-fit cosmology gives an indication of the quality of the photometry. A sample with more accurate photometry will have a smaller RMS. For SNe Ia from our survey, the RMS is 0.19 ± 0.04, which is only slightly larger than that measured for the 1st year SN Ia sample from SNLS, and equal to the median of all samples (shown as the rightmost dashed line in Figure 5.3, left panel).

The two middle panels show the tension between data-sets, the first with statistical errors only, and the second with statistical and systematic errors (see §5.3.5). Most samples land within 1 σ of the mean defined by all samples and about one third lie outside 1 σ, as expected for a normal distribution. No sample exceeds 2 σ. The right hand panel shows the slope of the residuals, which, for larger data sets, can be used to reveal Malmquist-like biases or calibration errors.

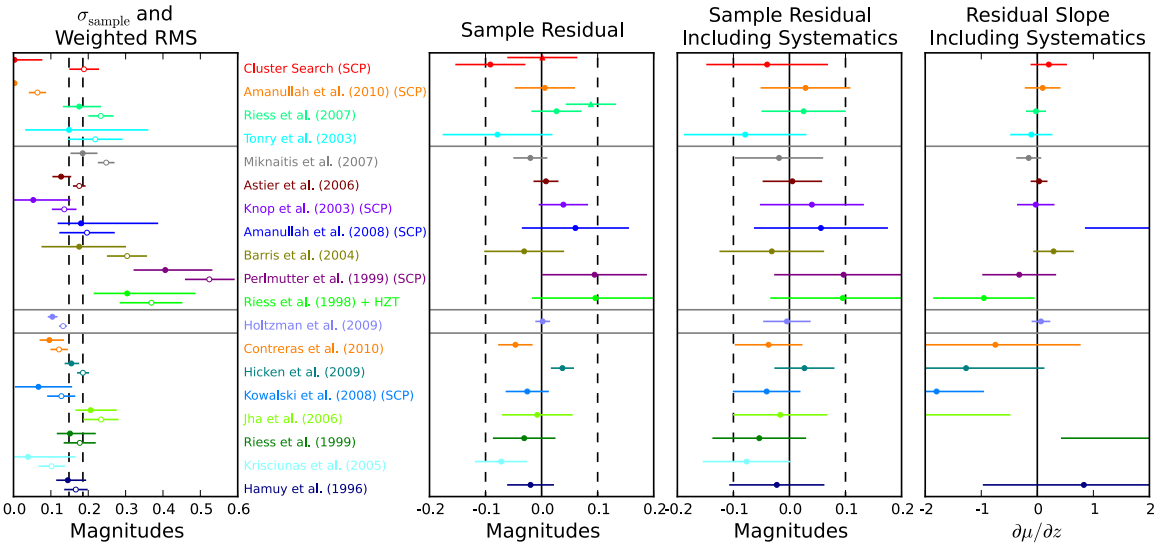

Figure 5.3. Diagnostics plot for the individual data sets. From left to right: irreducible sample dispersion (filled circles) and variance-weighted RMS about the best-fit model (open circles); the average sample residual from the best-fit model ($\mu_{\rm measured} - \mu_{\rm model}$) excluding and including systematic errors; and the best-fit slope of the Hubble residual (in magnitudes) versus redshift — $\partial\mu_{\rm residual}/\partial z$. Note that the errors on the sample dispersion include only statistical errors and do not include possible systematic errors. The confidence intervals on the weighed RMS are obtained with Monte-Carlo simulations. The triangles in the sample residual plot show the effect of including the filter shifts discussed in Section 5.3.4.

The supernovae from our sample are 1.5-σ brighter than the average sample. While the source of the difference may certainly be a simple statistical fluctuation, part of the difference might be attributable to errors in the filter responses of the ACS filters. (The difference is largely driven by the SNe Ia that have only ACS i_{775} and z_{850} data to constrain their light curves.) Based on photometric observations of spectrophotometric standards, Bohlin (2007b) report possible blueward shifts of 94 Å for the z_{850} filter and 57 Å for the i_{775} filter (with smaller shifts in bluer filters). The red triangle in the sample residual panel shows the effect of applying these shifts. The shifts also affect the GOODS supernovae. The green triangle shows the affect of applying the filter shifts to those data. Bohlin (2007b) notes that more data to confirm the filter shifts are needed, so we do not apply them in our primary analysis. Instead, we include the uncertainty in the filter curves as a systematic error, as described in §5.3.5.

Part of the difference could also be due to the correction that we apply for the recently discovered correlation between host galaxy mass and the luminosity of SNe Ia after the lightcurve width and color corrections have been applied. Many of the hosts in our sample are massive early type galaxies. In this analysis, the correction we use is smaller than the correction that has been noted by others. We add this difference as a systematic error, as described in §5.3.5.

Figure 5.4 shows the Hubble Diagram with SNe from the updated Union2 sample and the best-fit ΛCDM model. We add 14 SNe Ia from this work. (As discussed above,

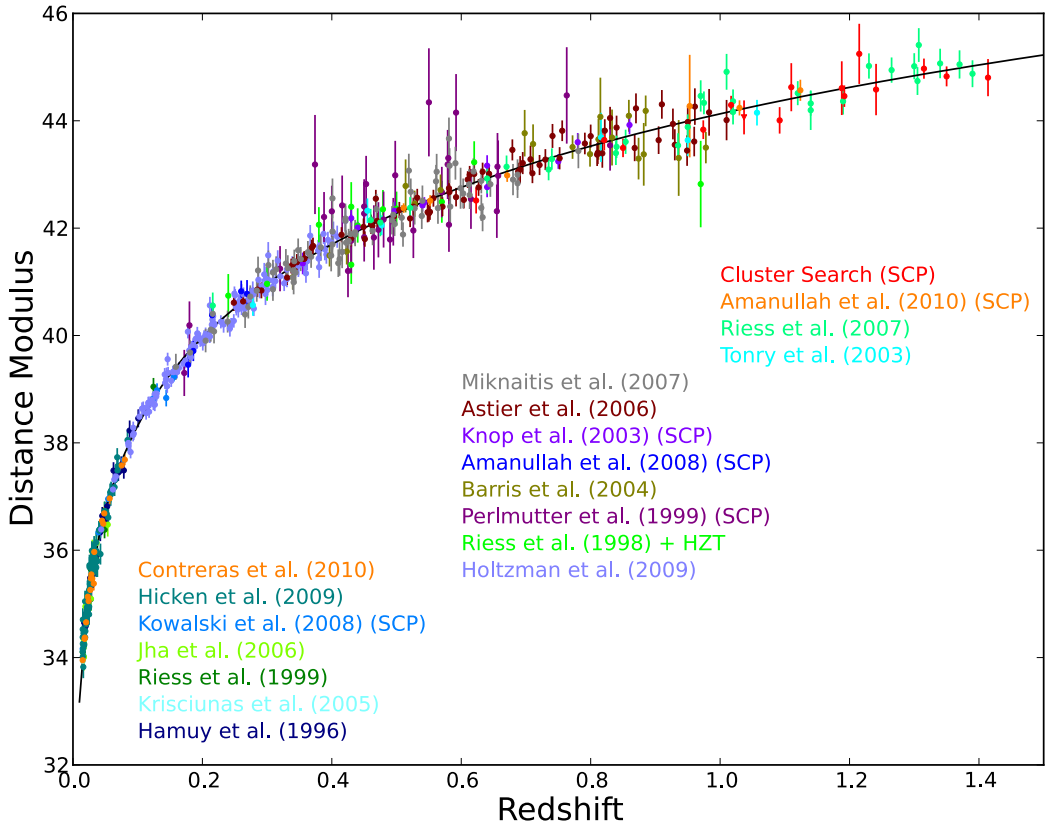

Figure 5.4. Hubble diagram for the Union2.1 compilation. The solid line represents the best-fit cosmology for a flat ΛCDM Universe for supernovae alone. SN SCP06U4 falls outside the allowed x_1 range and is excluded from the current analysis. When fit with a newer version of SALT2, this supernova passes the cut and would be included, so we plot it on the Hubble diagram, but with a red triangle symbol.

SN SCP06U4 is likely to be included in future analyses so it is included on the plot with a different symbol.) Ten (eleven with SN SCP06U4) are above a redshift of one, significantly increasing the number of well-measured supernovae above this redshift.

5.3.5 Systematic errors

In this chapter, we follow the systematics analysis we presented in Amanullah et al. (2010). Systematic errors that directly affect supernova distance measurements (calibration, and galactic extinction, for example) are treated as nuisance parameters to be fit simultaneously with the cosmology. Minimizing over these nuisance parameters gives additional terms to add to the distance modulus covariance matrix

$$U_{ij} = \sum_{\epsilon} \frac{d\mu_i(\alpha,\beta)}{d\epsilon} \frac{d\mu_j(\alpha,\beta)}{d\epsilon} \sigma_\epsilon^2 \ , \tag{5.5}$$

where the sum is over each of these distance systematic errors in the analysis. (Although the distance modulus depends on δ as well as α and β, the derivatives with respect to the zeropoints do not.) In this analysis, α and β have little interaction with cosmological parameters. When computing cosmological constraints, we therefore freeze the covariance matrix in order to avoid multiple matrix inversions[6]. Only when the α and β may vary significantly from the global best-fit (Table 5.5), do we update α and β.

Systematic errors that affect sample composition or the color and shape correction coefficients cannot be parameterized supernova-by-supernova in this way. These are incorporated by assigning each dataset its own constant covariance. This is an adequate treatment, as these systematic errors are subdominant.

There are two systematic errors that were not included in Amanullah et al. (2010), but are included in this analysis for the first time: a systematic error on the host-mass correction coefficient, δ (which might affect δ at the ~ 0.05 level), and uncertainties in the effective wavelengths of the ACS i_{775} and z_{850} filters.

In addition to updating the NICMOS F110W zeropoint and uncertainty, as described in §5.2.1, we revise the uncertainty assigned to the zeropoint for NICMOS F160W to account for the uncertainty in the count-rate non-linearity at this wavelength (de Jong et al. 2006). Table 5.3 gives the assumed zeropoint error for each filter.

We note that the nearby supernovae from targeted searches are sensitive to δ (relative to the untargeted searches) at the level of $(0.55 - 0.13)\Delta\delta \approx 0.02$ magnitudes, while the covariance weighted mean of the cluster supernovae varies with δ as $0.24\Delta\delta \approx 0.01$ magnitudes. We cannot propagate this systematic on a supernova-by-supernova basis, as this would be equivalent to fitting for δ, which we already do. Therefore, we include this error by adding a covariance of 0.02^2 to the nearby, targeted supernova surveys, a covariance of 0.01^2 to our new data-set, and $0.02 \cdot 0.01$ between these data-sets.

[6] As demonstrated in the Union2 appendix, these matrix inversions can be simplified at the expense of more matrix multiplication; the run-time does not change much.

Table 5.3. Assumed instrumental uncertainties for SNe in this work.

Source	Band	Uncertainty	Reference
HST	WFPC2	0.02	Heyer et al. (2004)
	ACS F850LP	0.01	Bohlin (2007b)
	ACS F775W	0.01	
	ACS F606W	0.01	
	ACS F850LP	94 Å	Bohlin (2007b)
	ACS F775W	57 Å	
	ACS F606W	27 Å	
	NICMOS J	0.024	Ripoche et al. (2013), Section 5.2.1
	NICMOS H	0.06	de Jong et al. (2006)
SNLS	g, r, i	0.01	Astier et al. (2006)
	z	0.03	
ESSENCE	R, I	0.014	Wood-Vasey et al. (2007)
SDSS	u	0.014	Kessler et al. (2009)
	g, r, i	0.009	
	z	0.010	
SCP: Amanullah et al. (2010)	R, I	0.03	Amanullah et al. (2010)
	J	0.02	
Other	U-band	0.04	Hicken et al. (2009)
	Other Band	0.02	Hicken et al. (2009)

Including uncertainties in filter effective wavelength is not as straightforward as including zeropoint uncertainties. Effective wavelength is only the first-order method of describing a filter. For a simple filter shift, as implemented here, $d\mu(\alpha, \beta)/d\lambda$ will undergo significant variations as supernova spectral features shift in and out of the filter. These are likely to be worse than the actual effect of simply reweighting filter throughput. Although in general these variations will get averaged out with different phases, redshifts, and additional filters, we have modeled a worst-case in accounting for this systematic (and even then it only affects the supernovae most dependent on z_{850}).

Table 5.4 shows the impact of each type of systematic error on our cosmological constraints, in combination with BAO, CMB, and H_0 data (see §5.4). For the purpose of constructing Table 5.4, we add, for each systematic error in the table, the contribution from just that systematic to the statistical-only covariance matrix. The confidence interval for constant w where the χ^2 is within 1 of the minimum χ^2 (the edges of this confidence interval are hereafter referred to with the notation $\Delta\chi^2 = 1$) is found iteratively; the plus and minus errors for constant w are averaged. The statistical-only constant w error bar is subtracted in quadrature, leaving the effect of each systematic on constant w. We also quote the effect of each systematic error of the $\Delta\chi^2 = 5.99$ confidence contour in the (w_0, w_a) plane; as this is two-dimensional, we subtract the area (not in quadrature) of the statistical-only contour.

Since the derived cosmology errors vary with the best-fit cosmology, after a given systematic error has been added, the supernova magnitudes are shifted so that the best-fit cosmology including that systematic matches the best-fit with statistical errors only. This magnitude adjustment (which is the same adjustment we use for blinding ourselves to the best-fit cosmology) consists of repeatedly computing the difference in distance modulus

Table 5.4. Effect on constant w error bars and area of the 95% $w_0 - w_a$ confidence contour (inverse DETF FoM) for each type of systematic error, when SN Ia constraints are combined with constraints from CMB, H_0, and BAO.

Source	Error on Constant w	Inverse DETF FoM
Vega	0.033	0.19
All Instrument Calibration	0.030	0.18
(ACS Zeropoints)	0.003	0.01
(ACS Filter Shift)	0.007	0.04
(NICMOS Zeropoints)	0.007	< 0.01
Malmquist Bias	0.020	0.07
Color Correction	0.020	0.07
Mass Correction	0.016	0.08
Contamination	0.016	0.05
Intergalactic Extinction	0.013	0.03
Galactic Extinction Normalization	0.010	0.01
Rest-Frame U-Band Calibration	0.009	< 0.01
Lightcurve Shape	0.006	< 0.01
Quadrature Sum of Errors/ Sum of Area (not used)	*0.061*	*0.68*
Summed in Covariance Matrix	0.048	0.42

between the best-fit cosmology and fiducial value and adding it to the supernovae.

As with the Union2 compilation, calibration systematics represent the largest contribution to the error on constant w. Here, we see that they are also the dominant systematics for (w_0, w_a). As noted by Amanullah et al. (2010), significantly smaller systematic errors are derived by adding each covariance in the covariance matrix, rather than adding the cosmological impacts together. This is due to the different redshift dependence of each systematic error, as well as some self-calibration that occurs as described in Amanullah et al. (2010).

Some potential systematic errors can be investigated by dividing the whole dataset into subsets. Table 5.5 shows many of these divisions. All of the numbers are computed including supernova systematics; the cosmological constraints are computed including BAO and CMB data. In short, we do not see any evidence of unknown systematic errors, requiring the cosmological impact to be smaller than the current errors.

The first subsets are subsets in redshift. These can be used to study possible evolution of correction coefficients for shape, color, and host mass. The redshift range 0.5 to 1 seems to show β and δ smaller in magnitude, but the revised SNLS sample (Guy et al. 2010) which uses a newer version of the calibration and lightcurve fitting (as well as many more supernovae), shows no signs of this. As we have already budgeted these systematic uncertainties, these updates will be within our error bars.

The next rows show the effect of changing δ from 0 to -0.08 (the size of the correction in Sullivan et al. (2010)). Because a large error on δ is already included in the systematic error covariance matrix, this has less than a 0.01 effect on w, about ten times smaller than it would have if we did not include this systematic.

Next, we consider systematics caused by potentially different populations of supernovae. We perform a cut on the best-fit true x_1 or c of each supernova (see Amanullah et al.

(2010) for details). The cosmology in each case is compatible with the cosmology derived from the whole sample.

We now look at each of the four largest datasets for evidence of tension. The only tension found is in the first-year SNLS sample (Astier et al. 2006). Here, β and δ are both at odds with the whole sample, but as noted above, we do not believe this is a cause for concern.

The final two rows show the high-redshift sample split by host type; this is discussed in §5.5.2.

5.4 Constraints on Dark Energy

Following Amanullah et al. (2010), we constrain the properties of dark energy first using SNe Ia alone (with and without systematics), and then by combining the constraints derived from SNe Ia with those derived from the 7-year WMAP data of the CMB (Komatsu et al. 2011), the position of the BAO peak from the combined analysis of the SDSS DR7 and 2dFGRS data (Percival et al. 2010), and the measurement of the Hubble constant (H_0) from Cepheids (Riess et al. 2011).

The rate of expansion at redshift z, $H(z)$, is described by the Friedman equation:

$$\begin{aligned} \frac{H^2(z)}{H_0^2} &= \Omega_m(1+z)^3 + \Omega_k(1+z)^2 \\ &\quad + \Omega_{\rm DE} \exp\left[\int 3(1+w(z)) {\rm dln}(1+z)\right], \end{aligned} \tag{5.6}$$

where H_0 is the rate of expansion today, Ω_m and $\Omega_{\rm DE}$ are the matter and dark energy density with respect to the critical density today, $w(z)$, is the dark energy equation-of-state parameter, and $\Omega_k = 1 - \Omega_m - \Omega_{\rm DE}$ is the spatial curvature density of the universe. Distances, such as the luminosity distance, depend on the integral of $1/H(z)$ over redshift.

In this section, we consider the following models for dark energy:

- ΛCDM: A cosmological constant in a flat universe.
- wCDM: A constant equation-of-state parameter in a flat universe.
- owCDM: A constant equation-of-state parameter in a curved universe.
- w_zCDM models: A time-varying equation-of-state parameter in universes with and without curvature.

The results for each of the models are listed in Table 5.6 and discussed in turn in the following sub-sections. Unless stated otherwise, the uncertainties represent the 68% confidence limits ($\Delta\chi^2 = 1$) and include both statistical uncertainties and systematic errors.

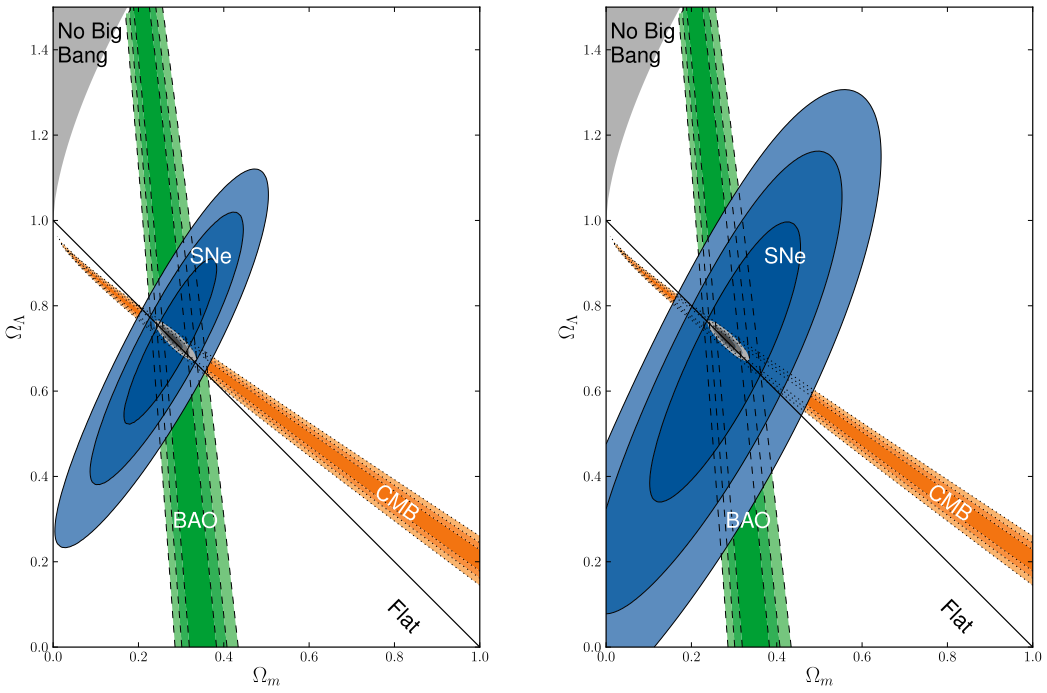

Figure 5.5. ΛCDM model: $68.3\%, 95.4\%$, and 99.7% confidence regions of the $(\Omega_m, \Omega_\Lambda)$ plane from SNe Ia combined with the constraints from BAO and CMB. The left panel shows the SN Ia confidence region only including statistical errors while the right panel shows the SN Ia confidence region with both statistical and systematic errors.

5.4.1 ΛCDM

In the ΛCDM model, the equation-of-state parameter is exactly -1 and does not vary with time. In a flat Universe, SNe Ia alone constrain the dark-energy density, Ω_Λ, to be $\Omega_\Lambda = 0.705^{+0.040}_{-0.043}$. In Figure 5.5, we show the confidence intervals on Ω_m and Ω_Λ from SNe, CMB and BAO. Both the individual constraints and the combined constraint are shown (the BAO constraints are computed with an $\Omega_m h^2$ prior from the CMB). The SN constraint is almost orthogonal to that of the CMB. Adding the constraints from CMB, BAO and H_0 reduces the uncertainty. Under the assumption of a flat Universe, the four probes yield

$$\Omega_\Lambda = 0.729^{+0.014}_{-0.014} \quad (\Lambda\mathrm{CDM} : \mathrm{SN} + \mathrm{CMB} + \mathrm{BAO} + \mathrm{H}_0).$$

In this ΛCDM model, the expansion of the universe switched from deceleration to acceleration at $z = 0.752 \pm 0.041$, which corresponds to a look back time of 6.62 ± 0.22 Gyr, about the half of the age of the universe. Equality between the energy density of dark energy and matter occurred later, at $z = 0.391 \pm 0.033$ or a look back time of 4.21 ± 0.27 Gyr.

If we remove the flatness prior (labeled as $o\Lambda$CDM in Table 5.6), the best-fit Ω_m and Ω_Λ change by a fraction of their errors with $\Omega_k = 0.002^{+0.005}_{-0.005}$.

5.4.2 wCDM : Constant Equation of State Parameter

In wCDM models, w is constant but is allowed to be different from -1. While few dark energy theories give $w \neq -1$ and yet constant (Copeland et al. 2006), constraints on the constant w model are still useful. The wCDM model contains fewer parameters than the dynamical dark energy models considered in the following section, yet a value different from $w = -1$ would still provide insights for alternative theories for dark energy.

In a flat universe ($\Omega_k = 0$), SNe Ia alone give $w = -1.001^{+0.348}_{-0.398}$. Adding the constraints from the other three probes tightens the constraint on w considerably, as the constraints from SNe Ia in the $\Omega_m - w$ parameter plane are almost orthogonal to those provided by BAO and the CMB (Figure 5.6).

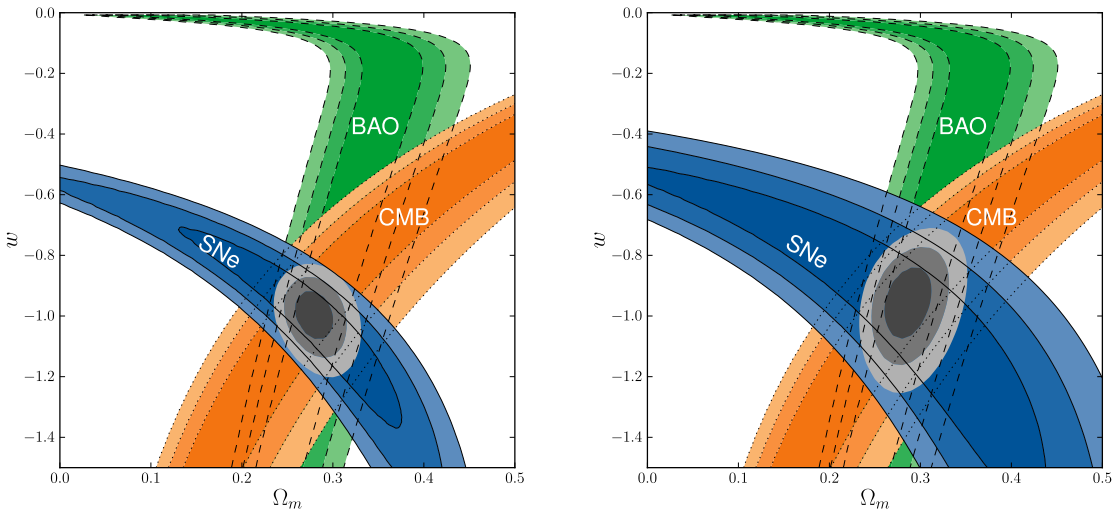

Figure 5.6. wCDM model: 68.3%, 95.4%, and 99.7% confidence regions in the (Ω_m, w) plane from SNe Ia BAO and CMB are shown in both panels. The left panel shows the SN Ia confidence region for statistical uncertainties only, while the right panel shows the confidence region including both statistical and systematic uncertainties. We note that CMB and SN Ia constraints are orthogonal, making this combination of cosmological probes very powerful for investigating the nature of dark energy.

In principle, a constraint on H_0 helps to break the degeneracy between Ω_m and h for CMB, which measures $\Omega_m h^2$ (Spergel et al. 2003). However, in this case adding supernova data helps more, as narrowing the degeneracy between Ω_m and w allows the CMB itself to constrain H_0. By combining all four probes, we find $w = -1.013^{+0.068}_{-0.073}$. As seen in Table 5.6, neither BAO nor H_0 currently make much of a difference in the error bars for this model.

5.4.3 $o w$CDM : Constant Equation of State in a Curved Universe

Inflation models generally predict that the curvature of the Universe, Ω_k, is $\sim 10^{-5}$ (Guth 1981; Liddle & Lyth 2000). In curved universes, SNe Ia play the critical role in

constraining w, while CMB+BAO constrain Ω_k and Ω_m. By combining all four probes, we find $\Omega_k = 0.002^{+0.007}_{-0.007}$ and $w = -1.003^{+0.091}_{-0.095}$. Even with the additional freedom for non-zero curvature, a flat universe is supported from observations. Among many cosmological parameters, the curvature of the universe is the most well-determined parameter.

We note CMB alone does not place a tight constraint on curvature[7], $\Omega_k = -0.102^{+0.085}_{-0.097}$ (Komatsu et al. 2011). In order to break the degeneracy between Ω_m Ω_k and H_0 that exists in the CMB constraints, we need to add constraints either from BAO or H_0; this reduces the curvature uncertainty by a factor of ten. However, the combination of these three probes does not place a tight constraint on the equation-of-state parameter w. SNe improve the constraint on w from CMB+BAO+H_0 by more than a factor of three.

5.4.4 Time Dependent Equation of State

We next examine models in which dark energy changes with time. For a wide range of dark energy models, it can be shown (Linder 2003b) that, to good approximation, the dark energy equation-of-state can be parametrized by

$$w(a) = w_0 + w_a(1 - a) \tag{5.7}$$

where $a = 1/(1 + z)$ is a scale factor. The ΛCDM model is recovered when $w_0 = -1$ and $w_a = 0$. The constraints on w_0 and w_a are shown in Figure 5.7 and Table 5.6.

The Dark Energy Task Force (Albrecht et al. 2006) proposed a figure of merit (FoM) for cosmological measurements equal to the inverse of the area of the 95% confidence contour in the $w_0 - w_a$ plane. When we make this measurement, using the $\Delta\chi^2 = 5.99$ contour, we find a FoM of 1.84 (statistical-only) and 1.04 (including systematics). Frequently, the FoM is also defined in terms of the 1σ errors ($\Delta\chi^2 = 1$); this FoM is 39.3 (statistical-only) and 22.6 (including systematics). Surprisingly, even with w_a floating, we still find an interesting constraint on Ω_k of ~ 0.02.

We next consider a model in which the dark-energy equation-of-state parameter is constant inside fixed redshift bins. This model has more parameters (and thus more freedom) than $w_0 - w_a$. The results are shown in Figure 5.8 and Table 5.6. We adopt the redshift bins used in Amanullah et al. (2010), so that a direct comparison can be made.

In the left panel with broad bins, we show a reasonably good measurement of the equation-of-state parameter from redshift 0 to 0.5. From redshift 0.5 to 1, there is no real constraint. For example, any scalar field model ($|w| < 1$) is reasonably compatible with the data. Above redshift 1, the constraints are weaker. $w \gtrsim 0$ is ruled out, as this violates early matter domination.

We separate the supernova and early universe constraints by defining a bin at redshift 1.6, as shown in the middle panel. This shifts the confidence interval for $w(1.0 < z < 1.6)$ towards higher w. Eliminating this division, and instead adding more bins up to redshift 0.5 (right panel), gives three constraints of moderate quality with a possible crossing of

[7] http://lambda.gsfc.nasa.gov/product/map/dr4/parameters.cfm

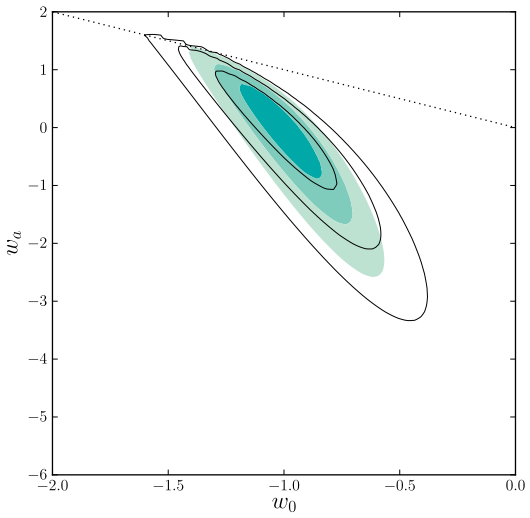

Figure 5.7. $68.3\%, 95.4\%$, and 99.7% confidence regions of the (w_0, w_a) plane from SNe combined with the constraints from BAO, CMB, and H_0, both with (solid contours) and without (shaded contours) systematic errors. Zero curvature has been assumed. Points above the dotted line ($w_0 + w_a > 0$) violate early matter domination and are disfavored by the data.

$w = -1$. No matter the binning, we will need more data extending above redshift 1 to investigate the dark energy equation-of-state parameter where the uncertainty is still very large.

To examine constraints on the existence of dark energy at different epochs, we study $\rho(z)$, which is the density of the dark energy and allowed to have different values in fixed redshift bins. Within each bin, ρ is constant. (Note that the discontinuities in $\rho(z)$ at the bin boundaries introduce discontinuities in $H(z)$.) We choose the same binning as above, but note that binned ρ and binned w models give different expansion histories. Our results are shown in Figure 5.9 and Table 5.7.

Although there is no real constraint on the equation-of-state parameter at redshift 0.5 to 1, dark energy is seen at high significance in both panels. There is weak evidence for the existence of dark energy above redshift 1, as can be seen in the left panel. However, if we again separate the supernova data and early universe constraints (right panel) we see neither probe has any constraint on the existence of dark energy above redshift 1.

5.5 Discussion

5.5.1 Improving the Constraints on Time-Varying w by Efficiently Adding $z > 1$ Supernovae

Beyond $z = 1$, we add 10 new well-measured SNe Ia to the Hubble diagram. The variance-weighted RMS scatter of the new sample is 0.20 ± 0.05 mag. As a comparison,

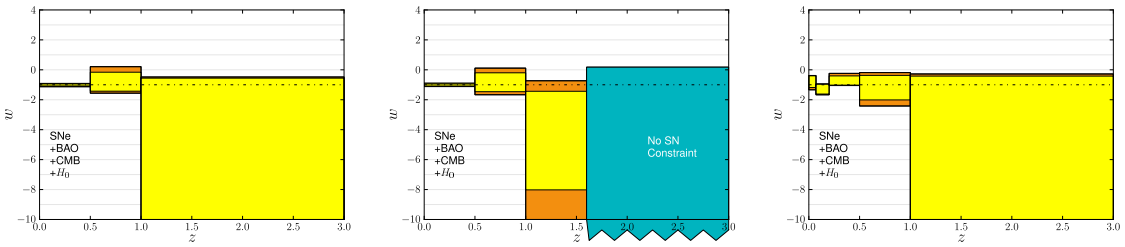

Figure 5.8. Constraints on $w(z)$, where $w(z)$ is assumed to be constant in each redshift bin, are plotted at the 68% probability level ($\Delta\chi^2 = 1$). Each panel shows different redshift binning. The results were obtained assuming a flat universe for the joint data set of SNe, BAO, CMB, and H_0, with (dark/orange) and without (light/yellow) SN systematics. The middle panel takes a closer look at the $z > 1$ constraints, while the right panel shows the effects of w binning at low redshift. In this panel the best fit values of w cross $w = -1$ twice at low redshift, an unusual feature in dark energy models. We note that the ΛCDM model is consistent with our $w(z)$ constraints for each of these binnings.

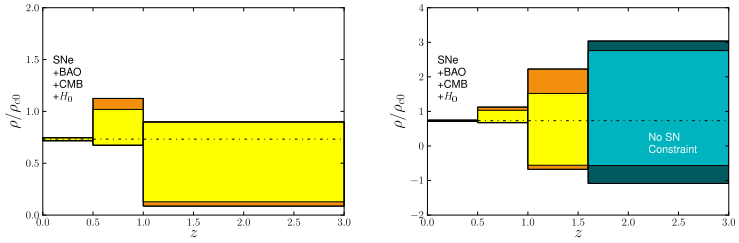

Figure 5.9. Redshift evolution of dark energy density: Constraints on $\rho(z)$ are shown as a function of redshift, where $\rho(z)$ is the density of the dark energy at a given redshift bin and assumed to be constant within the redshift bin. $\rho(z)$ is normalized by the critical density today (ρ_{c0}) and is plotted at the 68% probability level ($\Delta\chi^2 = 1$). The results were obtained assuming a flat Universe for the joint data set of SNe Ia, BAO, CMB, and H_0, with (dark/orange) and without (light/yellow) SN systematics. The two panels demonstrate different redshifts binning and have different scales.

the 15 $z > 1$ SNe Ia from the GOODS survey that pass our Union2 selection cuts have a variance-weighted RMS scatter of 0.25 ± 0.05 mag. The new sample almost doubles the weight of HST-discovered SNe Ia beyond $z = 1$. The increase provides improvements on the most difficult-to-measure parameters, those that describe the time-varying properties of dark energy: $\rho(z)$ and $w(z)$ at the higher redshifts. In particular, the supernovae from this search improve the constraint on $\rho(z)$ at redshifts $1.0z < 1.6$ by 28% (statistical errors only) and 18% (including supernova systematics) after adding the constraints from the CMB, BAO and H_0 (using the binning illustrated in the right panel of Figure 5.9). (It is more difficult to compare binned w results, as the constraints are much less gaussian and more sensitive to the location of the best fit.)

The new sample is also obtained with greater observing efficiency with HST. Considering the number of $z > 1$ SNe Ia that make the Union2 selection cuts, the yield of SNe Ia increases from a rate of one SN Ia per 43 HST orbits in the GOODS survey to one SN Ia per 22 HST orbits in this survey.

5.5.2 Splitting the sample according to host galaxy type

SNe Ia are well-standardized with a small dispersion in magnitudes across the whole class. Any clues to heterogeneous characteristics therefore offer exciting possibilities to *further* improve standardization, enhancing the use of SNe as a cosmological probe. There is now evidence from studies of large samples of SNe Ia at both low and intermediate redshifts ($0 < z \lesssim 0.8$) that SN Ia properties are related to the properties of the host. The clearest of these is the relation between light curve width and the specific star formation rate. SNe Ia in passive galaxies tend to have narrower light curves than SNe Ia that are in galaxies that are actively forming stars.

More than two-thirds of our new SNe Ia beyond $z = 0.9$ are hosted by early-type galaxies (Meyers et al. (2011)). In field surveys, such as the GOODS survey, this ratio is inverted. By combining SNe Ia from our HST Cluster SN Survey and GOODS, together with our $z > 0.9$ SNe Ia in Amanullah et al. (2010), which have HST images of the host, we can create a sample of SNe Ia that has roughly equal numbers when split according to host type. When split this way, we find that $z > 1$ SNe Ia in early galaxies rise and fall more quickly than SNe Ia in later host types, thus extending the redshift interval over which the effect is now detected. Finding that low and high redshift SNe Ia follow similar trends gives us confidence that we can use very distant events to constrain cosmological parameters. This finding is reported in more detail in Meyers et al. (2011).

There is also evidence from SNe Ia at low and intermediate redshifts for other correlations with host type. Sullivan et al. (2010) find that both β and the RMS scatter about the Hubble diagram are smallest for SNe Ia in passive galaxies. These trends suggest that dust plays a greater role in reddening and dimming SNe Ia in late-type galaxies. We examined our $z > 0.9$ sample for evidence of similar correlations using our host classification from Tables 3 and 4 of Meyers et al (2011).

After correcting SN Ia luminosities for lightcurve shape, SN Ia color and host galaxy mass (with the global values of these correction coefficients), we measure a sample dispersion of $0.14^{+0.11}_{-0.08}$ mag for SNe Ia in early-type galaxies and $0.14^{+0.06}_{-0.05}$ mag for SNe Ia in late-type galaxies. In terms of the RMS, we find 0.23 ± 0.05 mag and 0.26 ± 0.05 mag for early and late-type samples, respectively. The uncertainties are currently too large to distinguish between the two samples. Similarly for β, the errors are larger than the difference between the two samples, as seen in Table 5.5. Clearly, higher quality data of a larger number of $z > 0.9$ SNe Ia in both early and late-type galaxies are required before the trends that are seen at low redshift can be detected in high redshift samples.

We also examined the error-weighted difference in the brightness of SNe Ia in the two samples after correcting for lightcurve shape and color, but without correcting for the host-mass luminosity relation (setting $\delta = 0$) and find that SNe Ia in early-type galaxies are 0.18 ± 0.09 mag brighter. Since early-type galaxies are typically more massive than late-type galaxies, this 2σ difference, if confirmed with larger statistics, may be related to host galaxy mass.

5.5.3 Future directions with current instrumentation.

Due to the much improved sensitivity of the WFC3 IR detector, it will be feasible to measure $z > 1$ SNe with much better precision. The color measurement errors (~ 0.03 in $B - V$) can be made comparable to the color measurement errors in the SDSS supernova survey (Smith et al. 2002; Holtzman et al. 2008). Assuming that the intrinsic dispersion of SN Ia luminosities does not change with redshift, the variance weighted RMS of the WFC3 sample should be similar to that measured for the SDSS, i.e. ~ 0.14 mag. A well-observed SN Ia with WFC3 should have a statistical weight of two to three SNe Ia from the Cluster and GOODS surveys.

With a sufficient number of well-measured $z > 1$ SNe Ia with WFC3, it should be possible to search for the correlations between the properties of SNe Ia and their hosts that are seen at lower redshifts. As discussed above, current samples at $z > 1$ are too small to detect most of these differences. With the improved WFC3 photometry, only 40 SNe Ia, split evenly between early and late-type hosts, would be needed to constrain a difference in β to an uncertainty of 0.4, which is about half the difference found for lower redshift SNe Ia (Sullivan et al. 2010). These samples would be just enough to see evidence of the lower RMS for passive hosts seen by Sullivan et al. (2010).

Current WFC3 SN Ia surveys target empty fields, which means that there will be few SNe Ia in passive host galaxies. A WFC3 SN Ia survey that spends part of its time targeting $z \gtrsim 1$ clusters would ensure a better balance between host types while increasing the overall yield.

In order to investigate the figure of merit constraints possible with WFC3, we simulate a sample of 40 supernovae at redshift 1.2 and add this sample into the current compilation. As there is a hard wall at $w_0 + w_a = 0$ when including BAO and CMB data, we simply fix Ω_m, rather than including BAO and CMB data (the alternative would be to adjust the supernova magnitudes to a cosmology model far away from the wall). When adding these supernovae, the statistical figure of merit improves by 39%. By the same metric, the current cluster sample improves the figure of merit by 10%.

5.5.4 Reducing the Systematic Errors for Future Surveys

As has been stressed by several authors, systematic errors are now larger than statistical errors. To fully utilize the potential of current and future SN Ia surveys to constrain cosmology, it will be necessary to reduce these errors significantly.

The largest current source of systematic uncertainty is calibration. Calibration uncertainties can be split into uncertainties related to the primary standard, and uncertainties in instrumental zeropoints and band passes. In principle, all of these uncertainties can be reduced by establishing a network of well-calibrated standard stars and monitoring telescope system throughputs (Regnault et al. 2009). The Sloan Digital Sky Survey demonstrated that a 1% relative photometric calibration is possible with the current standard star network and system throughput monitoring (Doi et al. 2010).

The ongoing Nearby Supernova Factory (SNf) project (Aldering et al. 2002) is aiming to provide the network of standard stars. SNf will also address the systematic uncertainty due to host-mass correction since the range of host masses would become comparable to that of high redshift for the first time. Additionally, the comprehensive SN Ia spectral time series from the SNf will allow one to tackle systematic uncertainties related to modeling of the lightcurves.

In the future, recently approved experiments such as ACCESS (Absolute Color Calibration Experiment for Standard Stars Kaiser et al. 2010) and the proposed NIST STARS project (National Institute for Standards and Technology McGraw et al. 2010; Zimmer et al. 2010) are aiming to achieve sub-percent absolute flux calibration for the network of stars in the wavelength range of visible to NIR. With this network of stars and with new techniques for monitoring throughput of the telescopes (Stubbs et al. 2007), we will be able to cross-calibrate systems and reduce the systematic errors below the statistical errors.

5.6 Summary and Conclusions

This chapter presents the NICMOS photometry of the HST Cluster Supernova Search SNe, a survey run by the Supernova Cosmology Project to search for SNe Ia in fields centered on 25 distant galaxy clusters (Dawson et al. 2009). We implement new techniques to improve the accuracy of this photometry photometry. In particular, for data taken with NICMOS, which samples the rest-frame B and V-bands of $z > 1$ SNe Ia, we use a more direct, more accurate measure of the NICMOS zeropoint Ripoche et al. (2013), and we remove the residual background that persists after standard processing of NICMOS data with the `CALNICA` pipeline (Hsiao et al. 2010).

Following the procedures outlined in Chapters 2 and 4, we add our SNe Ia to the Union2 compilation. Fourteen of the 20 SNe Ia of our supernovae pass the Union2 selection cuts. Ten of them are at $z > 1$. The strategy of targeting high-redshift galaxy clusters results in factor of two improvement in the yield per HST orbit of well-measured SNe Ia beyond $z = 1$ and a factor of three to five improvement for SNe hosted by early-type galaxies. For WFC3, with its smaller field of view, the advantage of a cluster search is even greater.

We use the new Union2.1 sample to constrain the properties of dark energy. SNe Ia alone constrains the existence of dark energy to very high significance. After adding constraints from the CMB, BAO, and H_0 measurements, we provide the tightest limits yet on the evolution of dark energy with time: $w_a = 0.14^{+0.60}_{-0.76}$. Our sample improves the constraints on binned ρ by 18% (including systematics) in the difficult-to-measure high redshift bin, $1.0 < z < 1.6$. Even with a time-varying w_0-w_a model, the universe is constrained to be flat with an accuracy of 2% in Ω_k.

The results from this new cluster-hosted supernova sample point the way to the next steps that are now possible with the WFC3 on HST, an instrument that can obtain high signal-to-noise, multifilter SN Ia lightcurves at $z > 1$. The cluster approach, used in this work, would make it feasible to build a significantly larger sample at these highest redshifts,

evenly balanced between early and late-type hosts. With such a sample, we can mitigate the effects of dust and evolution that may ultimately limit constraints on time-varying w. [8]

[8] Financial support for the work presented in this chapter was provided by NASA through program GO-10496 from the Space Telescope Science Institute, which is operated by AURA, Inc., under NASA contract NAS 5-26555. This work was also supported in part by the Director, Office of Science, Office of High Energy and Nuclear Physics, of the U.S. Department of Energy under Contract No. AC02-05CH11231, as well as a JSPS core-to-core program "International Research Network for Dark Energy" and by JSPS research grant 20040003. Support for MB was provided by the W. M. Keck Foundation. The work of SAS was performed under the auspices of the U.S. Department of Energy by Lawrence Livermore National Laboratory in part under Contract W-7405-Eng-48 and in part under Contract DE-AC52-07NA27344. The work of PE, JR, and DS was carried out at the Jet Propulsion Laboratory, California Institute of Technology, under a contract with NASA. TM and YI have been financially supported by the Japan Society for the Promotion of Science through its Research Fellowship. HH acknowledges support from a VIDI grant from the Netherlands Organization for Scientific Research (NWO) and a Marie Curie International Reintegration Grant. NS, CL and SP wish to thank the support and hospitality of the Aspen Center for Physics, where much of this work was written. We would like to thank Jay Anderson, L. E. Bergeron, Ralph Bohlin, Roelof de Jong, Anton Koekemoer, Jennifer Mack, Bahram Mobasher, Adam Riess, Kenneth Sembach, and ACS and NICMOS team at Space Telescope Institute for their advice on the HST data calibration. We also thank Alex Conley for calibration discussions. Finally, we would like to thank our referee, who carefully read this work and gave valuable feedback.

Table 5.5. Constraints on standardization and cosmological parameters for subsets. M_B is the B-band corrected absolute magnitude; α, β, and δ are the lightcurve shape, color, and host mass correction coefficients, respectively. The outlier rejection is redone each time, so the totals may not add up to the whole sample. The constraints are computed including BAO, CMB, and H_0 constraints and supernova systematic errors.

Subset	Number	$M_B(h=0.7)$	α	β	δ	Ω_m	w
Whole Sample							
$z \geq 0.015$	580	$-19.321^{+0.030}_{-0.030}$	$0.121^{+0.007}_{-0.007}$	$2.47^{+0.06}_{-0.06}$	$-0.032^{+0.031}_{-0.031}$	$0.271^{+0.015}_{-0.014}$	$-1.013^{+0.068}_{-0.074}$
Correction Coefficients, Split by Redshift							
$0.015 \leq z \leq 0.10$	175	$-19.328^{+0.037}_{-0.038}$	$0.118^{+0.011}_{-0.011}$	$2.57^{+0.08}_{-0.08}$	$-0.027^{+0.054}_{-0.054}$	0.270 (fixed)	-1.000 (fixed)
$0.100 \leq z \leq 0.25$	75	$-19.371^{+0.054}_{-0.054}$	$0.146^{+0.019}_{-0.019}$	$2.56^{+0.18}_{-0.17}$	$-0.087^{+0.060}_{-0.060}$	0.270 (fixed)	-1.000 (fixed)
$0.250 \leq z \leq 0.50$	152	$-19.317^{+0.046}_{-0.046}$	$0.116^{+0.014}_{-0.013}$	$2.46^{+0.12}_{-0.12}$	$-0.042^{+0.066}_{-0.066}$	0.270 (fixed)	-1.000 (fixed)
$0.500 \leq z \leq 1.00$	137	$-19.307^{+0.048}_{-0.049}$	$0.124^{+0.019}_{-0.019}$	$1.46^{+0.19}_{-0.19}$	$0.023^{+0.060}_{-0.060}$	0.270 (fixed)	-1.000 (fixed)
$z \geq 1.000$	25	$-19.289^{+0.217}_{-0.254}$	$-0.019^{+0.072}_{-0.076}$	$3.48^{+1.13}_{-0.89}$	$-0.151^{+0.384}_{-0.446}$	0.270 (fixed)	-1.000 (fixed)
Effect of δ on w							
$z \geq 0.015$	580	$-19.340^{+0.026}_{-0.026}$	$0.123^{+0.007}_{-0.007}$	$2.47^{+0.06}_{-0.06}$	-0.080 (fixed)	$0.272^{+0.015}_{-0.014}$	$-1.004^{+0.067}_{-0.072}$
$z \geq 0.015$	580	$-19.303^{+0.031}_{-0.031}$	$0.120^{+0.007}_{-0.007}$	$2.47^{+0.06}_{-0.06}$	0.000 (fixed)	$0.271^{+0.015}_{-0.014}$	$-1.013^{+0.069}_{-0.075}$
Cosmological Results, Split by Lightcurve Color and Shape							
$c \geq 0.05$	256	$-19.387^{+0.037}_{-0.038}$	$0.118^{+0.011}_{-0.011}$	$2.77^{+0.09}_{-0.09}$	$-0.057^{+0.052}_{-0.052}$	$0.269^{+0.015}_{-0.014}$	$-1.028^{+0.077}_{-0.084}$
$c \leq 0.05$	321	$-19.323^{+0.030}_{-0.030}$	$0.125^{+0.011}_{-0.010}$	$1.29^{+0.32}_{-0.33}$	$-0.057^{+0.038}_{-0.038}$	$0.275^{+0.015}_{-0.014}$	$-0.982^{+0.069}_{-0.075}$
$x_1 \geq -0.25$	311	$-19.366^{+0.041}_{-0.041}$	$0.020^{+0.026}_{-0.025}$	$2.58^{+0.10}_{-0.10}$	$-0.004^{+0.047}_{-0.047}$	$0.269^{+0.015}_{-0.014}$	$-1.037^{+0.077}_{-0.085}$
$x_1 \leq -0.25$	269	$-19.386^{+0.044}_{-0.045}$	$0.152^{+0.021}_{-0.020}$	$2.43^{+0.08}_{-0.08}$	$-0.087^{+0.050}_{-0.050}$	$0.267^{+0.015}_{-0.014}$	$-1.045^{+0.077}_{-0.084}$
Correction Coefficients and M_B for the Large Datasets							
Hicken et al. (2009)	94	$-19.314^{+0.055}_{-0.055}$	$0.115^{+0.015}_{-0.015}$	$2.74^{+0.11}_{-0.11}$	$-0.053^{+0.098}_{-0.099}$	0.270 (fixed)	-1.000 (fixed)
Holtzman et al. (2009)	129	$-19.336^{+0.051}_{-0.051}$	$0.149^{+0.014}_{-0.013}$	$2.40^{+0.15}_{-0.14}$	$-0.061^{+0.050}_{-0.050}$	0.270 (fixed)	-1.000 (fixed)
Miknaitis et al. (2007)	74	$-19.325^{+0.078}_{-0.080}$	$0.113^{+0.037}_{-0.035}$	$2.49^{+0.17}_{-0.16}$	0.000 (fixed)	0.270 (fixed)	-1.000 (fixed)
Astier et al. (2006)	71	$-19.292^{+0.047}_{-0.048}$	$0.145^{+0.019}_{-0.018}$	$1.70^{+0.18}_{-0.18}$	$-0.023^{+0.040}_{-0.040}$	0.270 (fixed)	-1.000 (fixed)
$z > 0.9$, Split by Galaxy Host							
Early Type $z > 0.9$	13	$-19.388^{+0.139}_{-0.186}$	$0.112^{+0.139}_{-0.151}$	$3.16^{+1.84}_{-1.26}$	0.000 (fixed)	0.270 (fixed)	-1.000 (fixed)
Late Type $z > 0.9$	15	$-19.141^{+0.067}_{-0.067}$	$0.094^{+0.049}_{-0.041}$	$0.49^{+0.85}_{-0.69}$	0.000 (fixed)	0.270 (fixed)	-1.000 (fixed)

Table 5.6. Fit results on cosmological parameters Ω_M, w_0, w_a and Ω_k. The parameter values are followed by their statistical (first column) and statistical and systematic (second column) 1σ ($\Delta\chi^2 = 1$) uncertainties. For the fits including curvature and time-varying w, the confidence intervals can be quite non-gaussian and we also show $\Delta\chi^2 = 4$ confidence intervals (with and without systematics) for comparison. [a] $\Delta\chi^2 = 4.0$

Fit	Ω_m	Ω_m w/ Sys	Ω_k	Ω_k w/ Sys	w_0	w_0 w/ Sys	w_a	w_a w/ Sys
BAO+CMB+H_0	$0.267^{+0.015}_{-0.014}$		0 (fixed)		-1 (fixed)		0 (fixed)	
SNe	$0.277^{+0.022}_{-0.021}$	$0.295^{+0.043}_{-0.040}$	0 (fixed)	0 (fixed)	-1 (fixed)	-1 (fixed)	0 (fixed)	0 (fixed)
SNe+BAO+H_0	$0.288^{+0.020}_{-0.019}$	$0.314^{+0.034}_{-0.031}$	0 (fixed)	0 (fixed)	-1 (fixed)	-1 (fixed)	0 (fixed)	0 (fixed)
SNe+CMB	$0.272^{+0.017}_{-0.017}$	$0.274^{+0.024}_{-0.022}$	0 (fixed)	0 (fixed)	-1 (fixed)	-1 (fixed)	0 (fixed)	0 (fixed)
SNe+CMB+H_0	$0.262^{+0.015}_{-0.014}$	$0.258^{+0.018}_{-0.017}$	0 (fixed)	0 (fixed)	-1 (fixed)	-1 (fixed)	0 (fixed)	0 (fixed)
SNe+BAO+CMB	$0.278^{+0.014}_{-0.013}$	$0.282^{+0.017}_{-0.016}$	0 (fixed)	0 (fixed)	-1 (fixed)	-1 (fixed)	0 (fixed)	0 (fixed)
SNe+BAO+CMB+H_0	$0.271^{+0.012}_{-0.012}$	$0.271^{+0.014}_{-0.014}$	0 (fixed)	0 (fixed)	-1 (fixed)	-1 (fixed)	0 (fixed)	0 (fixed)
BAO+CMB+H_0	$0.269^{+0.015}_{-0.014}$		$0.002^{+0.005}_{-0.005}$		-1 (fixed)		0 (fixed)	
SNe+CMB	$0.278^{+0.024}_{-0.023}$	$0.298^{+0.047}_{-0.044}$	$-0.002^{+0.009}_{-0.009}$	$-0.007^{+0.013}_{-0.014}$	-1 (fixed)	-1 (fixed)	0 (fixed)	0 (fixed)
SNe+CMB+H_0	$0.260^{+0.015}_{-0.015}$	$0.255^{+0.019}_{-0.017}$	$0.005^{+0.006}_{-0.006}$	$0.005^{+0.005}_{-0.006}$	-1 (fixed)	-1 (fixed)	0 (fixed)	0 (fixed)
SNe+BAO+CMB	$0.282^{+0.015}_{-0.014}$	$0.286^{+0.018}_{-0.017}$	$-0.004^{+0.006}_{-0.006}$	$-0.004^{+0.006}_{-0.007}$	-1 (fixed)	-1 (fixed)	0 (fixed)	0 (fixed)
SNe+BAO+CMB+H_0	$0.271^{+0.013}_{-0.012}$	$0.272^{+0.014}_{-0.014}$	$0.002^{+0.005}_{-0.005}$	$0.002^{+0.005}_{-0.005}$	-1 (fixed)	-1 (fixed)	0 (fixed)	0 (fixed)
BAO+CMB+H_0	$0.263^{+0.016}_{-0.015}$		0 (fixed)		$-1.082^{+0.099}_{-0.112}$		0 (fixed)	
SNe	$0.281^{+0.067}_{-0.092}$	$0.296^{+0.102}_{-0.180}$	0 (fixed)	0 (fixed)	$-1.011^{+0.208}_{-0.231}$	$-1.001^{+0.348}_{-0.398}$	0 (fixed)	0 (fixed)
SNe+BAO+H_0	$0.309^{+0.029}_{-0.028}$	$0.320^{+0.035}_{-0.033}$	0 (fixed)	0 (fixed)	$-1.097^{+0.091}_{-0.106}$	$-1.076^{+0.117}_{-0.133}$	0 (fixed)	0 (fixed)
SNe+CMB	$0.271^{+0.018}_{-0.017}$	$0.279^{+0.025}_{-0.023}$	0 (fixed)	0 (fixed)	$-0.983^{+0.051}_{-0.056}$	$-0.955^{+0.075}_{-0.079}$	0 (fixed)	0 (fixed)
SNe+CMB+H_0	$0.262^{+0.016}_{-0.015}$	$0.259^{+0.018}_{-0.017}$	0 (fixed)	0 (fixed)	$-0.990^{+0.049}_{-0.054}$	$-1.003^{+0.064}_{-0.069}$	0 (fixed)	0 (fixed)
SNe+BAO+CMB	$0.278^{+0.014}_{-0.014}$	$0.285^{+0.018}_{-0.017}$	0 (fixed)	0 (fixed)	$-0.993^{+0.052}_{-0.055}$	$-0.951^{+0.075}_{-0.081}$	0 (fixed)	0 (fixed)
SNe+BAO+CMB+H_0	$0.272^{+0.013}_{-0.013}$	$0.271^{+0.014}_{-0.014}$	0 (fixed)	0 (fixed)	$-1.008^{+0.050}_{-0.054}$	$-1.013^{+0.068}_{-0.073}$	0 (fixed)	0 (fixed)
BAO+CMB+H_0	$0.247^{+0.020}_{-0.018}$		$-0.013^{+0.009}_{-0.007}$		$-1.391^{+0.252}_{-0.252}$		0 (fixed)	
SNe+CMB	$0.281^{+0.069}_{-0.087}$	$0.295^{+0.109}_{-0.161}$	$-0.003^{+0.034}_{-0.027}$	$-0.005^{+0.067}_{-0.041}$	$-1.007^{+0.179}_{-0.194}$	$-0.993^{+0.299}_{-0.331}$	0 (fixed)	0 (fixed)
SNe+CMB+H_0	$0.249^{+0.020}_{-0.018}$	$0.248^{+0.020}_{-0.018}$	$0.010^{+0.008}_{-0.008}$	$0.013^{+0.011}_{-0.010}$	$-0.937^{+0.063}_{-0.070}$	$-0.893^{+0.100}_{-0.109}$	0 (fixed)	0 (fixed)
SNe+BAO+CMB	$0.283^{+0.016}_{-0.015}$	$0.287^{+0.018}_{-0.017}$	$-0.004^{+0.007}_{-0.007}$	$-0.002^{+0.008}_{-0.008}$	$-1.012^{+0.058}_{-0.062}$	$-0.975^{+0.094}_{-0.098}$	0 (fixed)	0 (fixed)
SNe+BAO+CMB+H_0	$0.272^{+0.013}_{-0.013}$	$0.272^{+0.015}_{-0.014}$	$0.002^{+0.006}_{-0.006}$	$0.002^{+0.007}_{-0.007}$	$-1.006^{+0.056}_{-0.060}$	$-1.003^{+0.091}_{-0.095}$	0 (fixed)	0 (fixed)
SNe+CMB	$0.273^{+0.022}_{-0.020}$	$0.281^{+0.043}_{-0.028}$	0 (fixed)	0 (fixed)	$-1.006^{+0.165}_{-0.182}$	$-0.993^{+0.263}_{-0.307}$	$0.11^{+0.75}_{-0.77}$	$0.17^{+1.08}_{-1.19}$
SNe+CMB+H_0	$0.259^{+0.017}_{-0.016}$	$0.256^{+0.019}_{-0.017}$	0 (fixed)	0 (fixed)	$-0.928^{+0.142}_{-0.143}$	$-0.880^{+0.222}_{-0.222}$	$-0.29^{+0.60}_{-0.66}$	$-0.52^{+0.86}_{-0.98}$
SNe+BAO+CMB	$0.278^{+0.014}_{-0.014}$	$0.284^{+0.018}_{-0.017}$	0 (fixed)	0 (fixed)	$-1.052^{+0.126}_{-0.120}$	$-1.013^{+0.183}_{-0.173}$	$0.30^{+0.48}_{-0.62}$	$0.26^{+0.57}_{-0.74}$
SNe+BAO+CMB+H_0	$0.271^{+0.013}_{-0.013}$	$0.270^{+0.015}_{-0.014}$	0 (fixed)	0 (fixed)	$-1.021^{+0.123}_{-0.117}$	$-1.046^{+0.179}_{-0.170}$	$0.07^{+0.49}_{-0.60}$	$0.14^{+0.60}_{-0.76}$
SNe+CMB	$0.177^{+0.086}_{-0.093}$	$0.190^{+0.208}_{-0.154}$	$0.075^{+0.065}_{-0.128}$	$0.073^{+0.115}_{-0.141}$	$-0.988^{+0.176}_{-0.202}$	$-0.969^{+0.284}_{-0.345}$	$0.90^{+0.26}_{-3.88}$	$0.89^{+0.43}_{-5.25}$
SNe+CMB+H_0	$0.247^{+0.020}_{-0.018}$	$0.255^{+0.026}_{-0.024}$	$0.014^{+0.026}_{-0.012}$	$0.036^{+0.016}_{-0.032}$	$-0.998^{+0.158}_{-0.224}$	$-1.106^{+0.355}_{-0.149}$	$0.36^{+0.85}_{-0.86}$	$1.05^{+0.20}_{-1.75}$
SNe+BAO+CMB	$0.283^{+0.019}_{-0.017}$	$0.286^{+0.022}_{-0.023}$	$-0.004^{+0.017}_{-0.010}$	$-0.001^{+0.037}_{-0.013}$	$-1.010^{+0.169}_{-0.178}$	$-0.997^{+0.266}_{-0.293}$	$-0.01^{+1.04}_{-1.05}$	$0.13^{+1.16}_{-1.57}$
SNe+BAO+CMB+H_0	$0.270^{+0.014}_{-0.013}$	$0.274^{+0.016}_{-0.015}$	$0.025^{+0.008}_{-0.008}$	$0.027^{+0.012}_{-0.011}$	$-1.218^{+0.069}_{-0.072}$	$-1.198^{+0.100}_{-0.112}$	$1.21^{+0.10}_{-1.14}$	$1.19^{+0.13}_{-0.13}$
SNe+BAO+CMB+H_0 [a]	$0.270^{+0.029}_{-0.026}$	$0.274^{+0.032}_{-0.029}$	$0.025^{+0.016}_{-0.035}$	$0.027^{+0.026}_{-0.036}$	$-1.218^{+0.425}_{-0.147}$	$-1.198^{+0.293}_{-0.227}$	$1.21^{+0.19}_{-2.49}$	$1.19^{+0.27}_{-2.40}$

		$z < 0.5$	$0.5 < z < 1.0$	$1.0 < z < 1.6$	$z > 1.6$ [a]
w(z)	Stat Only:	$-1.013^{+0.067}_{-0.069}$	$-0.78^{+0.58}_{-0.68}$	$-3.7^{+2.2}_{-4.4}$	< 0.18
	w/ Sys:	$-1.006^{+0.110}_{-0.113}$	$-0.69^{+0.80}_{-0.98}$	$-3.9^{+3.2}_{-8.2}$	< 0.24
$\rho_{\rm DE}(z)/\rho_{c0}$	Stat Only:	$0.732^{+0.013}_{-0.014}$	$0.85^{+0.18}_{-0.17}$	$0.23^{+1.29}_{-0.79}$	$0.9^{+1.9}_{-1.5}$
	w/ Sys:	$0.731^{+0.014}_{-0.015}$	$0.88^{+0.24}_{-0.21}$	$0.33^{+1.90}_{-1.00}$	$0.7^{+2.4}_{-1.8}$

Table 5.7. Constraints on redshift binned equation of state w and density ρ (normalized by the current critical density). The constraints are computed including SNe, BAO, H_0, and CMB data. This redshift binning corresponds to the middle panel of Figure 5.8 and the right panel of Figure 5.9 . [a]We note that the weak constraints in these bins come mostly from the CMB (which tells us that the early universe was matter-dominated) and are only indirectly constrained by supernovae.

CHAPTER 6

Mingus: A $z = 1.71$ SN Ia

There was one probable high-redshift SN Ia in GOODS unpublished after an SCP search of GOODS. Its photometric redshift placed it at $z \sim 1.6$, but the spectrum and exact redshift were considered inconclusive. A recent serendipitous archival *HST* Wide Field Camera 3 (WFC3) grism spectrum contributed a key element of its confirmation by giving a host-galaxy redshift of 1.713 ± 0.007. With the redshift of the probable host galaxy known, the other observations could be interpreted. The *HST* Advanced Camera for Surveys (ACS) spectrum has almost negligible contamination from the host or neighboring galaxies. Although the rest frame sampled range is too blue to include any Si II line, a principal component analysis allowed confirmation as a Type Ia supernova with 92% confidence. Until 2013, this was the most distant SN Ia with spectroscopic confirmation. It remains the most distant Ia with a precision color measurement, allowing for tests of population drift (although limited by the sample size of one). We present the ACS WFC and NICMOS 2 photometry and ACS and WFC3 spectroscopy. Our derived supernova distance agrees with the prediction of ΛCDM, and the precision of this distance is a testament to the capabilities of *HST*.[1]

6.1 Introduction

Over the past 15 years, *HST* has played an integral role in measuring cosmological parameters through the Type Ia supernova Hubble diagram (Perlmutter et al. 1997; Garnavich et al. 1998; Riess et al. 1998; Perlmutter et al. 1999; Knop et al. 2003; Riess et al. 2004, 2007; Amanullah et al. 2010; Suzuki et al. 2012). With its low background and diffraction-limited imaging, *HST* is capable of measuring supernovae at redshifts that are very difficult from the ground. Measuring very distant supernovae breaks degeneracies in the lower-redshift Hubble diagram, enabling us to probe the nature of dark energy at redshifts above $z \sim 0.5$ independently of its low-redshift behavior. In this chapter, I present the most distant cosmologically useful supernova to date and show that even at this distance, *HST* can

[1] This chapter was previously published as Rubin et al. (2013).

still make measurements with precision.

6.2 Search and Followup

SN SCP-0401 was found in the GOODS North Field (Dickinson et al. 2003) as part of a supernova survey with sets of supernova followup that were alternated between the Supernova Cosmology Project (SCP)[2] and the Higher-Z SN Search Team[3]. Four epochs of ACS F850LP and F775W (these are z and i-band filters) observations were obtained, with a cadence of $\sim$ 7 weeks. In the first cadenced epoch (2004 April 3), this candidate was discovered in the reference-subtracted[4] F850LP image with a signal-to-noise ratio of 9 (Vega magnitude 25.2, see details of photometry in Section 6.4). In the concurrent F775W image, it had a signal-to-noise ratio of 2 (Vega 26.5). Because the red observed color implied a possible very-high-redshift SN Ia, we followed it with ACS F850LP and Near Infrared Camera and Multi-Object Spectrometer (NICMOS 2) F110W and F160W (very broad J and H-band filters) photometry, and ACS G800L grism spectroscopy[5].

The sky in the vicinity of the SN is shown in Figure 6.1[6]. The likely host is the late-type galaxy at redshift 1.713 (see Section 6.3.2) centered $0.8''$ away. This corresponds to only 7 kpc if the SN and galaxy are at the same distance. Light from this galaxy is visible at the location of the supernova and no other galaxies down to a magnitude limit of AB ~ 26.5 F775W are within $3.5''$. In the F775W and redder data, this galaxy has two cores, indicating a possible merger. The consistency of the colors of these cores (always < 0.3 mag, typically < 0.1) over the wide range of 4350Å to 16000Å makes it extremely likely that these cores are at the same redshift.

6.3 Spectroscopy

6.3.1 ACS Grism Observations of SN and Host

We obtained eleven orbits of spectroscopy with the ACS G800L grism nine days after the discovery epoch. The light curve fit (Section 6.5.1) indicates that the spectrum was taken 2 ± 3 rest-frame days after rest-frame B-maximum. We extracted spectra for the likely host and SN with aXe (Kümmel et al. 2009). No conclusive features or lines were apparent in the spectrum of the galaxy, nor did the two cores give significantly different spectra.

[2]HST GO Program 9727

[3]HST GO Program 9728

[4]The reference images for this field come from Program ID 9583.

[5]This supernova is referred to in the HST archive as SN150G and elsewhere by its nickname "Mingus" (Gibbons et al. 2004).

[6]In addition to the other datasets, data from HST GO Program 10339 was used for this figure and the subsequent host-galaxy analysis.

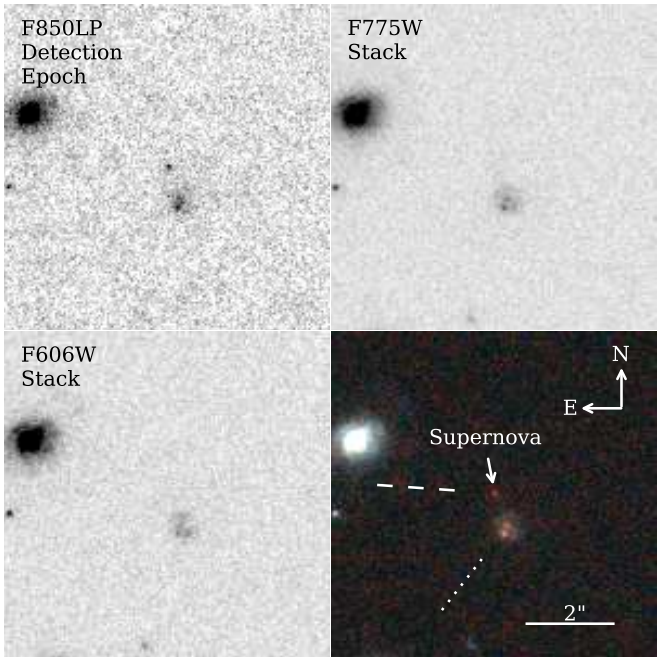

Figure 6.1. ACS images of the supernova location. The lower right panel shows a three-component color image composed from: an F606W stack (blue), F775W stack (green), and the F850LP SN detection epoch (red), which are shown in the remaining panels. The lines indicate the dispersion direction in ACS (dashed) and WFC3 (dotted) spectroscopy. The supernova coordinates are 12:37:09.5 +62:22:15.5 (J2000.0).

6.3.2 Wide Field Camera 3 Grism Observations of the Host

As a fortunate coincidence, two orbits of WFC3 IR G141 grism spectroscopy were taken in this region of GOODS North on 2010-09-26[7]. Although the F140W direct image missed the host galaxy, the grism dispersed the host into the field of view. Matching objects between ACS F850LP imaging and the direct image allowed us to compute the position of the host galaxy for use by aXe.

The host galaxy spectrum is shown in Figure 6.2, along with the best-fit template derived by scaling principal components of SDSS spectra (Aihara et al. 2011). Only one feature is detected at very high statistical significance: an emission feature at 13600Å. The only reasonable match to the spectrum between redshift 1.0 and 2.0 is one centered on redshift 1.713. The emission feature is then made up of a blend of the [OIII]$\lambda\lambda$ 4959, 5007Å doublet. No other emission lines are required to appear in the wavelength range of either grism spectrum for this to be a credible template match. We also see possible absorption from Hγ and Hβ (4340Å, and 4861Å rest-frame wavelengths, respectively), but at lower statistical significance. As we are not sure which core (or both) emit the [OIII], we take a conservative $0.1''$ separation $= 36$Å systematic uncertainty in the observer-frame wavelength of the lines. This translates to a 0.007 uncertainty on the redshift, which dominates

[7]Data from HST GO Program 11600

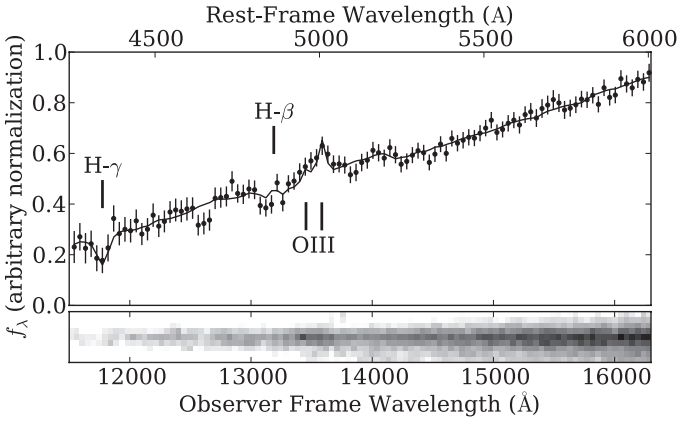

Figure 6.2. Upper panel: Extracted WFC3 IR spectrum of the likely host galaxy with template fit using SDSS galaxy principal components (solid line). The best-fit (and only reasonable) redshift is 1.713. We note that including the ACS grism data for the host (5500Å to 10000Å) has no effect on the fit. Lower panel: 2D WFC3 spectrum, spanning 103 pixels. Some of the flux visible at longer wavelengths than the features is contamination.

the other sources of uncertainty.

6.3.3 Typing

aXe resamples the grism data, correlating neighboring flux measurements. This can be seen by eye in the spectrum (points with errorbars in Figure 6.3), that is, the difference between neighboring flux measurements is generally smaller than one would expect from the indicated error bars. These positive correlations reduce the statistical significance of spectral features, so a quantitative understanding of these correlations is crucial. By examining blank sky, we find that the correlation between neighboring errors is 0.4 (and confirm the accuracy of the on-diagonal errors reported by aXe). The weight of the spectrum scales with the correlation between neighbors (ρ) as $1/(1+2\rho)$ (see Appendix A.2 for the derivation). The weight of the spectrum is thus reduced by 44% compared to a naive reading of the aXe error bars. All χ^2 values in this work are computed using a covariance matrix containing nearest-neighbor correlations.

As our supernova spectrum misses the Si II $\lambda6355$ (Wheeler & Levreault 1985; Uomoto & Kirshner 1985; Panagia 1985) and Si II $\lambda4130$ (Clocchiatti et al. 2000) lines normally used for confirming SNe Ia, we use statistical methods for classifying SN SCP-0401.

We first begin by collecting the comparison rest-frame UV spectra available to us. A useful list of SNe observed with the *HST* and the *International Ultraviolet Explorer* (*IUE*) is Panagia (2003), with an updated list, including *Swift*-observed, in Brown (2009). We obtained *IUE* spectra and *HST* spectra from the Mikulski Archive for Space Telescopes (MAST)[8], and Swift spectra from the SUSPECT archive[9]. More recent spectra were found

[8] http://archive.stsci.edu/

[9] http://suspect.nhn.ou.edu

by searching MAST, others came from the literature. A summary of all data is given in Table 6.1; we collect 94 spectra in total from 33 SNe, all within ~ 2 weeks of B or V-maximum (whichever is quoted in the literature).

Our goal is to compare these spectra to the spectrum of SN SCP-0401, extracting a probability of matching for each. Unfortunately, most of the data are from the IUE, and only extend to ~ 3300Å observer-frame, rather than 3600Å as we have with SN SCP-0401 (a related issue is the presence of noise in the comparison spectra). This limitation complicates the comparison of these spectra to SN SCP-0401.

Another, more subtle, issue is also relevant. We note that simply converting a χ^2 per degree of freedom to a probability (e.g., Rodney et al. 2012) is never appropriate when comparing different models to the same data. $\Delta\chi^2$ values (the difference in χ^2 between models) can be converted into probabilities, but this requires knowing the dimensionality of the parameter space[10].

We can address both issues (limited coverage and estimating dimensionality) by performing a principal component analysis of all spectra in the UV. The details are discussed in Appendix A.3. After computing the mean and first two principal components, we can compute a $\Delta\chi^2$ between SN SCP-0401 and every other spectrum in turn. We fit SN SCP-0401 and another spectrum with the projections onto the components constrained to be the same (we allow them to have different normalizations); this gives us a joint χ^2. We then subtract the χ^2 values for SN SCP-0401 and the other spectrum when they are allowed to have different projections. This $\Delta\chi^2$ value gives us the probability that the SNe have different true projections given the observed data. We then subtract this value from 1 to get a "matching probability."

These results are summarized in Table 6.2. Thirteen SNe have matching probabilities above 0.05; twelve of these (and all of the top six) are SNe Ia. The average matching probability of a SN Ia is 41.8%; the average probability for a core-collapse SN is 3.4%. The probability of SN SCP-0401 being a Ia from the spectrum alone (assuming an equal fraction of SNe Ia and CC SNe; see below) is therefore $41.8/(3.4+41.8) = 92\%$. In Figure 6.3, we plot the best-matching spectrum of the five best-matching SNe of each type. Of the CC SNe, only SN1983N is a credible match spectroscopically, although this supernova was two magnitudes fainter at maximum than a typical SN Ia (Prabhu 1985).

We now must evaluate the relative ratio of CC SNe to SNe Ia at redshift 1.713 for SNe with comparable brightness to SNe Ia. Bazin et al. (2009) present both photometrically and spectroscopically classified SNe from the Supernova Legacy Survey and the associated absolute magnitudes (their definition is similar to a V-band AB absolute magnitude). For SNe with brightness comparable to most SNe Ia (~ -19), they find a SN Ia to CC rate of $\sim$5-to-1 at redshift 0.3. However, at redshift 1.713, the star-formation rate is ~ 5 times higher than at redshift 0.3 (Hopkins & Beacom 2006), raising the core-collapse rate by approximately the same value. The SN Ia rate is equal to within the error bars (tens of

[10] A well-known example is the 68.3% confidence interval, which is given (in the assumption of Gaussian errors and an approximately linear model) by $\Delta\chi^2 < 1$ in one dimension and $\Delta\chi^2 < 2.30$ in two.

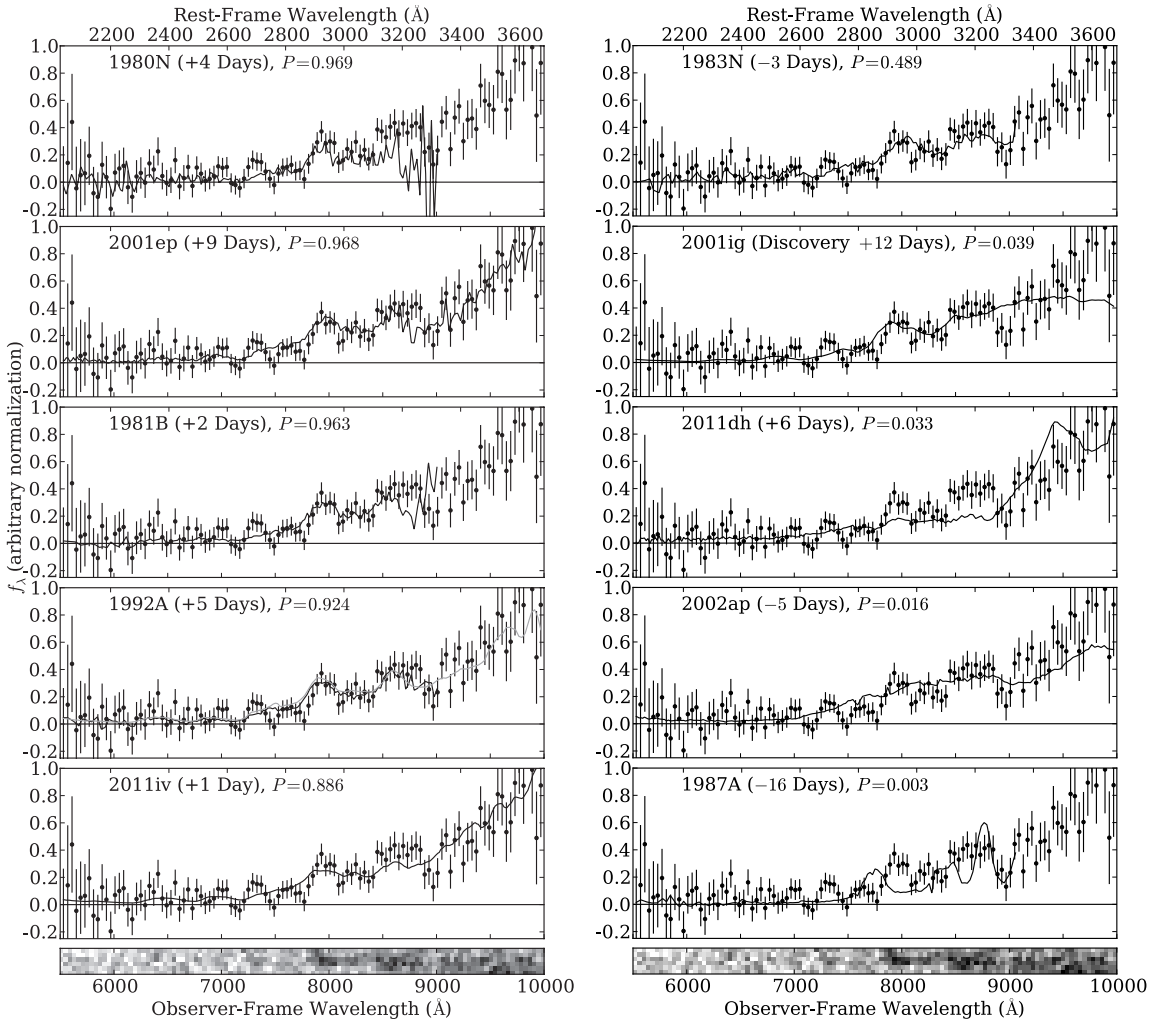

Figure 6.3. Each panel shows a comparison between SN SCP-0401 (points with error bars) and another SN. The five best-matching comparison SNe Ia are shown in the left panels; the five best-matching comparison CC SNe are shown in the right panels. For each comparison SN, only the best-matching epoch is shown. The best visual match is SN1992A (left, third from top); we have overlaid additional data from a phase of +8 days that covers the full rest-frame wavelength range (light grey), showing that the match continues for the full spectrum. Of the 17 CC SNe (the best five of which are shown here), only SN1983N is a possible match, although as noted in the text, this SN is two magnitudes fainter at max than a typical SN Ia. Bottom panels: 2D SN SCP-0401 spectrum, spanning 112 pixels. Some of the flux visible in the very reddest wavelengths is contamination from a nearby galaxy.

percent) at redshift 0.3 and redshift 1.713 (Barbary et al. 2012b), so both classes of SNe are comparably common at this redshift. We therefore retain the 92% confidence that was derived ignoring the rates.

It is also encouraging that the spectrum of SN SCP-0401 matches the theoretical SN Ia spectra of Lentz et al. (2000) derived from the W7 model (Nomoto et al. 1984) (see Table

6.2). The best match is for the unscaled heavy element abundance (that is, no change from W7).

As a less-likely possibility, we investigate the possibility that the nearby galaxy is not the host. We use the spectra with broad wavelength coverage (almost all of those in Table 6.1 except the IUE spectra) and match them against SN SCP-0401 with the redshift floating. It is reassuring that the best match is a Ia (SN1992A) at redshift 1.72, at least for this limited set of SNe.

This analysis may turn out to be conservative. In the Lick Observatory Supernova Search volume-limited sample (Li et al. 2011), the ratio of SNe II to SNe Ibc is about 3-to-1, similar to what we have in our sample of spectra. However, the SNe Ibc are fainter on average than SNe II; in Bazin et al. (2009), the ratio appears to be higher (in the luminosity range of SNe Ia). If SNe Ibc are the only plausible non-Ia match to SN SCP-0401, then our confidence that SN SCP-0401 is a SN Ia may get stronger simply from revised rates. It is also possible that no SNe Ibc are credible matches to SN SCP-0401, and more wavelength coverage of SN1983N would have shown us that it does not match. In the future, additional core-collapse comparison spectra will resolve this question.

6.4 SN Photometry

We used similar techniques for the SN photometry as were used in Chapter 5; these are summarized below. In the spirit of "blinded" analysis, we finalize the photometry before looking at the light curve or distance modulus. We give our photometry in Table 6.3.

6.4.1 ACS Photometry

We begin by iteratively combining each epoch with MultiDrizzle (Fruchter & Hook 2002; Koekemoer et al. 2002) and aligning all epochs. Aperture photometry with a three-pixel radius ($0.15''$) is computed for all epochs, with the zero level set by the many epochs without the SN. As the pixel values in the resampled images are correlated, the background error is derived empirically (by placing many three-pixel radius apertures in object-free parts of the image), and the Poisson error of the aperture flux is added in quadrature. We use a zeropoint of 23.909 (Vega = 0) for the F850LP data, derived in Suzuki et al. (2012) along with the effective throughput, and 25.291 (Vega = 0) for the F775W data, from Bohlin (2007b).

6.4.2 NICMOS Photometry

The optimal radius for aperture photometry with NICMOS is approximately 1 pixel ($0.076''$), precluding any resampling of the NICMOS images. Following Chapter 5, we therefore performed the NICMOS photometry using analytic galaxy models (one for each filter) which were convolved with their PSFs and resampled to match the images. The

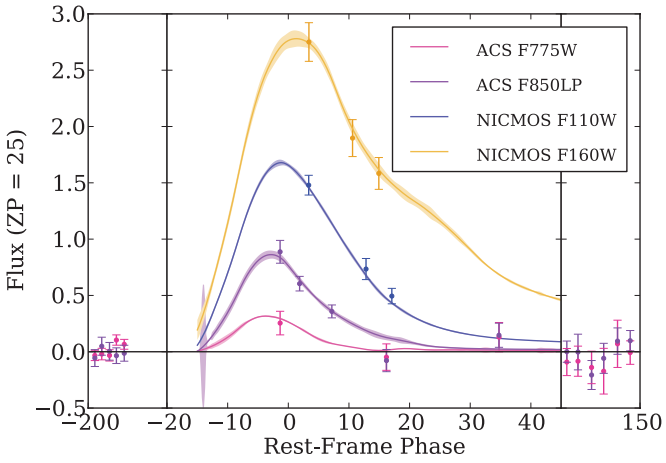

Figure 6.4. SALT2-2 fit to the photometry. To illustrate the quality of the F775W data, the F775W photometry is shown in this plot; as it is too blue for SALT2-2 to fit reliably, these data are not used in any analysis. The error snakes represent the model errors of SALT2-2.

supernova position and fluxes were modeled simultaneously using PSFs generated for each spectral energy distribution (SED) and band. As there are two cores for this galaxy, we use two azimuthally symmetric elliptical models (with radial variation described by splines) to model the cores (as the SN is reasonably far off-core, this is mainly needed to get the centroid of the model correct for each image). The remaining azimuthal asymmetry of the galaxy was modeled with a two-dimensional second-order spline, with nodes spaced every five pixels ($0.38''$).

While optimizing the host-galaxy model (e.g., the spline-node spacing), we use simulated SNe at dozens of positions at comparable separation from the galaxy to check for any bias or unexplained variance in the photometry. No bias is seen at the 0.01 magnitude level in either band. However, the final epoch in F110W shows a small amount of unexplained variance (χ^2/degree of freedom 1.35) for the recovered fluxes around the true flux, possibly due to slight South Atlantic Anomaly persistence. We rescale the photometry error bar for this epoch to make the χ^2 per degree of freedom 1.

We used a NICMOS F110W zeropoint of 23.757 AB (23.029 Vega = 0) (Ripoche et al. 2013) and a NICMOS F160W zeropoint of 22.16 (Vega = 0) (see discussion in Section 4.3.1).

6.5 Analysis

6.5.1 Light-Curve Fit

We fit the light curve of the SN with SALT2-2 (Guy et al. 2010), a principal component expansion of type Ia supernova SEDs. The fit parameters are the date of rest-frame B-band

maximum, the magnitude at maximum (m_B), the broadband color (c, similar to a rest-frame $B-V$ color), and light-curve width (x_1, the next supernova principal component after color). We find $m_B, x_1, c = (26.14, 0.2, -0.10)$. The best-fit template is shown in Figure 6.4. The corrected-distance-modulus statistical error is only 0.15 mag. (This value does not include Hubble diagram dispersion that cannot be removed with the magnitude corrections detailed in Section 6.6.) As we lack a measurement on the rise of SN SCP-0401, the date-of-maximum constraints are asymmetric. We derive the distance modulus uncertainty by sampling from the true corrected distance modulus distribution (by running a Metropolis-Hastings Monte Carlo using the SALT2-2 model). There is a fortuitous cancellation between the date of maximum and the light curve parameters: moving the date of maximum earlier brightens the peak magnitude while increasing the light-curve width and making the color slightly bluer. After applying the corrections in Section 6.6, the corrected-magnitude likelihood is well-constrained (and is Gaussian).

6.5.2 Host Stellar Mass

As SALT2 Hubble residuals are correlated with host-galaxy stellar mass (Kelly et al. 2010; Sullivan et al. 2010), we must estimate the host mass for SN SCP-0401. We used a Z-PEG (Le Borgne & Rocca-Volmerange 2002) fit to broad-band galaxy photometry, similar to the methods used in those papers. Using aperture photometry with a $1''$ radius, and zero-points from Bohlin (2007b), we derived the following AB magnitudes for the host galaxy: 25.7 (F435W), 25.2 (F606W), 24.2 (F775W), 23.4 (F850LP), and 20.0 (F160W, Vega = 0). To accurately fit all photometry, Z-PEG requires a template with age 5 Gyr, which is older than the universe at this redshift (4 Gyr). The stellar mass confidence interval when enforcing an age-of-the-universe constraint is essentially contained inside the confidence interval when allowing age to be unconstrained. To be conservative, we do not enforce this constraint, obtaining a $\log_{10}$ stellar mass of $11.2^{+0.1}_{-0.4}$, easily putting this galaxy inside the high-mass ($> 10^{10} M_{\odot}$) category.

6.5.3 Systematic Errors

Calibration

Fitting an accurate corrected magnitude requires fitting an accurate color (c). The farther apart the filters used are in wavelength, the less (uncorrelated) calibration uncertainties affect the derived c, and therefore the derived corrected magnitude. For a given range of wavelength coverage, measuring a supernova in more filters will also decrease the sensitivity of the fit to any given miscalibration (again assuming independent calibration uncertainties for the data in each filter). With three passbands within the SALT2-2 range and a long wavelength baseline, the SN distance modulus we derive from the light curve fit is more resilient against calibration uncertainties than most high-redshift SNe distances. Our distance modulus is most sensitive to the F160W zeropoint, with $\partial\mu/\partial$(F160W zeropoint)

=1.5 (that is, a change in the F160W zeropoint of 0.01 magnitudes changes the corrected magnitude by 0.015), a factor of two better than is typically achieved with only one color. The other calibration uncertainties combine to a systematic error of only ~ 0.01 mag on the distance modulus.

The NICMOS 2 F160W data are affected by a count-rate nonlinearity of 0.026 ± 0.015 mag/dex (de Jong et al. 2006), which adds an effective zeropoint uncertainty of 0.06 magnitudes at the flux level of high-redshift SNe, assuming a power-law dependence of the non-linearity over the full range of flux between the standard stars and the SNe (4-5 dex). Based on the F110W results of Ripoche et al. (2013), we add an uncertainty of 0.03 magnitudes to account for possible deviation from a power law. We will improve this uncertainty with a future recalibration of the F160W non-linearity using the techniques in Ripoche et al. in a future paper.

Malmquist Bias

Most SNe Ia at redshift 1.71 would be too faint to be found by the search, even at maximum brightness. Malmquist bias is therefore present. Most of this bias is taken out by making the corrections we describe in Section 6.6, but some bias remains. (If it were possible to perfectly correct SNe, such that all SNe were equally bright after correction, no Malmquist bias would remain.) A simple simulation (detailed further in Rubin et al., in prep) that selects SNe from the parent distribution and determines if they could be found at redshift 1.71 allows us to estimate that this remaining Malmquist bias is about 0.08 mag.

If there are SNe at high enough significance to find, but not to get a spectrum of, there may be additional Malmquist bias. We investigate this possibility here using the observed spectrum of SN SCP-0401. The faintest supernova we could have found would be S/N ~ 5, rather than S/N ~ 9. Increasing the noise in the spectrum by a factor 1.8 allows more supernovae of both types to match the spectrum. The net effect is to lower the confidence of being a Ia to 86%, in which case we would still use the supernova for cosmological analysis. (In Section 2.3.3, we showed that the analysis is robust to this level of non Ia contamination.)

The largest contributors to the Malmquist bias uncertainty are the magnitude cut for the search (which we take to be uncertain at the 0.2 mag level) and the uncorrected residual dispersion of SNe at redshift 1.71 (which we take to be 0.20 ± 0.05 (see discussions below in Sections 6.5.3 and 6.6). Each of these contributes about 0.03 magnitudes to the Malmquist bias uncertainty. Therefore, the total uncertainty, which would correlate from supernova-to-supernova were there others like it, is about 0.04 mag.

Lensing

The bright spiral galaxy $3.5''$ away from the supernova (visible to its upper left in Figure 6.1) is at redshift 0.64 (Cowie et al. 2004), and is thus a potential source of gravitational

magnification for the supernova. Here, we provide a rough estimate of the size of this effect.

As with the host galaxy, we used Z-PEG to derive the stellar mass. For this larger (apparent size) galaxy, we used a $1.5''$ radius, and obtained the following AB magnitudes: 23.5 (F435W), 22.7 (F606W), 21.8 (F775W), and 21.5 (F850LP). We use the Z-PEG stellar mass of $4 \times 10^{10} M_{\odot}$ with the relation between stellar mass and halo mass from Guo et al. (2010) to derive the total mass of the halo, $1.4 \times 10^{12} M_{\odot}$. Assuming a singular isothermal sphere model, with $M_{200} \sim M_{\rm halo}$, we find a magnification of 1.08 (using the Navarro et al. (1996) NFW profile provides virtually the same answer). This number is not the magnification of the supernova; had the lensing galaxy not been there, the supernova would likely be slightly de-magnified (compared to a filled-beam distance modulus). Holz & Linder (2005) find that the scatter due to lensing is approximately $0.093z = 0.16$ magnitudes at this redshift. We include this uncertainty in our distance modulus error (as noted below) and see no evidence that SN SCP-0401 is magnified or de-magnified by more than this.

The mean magnification of supernova fluxes is zero at a given redshift. (Selection effects can bias the observed SNe to higher magnification, but Jönsson et al. (2006) see no evidence of this in the Riess et al. (2004) sample.) However, we fit our cosmological constraints in log(flux) (magnitudes), where the mean magnification is not zero (as supernova fluxes are roughly log-normally distributed, and we use least-squares fitting, fitting in magnitudes is appropriate). We evaluate the lensing bias from working with magnitudes using the distributions of Wang et al. (2002) and find it to be 0.01 mag (biased faint). In principle, most of this bias is well-understood (from knowledge of the corrected supernova luminosity distribution and the lensing distribution) and could be removed.

6.6 Conclusions

We apply the corrections detailed in Chapter 5 to obtain a SALT2-2 distance modulus corrected for x_1, c, and host mass, reproduced here.

$$\mu_B = m_B + \alpha \cdot x_1 - \beta \cdot c + \delta \cdot P(m_\star^{\rm true} < m_\star^{\rm threshold}) - M_B \,, \tag{6.1}$$

where α is the light-curve-width-correction coefficient, β is the color-correction coefficient, δ is the host-mass-correction coefficient, and M_B is the ($h = 0.70$) absolute B-magnitude. In addition to the propagated lightcurve fit uncertainties, we add in quadrature the distance modulus scatter due to lensing (above) and $\sigma_{\rm sample}$, the error needed to get a χ^2 per degree of freedom of 1 around the Hubble line for the GOODS SNe. We take $M_B = -19.09$, $\alpha = 0.14$, $\beta = 3.1$, $\delta = -0.07$, $\sigma_{\rm sample} = 0.11$ (Rubin et al., in prep) and find a distance modulus (no magnification or Malmquist bias correction) of 45.57 ± 0.24 statistical, $\pm \sim 0.1$ systematic. This is fully consistent with the value of 45.60 predicted from a flat $\Omega_m = 0.27$ ΛCDM universe. Figure 6.5 shows the Hubble diagram from Chapter 5 with SN SCP-0401 and Primo (Rodney et al. 2012) added. As SALT was updated from version 2-1 to 2-2 after this plot was made, we refit SN SCP-0401 with the older SALT2-1 for the purposes

of making this figure. The change in distance modulus is 0.01 magnitudes between the two versions.

The quality of these results at this extremely high redshift sets a new standard. Most SNe at $z > 1.5$ have incomplete or not cosmologically useful lightcurves (SN 1997ff from Riess et al. (2001), 2003ak from Riess et al. (2004), Subaru-Discovered SNe from Graur et al. (2011)). Primo (Rodney et al. 2012) has a lower-precision color measurement than SN SCP-0401, although its better x_1 measurement (by virtue of pre-maximum data) gives it a comparable distance modulus error. All of these previous SNe had no spectroscopic confirmation, or in the case of Primo, a host-contaminated spectrum providing inconclusive confirmation.

It has appeared likely that SNe at this redshift could be measured with sufficient color precision to allow a direct comparison to lower-redshift SNe. With this one SN, we now see a first example of this in Figure 6.6, a plot with a baseline of almost ten billion years (the approximate look back time of this SN). The Hubble residual of SN SCP-0401 is compatible with the x_1 and c corrections derived at lower redshift (or a deviation from ΛCDM of the Hubble diagram cancels the change in the relations). This figure also shows that the fitted x_1 and c of SN SCP-0401 are well within the distribution of lower-redshift supernovae that could be found in this F850LP search at redshift 1.71 (black points).

While the spectrum, light-curve corrections, and distance modulus of SN SCP-0401 so far indicate compatibility with ΛCDM and little evolution, this single SN by itself can only provide weak constraints. It does, however, begin to illustrate what can be accomplished if one adds a whole population of such well-measured SNe at the very-high-redshift end of the Hubble diagram. Building this sample can now be done much more efficiently since the *HST* WFC3 greatly improved throughput makes these high S/N measurements easier, so this goal is now within reach. [11]

[11] We would like to thank Henry Ferguson of the Space Telescope Science Institute for ensuring fast turnaround for these time-critical observations. We would also like to thank Bahram Mobasher for providing photometric redshifts for the host galaxies of our candidates. The archival WFC3 data used to obtain the host redshift were taken under HST GO Program 11600, PI Benjamin Weiner. We would like to thank the SUSPECT archive for their part in assembling our collection of spectra. Finally we thank the anonymous referee, whose feedback greatly improved this manuscript.

Financial support for the work presented in this chapter was provided by NASA through program GO-9727 from the Space Telescope Science Institute, which is operated by AURA, Inc., under NASA contract NAS 5-26555. This work was also partially supported by the Director, Office of Science, Department of Energy, under grant DE-AC02-05CH11231.

Table 6.1. Sources of data for the principal component analysis, indicating the SN type, source, and phase (phase range for many collected spectra from the same SN). *IUE* is the *International Ultraviolet Explorer*, *HST* FOS/ STIS are the *Hubble Space Telescope* Faint Object Spectrograph and Space Telescope Imaging Spectrograph, and *Swift* UVOT is the *Swift* Ultraviolet/Optical Telescope. The *IUE* spectra extend blueward of ~ 3300Å rest frame, the *HST*, *Swift*, and Lentz spectra cover the whole wavelength range, the spectrum of 1997ap covers redward of ~ 2700Å rest frame, and the Ellis composite covers redward of ~ 2800Å rest frame.

SN	Type	Type Reference	Phase	Date of Maximum Reference	Source and Program ID
1978G	II	Ward et al. (1978)	Discovery +5, +16	Ward et al. (1978)	*IUE* OD7AB
1979C	II	Mattei et al. (1979)	+6 to +16	de Vaucouleurs et al. (1981)	*IUE* CVBCW, ESATO, UKTOO, CVBCW
1980K	II	Kirshner & Bryan (1980)	~ 0	Buta (1982)	*IUE* VILSP, CVBCW, UKTOO
1980N	Ia	Blanco et al. (1980)	-1 to +12	Hamuy et al. (1991a)	*IUE* CVBCW, VILSP
1981B	Ia	Vettolani et al. (1981)	+2, +3	Branch et al. (1983)	*IUE* VILSP, NP314
1982B	Ia	Szeidl et al. (1982)	+2	Ciatti et al. (1988)	*IUE* NP586
1983G	Ia	Wamsteker et al. (1983)	+3, +6, +9	Buta et al. (1985)	*IUE* SNFRK, FE022
1983N	1b	Prabhu (1985)	-13 to +13	N. Panagia, in Branch et al. (2002)	*IUE* FE022, FETOO, SNFRK, OD15K
1985L	II	Filippenko et al. (1985)	+12	Kimeridze & Tsvetkov (1989)	*IUE* HQTOO
1987A	II	Herald et al. (1987)	-16, 0, +14	Gouiffes et al. (1988)	*IUE* OD17Y
1989B	Ia	Korth (1989)	-9, -10	Prabhu & Krishnamurthi (1990)	*IUE* STKRK
1989M	Ia	Kharadze et al. (1989)	0 to +13	Kimeridze & Tsvetkov (1991)	*IUE* LETOO, SNLRK, LE059
1990M	Ia	Sonneborn et al. (1990)	-6, -3	Polcaro & Viotti (1991)	*IUE* SNMRK
1990N	Ia	Maury et al. (1990)	-10 to +4	Leibundgut et al. (1991)	*IUE* SNMRK
1990W	Ic	della Valle et al. (1990)	+4	della Valle et al. (1990)	*IUE* SNMRK
1991T	Ia	Hamuy et al. (1991b)	+8, +10	Phillips et al. (1992)	*IUE* METOO, SNMRK
1992A	Ia	Liller et al. (1992)	-2 to +11	Suntzeff et al. (1992)	*IUE* SNNRK and *HST* FOS 4016
1993J	IIb	Prabhu (1995)	-11, -3	Prabhu (1995)	*IUE* SNORK and *HST* FOS 4528
1994I	Ic	Filippenko et al. (1994)	+10	Richmond, in Sasaki et al. (1994)	*HST* FOS 5623
1997ap	Ia	Perlmutter et al. (1998)	-2	Perlmutter et al. (1998)	Keck II, Perlmutter et al. (1998)
1998S	II	Li et al. (1998)	+4	Liu et al. (2000)	*HST* STIS 7434
1999em	II	Jha et al. (1999)	+5	Hamuy et al. (2001)	*HST* STIS 8243
2001eh	Ia	Ganeshalingam et al. (2001)	+7	SALT2-2 fit to Hicken et al. (2009)	*HST* STIS 9114
2001ep	Ia	Matheson et al. (2001)	+9, +15	SALT2-2 fit to Hicken et al. (2009)	*HST* STIS 9114
2001ig	IIb	Phillips et al. (2001)	Discovery +4, +12	Evans et al. (2001)	*HST* STIS 9114
2002ap	Ic	Kawabata et al. (2002)	-5	Foley et al. (2003)	*HST* STIS 9114
2005cf	Ia	Modjaz et al. (2005a)	-9 to +4	SALT2-2 fit to Hicken et al. (2009)	*Swift* UVOT, Bufano et al. (2009)
2005cs	II	Modjaz et al. (2005b)	+9, +11	Pastorello et al. (2009)	*Swift* UVOT, Bufano et al. (2009)
2006jc	Ib	Immler (2005)	0	Foley et al. (2007)	*Swift* UVOT, Bufano et al. (2009)
2010al	II	Kirshner et al. (2010)	< 0	Kirshner et al. (2010)	*HST* STIS 11654
2011dh	IIb	Stringfellow et al. (2011)	+6	Tsvetkov et al. (2012)	*HST* STIS 12540
2011iv	Ia	Drescher et al. (2011)	+1	Foley et al. (2012)	*HST* STIS 12592, Foley et al. (2012)
SNLS	Ia	Ellis et al. (2008)	0	Ellis et al. (2008)	Ellis et al. (2008)
Ia Model	Ia	Lentz et al. (2000)	0 (Explosion +20)	Lentz et al. (2000)	Lentz et al. (2000)

Table 6.2. Probabilities of each supernova matching SN SCP-0401. The values are taken from the principal-component-like analysis described in Section 6.3.3 and Appendix A.3. Only probabilities greater than 0.05 are shown.

Supernova	Type	Probability of Match
SN1980N	Ia	0.969
SN2001ep	Ia	0.968
SN1981B	Ia	0.963
SN1992A	Ia	0.924
SN2011iv	Ia	0.886
SN1990N	Ia	0.610
Lentz et al. (2000)	Ia Model	0.514
SN1983N	Ib	0.489
SN2001eh	Ia	0.420
SN1989M	Ia	0.316
SN1982B	Ia	0.244
SN1990M	Ia	0.157
SN1989B	Ia	0.139
SN1991T	Ia	0.059

Table 6.3. Photometry of SN SCP-0401. Due to the uncertainty on the galaxy models, the NICMOS F110W statistical errors share an off-diagonal covariance of 3.46e-5 DN/s^2, while the F160W errors share a separate off-diagonal covariance of 1.97e-5 DN/s^2. The ACS statistical errors are diagonal.

MJD	PID	Camera	Filter	Exposure (s)	Flux (DN/s)	Flux Error (DN/s)	Vega=0 Zeropoint
52600.72	9583	ACS WFC	F775W	1120.0	−0.0426	0.0599	25.291
52600.75	9583	ACS WFC	F850LP	2400.0	−0.0206	0.0274	23.909
52643.38	9583	ACS WFC	F775W	1000.0	−0.0271	0.0669	25.291
52643.43	9583	ACS WFC	F850LP	2120.0	0.0180	0.0293	23.909
52691.46	9583	ACS WFC	F775W	960.0	−0.0422	0.0655	25.291
52691.52	9583	ACS WFC	F850LP	2060.0	0.0014	0.0288	23.909
52734.16	9583	ACS WFC	F775W	960.0	0.1358	0.0599	25.291
52734.22	9583	ACS WFC	F850LP	2000.0	−0.0128	0.0255	23.909
52782.70	9583	ACS WFC	F775W	960.0	0.0864	0.0573	25.291
52782.78	9583	ACS WFC	F850LP	2080.0	−0.0048	0.0259	23.909
53098.41	9727	ACS WFC	F850LP	1600.0	0.3249	0.0371	23.909
53098.43	9727	ACS WFC	F775W	400.0	0.3328	0.1369	25.291
53107.15	9727	ACS WFC	F850LP	4564.0	0.2213	0.0237	23.909
53111.21	9727	NICMOS 2	F110W	2687.9	0.2427	0.0144	23.029
53111.31	9727	NICMOS 2	F160W	5375.7	0.2011	0.0125	22.160
53121.57	9727	ACS WFC	F850LP	4384.0	0.1311	0.0210	23.909
53130.83	9727	NICMOS 2	F160W	5375.7	0.1387	0.0120	22.160
53136.86	9727	NICMOS 2	F110W	2687.9	0.1205	0.0154	23.029
53142.59	9727	NICMOS 2	F160W	8063.6	0.1158	0.0103	22.160
53145.98	9728	ACS WFC	F775W	400.0	−0.0623	0.1536	25.291
53146.01	9728	ACS WFC	F850LP	1600.0	−0.0287	0.0361	23.909
53148.41	9727	NICMOS 2	F110W	8063.6	0.0811	0.0113	23.029
53196.34	9727	ACS WFC	F850LP	1600.0	0.0536	0.0392	23.909
53196.37	9727	ACS WFC	F775W	400.0	0.1695	0.1701	25.291
53244.51	9728	ACS WFC	F775W	400.0	−0.1195	0.1573	25.291
53244.54	9728	ACS WFC	F850LP	1600.0	0.0003	0.0345	23.909
53284.82	10339	ACS WFC	F775W	375.0	−0.1097	0.1749	25.291
53284.84	10339	ACS WFC	F850LP	1400.0	−0.0009	0.0580	23.909
53333.94	10339	ACS WFC	F775W	400.0	−0.1821	0.1886	25.291
53333.98	10339	ACS WFC	F850LP	1540.0	−0.0756	0.0471	23.909
53377.72	10339	ACS WFC	F775W	355.0	−0.2258	0.2653	25.291
53377.74	10339	ACS WFC	F850LP	1520.0	−0.0214	0.0488	23.909
53427.73	10339	ACS WFC	F775W	375.0	0.0921	0.2744	25.291
53427.76	10339	ACS WFC	F850LP	1540.0	0.0346	0.0429	23.909
53473.53	10339	ACS WFC	F775W	425.0	−0.0096	0.1364	25.291
53473.55	10339	ACS WFC	F850LP	1700.0	0.0359	0.0331	23.909

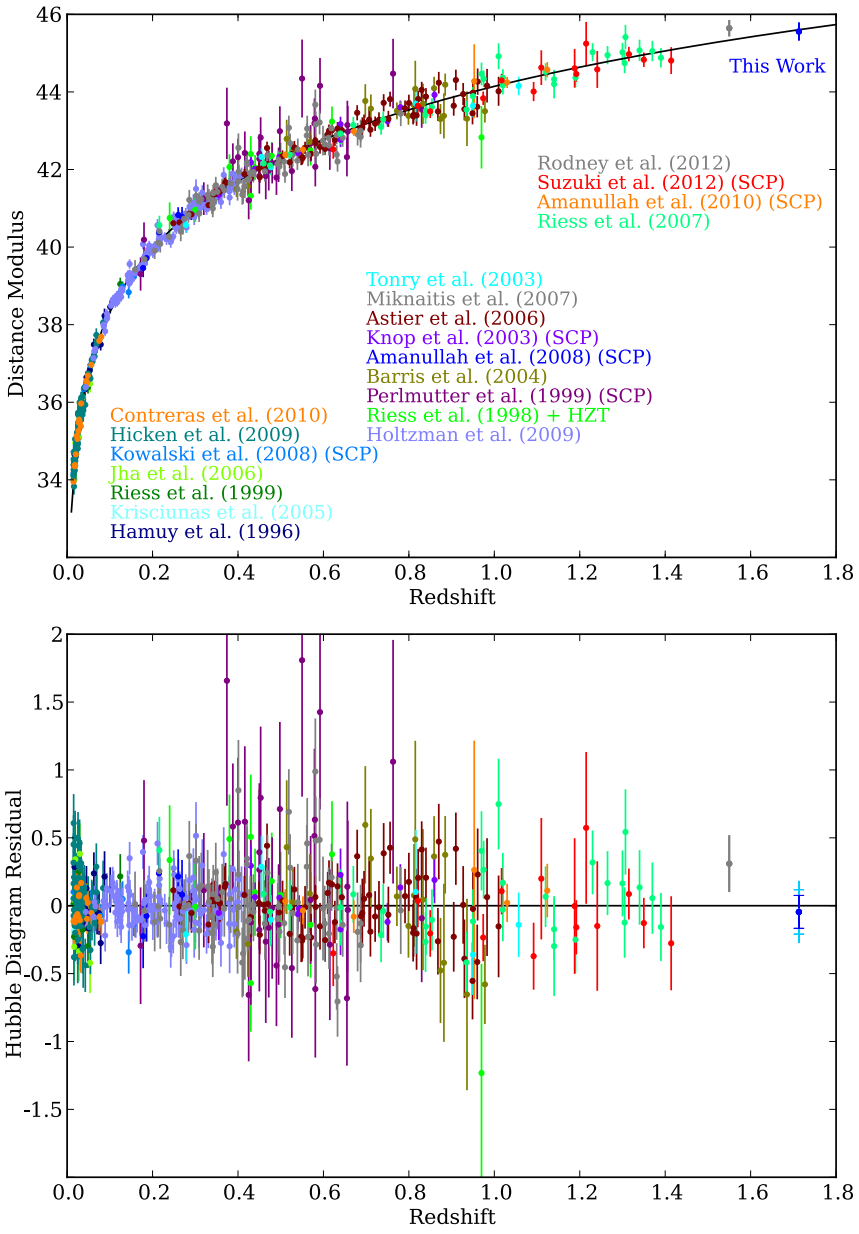

Figure 6.5. Top Panel: Union2.1 Hubble diagram (with the best-fit flat ΛCDM model) with Primo (Rodney et al. 2012) and SN SCP-0401 added. Bottom Panel: Hubble diagram residuals. The inner (blue) error bars on SN SCP-0401 show the uncertainty of the light-curve fit. The middle (capped, cyan) error bars include the sample dispersion; the outer error bars include the lensing dispersion. Future analyses including spectral information or gravitational lensing correction might improve these outer error bars.

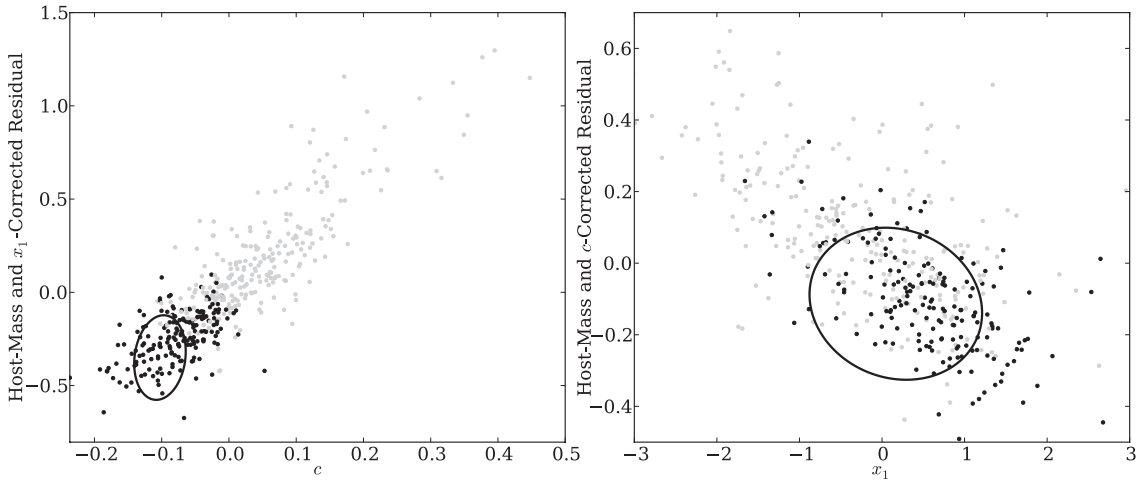

Figure 6.6. Plot of Hubble residuals (from the best-fit flat ΛCDM model) against c (left panel) and x_1 (right panel). In the left panel, the distance moduli have been corrected for x_1 and host mass, revealing the c-brightness relation. Similarly, the distance moduli in the right panel are corrected for c and host mass. Each ellipse represents the ($\Delta\chi^2 = 1$) SALT2-2 Gaussian approximation to the likelihood for SN SCP-0401; projecting the uncertainty to each axis gives the 1-σ error bars on each parameter. The points are comparison supernovae taken from Rubin et al. (in prep); for clarity, only SNe measured to better than 0.05 mag in c are shown. The black points represent SNe that would be bright enough in F850LP (at peak) to have been found at redshift 1.71 in our search.

CHAPTER 7

Conclusions

7.1 Summary

Over the last five years, the Union compilations have become significant resources for the community, supplying hundreds of analyses with ready-to-use SN distances. We have developed a framework for light-curve fits, quality cuts, outlier rejection, and computing the uncertainty covariance matrix. All of this, and all subsequent revisions, were developed "blinded" to the cosmological constraints.

We regard our blinding procedure as good practice, but it is possible it will be regarded in hindsight to be more important than that. The Supernova Legacy Survey (SNLS) team has completed their own compilation and analysis of systematic uncertainties (Conley et al. 2011), releasing a set of distances with a covariance matrix. These results were unfortunately not developed blinded. Their best-fit cosmology results ($\Omega_m = 0.23 \pm 0.04$ for a flat universe) were very compatible with, e.g., WMAP. However, the recent Planck cosmology analysis (Planck Collaboration et al. 2013) shows that the Union2.1 constraints are significantly more compatible with the Planck results than the SNLS constraints. About half the difference between our results and the SNLS SALT2 results seems to be attributable to the rest-frame U-band systematic error treatment.[1] This is potentially an interesting philosophical difference, as we include the U-band systematics as inferred from real data, rather than estimating them from propagation of uncertainties (which gives a smaller error bar). Given the anxieties surrounding publishing discrepant results, is unclear whether the SNLS team would have published their results as they currently stand if the Planck collaboration had released their results first (or if they would have, for example, assigned larger error bars).

[1] The SNLS results also rely on another light-curve fitter, SiFTO, which is more discrepant. However, we do not have experience validating this fitter and cannot comment on the level of biases (if any) in its fit results. More work is clearly needed to understand these issues, especially as SALT2 and SiFTO gave extremely similar results to each other in Conley et al. (2008).

7.2 Bayesian Improvements

The analyses presented in this dissertation gave the best cosmological constraints at the time of their original publication, but I believe we can do better. In particular, the frequentist, least-squares framework prevents the ideal use of the data. In the remainder of this chapter, I outline a research agenda that improves upon current weaknesses of this framework. In short, the end goal would be to have a full generative model for every supernova observation in the compilation, extracting the maximal amount of information. I list the potential improvements in order of increasing importance.

7.2.1 Fitting the "Sample Dispersions" ($\sigma_{\rm sample}$)

We fit each supernova sample independently for the Hubble diagram dispersion necessary to reach $\chi^2/\mathrm{DoF} = 1$, as described in Section 2.3.3. As shown in Figure 5.3, these values can vary significantly, illustrating the range of dataset quality. A Bayesian treatment of this fit would allow the $\sigma_{\rm sample}$ values to be marginalized over as part of the cosmology analysis as discussed by (Kim 2011; March et al. 2012). This simultaneous fit would have the property that samples in tension will have larger sample dispersions. As we do not observe any tension between samples that cannot be explained by known systematic uncertainties (also shown in Figure 5.3), I do not believe this is a serious concern.

7.2.2 Non-Ia and Peculiar Ia SN Rejection

Currently, we only apply mild cuts in SALT light-curve parameters (Section 5.3.3). However, there is far more information in the light curves that we are not using. We could fit each light curve with a range of SN templates, and assign it a probability of being a normal Ia (extensions of this analysis might distinguish between subclasses of SNe Ia). This probability could be used in computing cosmological constraints by constructing a model of both the Ia magnitude distribution and contaminating magnitude distribution(s). Such a "mixture model" was suggested by Kunz et al. (2007).

As discussed in Section 2.3.3, the current Union outlier rejection is based on sigma clipping about the median of a supernova sample. It can only exclude or include a supernova, rather than handle a probabilistic classification. This technique has the benefit that any tensions between samples are left intact by the outlier rejection. However, as noted above, we have not found any tensions that are significant enough to worry about in this regard.

7.2.3 Calibration Uncertainties

A significant amount of value could be had by marginalizing over parameters describing calibration uncertainties (Kim & Miquel 2006). We incorporate a variant of this currently, where the calibration uncertainties are effectively fit at the same time as the Hubble diagram

(Section A.1.2). However, this throws out the information contained in the light curves, as the Hubble diagram only directly relies on the light curve fit parameters, and not the photometry. As an illustration of why this is a problem, consider the situation of photometry from one band showing tension with photometry from the other bands. A global fit including the light curves and the calibration uncertainties would reveal the tension and help to relieve it, while the current analysis can only deweight the supernovae observed including this band (and only then if the tension is known and accounted for in the uncertainty on the zeropoint).

7.2.4 Supernova Diversity

The most value of a global analysis is the training of the templates (and associated parameters) simultaneously with the cosmology. As no SN fitting procedure (either a parameterized model or template matching) can reproduce all observed SNe, we must include a (wavelength and phase-dependent) model of the unexplained dispersion. The SALT2 model currently in use is crude (ignoring such effects as correlation between wavelengths). Furthermore, uncertainties in this model must be propagated into the cosmological fits in an approximate manner, as a least-squares fit cannot properly include uncertainty on uncertainties.

Bibliography

Abrahamse, A., Albrecht, A., Barnard, M., & Bozek, B. 2008, Phys. Rev. D, 77, 103503

Aguirre, A. 1999, ApJ, 525, 583

Aihara, H., Allende Prieto, C., An, D., et al. 2011, ApJS, 193, 29

Albrecht, A., Bernstein, G., Cahn, R., et al. 2006, arXiv:astro-ph/0609591

Aldering, G. 2005, New Astronomy Review, 49, 346

Aldering, G., Adam, G., Antilogus, P., et al. 2002, in Presented at the Society of Photo-Optical Instrumentation Engineers (SPIE) Conference, Vol. 4836, Survey and Other Telescope Technologies and Discoveries. Edited by Tyson, J. Anthony; Wolff, Sidney. Proceedings of the SPIE, Volume 4836, pp. 61-72 (2002)., ed. J. A. Tyson & S. Wolff, 61–72

Amanullah, R., Mörtsell, E., & Goobar, A. 2003, A&A, 397, 819

Amanullah, R., Stanishev, V., Goobar, A., et al. 2008, A&A, 486, 375

Amanullah, R., Lidman, C., Rubin, D., et al. 2010, ApJ, 716, 712

Amendola, L., Baldi, M., & Wetterich, C. 2008, Phys. Rev. D, 78, 023015

Astier, P., Guy, J., Regnault, N., et al. 2006, A&A, 447, 31

Barbary, K., Aldering, G., Amanullah, R., et al. 2012a, ApJ, 745, 32

—. 2012b, ApJ, 745, 31

Barker, E. A., Laidler, V. G., & Koekemoer, A. M. 2007, Removing Post-SAA Persistence in NICMOS Data, Tech. rep.

Barris, B. J., Tonry, J. L., Blondin, S., et al. 2004, ApJ, 602, 571

Bartelmann, M., Doran, M., & Wetterich, C. 2006, A&A, 454, 27

Bazin, G., Palanque-Delabrouille, N., Rich, J., et al. 2009, A&A, 499, 653

Bergström, L., Goliath, M., Goobar, A., & Mörtsell, E. 2000, A&A, 358, 13

Blanco, V. M., Schweizer, F., Moffat, A. F. J., et al. 1980, IAU Circ., 3556, 2

Blondin, S., Prieto, J. L., Patat, F., et al. 2009, ApJ, 693, 207

Bohlin, R. C. 2007a, in Astronomical Society of the Pacific Conference Series, Vol. 364, The Future of Photometric, Spectrophotometric and Polarimetric Standardization, ed. C. Sterken, 315–+

Bohlin, R. C. 2007b, Photometric Calibration of the ACS CCD Cameras, Tech. rep.

Bohlin, R. C., & Gilliland, R. L. 2004, AJ, 127, 3508

Bohlin, R. C., J., L. D., & Riess, A. 2005, Grism Sensitivities and Apparent Non-Linearity, Tech. rep.

Bohlin, R. C., Riess, A., & de Jong, R. 2006, NICMOS Count Rate Dependent Non-Linearity in G096 and G141, Tech. rep.

Bousso, R. 2002, Reviews of Modern Physics, 74, 825

Branch, D., Lacy, C. H., McCall, M. L., et al. 1983, ApJ, 270, 123

Branch, D., Benetti, S., Kasen, D., et al. 2002, ApJ, 566, 1005

Brown, P. J. 2009, PhD thesis, The Pennsylvania State University

Bruzual, G., & Charlot, S. 2003, MNRAS, 344, 1000

Bufano, F., Immler, S., Turatto, M., et al. 2009, ApJ, 700, 1456

Buta, R. J. 1982, PASP, 94, 578

Buta, R. J., Corwin, Jr., H. G., & Opal, C. B. 1985, PASP, 97, 229

Cahn, R. N., de Putter, R., & Linder, E. V. 2008, J. Cosmology Astropart. Phys., 11, 15

Caldwell, R. R., Komp, W., Parker, L., & Vanzella, D. A. T. 2006, Phys. Rev. D, 73, 023513

Caldwell, R. R., & Linder, E. V. 2005, Physical Review Letters, 95, 141301

Cardelli, J. A., Clayton, G. C., & Mathis, J. S. 1989, ApJ, 345, 245

Chotard, N., Gangler, E., Aldering, G., et al. 2011, A&A, 529, L4

Ciatti, F., Barbon, R., Cappellaro, E., & Rosino, L. 1988, A&A, 202, 15

Clocchiatti, A., Phillips, M. M., Suntzeff, N. B., et al. 2000, ApJ, 529, 661

Conley, A., Carlberg, R. G., Guy, J., et al. 2007, ApJ, 664, L13

Conley, A., Goldhaber, G., Wang, L., et al. 2006a, ApJ, 644, 1

Conley, A., Howell, D. A., Howes, A., et al. 2006b, AJ, 132, 1707

Conley, A., Sullivan, M., Hsiao, E. Y., et al. 2008, ApJ, 681, 482

Conley, A., Guy, J., Sullivan, M., et al. 2011, ApJS, 192, 1

Contreras, C., Hamuy, M., Phillips, M. M., et al. 2010, AJ, 139, 519

Copeland, E. J., Sami, M., & Tsujikawa, S. 2006, International Journal of Modern Physics D, 15, 1753

Couch, W. J., Perlmutter, S., Newburg, H. J. M., et al. 1991, Proceedings of the Astronomical Society of Australia, 9, 261

Cowie, L. L., Barger, A. J., Hu, E. M., Capak, P., & Songaila, A. 2004, AJ, 127, 3137

D. S. Hayes, L. E. Pasinetti, & A. G. D. Philip, ed. 1985, IAU Symposium, Vol. 111, Calibration of fundamental stellar quantities; Proceedings of the Symposium, Como, Italy, May 24-29, 1984, ed. D. S. Hayes, L. E. Pasinetti, & A. G. D. Philip

Dahlen, T., McLaughlin, H., Laidler, V., et al. 2008, Improvements to Calnica, Tech. rep.

Davis, T. M., Mörtsell, E., Sollerman, J., et al. 2007, ApJ, 666, 716

Dawson, K. S., Aldering, G., Amanullah, R., et al. 2009, AJ, 138, 1271

de Jong, R. S., Bergeron, E., Riess, A., & Bohlin, R. 2006, NICMOS count-rate dependent nonlinearity tests using flatfield lamps, Tech. rep.

de Putter, R., & Linder, E. V. 2007, arXiv:astro-ph/0710.0373

de Vaucouleurs, G., de Vaucouleurs, A., Buta, R., Ables, H. D., & Hewitt, A. V. 1981, PASP, 93, 36

Deffayet, C., Dvali, G., & Gabadadze, G. 2002, Phys. Rev. D, 65, 044023

della Valle, M., Pasquini, L., Phillips, M., & McCarthy, P. 1990, IAU Circ., 5079, 1

Dick, J., Knox, L., & Chu, M. 2006, J. Cosmology Astropart. Phys., 7, 1

Dickinson, M., Giavalisco, M., & GOODS Team. 2003, in The Mass of Galaxies at Low and High Redshift, ed. R. Bender & A. Renzini, 324

Dimopoulos, S., & Thomas, S. 2003, Physics Letters B, 573, 13

Doi, M., Tanaka, M., Fukugita, M., et al. 2010, AJ, 139, 1628

Doran, M., & Robbers, G. 2006, J. Cosmology Astropart. Phys., 6, 26

Doran, M., Robbers, G., & Wetterich, C. 2007a, Phys. Rev. D, 75, 023003

Doran, M., Stern, S., & Thommes, E. 2007b, J. Cosmology Astropart. Phys., 4, 15

Drescher, C., Parker, S., Brimacombe, J., Noguchi, T., & Nakano, S. 2011, Central Bureau Electronic Telegrams, 2940, 1

Dunkley, J., et al. 2008, arXiv:0803.0586 [astro-ph]

Dutta, K., & Sorbo, L. 2007, Phys. Rev. D, 75, 063514

Dvali, G., Gabadadze, G., & Porrati, M. 2000, Physics Letters B, 485, 208

Eisenstein, D. J., Zehavi, I., Hogg, D. W., et al. 2005, ApJ, 633, 560

Ellis, R. S., Sullivan, M., Nugent, P. E., et al. 2008, ApJ, 674, 51

Evans, R. O., White, B., & Bembrick, C. 2001, IAU Circ., 7772, 1

Fadeyev, V., Aldering, G., & Perlmutter, S. 2006, PASP, 118, 907

Filippenko, A. V., Sargent, W. L. W., Kriss, G., et al. 1985, IAU Circ., 4080, 1

Filippenko, A. V., Matheson, T., Barth, A. J., et al. 1994, IAU Circ., 5964, 1

Folatelli, G., Phillips, M. M., Burns, C. R., et al. 2010, AJ, 139, 120

Foley, R. J., Narayan, G., Challis, P. J., et al. 2010, ApJ, 708, 1748

Foley, R. J., Smith, N., Ganeshalingam, M., et al. 2007, ApJ, 657, L105

Foley, R. J., Papenkova, M. S., Swift, B. J., et al. 2003, PASP, 115, 1220

Foley, R. J., Kromer, M., Howie Marion, G., et al. 2012, ApJ, 753, L5

Frieman, J. A., Hill, C. T., Stebbins, A., & Waga, I. 1995, Physical Review Letters, 75, 2077

Fruchter, A. S., & Hook, R. N. 2002, PASP, 114, 144

Fukugita, M., Ichikawa, T., Gunn, J. E., et al. 1996, AJ, 111, 1748

Ganeshalingam, M., Li, W. D., Chornock, R., & Filippenko, A. V. 2001, IAU Circ., 7714, 4

Garnavich, P. M., Kirshner, R. P., Challis, P., et al. 1998, ApJ, 493, L53

Gibbons, R. A., Knop, R. A., Kuznetsova, N., & Supernova Cosmology Project Collaboration. 2004, in Bulletin of the American Astronomical Society, Vol. 36, American Astronomical Society Meeting Abstracts, 1460

Goldhaber, G., Groom, D. E., Kim, A., et al. 2001, ApJ, 558, 359

Goobar, A. 2008, ApJ, 686, L103

Goobar, A., Bergström, L., & Mörtsell, E. 2002, A&A, 384, 1

Goobar, A., Hannestad, S., Mörtsell, E., & Tu, H. 2006, J. Cosmology Astropart. Phys., 6, 19

Gott, J. R. I., Vogeley, M. S., Podariu, S., & Ratra, B. 2001, ApJ, 549, 1

Gouiffes, C., Rosa, M., Melnick, J., et al. 1988, A&A, 198, L9

Graur, O., Poznanski, D., Maoz, D., et al. 2011, MNRAS, 417, 916

Guo, Q., White, S., Li, C., & Boylan-Kolchin, M. 2010, MNRAS, 404, 1111

Guth, A. H. 1981, Phys. Rev. D, 23, 347

Guy, J., Astier, P., Nobili, S., Regnault, N., & Pain, R. 2005, A&A, 443, 781

Guy, J., Astier, P., Baumont, S., et al. 2007, A&A, 466, 11

Guy, J., Sullivan, M., Conley, A., et al. 2010, A&A, 523, A7

Hager, W. W. 1989, SIAM Rev., 31, 221

Hamuy, M., Phillips, M. M., Maza, J., et al. 1991a, AJ, 102, 208

Hamuy, M., Phillips, M. M., Silva, D., Lubcke, G., & Steffey, P. 1991b, IAU Circ., 5251, 1

Hamuy, M., Phillips, M. M., Suntzeff, N. B., et al. 1996a, AJ, 112, 2391

—. 1996b, AJ, 112, 2408

Hamuy, M., Pinto, P. A., Maza, J., et al. 2001, ApJ, 558, 615

Hawking, S. W., & Israel, W. 1987, Three hundred years of gravitation, 604

Herald, D., McNaught, R. H., Morel, M., et al. 1987, IAU Circ., 4317, 1

Heyer, I., Richardson, M., Whitmore, B., & Lubin, L. 2004, The Accuracy of WFPC2 Photometric Zeropoints

Heyer, I., Richardson, M., Whitmore, B., & Lubin, L. 2004, The Accuracy of WFPC2 Photometric Zeropoints, Tech. rep.

Hicken, M., Challis, P., Jha, S., et al. 2009, ApJ, 700, 331

Hoeflich, P., Wheeler, J. C., & Thielemann, F. K. 1998, ApJ, 495, 617

Holtzman, J. A., Marriner, J., Kessler, R., et al. 2008, AJ, 136, 2306

Holz, D. E., & Linder, E. V. 2005, ApJ, 631, 678

Hopkins, A. M., & Beacom, J. F. 2006, ApJ, 651, 142

Howell, D. A., Sullivan, M., Conley, A., & Carlberg, R. 2007, ApJ, 667, L37

Hsiao, E. Y., Conley, A., Howell, D. A., et al. 2007, ApJ, 663, 1187

Hsiao, E. Y., Suzuki, N., Ripoche, P., et al. 2011, in The 2010 HST Calibration Workshop, ed. S. Deustua, C. Oliveira

Huterer, D., & Starkman, G. 2003, Physical Review Letters, 90, 031301

Immler, S. 2005, in Chandra Proposal, 2292

Jha, S., Challis, P., Garnavich, P., et al. 1999, IAU Circ., 7296, 2

Jha, S., Riess, A. G., & Kirshner, R. P. 2007, ApJ, 659, 122

Jha, S., Kirshner, R. P., Challis, P., et al. 2006, AJ, 131, 527

Jönsson, J., Dahlén, T., Goobar, A., et al. 2006, ApJ, 639, 991

Kaiser, M. E., Kruk, J. W., McCandliss, S. R., et al. 2010, ArXiv:1001.3925, arXiv:1001.3925

Kallosh, R., Kratochvil, J., Linde, A., Linder, E. V., & Shmakova, M. 2003, J. Cosmology Astropart. Phys., 10, 15

Kawabata, K. S., Jeffery, D. J., Iye, M., et al. 2002, in 8th Asian-Pacific Regional Meeting, Volume II, ed. S. Ikeuchi, J. Hearnshaw, & T. Hanawa, 333–334

Kelly, P. L., Hicken, M., Burke, D. L., Mandel, K. S., & Kirshner, R. P. 2010, ApJ, 715, 743

Kessler, R., Becker, A. C., Cinabro, D., et al. 2009, ApJS, 185, 32

Kharadze, E. K., Pskovsky, Y. P., Kimeridze, G. N., et al. 1989, IAU Circ., 4802, 1

Kim, A. G. 2011, PASP, 123, 230

Kim, A. G., & Miquel, R. 2006, Astroparticle Physics, 24, 451

Kim, A. G., Thomas, R. C., Aldering, G., et al. 2013, ApJ, 766, 84

Kimeridze, G. N., & Tsvetkov, D. Y. 1989, Astrofizika, 31, 17

—. 1991, Soviet Ast., 35, 168

Kirshner, R., & Bryan, J. 1980, IAU Circ., 3534, 2

Kirshner, R., Blondin, S., Chevalier, R., et al. 2010, The Astronomer's Telegram, 2513, 1

Knop, R. A., Aldering, G., Amanullah, R., et al. 2003, ApJ, 598, 102

Koekemoer, A. M., Fruchter, A. S., Hook, R. N., & Hack, W. 2002, in The 2002 HST Calibration Workshop : Hubble after the Installation of the ACS and the NICMOS Cooling System, ed. S. Arribas, A. Koekemoer, & B. Whitmore, 337

Komatsu, E., Dunkley, J., Nolta, M. R., et al. 2009, ApJS, 180, 330

Komatsu, E., Smith, K. M., Dunkley, J., et al. 2011, ApJS, 192, 18

Korth, S. 1989, BAV Rundbrief, 38, 88

Kowalski, M., Rubin, D., Aldering, G., et al. 2008, ApJ, 686, 749

Krisciunas, K., Phillips, M. M., Stubbs, C., et al. 2001, AJ, 122, 1616

Krisciunas, K., Phillips, M. M., Suntzeff, N. B., et al. 2004a, AJ, 127, 1664

Krisciunas, K., Suntzeff, N. B., Phillips, M. M., et al. 2004b, AJ, 128, 3034

Kümmel, M., Walsh, J. R., Pirzkal, N., Kuntschner, H., & Pasquali, A. 2009, PASP, 121, 59

Kunz, M., Bassett, B. A., & Hlozek, R. A. 2007, Phys. Rev. D, 75, 103508

Lambda-website. 2008, http://lambda.gsfc.nasa.gov/product/map/dr3/parameters.cfm

Lampeitl, H., Smith, M., Nichol, R. C., et al. 2010, ApJ, 722, 566

Landolt, A. U. 1992, AJ, 104, 340

Le Borgne, D., & Rocca-Volmerange, B. 2002, A&A, 386, 446

Leibundgut, B., Kirshner, R. P., Filippenko, A. V., et al. 1991, ApJ, 371, L23

Lentz, E. J., Baron, E., Branch, D., Hauschildt, P. H., & Nugent, P. E. 2000, ApJ, 530, 966

Li, W., Leaman, J., Chornock, R., et al. 2011, MNRAS, 412, 1441

Li, W.-D., Li, C., Filippenko, A. V., & Moran, E. C. 1998, IAU Circ., 6829, 1

Liddle, A. R., & Lyth, D. H. 2000, Cosmological Inflation and Large-Scale Structure, ed. Liddle, A. R. & Lyth, D. H.

Liller, W., Brown, N., McNaught, R. H., et al. 1992, IAU Circ., 5428, 1

Linder, E. V. 1988a, A&A, 206, 190

—. 1988b, A&A, 206, 190

—. 2003a, Physical Review Letters, 90, 091301

—. 2003b, Physical Review Letters, 90, 091301

—. 2004, Phys. Rev. D, 70, 023511

—. 2006, Phys. Rev. D, 73, 063010

—. 2007, arXiv:astro-ph/0708.0024

—. 2008a, Reports on Progress in Physics, 71, 056901

—. 2008b, General Relativity and Gravitation, 40, 329

Linder, E. V., & Cahn, R. N. 2007, Astroparticle Physics, 28, 481

Linder, E. V., & Huterer, D. 2005, Phys. Rev. D, 72, 043509

Linder, E. V., & Miquel, R. 2004, Phys. Rev. D, 70, 123516

Linder, E. V., & Robbers, G. 2008, J. Cosmology Astropart. Phys., 6, 4

Liu, Q.-Z., Hu, J.-Y., Hang, H.-R., et al. 2000, A&AS, 144, 219

Mannucci, F., Della Valle, M., & Panagia, N. 2006, MNRAS, 370, 773

March, M. C., Karpenka, N. V., Feroz, F., & Hobson, M. P. 2012, ArXiv e-prints, arXiv:1207.3705

Matheson, T., Jha, S., Challis, P., Kirshner, R., & Huchra, J. 2001, IAU Circ., 7731, 3

Mattei, J., Johnson, G. E., Rosino, L., Rafanelli, P., & Kirshner, R. 1979, IAU Circ., 3348, 1

Maury, A., Thouvenot, E., Buil, C., et al. 1990, IAU Circ., 5039, 1

McGraw, J. T., Zimmer, P. C., Ackermann, M. R., et al. 2010, in Society of Photo-Optical Instrumentation Engineers (SPIE) Conference Series, Vol. 7739, Society of Photo-Optical Instrumentation Engineers (SPIE) Conference Series

Melbourne, J., Dawson, K. S., Koo, D. C., et al. 2007, AJ, 133, 2709

Ménard, B., Kilbinger, M., & Scranton, R. 2010, MNRAS, 406, 1815

Ménard, B., Nestor, D., Turnshek, D., et al. 2008, MNRAS, 385, 1053

Ménard, B., Scranton, R., Fukugita, M., & Richards, G. 2009, ArXiv e-prints, arXiv:0902.4240

Meyers, J., Aldering, G., Amanullah, R., et al. 2011, ApJ *submitted*

Miknaitis, G., Pignata, G., Rest, A., et al. 2007, ApJ, 666, 674

Mobasher, B., & Riess, A. 2005, A Test of Possible NICMOS Non-linearity, Tech. rep.

Modjaz, M., Kirshner, R., Challis, P., & Berlind, P. 2005a, Central Bureau Electronic Telegrams, 160, 1

Modjaz, M., Kirshner, R., Challis, P., & Hutchins, R. 2005b, Central Bureau Electronic Telegrams, 174, 1

Morokuma, T., Tokita, K., Lidman, C., et al. 2010, PASJ, 62, 19

Mörtsell, E., & Goobar, A. 2003, Journal of Cosmology and Astro-Particle Physics, 9, 9

Mota, D. F., Pettorino, V., Robbers, G., & Wetterich, C. 2008, Physics Letters B, 663, 160

Navarro, J. F., Frenk, C. S., & White, S. D. M. 1996, ApJ, 462, 563

Nobili, S., & Goobar, A. 2008, A&A, 487, 19

Nobili, S., Amanullah, R., Garavini, G., et al. 2005, A&A, 437, 789

Nobili, S., Fadeyev, V., Aldering, G., et al. 2009, ApJ, 700, 1415

Nomoto, K., Thielemann, F., & Yokoi, K. 1984, ApJ, 286, 644

Nugent, P., Kim, A., & Perlmutter, S. 2002, PASP, 114, 803

Östman, L., & Mörtsell, E. 2005, Journal of Cosmology and Astro-Particle Physics, 2, 5

Panagia, N. 1985, in Lecture Notes in Physics, Berlin Springer Verlag, Vol. 224, Supernovae as Distance Indicators, ed. N. Bartel, 14–33

Panagia, N. 2003, in Lecture Notes in Physics, Berlin Springer Verlag, Vol. 598, Supernovae and Gamma-Ray Bursters, ed. K. Weiler, 113–144

Parker, L., & Raval, A. 2000, Phys. Rev. D, 62, 083503

Parodi, B. R., Saha, A., Sandage, A., & Tammann, G. A. 2000, ApJ, 540, 634

Pastorello, A., Valenti, S., Zampieri, L., et al. 2009, MNRAS, 394, 2266

Patat, F., Chandra, P., Chevalier, R., et al. 2007, Science, 317, 924

Percival, W. J., Cole, S., Eisenstein, D. J., et al. 2007, MNRAS, 381, 1053

Percival, W. J., Reid, B. A., Eisenstein, D. J., et al. 2010, MNRAS, 401, 2148

Perlmutter, S., Pennypacker, C., Goldhaber, G., et al. 1994, in Bulletin of the American Astronomical Society, Vol. 26, American Astronomical Society Meeting Abstracts #184, 965

Perlmutter, S., Gabi, S., Goldhaber, G., et al. 1997, ApJ, 483, 565

Perlmutter, S., Aldering, G., della Valle, M., et al. 1998, Nature, 391, 51

Perlmutter, S., Aldering, G., Goldhaber, G., et al. 1999, ApJ, 517, 565

Phillips, M. M. 1993, ApJ, 413, L105

Phillips, M. M., Suntzeff, N. B., Krisciunas, K., et al. 2001, IAU Circ., 7772, 2

Phillips, M. M., Wells, L. A., Suntzeff, N. B., et al. 1992, AJ, 103, 1632

Planck Collaboration, Ade, P. A. R., Aghanim, N., et al. 2013, ArXiv e-prints, arXiv:1303.5076

Polcaro, V. F., & Viotti, R. 1991, A&A, 242, L9

Prabhu, T. P. 1985, Bulletin of the Astronomical Society of India, 13, 68

—. 1995, Journal of Astrophysics and Astronomy Supplement, 16, 317

Prabhu, T. P., & Krishnamurthi, A. 1990, A&A, 232, 75

Regnault, N., Conley, A., Guy, J., et al. 2009, A&A, 506, 999

Riess, A., & Bergeron, E. 2008, Bright Earth Persistence in NICMOS, Tech. rep.

Riess, A. G., Press, W. H., & Kirshner, R. P. 1996, ApJ, 473, 88

Riess, A. G., Filippenko, A. V., Challis, P., et al. 1998, AJ, 116, 1009

Riess, A. G., Kirshner, R. P., Schmidt, B. P., et al. 1999, AJ, 117, 707

Riess, A. G., et al. 2001, ApJ, 560, 49

Riess, A. G., Strolger, L.-G., Tonry, J., et al. 2004, ApJ, 607, 665

Riess, A. G., Strolger, L.-G., Casertano, S., et al. 2007, ApJ, 659, 98

Riess, A. G., Macri, L., Casertano, S., et al. 2009, ApJ, 699, 539

—. 2011, ApJ, 730, 119

Ripoche, P., Aldering, G., Amanullah, R., et al. 2013, ApJ *submitted*

Rodney, S. A., Riess, A. G., Dahlen, T., et al. 2012, ApJ, 746, 5

Rubin, D., Linder, E. V., Kowalski, M., et al. 2009, ApJ, 695, 391

Rubin, D., Knop, R. A., Rykoff, E., et al. 2013, ApJ, 763, 35

Ruiz-Lapuente, P. 2007, Class. Quant. Grav., 24, 91

Rydbeck, S., Fairbairn, M., & Goobar, A. 2007, J. Cosmology Astropart. Phys., 5, 3

Sakharov, A. D. 1968, Soviet Physics Doklady, 12, 1040

Sánchez, A. G., & Cole, S. 2008, MNRAS, 243

Sasaki, M. 1987, MNRAS, 228, 653

Sasaki, M., Kosugi, G., Ishigaki, T., et al. 1994, PASJ, 46, L187

Scannapieco, E., & Bildsten, L. 2005, ApJ, 629, L85

Scherrer, R. J., & Sen, A. A. 2008, Phys. Rev. D, 77, 083515

Schlegel, D. J., Finkbeiner, D. P., & Davis, M. 1998, ApJ, 500, 525

Schmidt, B. P., Suntzeff, N. B., Phillips, M. M., et al. 1998, ApJ, 507, 46

Seljak, U., Slosar, A., & McDonald, P. 2006, J. Cosmology Astropart. Phys., 10, 14

Simon, J. D., Gal-Yam, A., Gnat, O., et al. 2009, ApJ, 702, 1157

Smith, J. A., Tucker, D. L., Kent, S., et al. 2002, AJ, 123, 2121

Sonneborn, G., Kirshner, R., della Valle, M., et al. 1990, IAU Circ., 5034, 1

Spergel, D. N., Verde, L., Peiris, H. V., et al. 2003, ApJS, 148, 175

Stringfellow, G. S., Howell, S. B., Probst, R., & Seebode, S. 2011, The Astronomer's Telegram, 3428, 1

Stritzinger, M., Suntzeff, N. B., Hamuy, M., et al. 2005, PASP, 117, 810

Strovink, M. 2007, ApJ, 671, 1084

Stubbs, C. W., & Tonry, J. L. 2006, ApJ, 646, 1436

Stubbs, C. W., High, F. W., George, M. R., et al. 2007, PASP, 119, 1163

Sullivan, M., Ellis, R. S., Aldering, G., et al. 2003, MNRAS, 340, 1057

Sullivan, M., Le Borgne, D., Pritchet, C. J., et al. 2006, ApJ, 648, 868

Sullivan, M., Conley, A., Howell, D. A., et al. 2010, ArXiv e-prints, arXiv:1003.5119

Suntzeff, N., Parker, J., Hunter, D., et al. 1992, IAU Circ., 5432, 2

Suzuki, N., Rubin, D., Lidman, C., et al. 2012, ApJ, 746, 85

Szeidl, B., Lovas, M., Barbon, R., et al. 1982, IAU Circ., 3671, 1

Tegmark, M., Eisenstein, D. J., Strauss, M. A., et al. 2006, Phys. Rev. D, 74, 123507

Thatte, D., Dahlén, T., et al. 2009, NICMOS Data Handbook

Tonry, J. L., Schmidt, B. P., Barris, B., et al. 2003, ApJ, 594, 1

Tripp, R. 1998, A&A, 331, 815

Tripp, R., & Branch, D. 1999, ApJ, 525, 209

Tsvetkov, D. Y., Volkov, I. M., Sorokina, E., et al. 2012, Peremennye Zvezdy, 32, 6

Uomoto, A., & Kirshner, R. P. 1985, A&A, 149, L7

Vettolani, G., Marano, B., Zitelli, V., et al. 1981, IAU Circ., 3584, 1

Walker, E. S., Hook, I. M., Sullivan, M., et al. 2011, MNRAS, 410, 1262

Wamsteker, W., Talavera, A., Machetto, F., et al. 1983, IAU Circ., 3791, 2

Wang, L. 2005, ApJ, 635, L33

Wang, L., Goldhaber, G., Aldering, G., & Perlmutter, S. 2003, ApJ, 590, 944

Wang, L., Strovink, M., Conley, A., et al. 2006, ApJ, 641, 50

Wang, X., Li, W., Filippenko, A. V., et al. 2008, ApJ, 675, 626

Wang, Y., Holz, D. E., & Munshi, D. 2002, ApJ, 572, L15

Ward, M. J., Blades, J. C., & Griffiths, R. E. 1978, IAU Circ., 3309, 1

Weinberg, S. 2008, Cosmology (Oxford University Press)

Wetterich, C. 1988, Nuclear Physics B, 302, 668

—. 2007, Physics Letters B, 655, 201

Wheeler, J. C., & Levreault, R. 1985, ApJ, 294, L17

Wood-Vasey, W. M., Miknaitis, G., Stubbs, C. W., et al. 2007, ApJ, 666, 694

Wright, E. L. 2007, ApJ, 664, 633

Yao, W. M., et al. 2006, J. Phys., G33, 1

Zimmer, P. C., McGraw, J. T., Ackermann, M. R., et al. 2010, in Society of Photo-Optical Instrumentation Engineers (SPIE) Conference Series, Vol. 7735, Society of Photo-Optical Instrumentation Engineers (SPIE) Conference Series

Zlatev, I., Wang, L., & Steinhardt, P. J. 1999, Physical Review Letters, 82, 896

APPENDIX A

Statistical Notes

A.1 Nuisance Parameters as Covariances

Suppose that observations $\boldsymbol{y}$ are modeled by $\boldsymbol{F}(\boldsymbol{\theta})$, where some of the parameters enter into the model linearly ($\boldsymbol{\theta}^L$) while some enter non-linearly ($\boldsymbol{\theta}^N$). The χ^2 can be written as

$$\chi^2(\boldsymbol{\theta}) = (\boldsymbol{y} - (\boldsymbol{F}_N(\boldsymbol{\theta}^N) + H\boldsymbol{\theta}^L))^T V^{-1} (\boldsymbol{y} - (\boldsymbol{F}_N(\boldsymbol{\theta}^N) + H\boldsymbol{\theta}^L)) \tag{A.1}$$

where V is the covariance matrix of the observations, and H is the Jacobian matrix of the model with respect to the $\boldsymbol{\theta}^L$. Taking the derivative of the χ^2 and setting it to zero gives the analytic formula for the best-fit $\boldsymbol{\theta}^L$

$$\hat{\boldsymbol{\theta}^L} = (H^T V^{-1} H)^{-1} H^T V^{-1} (\boldsymbol{y} - \boldsymbol{F}_N(\boldsymbol{\theta}^N)) \equiv D(\boldsymbol{y} - \boldsymbol{F}_N(\boldsymbol{\theta}^N)) \; . \tag{A.2}$$

The likelihoods for the $\boldsymbol{\theta}^N$ can be found from this restricted parameter space where $\boldsymbol{\theta}^L = \hat{\boldsymbol{\theta}^L}$. Thus, the restricted χ^2 is given by:

$$\begin{aligned} \chi^2 &= ((I - HD)(\boldsymbol{y} - \boldsymbol{F}_N(\boldsymbol{\theta}^N)))^T V^{-1} (I - HD)(\boldsymbol{y} - \boldsymbol{F}_N(\boldsymbol{\theta}^N)) & \text{(A.3)} \\ &\equiv \boxed{(\boldsymbol{y} - \boldsymbol{F}_N(\boldsymbol{\theta}^N))^T U^{-1} (\boldsymbol{y} - \boldsymbol{F}_N(\boldsymbol{\theta}^N))} & \text{(A.4)} \end{aligned}$$

with U^{-1} given by

$$\begin{aligned} U^{-1} &= (I - HD)^T V^{-1} (I - HD) & \text{(A.5)} \\ &= \boxed{V^{-1} - V^{-1} H (H^T V^{-1} H)^{-1} H^T V^{-1}} \; . & \text{(A.6)} \end{aligned}$$

In this way, all of the $\boldsymbol{\theta}^L$ do not have to be explicitly included in the χ^2, as long as the weight matrix, U^{-1}, is updated appropriately. Note that U^{-1} may depend on $\boldsymbol{\theta}^N$.

A.1.1 Minimization over $x_1^{\rm true}$ and $c^{\rm true}$

When errors in the independent variable are present, the true values must be solved for as part of the fit (see discussion in Chapter 2). For one supernova, $\boldsymbol{y} = (m_B, x_1, c)$, while

the model is given by

$$(M_B + \mu(z, \text{cosmology}) - (\alpha x_1^{\text{true}} - \beta c^{\text{true}}), x_1^{\text{true}}, c^{\text{true}}) \; . \tag{A.7}$$

Using $\boldsymbol{\theta}^L = (x_1^{\text{true}}, c^{\text{true}})$ (M_B, α and β are global parameters and cannot be handled one supernova at a time), we have

$$H = \begin{pmatrix} -\alpha & \beta \\ 1 & 0 \\ 0 & 1 \end{pmatrix} \; . \tag{A.8}$$

The new χ^2 for this specific example (equation A.4) is given by equations 4.2 and 4.3.

A.1.2 Minimization over Systematic Errors

Suppose that we have two kinds of measurements: supernova distance measurements (N supernovae), and zeropoint measurements (M zeropoints). The true value of each zeropoint is given by $\text{ZP}_{\text{true}} = \text{ZP}_{\text{observed}} + \Delta\text{ZP}$. Because the uncertainties on the supernova distances are unrelated to the uncertainties on the zeropoints,

$$V = \begin{pmatrix} V_\mu & \\ & V_{\Delta\text{ZP}} \end{pmatrix} ,$$

where V_μ is an $N \times N$ block and $V_{\Delta\text{ZP}}$ is an $M \times M$ block. Similarly, $\boldsymbol{y}$ can be split into distances and zeropoints $\boldsymbol{y} = (\boldsymbol{y}_\mu, \boldsymbol{y}_{\Delta\text{ZP}} = \mathbf{0})$. The model for each supernova distance is given by

$$M_B + \mu(z, \text{cosmology}) - \sum_\lambda \frac{\partial(m_B + \alpha x_1 - \beta c)}{\partial \text{ZP}_\lambda} \Delta\text{ZP}_\lambda \; . \tag{A.9}$$

It is derived in the same way as in the previous section, with the substitutions $x_1 \rightarrow x_1 + \sum_\lambda \frac{\partial x_1}{\partial \text{ZP}_\lambda} \Delta\text{ZP}_\lambda$ and $c \rightarrow c + \sum_\lambda \frac{\partial c}{\partial \text{ZP}_\lambda} \Delta\text{ZP}_\lambda$. The model for the true offset of each zeropoint is simply ΔZP. Thus,

$$H = \begin{pmatrix} H_\mu \\ I \end{pmatrix} .$$

The upper block of U^{-1} is given by

$$U^{-1}_{\text{upper block}} = V_\mu^{-1} - V_\mu^{-1} H_\mu (V_{\Delta\text{ZP}}^{-1} + H_\mu^T V_\mu^{-1} H_\mu)^{-1} H_\mu^T V_\mu^{-1} \; ; \tag{A.10}$$

none of the other blocks enter into the χ^2. Inverting this block (see Hager (1989)) gives:

$$U = V_\mu + H_\mu V_{\Delta\text{ZP}} H_\mu^T \tag{A.11}$$

Equation A.11 gives us the terms we must add to the supernova distance modulus errors to correctly take the zeropoints into account.

A.2 Weight of a Spectrum with Nearest-Neighbor Correlations

Suppose we have a spectrum with nearest-neighbor correlation ρ between wavelength elements. We can write the spectrum covariance matrix as

$$C = \sigma \cdot (I + A) \cdot \sigma \tag{A.12}$$

where $\sigma_{ij} = \sigma_i \delta_{ij}$, I is the identity matrix, and $A_{ij} = \rho[\delta(|i - j| - 1)]$. We would like the total weight of the spectrum, the sum of C^{-1}. Writing

$$C^{-1} = \sigma^{-1} \cdot (I + A)^{-1} \cdot \sigma^{-1} \, , \tag{A.13}$$

we can focus on the $(I + A)^{-1}$ term. We begin by expanding this inverse as

$$(I + A)^{-1} = I + \sum_{k=1}^{\infty} (-1)^k A^k \tag{A.14}$$

We can now exchange the order of the matrix sum and series expansion and consider the sum of each term. The sum of I is N, while for very large matrices (so that we can ignore edge effects), the sum of A^k is $N(2\rho)^k$, which goes to zero if $|\rho| < 1/2$. The desired sum is then

$$\sum_{ij} (I + A)^{-1} = N \sum_{k=0}^{\infty} (-2\rho)^k = N/(1 + 2\rho) \tag{A.15}$$

for $|\rho| < 1/2$ as referenced in Section 6.3.1.

A.3 Spectral Principal Component Analysis

As discussed in Section 6.3.3, we use a principal component analysis to allow comparisons between spectra with limited wavelength coverage and non-negligible noise, as well as to help establish the dimensionality of the parameter space, so that $\Delta\chi^2$ values can be converted into probabilities. We have opted to perform this principal component analysis in $\log(\mathrm{flux})$ so that color variations can be more accurately modeled. As the signal-to-noise of most spectra is inadequate to simply take the log of the fluxes, we construct the principal components using an iterative fit.

We model each spectrum as

$$a_0 * c_0(\lambda) \exp[a_1 * c_1(\lambda) + a_2 * c_2(\lambda)] \tag{A.16}$$

where a_0 is the normalization, $c_0(\lambda)$ represents the mean, a_1 and a_2 are the projections onto the first and second components, and $c_1(\lambda)$ and $c_2(\lambda)$ are the first and second components.

We fit the mean and first component (0 and 1, above) and their projections first (with the second component fixed to zero). After convergence, we fit the mean and second component with the first component held fixed. This sequential procedure ensures that at every stage, the component we are fitting is the one that contributes the most variance remaining. We start versions of the fit with many randomly chosen initial values for the projections to ensure that we have a converged solution (the components are always initialized at zero). We exclude the models of Lentz et al. (2000) from training the components, but we do compute the projections to enable a quantitative comparison to SN SCP-0401.

We use an error floor to prevent extremely well-measured wavelength regions or spectra from dominating the analysis. The error floor required is that needed to obtain a χ^2 per degree of freedom of 1 for the residuals from the model. For our two-component analysis, this is S/N 5 per $\Delta\lambda/\lambda$ of 0.01 (a spectrum with $\Delta\lambda/\lambda$ of 0.001 would therefore be limited to S/N 1.6 per resolution element).

There is some ambiguity about how many principal components to use. Increasing the number allows for a smaller error floor (as more and more of the variance is described by the principal components). It also allows for better discrimination between spectra (e.g., spectra that are similar in the first two principal components may be dissimilar in the third). However, increasing the number also increases the $\Delta\chi^2$ values required for a given level of statistical significance. Two principal components are all that is necessary to fit almost all spectra to within the accuracy that the spectrum SN SCP-0401 has been measured; two are therefore used for the results of this work.

As a test, we also compute the probability of SN SCP-0401 being a Ia (see Section 6.3.3) using one component and three components. Our results are robust; we find 93% confidence using one component, 92% confidence using two, and 91% confidence using three components. It is important to note that we chose to use two components before seeing any of these probabilities.